Title

Development of Nanoflow High-Pressure Liquid Chromatography — Mass Spectrometry Methodologies and Application for Glycomic Biomarker Discovery

Permalink

https://escholarship.org/uc/item/6gf7s481

Author

Schindler, Ryan Lee

Publication Date

2024

Peer reviewed|Thesis/dissertation

Development of Nanoflow High-Pressure Liquid Chromatography – Mass Spectrometry
Methodologies and Application for Glycomic Biomarker Discovery

By

RYAN L. SCHINDLER
DISSERTATION

Submitted in partial satisfaction of the requirements for the degree of

DOCTOR OF PHILOSOPHY

in

Chemistry

in the

OFFICE OF GRADUATE STUDIES

of the

UNIVERSITY OF CALIFORNIA

DAVIS

Approved:

_____

CARLITO B. LEBRILLA, Chair

_____

GANG-YU LIU

_____

LEE-PING WANG

Committee in Charge

2024

i

ABSTRACT

Glycosylation is a keystone of mammalian cells found primarily on membrane proteins and lipids, extending into the extracellular space to form the outer-most membrane layer known as the glycocalyx. The physiological functions of glycans are still constantly being discovered in relation to specific glycan structures. These functions include alteration of protein tertiary structure, protection of the peptide backbone, and mediation of interactions. Each of these functionalities, namely the mediation of interactions, has been a recent focus in the field of glycomics. Glycans have been shown to play a significant role in signaling pathways, cancer pathology, neurodegeneration, immune response, and viral, bacterial, and fungal susceptibility pathology.

Glycan-mediated interactions are of unique interest in neural physiology and pathology. Previous research has shown aberrant glycosylation of both proteins and lipids to play a significant role in neurological diseases such as multiple sclerosis, Huntington's disease, and Alzheimer's disease. The complexity of elucidating pathology mechanisms stems from the diversity of glycan structures specific to each cell type and how they shape interactions *in vivo*.

Developing analytical methodologies that provide sensitive and reproducible profiles with structural information is critical to elucidate the mechanisms behind glycan interactions. The sheer structural diversity in glycans and their untemplated biosynthesis makes this challenging. The development of robust high-performance liquid chromatography-mass spectrometry workflows capable of generating structural profiles and their application was the primary focus presented in this work.

TABLE OF CONTENTS

Chapter III. Profiling Intact Glycosphingolipids with automated structural annotation and quantitation from human samples with Nanoflow Liquid Chromatography Mass Spectrometry

ABBREVIATIONS

Glc: Glucose

Gal: Galactose

Man: Mannose

Fuc: Fucose

GlcNAc: N-acetylglucosamine

GalNAc: N-acetylgalactosamine

Neu5Ac: N-acetylneuraminic acid

OAc – O-Acetylation

Lac: Lactonization

ER: Endoplasmic reticulum

Asn: Asparagine

Ser: Serine

Thr: Threonine

HM: High-mannose

H: Hybrid

C: Complex

F: Fucosylated

S: Sialylated

SF: Sialofucosylated

Cer: Ceramide

SPT: Serine palmitoyl transferase

KDSR: 3-Ketodyhydrosphingosine reductase

CerS: Ceramide synthase

DES: Dihydroceramide desaturase

FAD: Fatty acid desaturase

Cer-1P: Ceramide-1-phosphate

SM: Sphingomyelin

GSL: Glycosphingolipid

UGCG: Ceramide glucosyltransferase

UGT: Ceramide glucosyltransferase

GalCer: Cerebroside galactose ceramide

GlcCer: Cerebroside glucose ceramide

LacCer: Lactose ceramide

GBD: glycan-binding domain

mAb: Monoclonal antibody

IgG: Immunoglobulin G

Fc region: Fragment crystallizable region

S protein: Spike protein of SARS-CoV-2

Siglec: sialic acid binding immunoglobulin-like lectins

RTK: Receptor tyrosine kinase

EGFR: Epithelial growth factor receptor

AB42: Amyloid-beta 42 peptide

FGFR: Fibroblast growth factor receptor

TrkA: Tropomyosin receptor kinase A

C-Met: Mesenchymal-epithelial transition factor

PDGF: Platelet-derived growth factor

VEGF: Vascular endothelial growth factor

IR: Insulin receptor

PNGase F: Peptide - N -Glycosidase F

SPE: Solid phase extraction

LC: Liquid chromatography

ESI: Electrospray ionization

MS: Mass spectrometry / Mass spectrometer

nHPLC: Nanoflow high-pressure liquid chromatography

m/z: Mass-to-charge ratio

ppm: part per million

TOF: Time-of-Flight

CID: Collision-induced dissociation

CNS: Central nervous system

AD: Alzheimer's disease

hiMG: Human induced pluripotent stem cells-derived microglia

AβO: Aβ oligomer

LPS: lipopolysaccharide

CHAPTER I

Introduction to Glycans and Liquid Chromatography-Mass Spectrometry

Overview.

All natural eukaryotic cells produce and express glycans (sugar chains) with various functional purposes, termed the glycocalyx. Highly abundant sources of glycans in mammals are found on proteins as post-translational modifications and as sphingolipids. Protein glycosylation occurs on asparagine with N-linked glycans and serine or threonine with O-linked glycans. The glycan moiety is typically attached to membrane-bound species that extend into the extra-cellular space, forming a dense and complex outer layer. The various functions these biomolecules are responsible for include proper protein folding, membrane organization, protection, and the mediation of intra- and inter-cellular interactions. Biosynthesis of glycan structures is initiated in the endoplasmic reticulum (ER) and, unlike DNA, RNA, and proteins, are constructed in an untemplated manner based on the cell-specific activities of various glycan processing enzymes. This untemplated biosynthesis leads to a complex distribution of structures that vary in monosaccharide composition, degrees of polymerization, and tertiary structure, which mediate specific and overlapping interactions. The complex nature of these glycan structures has required the development of unique analytical methodologies and tools for their study. Liquid Chromatography - Mass spectrometry has been the most widely adopted instrumentation used in glycomic analysis due to its capability of separating structures in complex biological matrices to determine the overall glycan composition, quantitation, and elucidation of structural information.
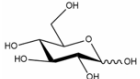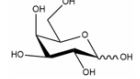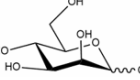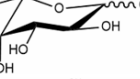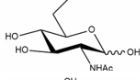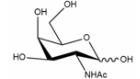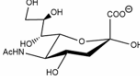
This introductory chapter first provides a background on the composition of mammalian glycans, where they are expressed, how they are synthesized, and their importance in biological

functions. Lastly, the chromatographic and mass spectrometric tools used to characterize the

glycocalyx will be discussed.

Monosaccharides in the human glycocalyx.

Glycans, or carbohydrates, are polymers constructed from glycosidic-bound monosaccharides, with oligosaccharides characterized as 1 to 20 linked monomer units and polysaccharides having > 20 degrees of polymerization.[1] Although hundreds of monosaccharides have been observed in nature, relatively few are used in constructing the human glycocalyx. Typically, hexoses (D-glucose, D-galactose, and D-mannose) and N-acetylated hexoses (N-acetyl-D-glucosamine and N-acetyl-D-galactosamine) are the most abundant monosaccharides found in glycans. 6-Deoxyhexoses (L-fucose) and nonulosonic acids (N-acetylneuraminic acid) are also common and tend to support or inhibit various interactions due to their unique structure and position of incorporation (Table 1.1).[2]

Table 1.1 The monosaccharides commonly found bound to human glycoproteins and glycolipids with abbreviations, representative symbols, and molecular structure.

Name	Abbreviation	Symbol	Molecular Structure
D-glucose	Glc		
D-galactose	Gal		
D-mannose	Man		
L-fucose	Fuc		
N-acetyl-D-glucosamine	GlcNAc		
N-acetyl-D-galactosamine	GalNAc		
N-acetylneuraminic acid	Neu5Ac		

Glycan linkages & modifications.

Glycan biosynthesis begins in the endoplasmic reticulum, where first glycan-lipid or glycan-protein linkages occur. Subsequent oligosaccharide elongation adds monosaccharides by a glycosidic linkage catalyzed by glycosyltransferase in either an α or β configuration (Figure 1.1).
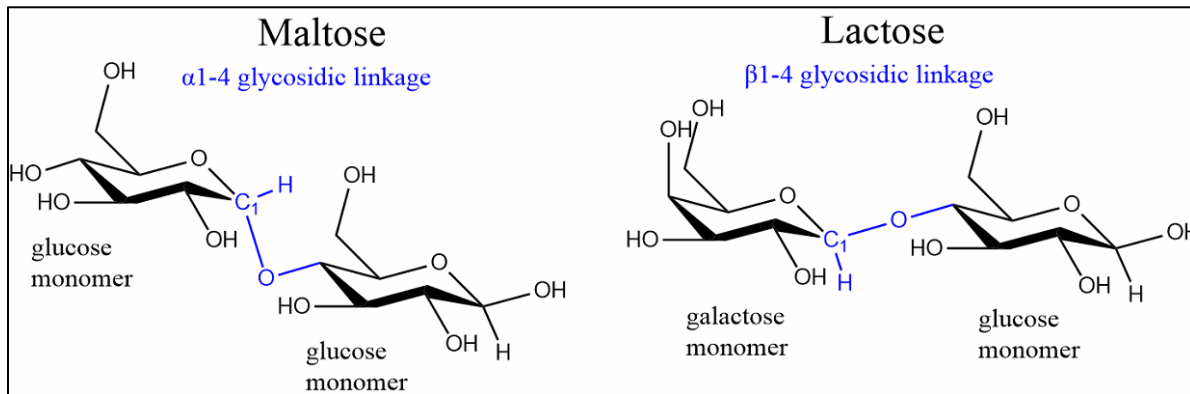
Figure 1.1 Example glycosidic linkages in the α- and β-conformation for simple disaccharides maltose and lactose.

Specific linkages are determined by the stereochemistry of the anomeric carbon (C1). This dynamic process is untemplated; final structures depend on substrate availability and enzyme activity. In addition to the structural diversity from monosaccharide structures and glycosidic linkages, modifications such as O-acetylation (OAc), sulfation, phosphorylation, and lactonization (Lac) are observed.[3]

N-Glycans

N-Glycans are a common post-translational modification contributing to protein folding and the overall tertiary structure. Biosynthesis begins with a covalently bound dolichol-phosphate to a protein's asparagine (Asn) with the sequence Asn-X-Ser/Thr, with X being any amino acid but proline. This first step of protein glycosylation occurs on the luminal side of the endoplasmic reticulum and provides the 14-monomer glycan structure from which all N-glycans are derived. Initial processing occurs first by hydrolyzing glycosidic bonds and removing glucose residues, which is accomplished by α-glucosidases I for the terminal α 1-2 residue and α-glucosidases II for the two subsequent α1-3 glucose.[4] The remaining structure, Man_9-$GlcNAc_2$-Asn, moves through the ER, where degradation-enhancing α-mannosidase I–like protein checks for correct protein folding. Next, glycoproteins are translocated to the Golgi, where they can skip further processing, resulting in a high-mannose structure (HM), Man_{9-5}-$GlcNAc_2$-Asn, or partially or fully processed to the N-glycan core structure, Man_3-$GlcNAc_2$-Asn, by mannosidase enzymes. Partial removal of terminal mannose results in a hybrid type (H) structure, whereas trimming down to the core sequence results in complex type (C) structures (Figure 1.2).
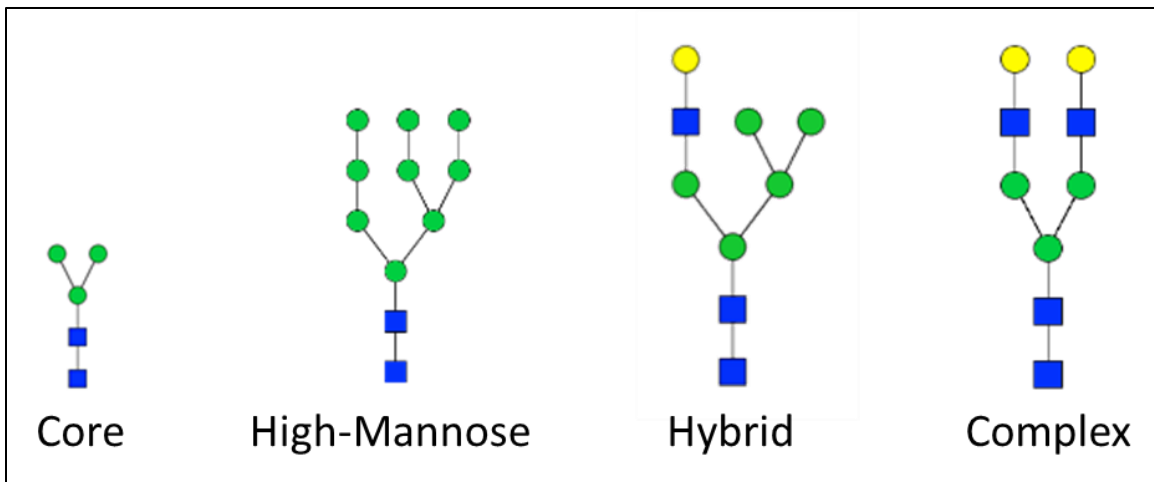
Figure 1.2 N-glycan structures, including the common core structure found in all N-glycans and structure types based on mannosidase processing of antennae.

The following N-glycan categorization refers to the number of antennae in complex structures where up to four branched antennae are possible, as well as GlcNAc bisection on the first core mannose (Figure 1.3).
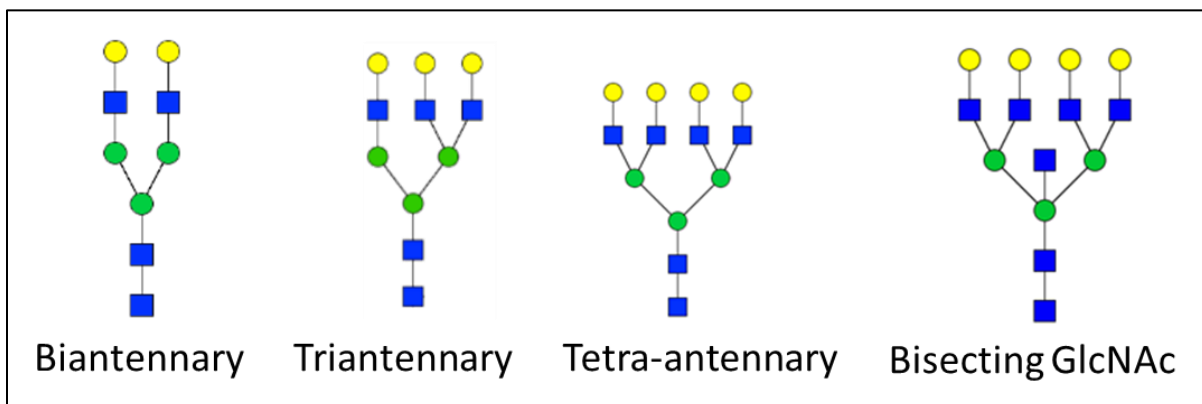
Figure 1.3 Complex type N-glycans categorization by antennae number and the bisecting type.

The last N-glycan categorization is based on the containment of fucose, sialic acid, or both. This distinction is made due to the increased functionality observed when these monosaccharides are incorporated into the glycan structure (Figure 1.4).[5]
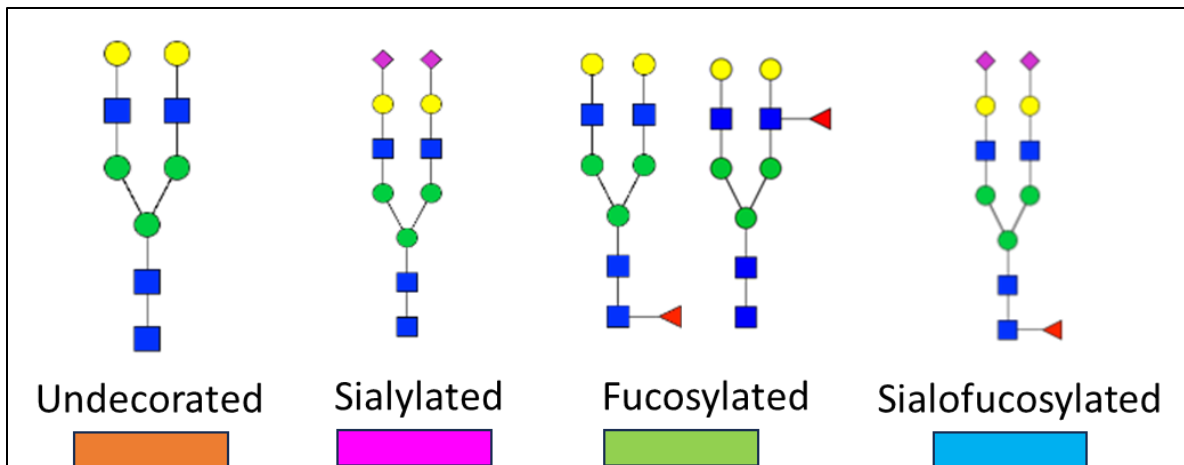
Figure 1.4 N-glycan categorization based on the incorporation of functional monosaccharides sialic acid (terminal) and fucose (core and branch).

Complex or hybrid N-glycans without fucose or sialic acid are termed undecorated. When sialic acid is incorporated, it is positioned at the terminal end of an antenna and mediates unique interactions due to its anionic moiety. Fucose can be bound on both the core and antennae. Core fucosylation typically promotes a glycan conformation that extends the structure away from the protein, encouraging interactions by increasing the structure's accessibility. Terminal fucosylation adds functionality for increased specificity of glycan binding substrates.

Glycosphingolipids

Sphingolipids are a category of amphipathic membrane lipids that contain a ceramide backbone positioned in the outer leaflet of the plasma membrane and a polar headgroup extending into the extra-cellular space. The two-tailed ceramide consists of a sphingoid base and N-linked acyl, both variable in chain length, unsaturated bonds, and degrees of hydroxylation. The second part of these bioactive molecules is the polar headgroup attached to C1 of the lipid, which can be a simple hydroxide, phosphate group, phosphocholine, glucose-galactose (cerebrosides), sulfated galactose (Sulfatides), or complex oligosaccharides like GM1 (Figure 1.5).[6]
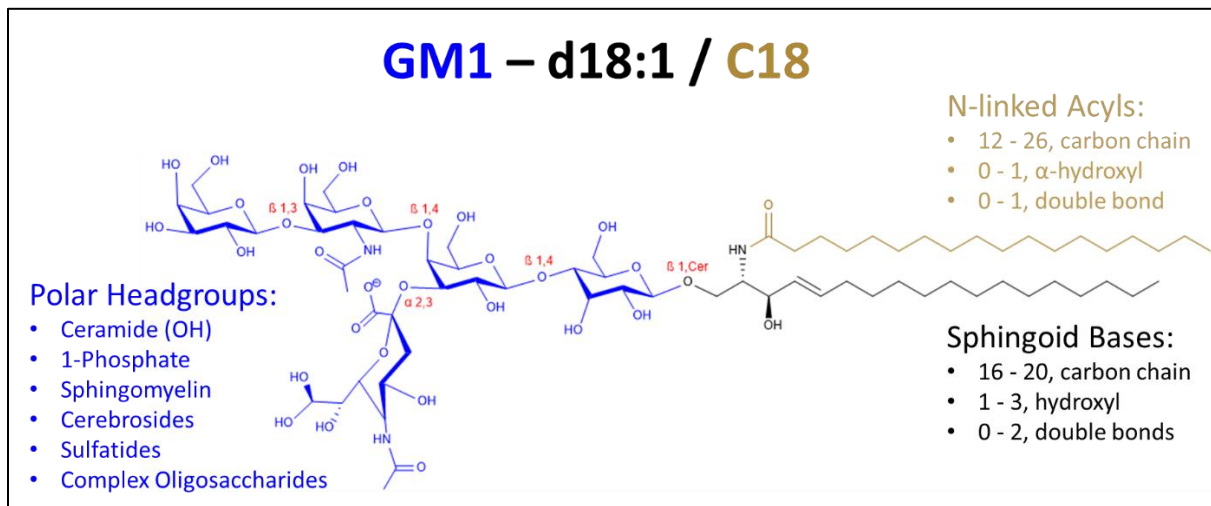
Figure 1.5 Example glycosphingolipid GM1 and sources of structural diversity observed in the headgroup, sphingoid base, and N-linked acyl group.

Biosynthesis of the lipid backbone occurs via either the de novo or salvage pathway. De novo sphingolipid synthesis begins in the endoplasmic reticulum, where the most common

sphingoid base, sphingosine (d18:1), is produced by several stepwise reactions. First, the decarboxylating condensation of L-serine and Palmitoyl-CoA (C16-CoA) by Serine palmitoyl transferase (SPT) occurs. SPT isoforms vary in specificity to produce additional sphingoid bases ranging from 16 to 20 carbons, with CN 20 commonly found in portions of the nervous system involved in motor function.[7] Next, 3-ketodyhydrosphingosine reductase (KDSR) reduces the c-3 oxygen producing dihydrosphingosine (d18:0), the precursor from which all other known sphingoid bases are derived. A family of ceramide synthases (CerS 1-6) attaches an N-linked fatty acid group ranging from 6 to 26 carbons to produce the two-tailed lipid dihydroceramide structures. Further processing by DES1 or bifunctional DES2 desaturate or hydroxylate C4 of the sphingoid base to produce ceramide (d18:1/FA) or 4-hydroxysphinganine (t18:0/FA).[8,9] Additional desaturation of the long-chain base's C14 by FAD3 results in 4-trans, 14-cis-Sphingediene (d18:2).[10] The last known naturally occurring sphingoid base, 6-hydroxy-4-sphingenine (t18:1), has an additional hydroxyl group at the C6 position and is found mainly in epidermal tissue.[11] The enzyme(s) that play a role in its biosynthesis are currently unknown (Figure 1.6).
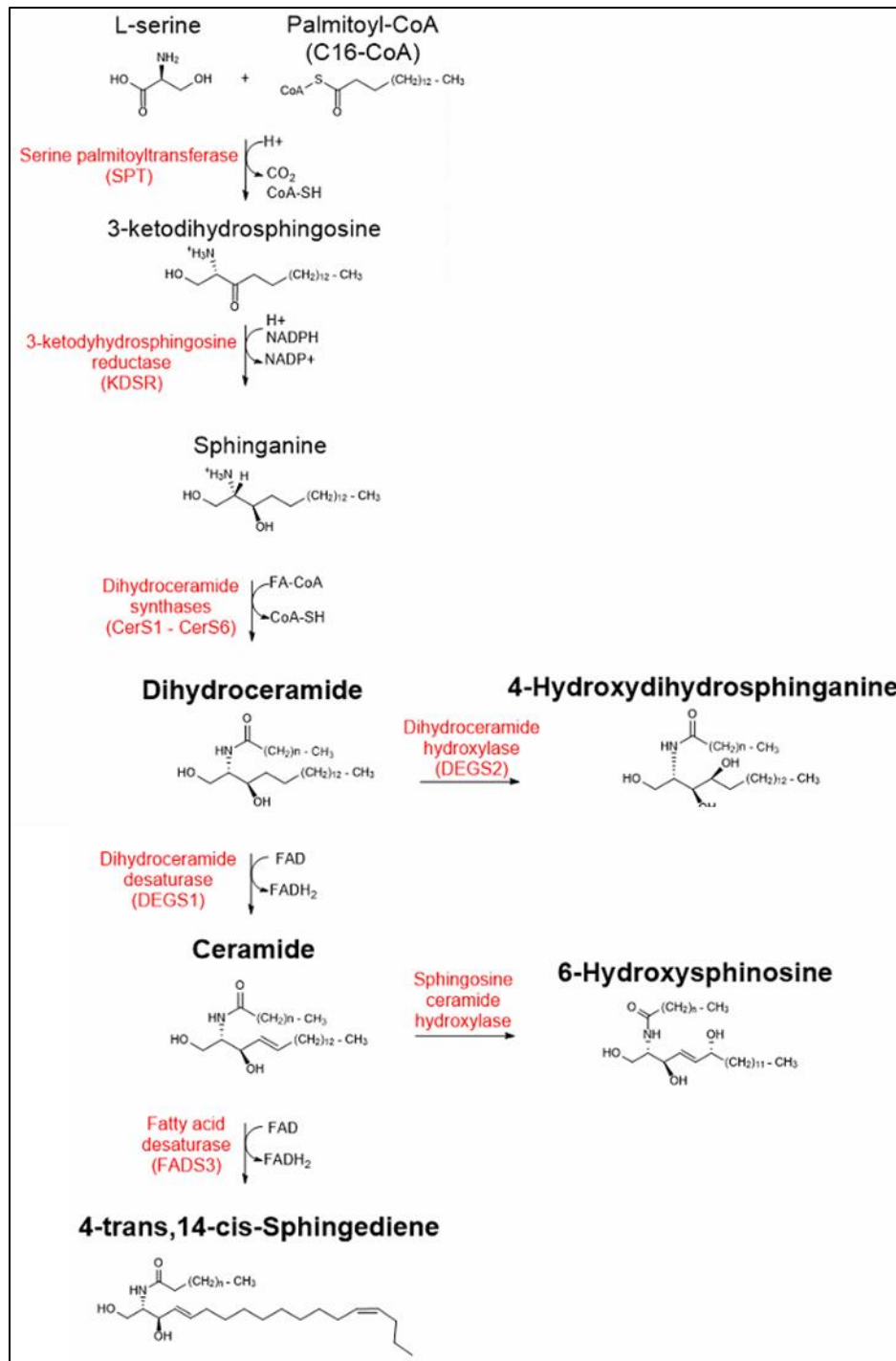
Figure 1.6 De novo synthesis with the substrates and enzymes involved in producing all sphingoid base structures observed in humans with specificity in position and stereochemistry of double bonds and hydroxyl groups.

Additional lipid modifications on the N-linked acyl group include the more common α-hydroxylation. ω-Hydroxylation occurring at the end of the tail is typically esterified and found in epithelial tissue. Desaturation, which typically occurs at the n-9 position of the acyl tail, is also possible.

Ceramide synthesis is also possible by the recycling of sphingolipids by what is referred to as the salvage pathway, which occurs in late endosomes and lysosomes. It involves several enzymes, including sphingomyelinases, glycosidases, ceramidases, and ceramide synthases, that hydrolyze the headgroup and de-acetylate the ceramide, resulting in sphingosine. Sphingosine can then be acetylated with a new fatty acid group, forming a lipid structure based on cellular needs. Recycling sphingolipids is a complex process for more than simply producing more ceramide, as phosphocholine, ceramides, and sphingosine have been shown to play an active role in cellular regulation as signaling molecules (Figure 1.7).[12]
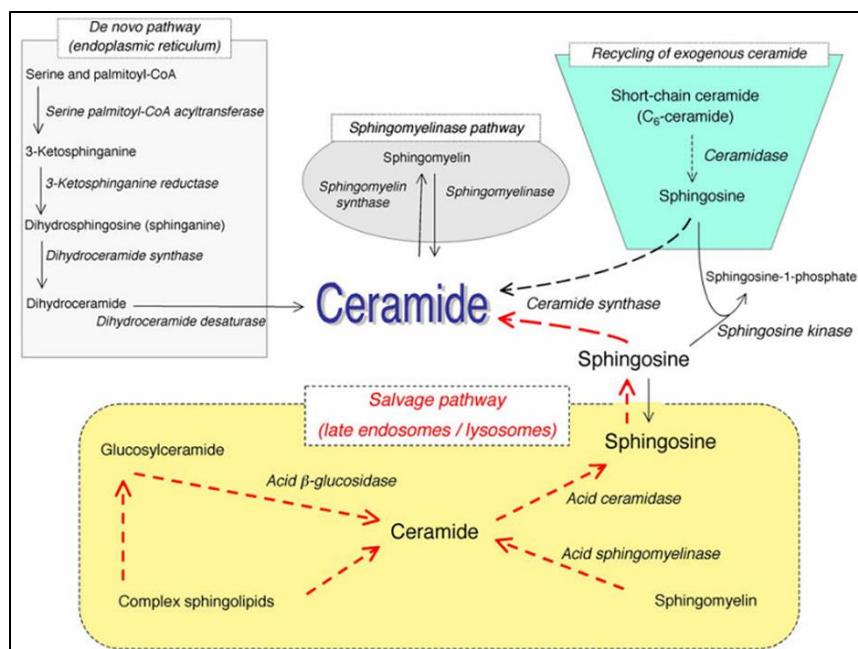
Figure 1.7 Flow chart of biosynthetic sphingolipid pathways, including de novo synthesis and the salvage pathway, which reuses sphingoid base structures. Adapted from: The sphingolipid salvage pathway in ceramide metabolism and signaling, 2008.

The nomenclature used to describe ceramides uses the same convention as typical fatty acid nomenclature. The sphingoid long-chain base is first described with a letter indicating the number of hydroxyl groups (mono-, di-, tri-, quat-) followed by a number for the total carbons and separated with a semicolon indicating the number of unsaturated bonds. The N-linked fatty acid is described following a slash with the carbon number (/C##); a # after a colon indicates the number of unsaturated bonds, and an "OH" indicates a hydroxyl group.

After the ceramide structure is completed, a headgroup can be added, which includes ceramide-1-phosphate (1P-), sphingomyelin (SM-), and glycans - referred to as glycosphingolipids (GSLs). GSL biosynthesis occurs in the Golgi where UDP-glucose or UDP-galactose is bound to the C1 of the ceramide through a glycosidic bond by ceramide

glucosyltransferase (UGCG) or ceramide glucosyltransferase (UGT), respectively. Structures with

a single monosaccharide incorporated are cerebrosides (GlcCer and GalCer). GalCer is the

precursor for structures referred to as the Gala-series, where typical structures include sulfated

(SM3) or sialylated (GM4) produced by Gal3-Sulfo Transferase I or Sialic acid Transferase-3Gal

V, respectively. GlcCer is elongated by ß4GalT6 with the addition of galactose to form lactosyl

ceramide (LacCer), the precursor for the ganglio-, globo-, isoglobo-, lacto-, neolacto-, and muco-

series GSLs (Figure 1.8).
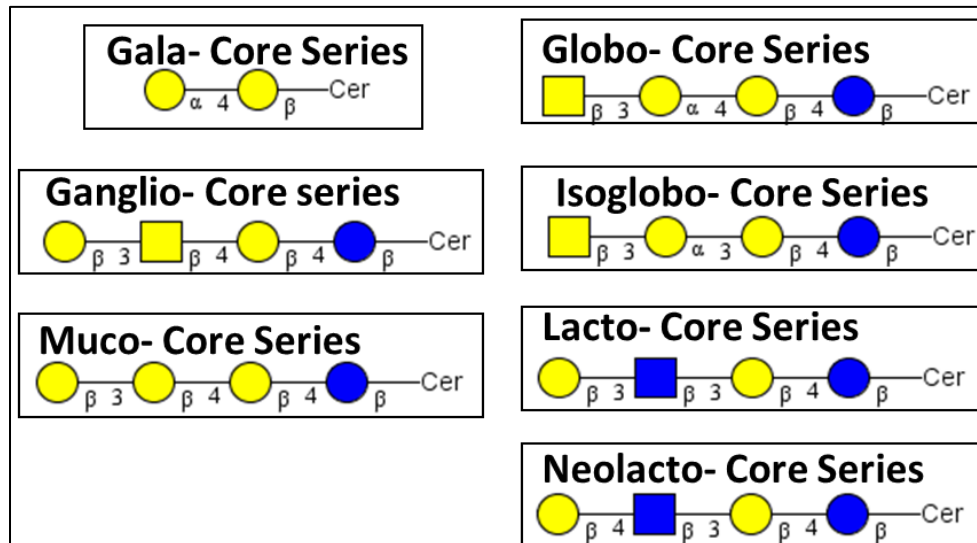
Figure 1.8 Ganglioside core structures expressed in humans based on sequence and glycosidic

bond stereochemistry.

Gangliosides are the most abundant glycosphingolipid structures in the central nervous

system and the only GSLs that contain sialic acids. Gangliosides are categorized into four main

groups based on the number of sialic acids bound to the first core galactose, with a- and b-

series gangliosides having the highest expression in the human brain (Figure 1.9).
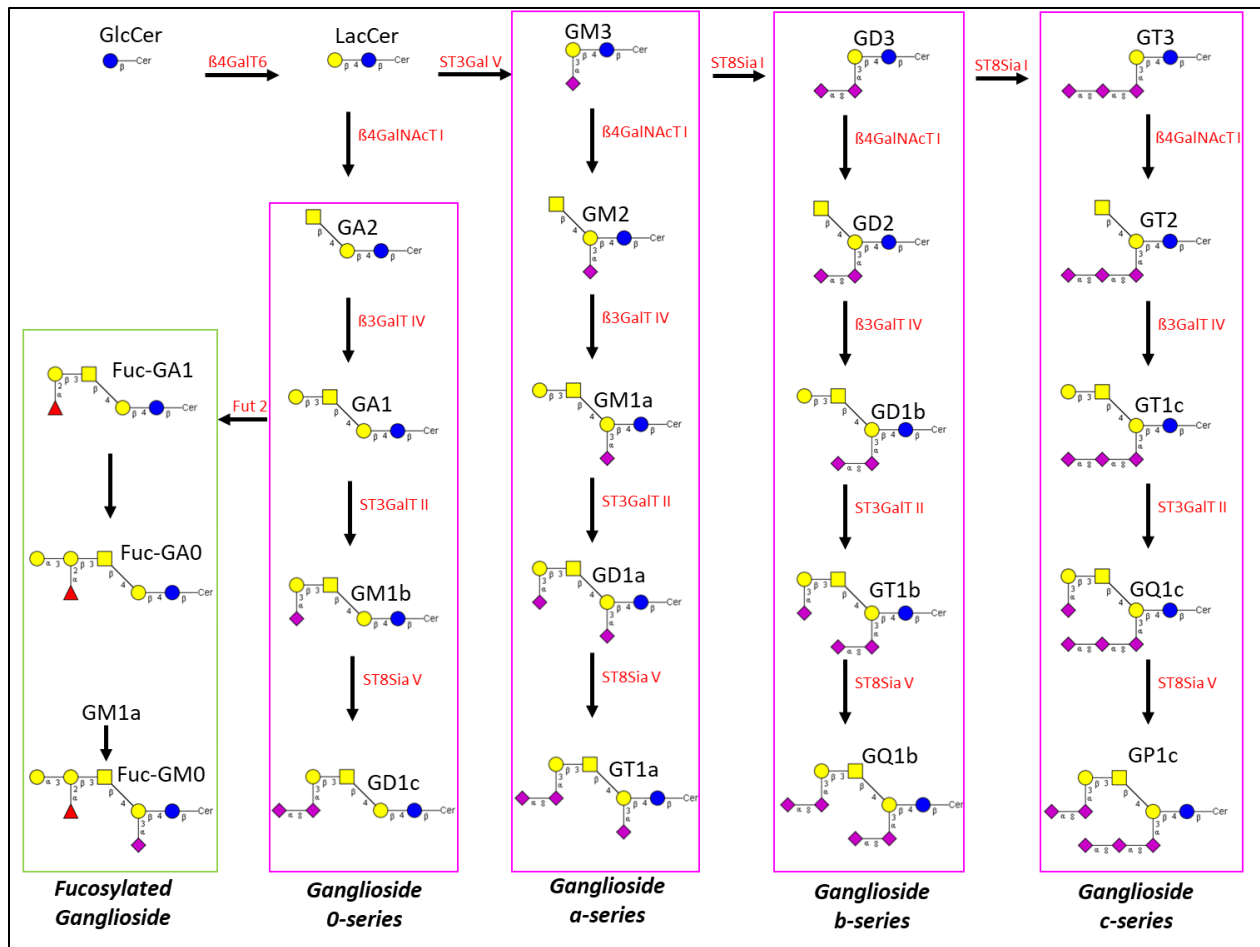
Figure 1.9 0-series, a-series, b-series, c-series, and fucosylated gangliosides, including the glycosyltransferase enzymes involved in their biosynthesis.

GSL nomenclature uses short-hand notation, which was termed at their first discovery. The first letter(s) describes the core structure, Gangliosides (G-), as an example. For gangliosides, the second letter represents the total number of neuraminic acid residues it contains. So, an oligosaccharide with a single sialic acid is denoted GM-. Next, a number describes the number of core neutral monosaccharides the structure contains, whereas GD1 describes a ganglioside with all four core monosaccharides and two sialic acid monomers.

Increasing digits correspond to truncation of the four monomer core, where GM3 contains two core neutral monosaccharides and a single sialic acid. Lastly, a lower-case letter describes what series a ganglioside is categorized under, where GD1a is a ganglioside with a complete core structure that contains two sialic acids of the a-series. Combining the headgroup and lipid nomenclature, an example GSL commonly found in human nervous tissue would be denoted GD1b – d18:1/C18.

Biological Functions of Glycans

Glycans are essential components of living cells, forming the glycocalyx that surrounds the cell and acts as a structural component for stability, protein folding, and protection. This dense outer shell is a physical barrier from invasive species such as viruses, bacteria, and fungi. Glycoproteins also use the glycan moiety to protect their polypeptide backbone by creating a steric hindrance that prevents protease activity. An essential function of glycans is their role in mediating interactions such as cellular recognition and modulation of signaling pathways. The proteins that bind to various glycan structures are broadly named lectins, which contain glycan-binding domains (GBDs) with specificities for both the monosaccharide sequence and glycosidic linkage.[13]

Monoclonal antibodies (mAB), such as immunoglobulin G (IgG), provide an excellent example of how N-glycosylation plays a prominent role in immune response where different glycan compositions affect the hydrodynamic radius, stability, and binding interactions.[14] IgG isoforms have a conserved glycosylation site (CH2-84.4) in the fragment crystallizable region (Fc region) that has been well characterized and found to express numerous glycoforms. Studies have found that incorporating specific glycan structures directly modulates the inflammatory immune response by promoting or inhibiting FcγRIII binding (Figure 1.10).[15] This phenomenon has major implications regarding the development of mAb therapies where the synthesis of amino acid sequence and the glycan structure are fine-tuned for individualized treatment.
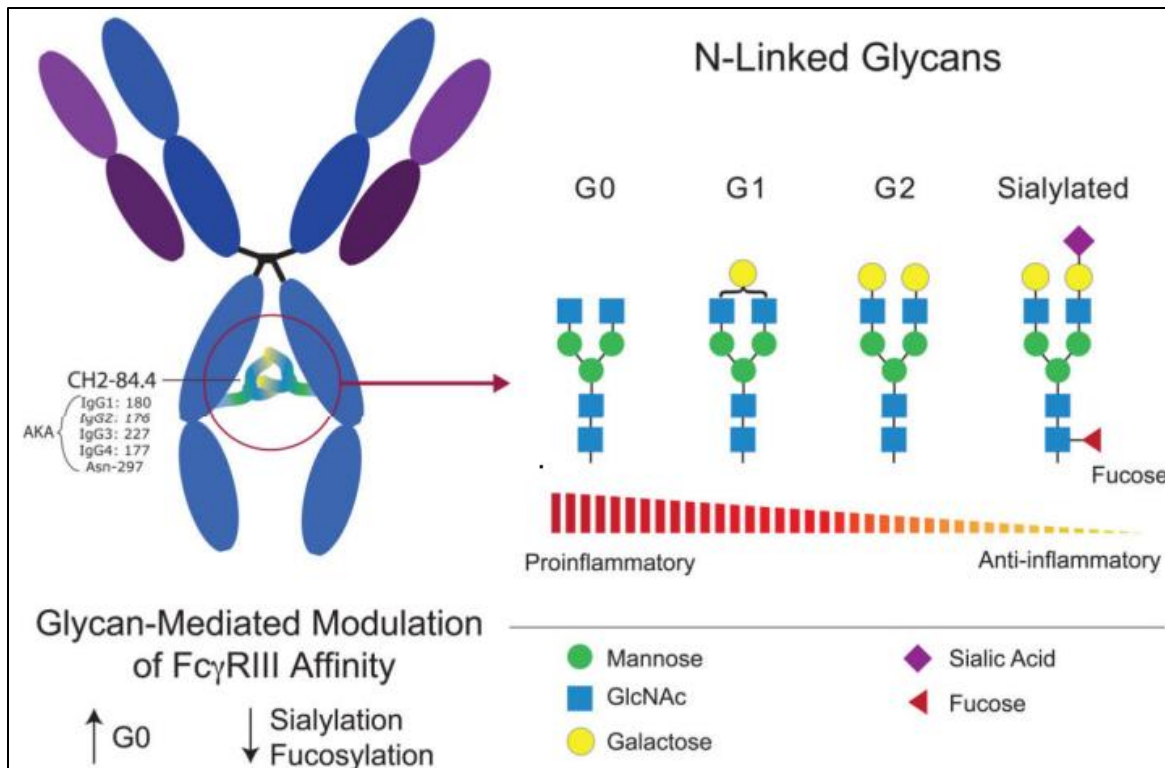
Figure 1.10 Ig heavy chain residue CH2-84.4 is post-translationally modified with the addition of an N-glycan, depicted here as a blue, green, and yellow Y-shaped structure between the two IgG heavy chains. This glycosylation site is conserved in all IgG subclasses (IgG1-4). To accommodate its CH2-84.4-linked glycan, IgG has a hydrophobic patch (not depicted). The CH2-84.4-linked glycan can be classified broadly as being either G0, G1, or G2. G0 glycans have a higher affinity for FcγRIII and are associated with a variety of autoimmune diseases. G0 glycans terminate with GlcNac residues and thus have zero galactose residues, hence their name. In contrast, G2 glycans terminate with two galactose residues. CH2-84.4 glycans can also be sialylated or fucosylated, which can bestow the antibody with anti-inflammatory properties because these modifications decrease Ig affinity for FcγRIII and also allow the antibody to interact with endogenous lectins on antigen presenting cells, e.g. sialylated antibodies likely bind to DC-SIGN. Adapted from: Glycans In The Immune System and The Altered Glycan Theory of Autoimmunity: A Critical Review, 2014.

Further, SARS-CoV-2, the virus responsible for the 2019 epidemic, provides an example of glycans' critical role in viral pathology. The spike protein (S protein) of SARS-CoV-2 is responsible for host-cell binding of the human ACE2 receptor and membrane fusion. This S protein-ACE2 interaction is the primary pathway for viral infection and a target in vaccine

development.[16] Glycoproteomic analysis of the S protein showed a highly glycosylated surface with 25 glycosites covering ~40% of the trimeric S protein.[17] Although expression of the S protein in different host systems produced consistent glycosites with a high degree of occupancy, the specific glycan structures produced depended on the processing enzymes specific to the system.[18] Functional studies focused on variable glycan structures and glycosite deletion mutations provided evidence of the importance of glycans in infectivity[19] and host immune system evasion[20] (Figure 1.11).
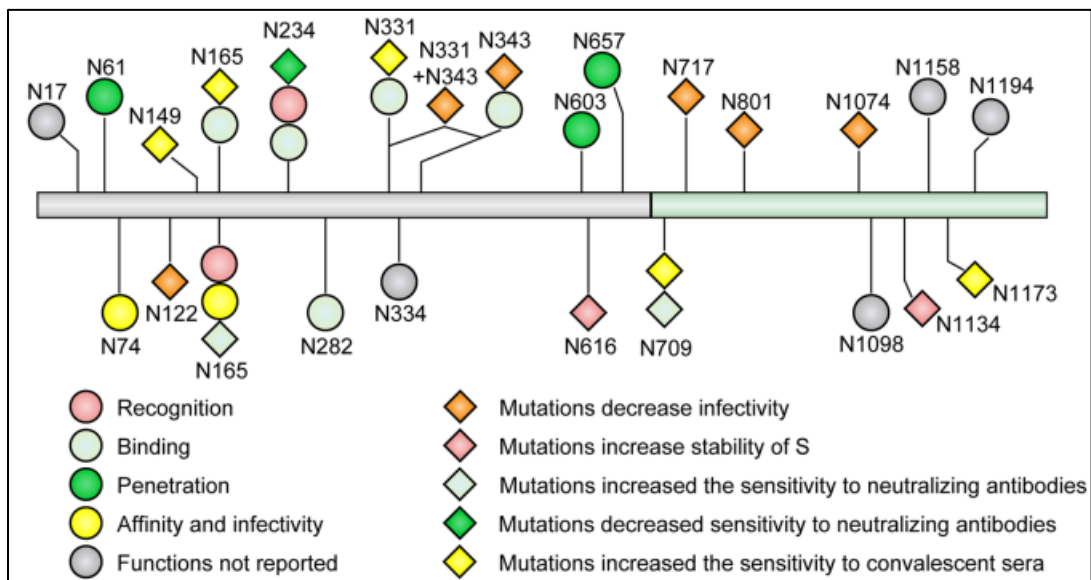
Figure 1.11 Glycosites of S protein and their functions. Different shapes and colors represent the corresponding functions, and the gray indicates that the functions of the sites are unknown. Adapted from: The glycosylation in SARS-CoV-2 and its receptor ACE2, 2021.

Siglecs (sialic acid binding immunoglobulin-like lectins) are a family of immunoregulatory cell-surface proteins that activate or deactivate the immune response upon binding to a glycan substrate.[21] Microglia, the CNS immune cells responsible for removing pathogens and damaged cells, express siglec-5/7-12/14 and siglec-3 (CD33), which regulate the neuroimmune response

upon binding.[22] Of note, increased expression of CD33 is correlated to a higher susceptibility to

AD where phagocytosis and the ability to clear misfolded proteins is inhibited upon ligand

binding, contributing to AD progression.[23] Myelinating oligodendrocytes in the CNS express

Myelin-associated glycoprotein (MAG, Siglec-4), which binds to terminal Neu5Ac α2-3 galactose

(GD1a, GT1b, etc.), in turn stabilizing the axon-myelin interface and inhibiting axon growth.[24,25]

The importance of siglecs for biological function is highlighted by their conservation among

mammals and the functional evolution observed in specific cell types (Figure 1.12).[26]
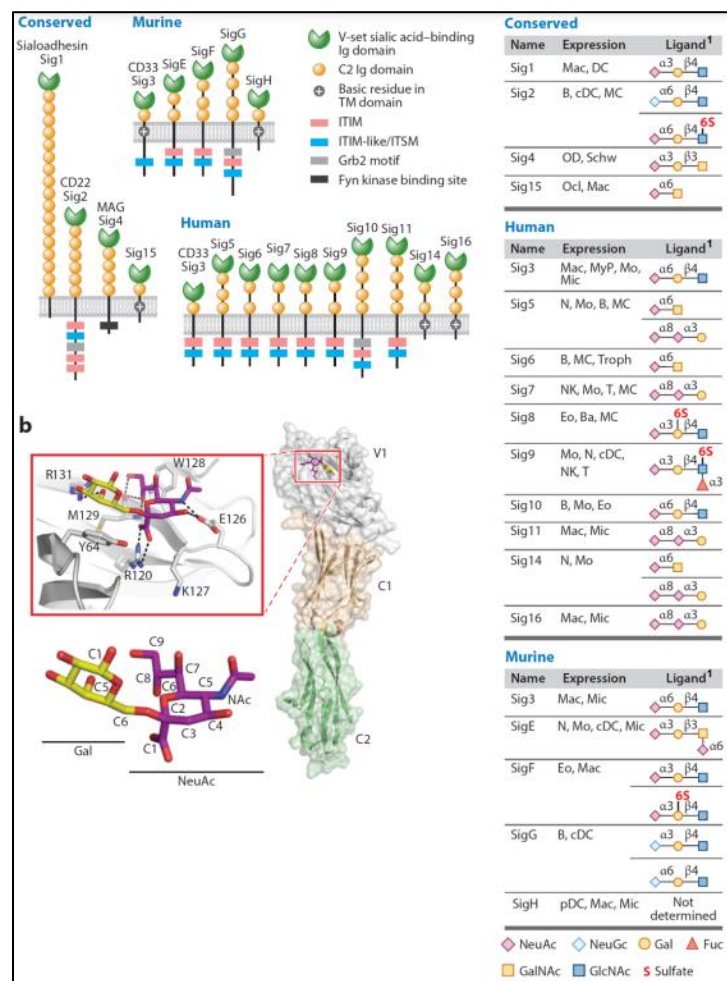
Figure 1.12 Human and murine Siglecs. (a) Structural features of functional human and murine Siglecs, including four members that are conserved in all mammals, and so-called CD33-related

Siglecs numbering five in mice and ten in humans (1, 2, 193). Each Siglec (Sig) has an N-terminal V-set immunoglobulin (Ig) domain that contains the conserved sialic acid–binding site and 1–16 C2 Ig domains. On the cytoplasmic side most Siglecs exhibit characteristic regulatory motifs including immunoreceptor tyrosine inhibitory motif (ITIM), ITIM-like, immunoreceptor tyrosine switch motif (ITSM), growth factor receptor-bound 2 (Grb2) motif, and a Fyn kinase binding site. Several other Siglecs contain positively charged amino acid residues in the transmembrane domain that can associate with activating adaptor proteins such as DAP12 with an immunoreceptor tyrosine activation motif (ITAM) (1, 2, 193, 224). (b) Crystal structure of a portion of human CD22 including the N-terminal V-set and two C-set Ig domains (right). An expanded view of the sialic acid–binding site with a bound ligand fragment (NeuAcα2–6Gal) shows interaction of the C-1 carboxyl group of the sialic acid with the conserved arginine (R120) found in all Siglecs (18). (c) Shown for each Siglec is its cell type expression and preferred natural sialoside ligand(s) (1, 35). Cell types are mainly white blood cells in the immune system, including B cells (B), basophils (Ba), conventional and plasmacytoid dendritic cells (cDC and pDC), Eosinophils (Eo), macrophages (Mac), mast cells (MC), microglia (Mic), monocytes (Mo), natural killer cells (NK), neutrophils (N), osteoclasts (Ocl), and T cells (T), and a few cell types outside the immune system such as oligodendrocytes (OD), Schwann cells (Sch), and placental trophoblasts (Troph). All Siglecs except Siglec-H are known to bind terminal sequences on glycans of glycoproteins and glycolipids, with some having high sequence specificity for their ligands (e.g., Sig2, Sig7, Sig8), while others exhibit a broader specificity (1). Abbreviations: MyP, myeloid progenitor; TM, transmembrane. Adapted from: Siglecs as Immune Cell Checkpoints in Disease, 2020.

Glycosphingolipids do not typically extend as far into the extracellular space as their glycoprotein counterparts but play a pivotal role in the biophysical membrane properties and organization. A unique behavior is observed in glycosphingolipids, where clustering occurs with cholesterol and membrane proteins to form bioactive microdomains on the outer leaflet of the plasma membrane. This clustering is due to several phenomena all related to their amphipathic structure. The ceramide backbone shows higher saturation than other membrane lipids, leading to tight, ordered stacking of sphingoid bases and acyl groups.[27] Secondly, the amide and hydroxyl moieties at the head of the ceramide promote clustering through electron donating and accepting interactions and stabilizing the lipid-water interface.[28] Lastly, the polar glycan headgroup promotes microdomain formation by significantly increasing the degree of

hydrophilic interactions with other GSLs and membrane proteins while also increasing the localized degree of hydration from surrounding water molecules.[29] This leads to the premise that glycan headgroup structures organize neighboring lipids and the bioactive proteins to create these highly functional domains responsible for numerous cellular processes. The central nervous system, where clustering into sub-synaptosomal regions of neurons, is highly enriched with gangliosides, which modulate the cellular influx of calcium, a key secondary messenger in neuronal signaling pathways.[30,31]

GSLs are also substrates for receptor tyrosine kinases (RTK), a family of N-glycosylated proteins involved in various complex cellular responses such as cell proliferation, adhesion, survival, and apoptosis.[32] A well-studied ganglioside-RTK interaction is the inhibition of epithelial growth factor receptor (EGFR) by ganglioside GM3 (Neu5Aca2-3LacCer). In short, upon GM3-EGFR binding autophosphorylation is inhibited, promoting the inactive conformation and resulting in anti-proliferation effects.[33] Interestingly, amyloid-beta 42 (AB42), a characteristic peptide which aggregates in AD, gave a positive signal that activated the EGFR pathway in animal models.[34] Although clinical trials using EGFR inhibitors showed poor efficacy in treating AD, the changes in EGFR signaling during the onset and progression of AD are still considered to play a significant role in the pathophysiology.[35] Additional ganglioside-interacting RTKs expressed in the human CNS which have been implicated to play a role in AD pathology include Fibroblast growth factor receptor (FGFR)[36], tropomyosin receptor kinase A (TrkA)[37], mesenchymal-epithelial transition factor (C-Met)[38], platelet-derived growth factor (PDGF)[39], vascular endothelial growth factor (VEGF)[40], and insulin receptor (IR)[41] (Figure 1.13).
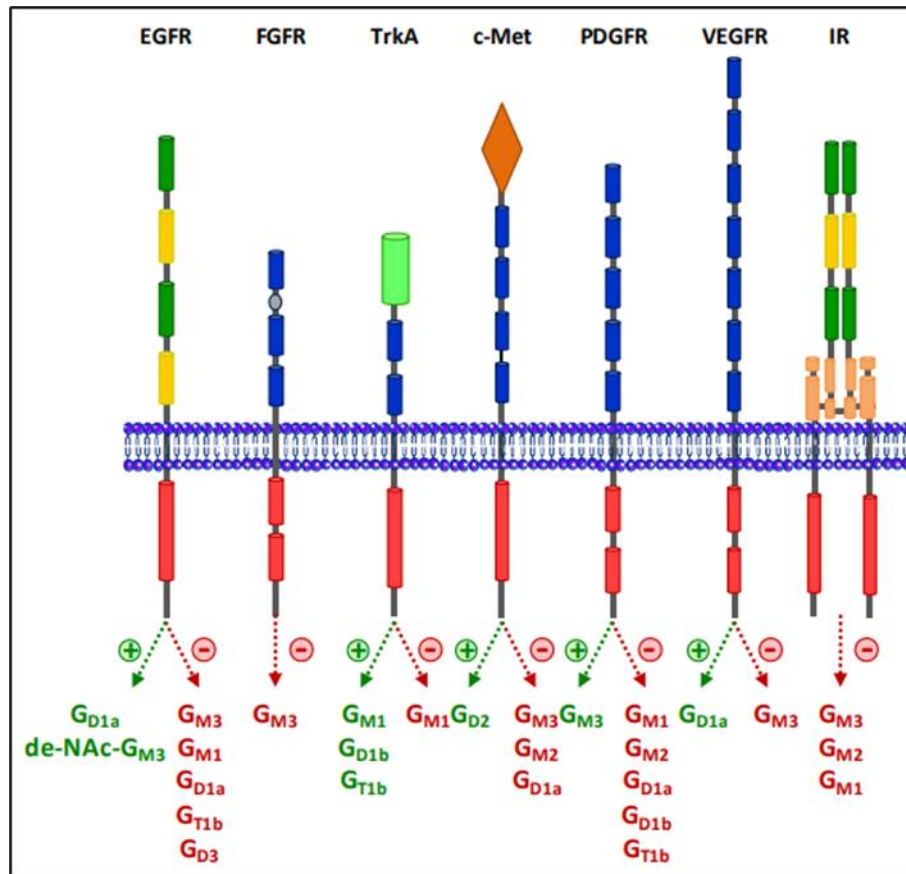
Figure 1.13 Receptor tyrosine kinase positive and negative signaling interactions with ganglioside structures. Adapted from: How Do Gangliosides Regulate RTKs Signaling, 2013.

With mounting evidence supporting glycans' essential role in biological systems, the need for analytical methodologies capable of deciphering the 'glycan code' is apparent. Difficulties characterizing the glycocalyx arise from the complex sample matrix observed in biological systems and the increased structural diversity when accounting for differences in glycan composition, glycosidic bond stereochemistry, and the substrate on which they are expressed. Liquid chromatography-mass spectrometry has become the preferred analytical technique due to its ability to separate unique glycoforms and matrix components and quantitatively generate structurally informative profiles with high sensitivity.

Nanoflow HPLC-MS/MS

Instrument Overview

High-performance liquid chromatography (HPLC) – electrospray ionization (ESI) – mass spectrometry (MS) is a technique used in the analysis of compounds within a complex matrix. Individual analytes are separated on a chromatographic column from other analytes and interferences. After separation, they are introduced from the liquid to gas phase and ionized by electrospray ionization. These gas phase ions are then detected by a mass spectrometer, where quantitative and structural information can be generated.

High-performance liquid chromatography background

High-performance liquid chromatography (HPLC) is a preferred technique for glycan analysis due to its ability to separate glycan structures and matrix interferences that would typically cause suppression of analyte signals and quantitative biases. The basic principle of chromatographic separation uses a solvent (mobile phase) that moves through a column packed with the stationary phase of a specific chemical structure. Molecules are separated based on their molecular structure, producing different affinities between the mobile and stationary phases, which affects the rate at which they partition. Using multiple solvents in an HPLC method, known as a gradient, allows for fine-tuned separations of closely related structures by gradually increasing the affinity of analytes to the mobile phase.

Multiple chromatographic formats differing in flow rates, pressures, and stationary phase chemistries have been used to separate glycan structures in complex mixtures. Due to the structural diversity of N-glycans and glycosphingolipids, these relatively low abundant

compounds are resolved into hundreds of peaks, resulting in the need for highly sensitive

instrumentation capable of detecting compounds at pico-mol concentrations. This necessity for

sensitivity makes nanoflow HPLC (nHPLC) an ideal chromatographic format that uses flow rates

between 100 to 1000 nL/min. These low flow rates improve the ionization of compounds by

minimizing the degree to which they are diluted before being introduced to the gas phase in

the ESI source.

Electrospray ionization background

ESI is used to generate gas phase ions from analytes that have been separated in liquid

chromatography for introduction to the mass spectrometer at atmospheric pressure. It is

commonly referred to as a soft-ionization technique due to its capability of producing intact,

multiply-charged precursor ions. The HPLC eluent, which contains the mobile phase and

separated analytes, flows through a capillary with a constant high-voltage current applied. In

positive mode, this current produces cations within the flowing solvent, sprayed in a fine mist

of charged droplets toward a counter electrode in the mass spectrometer. A heated drying gas

assists in the desolvation of the droplets, with two opposing forces governing the droplet's

behavior. The surface tension from interactions of the solvent molecules keeps the droplet

intact, producing the smallest possible surface area. Simultaneously, the cations within the

droplet repel each other with increasing force as the solvent is evaporated, following Coulomb's

law. Once the repulsive force exceeds the surface tension, the droplet splits in a coulomb

explosion producing smaller charged droplets.[45] This process is repeated until the solvent fully

evaporates, leaving the ionized precursor that traverses to the counter electrode in the mass

spectrometer (Figure 1.14). ESI using nanoliter flow rates requires more attention and

optimizations of source parameters, namely the nebulizer position, applied voltages, and drying gas flow and temperature to ensure reproducible data generation.
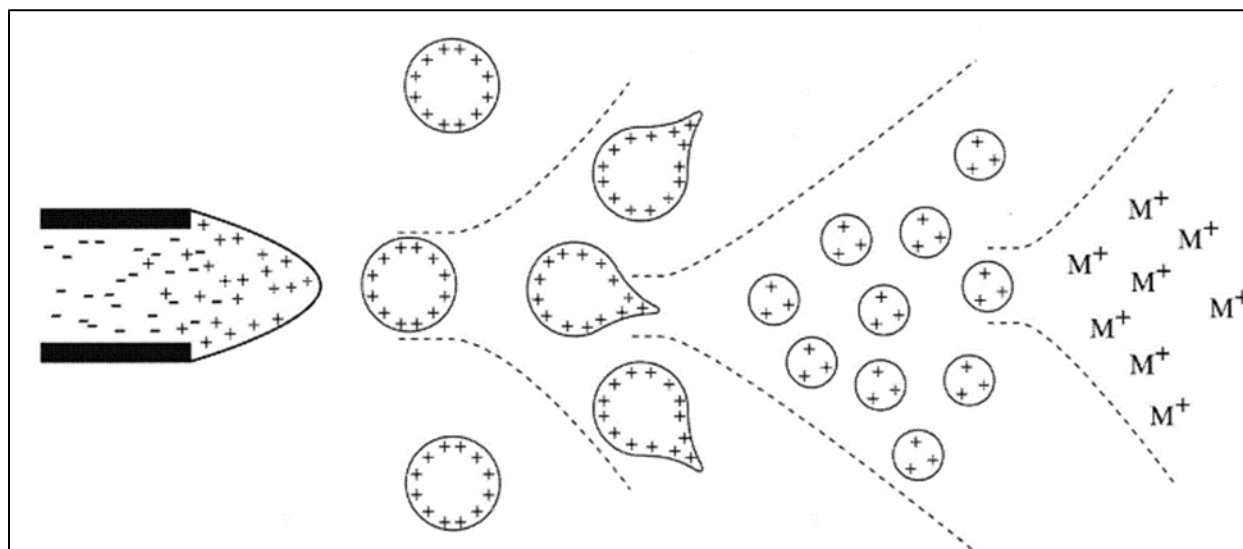
Figure 1.14 Depiction of positive mode electrospray ionization used to generate gas-phase cations for mass analyzation. Adapted from: Electrospray Ionization Mass Spectrometry: Principles and Clinical Applications, 2003.

Mass spectrometry background

Mass spectrometers (MS) are well-suited to analyze biological samples for their ability to distinguish gas-phase ionic species differing in their mass-to-charge ratio (m/z). The field of mass spectrometry was born with JJ Thompson's invention, the parabola spectrograph, which employed parallel magnetic and electric fields to induce a deflection of ionic species passing through it with a specific path dependent on the ion's charge and mass. Today, these same concepts have been applied and evolved to develop modern instrumentation capable of detecting large biomolecules at femtomole concentrations with less than one part-per-million (ppm) mass accuracy.

Upon ionization in an electric field, an ion's potential energy $\{E_p = ez\,U\}$ is converted to kinetic energy, $\{E_p = \frac{1}{2}m_i V^2 = ez\,U\}$ namely translational motion. This relationship connects experimental parameters (m/z & drift time) to instrumental parameters (distance s & voltage U).

$$V = \sqrt{\frac{2\,ez\,U}{m_i}} \qquad\qquad t_d = \frac{s}{\sqrt{2eU}} \times \sqrt{\frac{m_i}{z}} \qquad\qquad \frac{m_i}{z} = \frac{2\,e\,U\,t_d^2}{s^2}$$

In 1946, W.E. Stephens used this principle to create the first Time-of-Flight (TOF) mass analyzer, where an ion with a given m/z will have a measurable time in flight to travel a known distance. The initial TOF model was limited by the distance the ion could travel without colliding with gas-neutral gas molecules, referred to as the mean-free path, which determined its mass accuracy and, indirectly, its resolving power. Improvements to the initial design have been made, namely improved vacuum pumps, which minimize the number of collisions ions experience. Minimizing the number of gas molecules in the flight path directly improved the mass accuracy and allowed longer drift paths to increase the resolving capabilities. Commercial TOF mass analyzers have a mass accuracy < 5 ppm with a full width at half maximum resolving power of 60k.

The quadrupole mass analyzer, sometimes called a mass filter, is found in all modern mass spectrometers. It consists of four hyperbolic or cylinder-shaped rods with pairs held at the same potential with a direct current voltage (U, constant polarity) and alternating radiofrequency voltage (V, alternating current), producing asymptotes where the electric field is zero. Derivation U and V using the Mathieu equation produces instrumental parameters (a &q) for which a given m/z or m/z range will have a stable trajectory through the quadrupole. So,

with constant z-axis motion, ions can be selected to traverse through or be filtered out based on their m/z (Figure 1.15).[46]

The figure contains the following labels and equations:

$2U / V = 0.366$

0.237

Scan Line (Slope) $= \dfrac{a}{q} = \dfrac{2}{V}\dfrac{U}{} =$ Constant

$\underline{DC}$

$a = \dfrac{4\,ez\,U}{m_i r_o^2 \omega^2}$

m1

m2

m3

$2U / V =$ undefined

0.706

$\underline{AC\ (RF)} \quad q = \dfrac{2\,ez\,V}{m_i r_o^2 \omega^2}$

dq
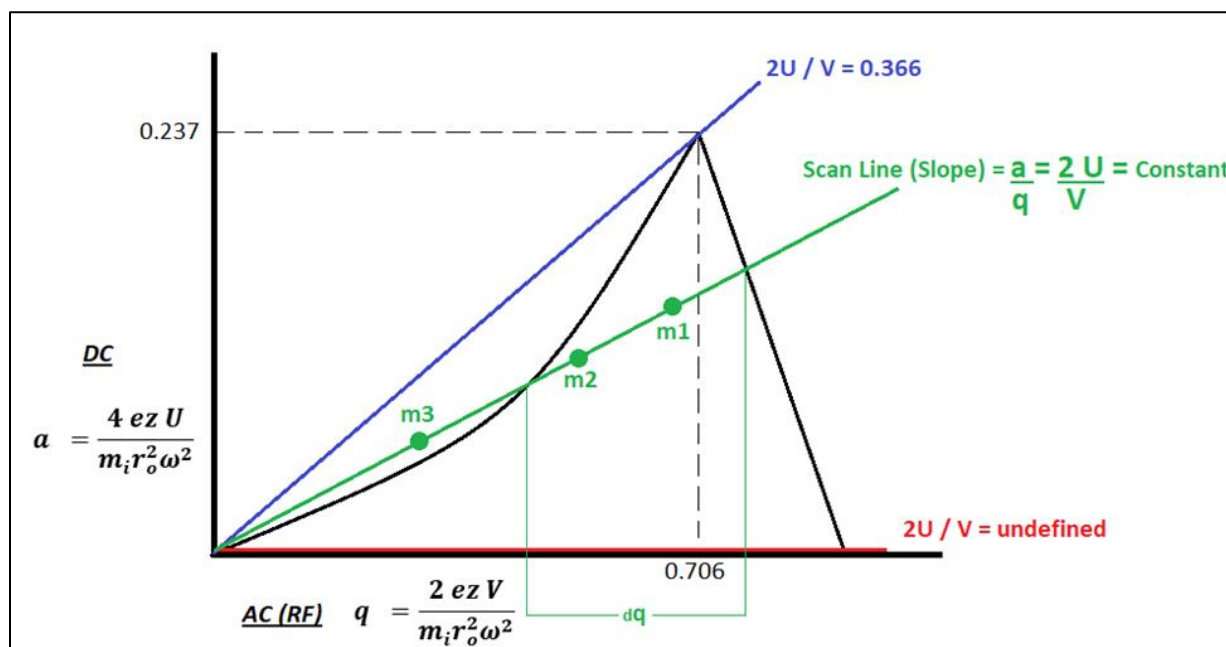
Figure 1.15 Mathieu stability diagram of instrumental parameters for a stable ion trajectory with a quadrupole mass analyzer.

Improvements to the quadrupole mass analyzer have been due to advances in mechanical accuracy in machining the rods and supports. Although these mass analyzers have poor mass accuracy and resolving power compared to other mass analyzers, their utility in mass filtering and adaptation to RF-only multipoles for ion transmission and collision cells has significantly increased the capabilities of modern-day mass spectrometers.

The development of RF multipoles was found to have steeper well potentials capable of generating a stable trajectory for wider m/z ranges. They are typically used in hybrid mass spectrometers as ion guides and collision cells. With the mass of a precursor being analyzed in MS_1, transmission through an RF multipole filled with inert gas will cause collisions that fragment the precursor ion, which can be detected with MS_2 to elucidate molecular structures.

This technique, termed collision-induced dissociation (CID), dramatically increases the breadth

of information a mass spectrometer can generate.[47]

Bioanalytical glycomic analysis

Sample Overview

A robust sample preparation was required to characterize the glycocalyx with a single sample sourced from cells, tissues, or serum. Difficulties in optimizing one preparation for all sample types stem from the significant variability in chemical properties and abundances of N-glycans and GSLs between each sample type and the differences in their matrix. Additional challenges lie with limitations in sample availability, where the collection can be an invasive procedure while growing cells have limitations due to time and yield. These sample limitations generated the need for highly sensitive methodologies to analyze low-abundant compounds with limited starting material reproducibly.

Sample preparation

The plasma membrane, where most glycan interactions occur, is enriched for cell cultures and tissue samples. We have developed a workflow that lyses the sample and then employs a series of (ultra)centrifugation steps to remove nuclear, cytoplasmic, and membrane-associated compounds using density gradients (Figure 1.16).[42]
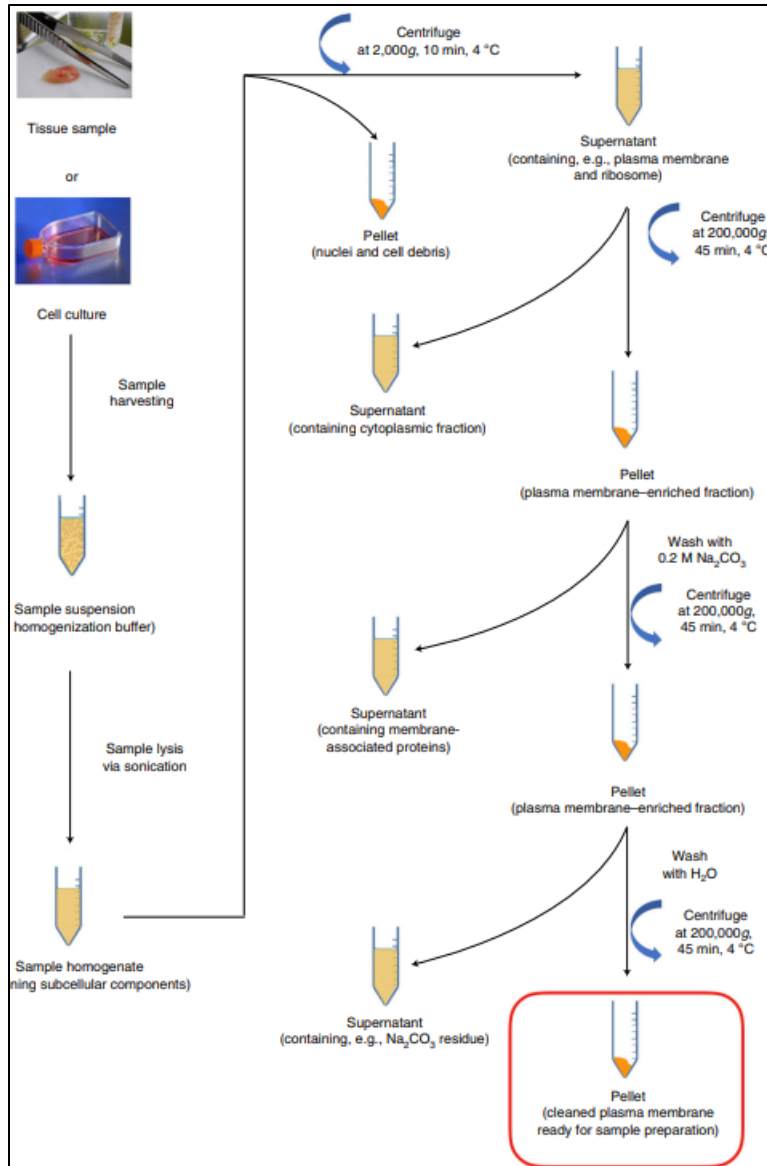
Figure 1.16 Plasma membrane enrichment for cells and tissues for glycocalyx profiling. Adapted from: Comprehensive structural glycomic characterization of the glycocalyxes of cells and tissues, 2020.

After membrane enrichment, the sample is diluted with 50mM HEPES with 2mM TCEP and heated at 100°C for two minutes to denature the proteins, making the glycan-lysine bond more accessible. N-Glycans are then enzymatically hydrolyzed using Peptide-N-Glycosidase F

(PNGase F), separating the glycan structure and lysine's amine of the peptide backbone. Samples are placed in a water bath at 37°C to convert the reducing end amine to the aldehyde form, minimizing the number of isomeric species for future chromatographic separation. N-Glycans are extracted in the supernatant after ultracentrifugation at 200k g for 45 minutes; the membrane pellet is stored at -20 °C until GSLs are prepared. The fraction with N-glycans is further enriched with solid phase extraction (SPE) using a porous graphitic carbon sorbent to remove buffers and additional contaminants. Once purified, they are concentrated to dryness and stored at -20 °C until analysis (Figure 1.17).
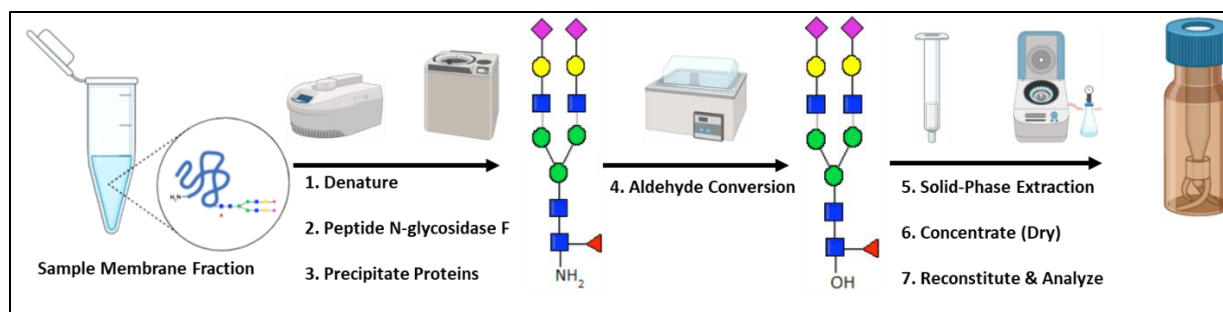
Figure 1.17 The preparation of N-glycan samples from glycoproteins involving enzymatic hydrolysis from the peptide backbone and glycan enrichment by solid phase extraction.

The remaining membrane fraction from the previous step is further processed for GSL analysis. Samples are diluted with a freshly prepared solution of water/MeOH/CHCL3 (3/8/4, v/v/v%) and sonicated for 30 minutes to extract the membrane lipids. The lipid-containing supernatant is transferred to a fresh vial, and precipitated proteins are stored at -20 °C for future O-glycan or proteomic analysis. Adding 0.1M potassium chloride to the lipid fraction induces a bilayer separation of amphipathic lipids (GSLs and phospholipids) in the top aqueous-rich layer and hydrophobic lipids in the bottom chloroform layer. The hydrophobic fraction is

dried and stored for future lipidomic analysis, while SPE is employed to purify the aqueous fraction. C-8 sorbent SPE retains the GSLs through hydrophobic interactions with the ceramide tail, removing salts, buffers, and hydrophilic contaminants. The remaining GSL fraction is concentrated by vacuum centrifugation and stored at -20 °C until ready for analysis (Figure 1.18).
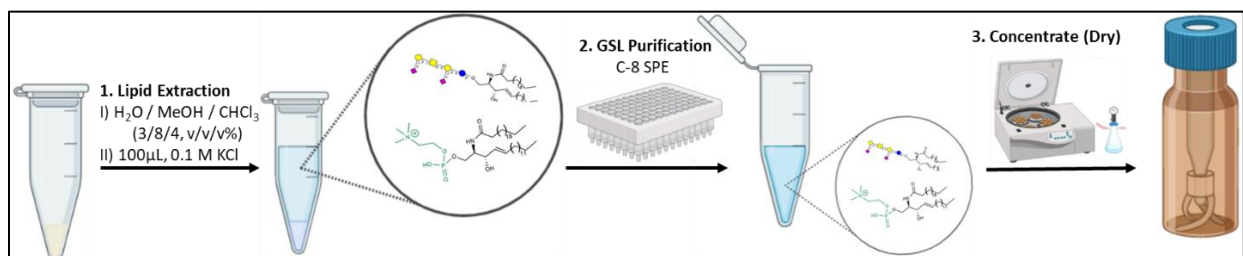
Figure 1.18 Preparation of glycosphingolipid samples by liquid-liquid extraction and enrichment with solid phase extraction.

N-Glycan chromatography

N-Glycans' separation uses a stationary phase of porous graphitic carbon (PGC) with mobile phases consisting of water and acetonitrile, a combination capable of separating isomeric structures. PGC is a unique stationary phase composed of layered 2-dimensional sheets that retain molecules by electron-donating and electron-accepting interactions through their partially filled P_z orbital.[43] The lone pairs of oxygen and carboxyl group of Neu5Ac interact with PGC through electron donation, inducing a dipole on the sorbent surface, resulting in stationary phase retention. Isomeric separation of these structures is due to the tertiary structure. N-glycans in a flat configuration can generate more simultaneous interactions, leading to a higher degree of retention and isomeric separation (Figure 1.19).[44] N-Glycans are

eluted as the mobile phase composition increases to higher acetonitrile concentrations, and the lone pair from the nitrogen atom displaces the PGC-glycan interactions.
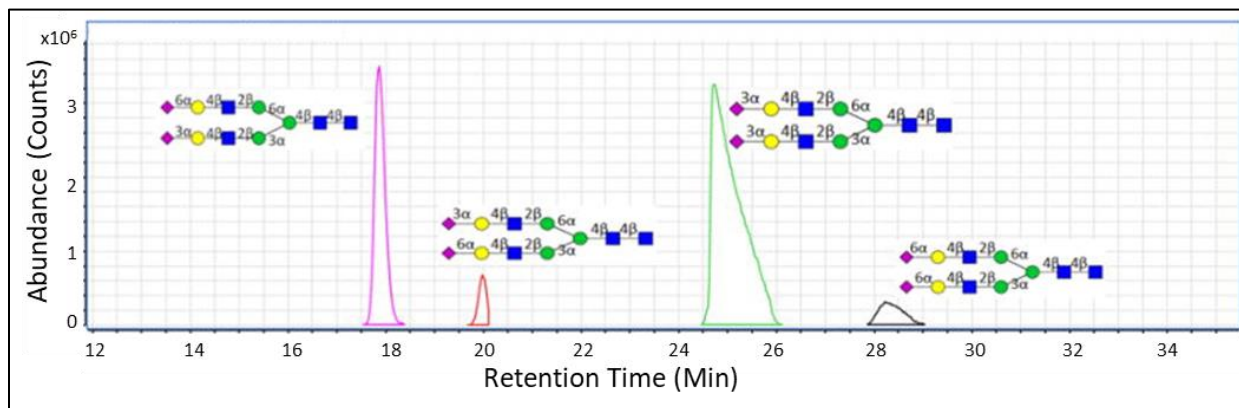
Figure 1.19 Porous graphitic carbon separation of isomeric N-glycans differing in sialic acid glycosidic bond stereochemistry. The retention mechanism is primarily dictated by the glycan composition with electron-withdrawing and -donating interactions between the lone pair electrons of the glycan and P-orbitals of the carbon stationary phase. Separation of isomeric glycans occurs due to differences in *shape where flatter structures have more simultaneous interactions, resulting in increased retention. Adapted from: A Method for In-Depth Structural Annotation of Human Serum Glycans That Yields Biological Variations, 2015.*

Glycosphingolipid chromatography

The separation of glycosphingolipids uses C-18 reverse-phase chromatography, which retains the analytes through hydrophobic interactions with the ceramide backbone. Separation of these biomolecules utilizes water, methanol, and isopropanol in the gradient elution. However, increased affinity to the mobile phase due to polar moieties on both the glycan and ceramide structure contribute to the resolution of compounds. Increasing sialic acid and neutral

monosaccharides on the headgroup and unsaturated bonds and hydroxyl groups on the lipid

decreases the overall retention of GSLs (Figure 1.20).
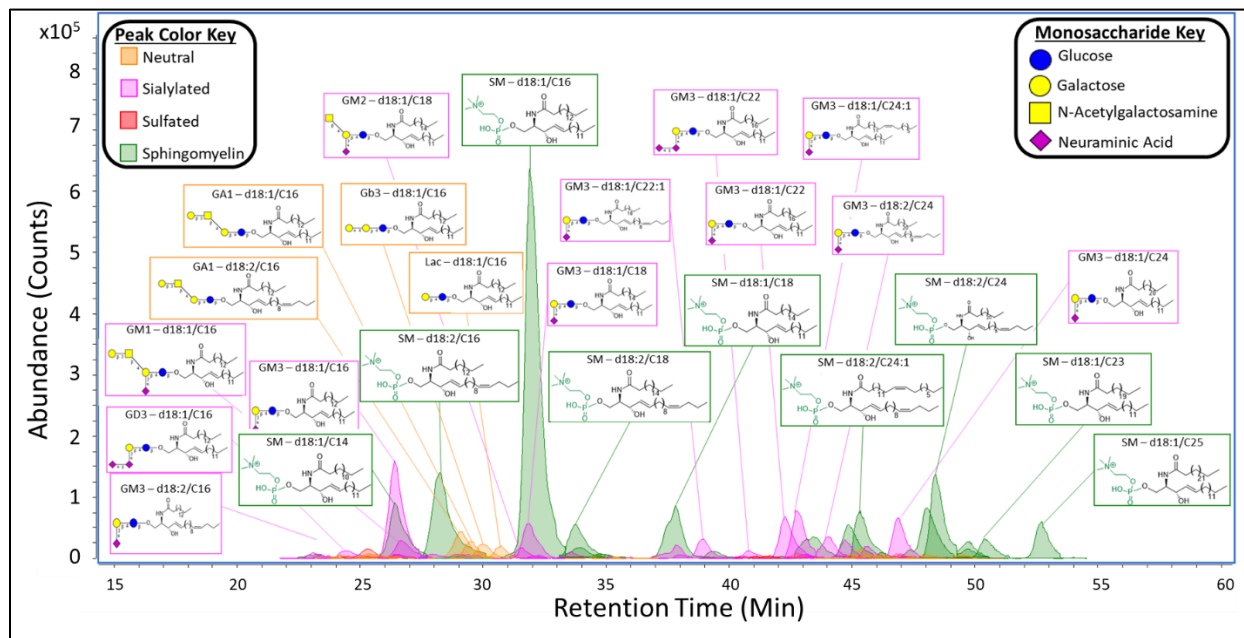
Figure 1.20 Separation of glycosphingolipids using reverse-phase C-18 nanoflow HPLC-Q/ToF. The profile was generated using a human serum pool, which is used as a quality control to monitor the sample preparation and instrument suitability. The major constituents included GM3, Lac, and SM headgroups.

Q/ToF Mass spectrometry for the analysis of glycans

After the separation of glycan analytes by nanoflow HPLC, the low pH eluent is

nebulized into charged droplets toward the ion transfer capillary. Each chromatographic

method required optimization of source parameters to ensure the drying gas temperature and

flow rate would completely desolvate the ionized glycan species while minimizing thermal

degradation. A counter electrode and ion guides generate an ion beam, which traverses to a

quadrupole mass analyzer where the highest abundant precursors are selected for untargeted

MS$_2$. The highly abundant precursors are then dissociated with N$_2$ gas using m/z-dependent

collision energies to generate structurally informative fragment ions. The fragment ions are

then pulsated, analyzed, and detected by the ToF, generating an MS$_2$ spectrum to identify

precursor structures (Figure 1.21).
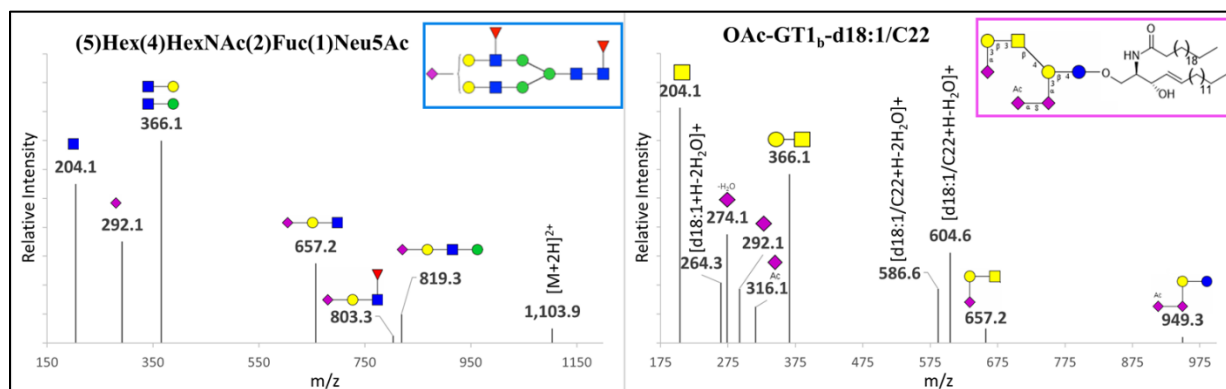
Figure 1.21 Example MS2 spectra from the dissociation of N-glycan (5)Hex(4)HexNAc(2)Fuc(1)Neu5Ac and glycosphingolipid OAc-GT1$_b$-d18:1/C22 with the collected glycan fragments used for identification.

REFERENCES

(1)   McNaught, A. D. Nomenclature of Carbohydrates. *Carbohydr Res* **1997**, *297* (1), 1–92. https://doi.org/10.1016/S0008-6215(97)83449-0.

(2)   El Khadem, H. S. *Carbohydrate Chemistry*; Elsevier, 1988. https://doi.org/10.1016/B978-0-12-236870-7.X5001-9.

(3)   Schnaar, R. L.; Sandhoff, R.; Tiemeyer, M.; Kinoshita, T. *Essentials of Glycobiology*, 4th ed.; Varki, C., Esko, J., Eds.; Cold Spring Harbor Laboratory Press: La Jolla, 2022.

(4)   Kornfeld, R.; Kornfeld, S. Assembly of Asparagine-Linked Oligosaccharides. *Annu Rev Biochem* **1985**, *54* (1), 631–664. https://doi.org/10.1146/annurev.bi.54.070185.003215.

(5)   Liu, Y.-C.; Yen, H.-Y.; Chen, C.-Y.; Chen, C.-H.; Cheng, P.-F.; Juan, Y.-H.; Chen, C.-H.; Khoo, K.-H.; Yu, C.-J.; Yang, P.-C.; Hsu, T.-L.; Wong, C.-H. Sialylation and Fucosylation of Epidermal Growth Factor Receptor Suppress Its Dimerization and Activation in Lung Cancer Cells. *Proceedings of the National Academy of Sciences* **2011**, *108* (28), 11332–11337. https://doi.org/10.1073/pnas.1107385108.

(6)   Merrill, A. H. Sphingolipid and Glycosphingolipid Metabolic Pathways in the Era of Sphingolipidomics. *Chemical Reviews*. October 12, 2011, pp 6387–6422. https://doi.org/10.1021/cr2002917.

(7)   Davis, D. L.; Mahawar, U.; Pope, V. S.; Allegood, J.; Sato-Bigbee, C.; Wattenberg, B. W. Dynamics of Sphingolipids and the Serine Palmitoyltransferase Complex in Rat Oligodendrocytes during Myelination. *J Lipid Res* **2020**, *61* (4), 505–522. https://doi.org/10.1194/jlr.RA120000627.

(8)   Ota, A.; Morita, H.; Naganuma, T.; Miyamoto, M.; Jojima, K.; Nojiri, K.; Matsuda, J.; Kihara, A. Bifunctional DEGS2 Has Higher Hydroxylase Activity toward Substrates with Very-Long-Chain Fatty Acids in the Production of Phytosphingosine Ceramides. *Journal of Biological Chemistry* **2023**, *299* (4). https://doi.org/10.1016/j.jbc.2023.104603.

(9)   Mizutani, Y.; Kihara, A.; Igarashi, Y. Identification of the Human Sphingolipid C4-Hydroxylase, HDES2, and Its up-Regulation during Keratinocyte Differentiation. *FEBS Lett* **2004**, *563* (1–3), 93–97. https://doi.org/10.1016/S0014-5793(04)00274-1.

(10)   Karsai, G.; Lone, M.; Kutalik, Z.; Thomas Brenna, J.; Li, H.; Pan, D.; von Eckardstein, A.; Hornemann, T. FADS3 Is a Δ14Z Sphingoid Base Desaturase That Contributes to Gender Differences in the Human Plasma Sphingolipidome. *Journal of Biological Chemistry* **2020**, *295* (7), 1889–1897. https://doi.org/10.1074/jbc.AC119.011883.

(11)   Robson, K. J.; Stewart, M. E.; Michelsen, S.; Lazo, N. D.; Downing, D. T. 6-Hydroxy-4-Sphingenine in Human Epidermal Ceramides. *J Lipid Res* **1994**, *35* (11), 2060–2068. https://doi.org/10.1016/s0022-2275(20)39952-1.

(12)   Kitatani, K.; Idkowiak-Baldys, J.; Hannun, Y. A. The Sphingolipid Salvage Pathway in Ceramide Metabolism and Signaling. *Cellular Signalling*. June 2008, pp 1010–1018. https://doi.org/10.1016/j.cellsig.2007.12.006.

(13) Mattox, D. E.; Bailey-Kellogg, C. Comprehensive Analysis of Lectin-Glycan Interactions Reveals Determinants of Lectin Specificity. *PLoS Comput Biol* **2021**, *17* (10). https://doi.org/10.1371/journal.pcbi.1009470.

(14) Zheng, K.; Bantog, C.; Bayer, R. The Impact of Glycosylation on Monoclonal Antibody Conformation and Stability. *MAbs* **2011**, *3* (6). https://doi.org/10.4161/mabs.3.6.17922.

(15) Maverakis, E.; Kim, K.; Shimoda, M.; Gershwin, M. E.; Patel, F.; Wilken, R.; Raychaudhuri, S.; Ruhaak, L. R.; Lebrilla, C. B. Glycans in the Immune System and The Altered Glycan Theory of Autoimmunity: A Critical Review. *Journal of Autoimmunity*. Academic Press February 1, 2015, pp 1–13. https://doi.org/10.1016/j.jaut.2014.12.002.

(16) Zhang, H.; Rostami, M. R.; Leopold, P. L.; Mezey, J. G.; O'Beirne, S. L.; Strulovici-Barel, Y.; Crystal, R. G. Expression of the SARS-CoV-2 ACE2 Receptor in the Human Airway Epithelium. *Am J Respir Crit Care Med* **2020**, *202* (2), 219–229. https://doi.org/10.1164/rccm.202003-0541OC.

(17) Grant, O. C.; Montgomery, D.; Ito, K.; Woods, R. J. Analysis of the SARS-CoV-2 Spike Protein Glycan Shield Reveals Implications for Immune Recognition. *Sci Rep* **2020**, *10* (1), 14991. https://doi.org/10.1038/s41598-020-71748-7.

(18) Gong, Y.; Qin, S.; Dai, L.; Tian, Z. The Glycosylation in SARS-CoV-2 and Its Receptor ACE2. *Signal Transduction and Targeted Therapy*. Springer Nature December 1, 2021. https://doi.org/10.1038/s41392-021-00809-8.

(19) Rudd, P. M.; Elliott, T.; Cresswell, P.; Wilson, I. A.; Dwek, R. A. Glycosylation and the Immune System. *Science (1979)* **2001**, *291* (5512), 2370–2376. https://doi.org/10.1126/science.291.5512.2370.

(20) HASÖKSÜZ, M.; KILIÇ, S.; SARAÇ, F. Coronaviruses and SARS-COV-2. *Turk J Med Sci* **2020**, *50* (SI-1), 549–556. https://doi.org/10.3906/sag-2004-127.

(21) Gonzalez-Gil, A.; Schnaar, R. L. Siglec Ligands. *Cells*. MDPI May 1, 2021. https://doi.org/10.3390/cells10051260.

(22) Galatro, T. F.; Holtman, I. R.; Lerario, A. M.; Vainchtein, I. D.; Brouwer, N.; Sola, P. R.; Veras, M. M.; Pereira, T. F.; Leite, R. E. P.; Möller, T.; Wes, P. D.; Sogayar, M. C.; Laman, J. D.; Den Dunnen, W.; Pasqualucci, C. A.; Oba-Shinjo, S. M.; Boddeke, E. W. G. M.; Marie, S. K. N.; Eggen, B. J. L. Transcriptomic Analysis of Purified Human Cortical Microglia Reveals Age-Associated Changes. *Nat Neurosci* **2017**, *20* (8), 1162–1171. https://doi.org/10.1038/nn.4597.

(23) Griciuc, A.; Serrano-Pozo, A.; Parrado, A. R.; Lesinski, A. N.; Asselin, C. N.; Mullin, K.; Hooli, B.; Choi, S. H.; Hyman, B. T.; Tanzi, R. E. Alzheimer's Disease Risk Gene Cd33 Inhibits Microglial Uptake of Amyloid Beta. *Neuron* **2013**, *78* (4), 631–643. https://doi.org/10.1016/j.neuron.2013.04.014.

(24) Collins, B. E.; Kiso, M.; Hasegawa, A.; Tropak, M. B.; Roder, J. C.; Crocker, P. R.; Schnaar, R. L. Binding Specificities of the Sialoadhesin Family of I-Type Lectins: Sialic Acid Linkage and Substructure Requirements for Binding of Myelin- Associated Glycoprotein, Schwann Cell Myelin

Protein, and Sialoadhesin. *Journal of Biological Chemistry* **1997**, *272* (27), 16889–16895. https://doi.org/10.1074/jbc.272.27.16889.

(25) McKerracher, L.; Rosen, K. M. MAG, Myelin and Overcoming Growth Inhibition in the CNS. *Frontiers in Molecular Neuroscience*. Frontiers Media S.A. September 7, 2015. https://doi.org/10.3389/fnmol.2015.00051.

(26) Duan, S.; Paulson, J. C. Siglecs as Immune Cell Checkpoints in Disease. *Annu Rev Immunol* **2020**, *38* (1), 365–395. https://doi.org/10.1146/annurev-immunol-102419-035900.

(27) Arumugam, S.; Schmieder, S.; Pezeshkian, W.; Becken, U.; Wunder, C.; Chinnapen, D.; Ipsen, J. H.; Kenworthy, A. K.; Lencer, W.; Mayor, S.; Johannes, L. Ceramide Structure Dictates Glycosphingolipid Nanodomain Assembly and Function. *Nat Commun* **2021**, *12* (1). https://doi.org/10.1038/s41467-021-23961-9.

(28) Sarmento, M. J.; Ricardo, J. C.; Amaro, M.; Šachl, R. Organization of Gangliosides into Membrane Nanodomains. *FEBS Letters*. Wiley Blackwell November 1, 2020, pp 3668–3697. https://doi.org/10.1002/1873-3468.13871.

(29) Sonnino, S.; Chiricozzi, E.; Grassi, S.; Mauri, L.; Prioni, S.; Prinetti, A. Gangliosides in Membrane Organization. In *Progress in Molecular Biology and Translational Science*; Elsevier B.V., 2018; Vol. 156, pp 83–120. https://doi.org/10.1016/bs.pmbts.2017.12.007.

(30) Gleichmann, M.; Mattson, M. P. *Neuronal Calcium Homeostasis and Dysregulation*; Vol. 14. www.liebertpub.com.

(31) Ledeen, R. W.; Wu, G. *Ganglioside Function in Calcium Homeostasis and Signaling**; 2002; Vol. 27.

(32) Julien, S.; Bobowski, M.; Steenackers, A.; Le Bourhis, X.; Delannoy, P. How Do Gangliosides Regulate RTKs Signaling? *Cells*. MDPI December 6, 2013, pp 751–767. https://doi.org/10.3390/cells2040751.

(33) Coskun, Ü.; Grzybek, M.; Drechsel, D.; Simons, K. Regulation of Human EGF Receptor by Lipids. **2011**, *108*. https://doi.org/10.1073/pnas.1105666108/-/DCSupplemental.

(34) Wang, L.; Chiang, H. C.; Wu, W.; Liang, B.; Xie, Z.; Yao, X.; Ma, W.; Du, S.; Zhong, Y. Epidermal Growth Factor Receptor Is a Preferred Target for Treating Amyloid-β-Induced Memory Loss. *Proc Natl Acad Sci U S A* **2012**, *109* (41), 16743–16748. https://doi.org/10.1073/pnas.1208011109.

(35) Mansour, H. M.; Fawzy, H. M.; El-Khatib, A. S.; Khattab, M. M. Potential Repositioning of Anti-Cancer EGFR Inhibitors in Alzheimer's Disease: Current Perspectives and Challenging Prospects. *Neuroscience*. Elsevier Ltd August 10, 2021, pp 191–196. https://doi.org/10.1016/j.neuroscience.2021.06.013.

(36) Turner, C. A.; Eren-Koçak, E.; Inui, E. G.; Watson, S. J.; Akil, H. Dysregulated Fibroblast Growth Factor (FGF) Signaling in Neurological and Psychiatric Disorders. *Seminars in Cell and Developmental Biology*. Academic Press May 1, 2016, pp 136–143. https://doi.org/10.1016/j.semcdb.2015.10.003.

(37)   Connor, B.; Young, D.; Lawlor, P.; Gai, W.; Waldvogel, H.; Faull, R. L. M.; Dragunow, M. Trk
         Receptor Alterations in Alzheimer's Disease. *Mol Brain* **1996**.

(38)   Hamasaki, H.; Honda, H.; Suzuki, S. O.; Hokama, M.; Kiyohara, Y.; Nakabeppu, Y.; Iwaki, T. Down-
         Regulation of MET in Hippocampal Neurons of Alzheimer's Disease Brains. *Neuropathology* **2014**,
         34 (3), 284–290. https://doi.org/10.1111/neup.12095.

(39)   Sil, S.; Periyasamy, P.; Thangaraj, A.; Chivero, E. T.; Buch, S. PDGF/PDGFR Axis in the Neural
         Systems. *Molecular Aspects of Medicine*. Elsevier Ltd August 1, 2018, pp 63–74.
         https://doi.org/10.1016/j.mam.2018.01.006.

(40)   Harris, R.; Miners, J. S.; Allen, S.; Love, S. VEGFR1 and VEGFR2 in Alzheimer's Disease. *Journal of
         Alzheimer's Disease* **2017**, *61* (2), 741–752. https://doi.org/10.3233/JAD-170745.

(41)   Leclerc, M.; Bourassa, P.; Tremblay, C.; Caron, V.; Sugère, C.; Emond, V.; Bennett, D. A.; Calon, F.
         Cerebrovascular Insulin Receptors Are Defective in Alzheimer's Disease. *Brain* **2023**, *146* (1), 75–
         90. https://doi.org/10.1093/brain/awac309.

(42)   Lafont, O. Applied Electrospray Mass Spectrometry. *Eur J Med Chem* **2002**, *37* (8), 707.
         https://doi.org/10.1016/S0223-5234(02)01393-4.

(43)   *Quadrupole Mass Spectrometry and Its Applications*; Dawson, P., Ed.; Elsevier, 1976.
         https://doi.org/10.1016/C2013-0-04436-2.

(44)   De Hoffmann, E. Tandem Mass Spectrometry: A Primer. *Journal of Mass Spectrometry*. 1996.
         https://doi.org/10.1002/(SICI)1096-9888(199602)31:2<129::AID-JMS305>3.0.CO;2-T.

(45)   Li, Q.; Xie, Y.; Wong, M.; Barboza, M.; Lebrilla, C. B. Comprehensive Structural Glycomic
         Characterization of the Glycocalyxes of Cells and Tissues. *Nat Protoc* **2020**, *15* (8), 2668–2704.
         https://doi.org/10.1038/s41596-020-0350-4.

(46)   Pereira, L. Porous Graphitic Carbon as a Stationary Phase in HPLC: Theory and Applications. *J Liq
         Chromatogr Relat Technol* **2008**, *31* (11–12), 1687–1731.
         https://doi.org/10.1080/10826070802126429.

(47)   Song, T.; Aldredge, D.; Lebrilla, C. B. A Method for In-Depth Structural Annotation of Human
         Serum Glycans That Yields Biological Variations. *Anal Chem* **2015**, *87* (15), 7754–7762.
         https://doi.org/10.1021/acs.analchem.5b01340.

CHAPTER II

Unique N-glycosylation signatures in Aβ oligomer- and lipopolysaccharide-activated

human iPSC-derived microglia

Author Information

Xinyu Tang[1]*, Ryan Lee Schindler[2]*, Jacopo Di Lucente[3], Armin Oloumi[2], Jennyfer Tena[2], Danielle Harvey[4], Carlito B. Lebrilla[2], Angela M. Zivkovic[1], Lee-Way Jin[3], Izumi Maezawa[3]**

[1]Department of Nutrition, University of California, Davis, California, USA.

[2]Department of Chemistry, University of California, Davis, California, USA.

[3]Department of Pathology and Laboratory Medicine and M.I.N.D. Institute, University of California Davis Medical Center, Sacramento, California, USA.

[4]Department of Public Health Sciences, University of California-Davis, Davis, CA, USA.

*Authors have equal contributions to the manuscript.

** Corresponding author

Author contributions

Izumi Maezawa, Lee-Way Jin, Carlito Lebrilla, Angela Zivkovic, Danielle Harvey: designed the study; Xinyu Tang, Izumi Maezawa, Lee-Way Jin, Ryan Lee Schindler, Angela Zivkovic wrote the article; Lee-Way Jin, Jacopo di Lucente, Ryan Lee Schindler, Armin Oloumi, Jennyfer Tena, and Izumi Maezawa: performed the experiments; Xinyu Tang, Ryan Lee Schindler, and Danielle Harvey: RNA-seq data and glycomic data analysis; Carlito Lebrilla: provided reagents, technologies.

Acknowledgments

ABSTRACT

N-glycosylation plays an important role in immune function, influencing the function of immune cells. Microglia are the immune cells in the central nervous system (CNS) and become pro-inflammatory/activated in Alzheimer's disease (AD). Cell surface glycosylation plays an important role in immune cells. However, the N-glycosylation and glycosphingolipid (GSL) signatures of activated microglia are poorly understood. Here, we study comprehensive combined transcriptomic and glycomic profiles using human induced pluripotent stem cells-derived microglia (hiMG). Distinct changes in N-glycosylation patterns in Aβ oligomer (AβO) and LPS-treated hiMG were observed. In AβO treated cells, the relative abundance of bisecting N-acetylglucosamine (GlcNAc) N-glycans decreased, corresponding with a downregulation of MGAT3, the gene responsible for bisecting GlcNAc N-glycan formation. N-glycans' sialylation increased in response to AβO, accompanied by an upregulation of genes involved in N-glycan sialylation (ST3GAL2, 4, and 6). Moreover, we found that the N-glycosylation signature of LPS-induced hiMG differed from that of AβO-induced hiMG. LPS-induced hiMG exhibited a decreased abundance of complex-type N-glycans, aligned with the downregulation of mannosidase genes (MAN1A1, MAN2A2, MAN1C1). Fucosylation increased in LPS-induced hiMG, aligned with upregulated fucosyltransferase 4 (FUT4) and downregulated alpha-L-fucosidase 1 (FUCA1) gene expression. However, the GSL profile did not exhibit significant changes in response to AβO or LPS activation. AβO- and LPS-specific glycosylation changes could contribute to impaired microglia function, highlighting glycosylation pathways as potential therapeutic targets for AD.

INTRODUCTION

Neuroinflammation plays a significant role in the initiation and progression of several central nervous system (CNS) disorders, including Alzheimer's disease (AD). The complexity of neuroinflammation reflects how microglia respond to internal and external changes to orchestrate inflammatory responses. Microglia are the innate immune cells of the CNS that survey and respond to various environmental challenges with multiple actions, resulting in phagocytosis of debris and release of cytokines and chemokines.[1] Prior to the development of specific immunohistochemical agents, a widely used classic histochemical method to detect microglia in brain sections was to employ lectins that recognize glycoconjugates,[2] implying the significance of glycosylation (i.e., post-translational addition of glycans to protein backbones) in microglial function. Recently, the study of changes in glycosylation upon neuroinflammation has gained increased interest;[3] however, how microglia respond to stimuli with glycosylation changes remains understudied.

AD pathology has highlighted the importance of microglia, given their role in orchestrating neuroinflammation and phagocytosis. In AD brains, microglia lose their homeostatic molecular signature and show profound functional impairments, such as increased production of pro-inflammatory cytokines, elevated reactive oxygen species, impaired phagocytosis, and increased inflammasome formation.[4] Recently, the pivotal roles of microglia-orchestrated neuroinflammation in AD have been established.[5-8] A generally accepted hypothesis states that activated microglia become functionally impaired and release cytotoxic substances and pro-inflammatory cytokines that cause neuronal damage and aggravate AD pathology.[5] While multiple factors may cause microglial activation in AD, early studies have

established that different species of Aβ aggregates are potent stimulants of microglia. Among them, we and others found that the small soluble Aβ oligomer (AβO) assembled from the Aβ42 peptide provides far stronger stimulation to induce microglial activation.[9,10] Aβ aggregates are recognized by a range of microglial pattern recognition receptors to induce mainly pro-inflammatory responses that could mediate Aβ-induced neurotoxicity, impair phagocytic function, and prime microglia to enhance their sensitivity and reactivity to inflammatory stimuli.[11] Understanding the mechanisms of such activations could reveal microglial therapeutic targets.

In the present study, we characterized the global glycosylation changes of human microglia following AβO stimulation, using stimulation with lipopolysaccharide (LPS), a widely used microglia activation approach, for comparison. We employed human induced pluripotent stem cell (iPSC)-derived microglia (hiMG) as a major model rather than the widely used primary cultures from neonatal rodents based on the following rationales. First, it was recognized that rodents are generally a better model for neuronal pathology than they are for microglial pathology,[12] and that for optimal translational validity, human microglia are recommended to be used to identify human-relevant molecular pathways and therapeutic targets.[13] Second, in contrast to the evolutionarily better conserved genetic codes and protein networks across species, there is no evidence for a universal "glycan code" akin to the genetic code or protein motif.[14,15] Rather, glycans vary immensely in structure and expression both within and between evolutionary lineages, and our knowledge about the glycan structural diversity between species remains limited.[15] Therefore, we consider that models of human cells would be suitable for our initial investigation of microglia glycosylation changes. Our profiling of hiMG identified the

specific glycan types and glycosylation genes altered in AβO- and LPS-activated human

microglia that may be involved in regulating their respective activation pathways.

METHODS

Human iPSC culture and microglia differentiation

Human iPSCs were obtained from ALSTEM.INC. (Richmond, CA). The line used in this study was Human iPS Cell Line 26 (Episomal, CD34+, ApoE3). Cells were plated onto Matrigel (Fisher) coated plates and cultured with mTeSR plus (Stemcell Technology). For microglia differentiation, we followed a previously described protocol.[16,17] Briefly, 2 x 106 iPSCs were plated onto Aggrewell 800 plates (Stemcell Technology) to form embryoid bodies (EBs) in mTeSR1 supplemented with Bone Morphogenetic Protein 4 (BMP4, 50 ng/ml)/ Vascular Endothelial Cell Growth Factor (VEGF, 50 ng/ml)/ Stem Cell Factor (SCF, 20 ng/ml) and culture for four days with daily medium change. On the fifth day, EBs were plated onto gelatin-coated 6-well plates with 20 EBs per well in X-VIVO15 (Lonza) supplemented with M-CSF (100ng/ml), IL-3 (25ng/ml), Glutamax (2mM), Penicillin/streptomycin (100U/ml and 100ug/ml) and β-mercaptoethanol (55uM), and the medium was changed weekly. After 3-4 weeks, floating primitive macrophage precursor (PMP) were collected and plated onto 12-well plates (5 x 10^4 cells/well), 6-well plates (3 x 10^5 cells/well), or 100 mm dishes (1.5 x 10^6 cells) and differentiated in microglia differentiation medium (Advanced DMEM/F12 supplemented with IL-34 (100ng/ml), GM-CSF (10ng/ml), N2 supplement (1x), Glutamax (2mM), Penicillin/streptomycin (100U/ml and 100ug/ml) and β-mercaptoethanol (55uM)) for two weeks. The cultures were routinely tested for mycoplasma.

For AβO and LPS stimulation, cells were treated with AβO (3 μM) and LPS (100 ng/ml) for 24 hours.

AβO and LPS preparation and treatment

AβO composed of Aβ1-42 peptide was prepared following a standard procedure[18] with a modification that the HFIP treated Aβ1-42 peptide (Bachem) was dissolved in DMSO and then diluted with Advanced DMEM/F12 culture medium instead of the F12 medium originally described, followed by incubation at 4°C for 24 hr and 10 min centrifugation at 10,000 x rpm at 4°C. This preparation of AβO has been extensively characterized in our laboratory.[9] Briefly, to ensure consistency of quality, a random sample from each batch was chosen and imaged using electron microscopy and atomic force microscopy to characterize the size and shape of the aggregates. The biological activities of each batch were confirmed by determining for AβO the neurotoxic activity, synaptic binding activity, and ability to rapidly induce exocytosis of MTT formazan, as described previously.[9]

RNA isolation, processing, and sequencing

Total RNA from cultured cells was extracted using RNeasy Plus Mini Kit (Qiagen). RNA quality evaluation (yield, purity, and integrity), cDNA library construction, and Illumina sequencing were performed by NovoGene (Sacramento, CA, USA).

Mapping and differential expression analysis

The reads in FASTQ files were mapped to the human reference genome hg38 using HISAT2.[19] The mapping rate was around 97%. The gene counts were summarized by featureCounts,[20] achieving a successful alignment of 70%-80% of the reads per library. Differential gene expression was analyzed using edgeR package[21] in R version 4.1.0 (R Foundation for Statistical Computing, Vienna, Austria). Low-expressed genes were dropped using the *filterByExpr()*

function. The filter step keeps genes that have count-per-million (CPM) above 10 in 70% of samples. The library sizes were recalculated after filtering. Sample-specific effects were removed by normalizing library sizes with the trimmed mean of M-values (TMM) method using the *calcNormFactors()* function. A negative binomial model with the quasi-likelihood (QL) F-test was applied to perform the differential expression analysis among diagnosis groups. First, gene counts with normalized library sizes were fitted to a negative binomial generalized linear model. Then, the dispersion was estimated using the *estimateDisp()* function. The QL dispersion estimation was calculated using the *glmQLFit()* function, followed by the *glmQLFTest()* function that conducted the quasi-likelihood (QL) F-test. Finally, we used the *topTags()* function to output significantly differentially expressed genes. P-values were adjusted for multiple hypothesis testing using Benjamini & Hochberg (BH) with a threshold of adjusted p-value ≤ 0.05.

Cell Membrane Enrichment

Samples were prepared for glycomic analysis based upon previously published methodologies.[22] Briefly, harvested cells were centrifuged at 2,000 RCF for ten minutes, after which the cell media was exchanged with 1.2 mL of 0.25 M sucrose (MilliporeSigma, Cat# S7903), 20mM HEPES (Thermo Fisher Scientific, 1 M, Cat# 15630080) adjusted to pH 7.4 with KOH (MilliporeSigma, Cat# P5958) and a 1:100 protease inhibitor cocktail (Calbio-chem, Cat# 539137) in water and pipette mixed gently. Cells were then lysed by sonication, where 60 joules of energy were applied to each sample over one minute. The homogenate was centrifuged at 2,000 RCF for 10 minutes at 4°C, and then the supernatant was transferred to 1.5 mL ultracentrifuge tubes, and the nucleus precipitate was discarded. The cell membrane was

precipitated by ultracentrifugation at 42,000 RCF for 45 minutes at 4°C, after which the cytoplasmic supernatant was discarded, taking care not to disturb the membrane pellet. Samples were resuspended in 0.5 mL of 0.2 M Na_2CO_3 (MilliporeSigma, Cat# P5958) in water and ultracentrifuged again, after which the supernatant, containing membrane-associated proteins, was discarded. A final ultracentrifugation step using the same conditions with 0.5 mL of water was done to wash and desalt the samples, discarding the supernatant afterward.

N-Glycan sample preparation

The enriched membrane fraction was then resuspended in 200 μL of 100 mM NH_4HCO_3 (MilliporeSigma, Cat# 09830) and 5 mM Dithiothreitol (Promega, Cat# V3151) in water to assist in protein denaturing. After gentle homogenization by pipette mixing, samples were placed in a 100°C water bath for two minutes with 10-second heating and cooling intervals to denature the membrane proteins further. After samples were cooled to room temperature, 2 μL of PNGase F (New England Biolabs, Cat #P0705L) was added to enzymatically hydrolyze the N-glycans from their protein substrates. Enzymatic cleavage and conversion of the resulting reducing end amides to hydroxyls occurred at 37°C for 18 hours. Samples were brought to a total volume of 600 μL with water and then ultracentrifuged using the previously described parameters. The supernatant containing the released N-glycans was transferred to a new vial, and the remaining membrane pellet was stored at -20°C until ready for glycosphingolipid processing. N-glycan samples were enriched using a porous graphitic carbon solid phase extraction plate (PGC-SPE, Glygen, Cat# FNSCAR800). SPE wells were first washed with elution solvent consisting of 80% acetonitrile, 0.1% trifluoroacetic acid in water (v/v) and then conditioned in wash solvent consisting of 40% acetonitrile, 0.05% trifluoroacetic acid in water (v/v). Samples were loaded

onto the solid phase and washed three times with 600 μL of washing solvent, and all liquids were discarded. N-glycans were then eluted with 600 μL of elution solvent into a new collection plate. The PGC plate was centrifuged at 150 RCF for each SPE step to ensure solvent flow-through quickly. Enriched N-glycan samples were concentrated by drying to completion in vacuum centrifugation and reconstituted in 30 μL of water prior to analysis.

N-Glycan analysis methodology

Released N-glycan analysis was conducted with an Agilent 1200 series ChipCube system operating in positive ion mode and a 6520 Q-TOF mass spectrometer. Chromatographic separations were performed utilizing a PGC-Chip II, 40 nL enrichment column, 75 x 43 mm analytical column, 5 μm (Agilent Technologies, G4240-62003). Mobile phase A (MPA) composition was 3% acetonitrile and 0.1% formic acid in water (v/v). The composition of mobile phase B (MPB) was 90% acetonitrile and 1% formic acid in water (v/v). Samples were cooled with a 4°C sample tray, and 5μL was injected by the autosampler, loaded onto the enrichment column, and washed for 10 minutes with 100% MPA at 3μL/min. Next, the chip valve switched to analysis mode, moving the enrichment column in line, and the analytical gradient began with a flow rate of 0.3 μL/min. 0% MPB was held from 0 to 2 minutes; at 20 minutes, MPB reached 16%; at 40 minutes, MPB reached 72%; and at 42 minutes, MPB reached 100%. The 100% MPB wash was held until 52 minutes and decreased back to 0% MPB at 54 minutes; the equilibration of the starting composition was held until 65 minutes. Source parameters used nitrogen as the drying gas with a temperature of 325°C flowing at 5L/min and a capillary voltage of 1800V. Auto MS/MS acquisition mode allowed four precursors per cycle with a threshold of 2000 counts and quadrupole filtering with a narrow isolation width for the 600-2000 m/z range. Collision-

induced disassociation with N2 gas used a precursor-dependent formula y=1.8*(m/z)/100-3.6 to determine individual collision energies with a 100-2000 m/z range. Continual mass correction with a reference calibration standard of 1221.990637 m/z was used (Agilent Technologies, HP-1221). N-glycan compound verification used MassHunter Qual B08.00 software with the 'Find by Molecular Feature' algorithm and an in-house database containing N-glycan monoisotopic masses and descriptive information.

Sphingolipid sample preparation

The membrane pellet from the initial steps was removed from -20°C storage and allowed to acclimate to room temperature. Samples were resuspended in 500 μL of freshly prepared sphingolipid extraction solvent consisting of water/methanol/chloroform (3:8:4, v/v%) and sonicated for 15 minutes to assist in solvation. Proteins were precipitated by centrifugation at 8,800 RCF for 5 minutes, and the supernatant was transferred to a new 1.5 mL Eppendorf vial. A bilayer phase separation was induced by adding 100 μL of 0.1 M KCl (MilliporeSigma, Cat#104936). The top aqueous-rich layer containing the sphingolipids of interest was transferred to a new vial and dried by vacuum centrifugation. Sphingolipid samples were enriched using a C-8 solid phase extraction plate (Glygen, Cat# FNSC08.800). SPE wells were first washed with elution solvent consisting of methanol/isopropyl alcohol (1:1, v/v%) and then conditioned in wash solvent consisting of methanol/water (1:1, v/v%). Samples were reconstituted with wash solvent, loaded onto the solid phase by gravity, and reloaded the flow-through. Sample wells were washed three times with 600 μL of washing solvent, and all liquids were discarded. Sphingolipids were then eluted with 400 μL of elution solvent into a new collection plate. For each SPE step, the C-8 plate was allowed to be gravity-loaded to ensure

analyte binding. Enriched sphingolipid samples were concentrated by drying to completion in vacuum centrifugation and reconstituted in 20 µL of water/methanol (1:1, v/v%) prior to analysis.

Sphingolipid analysis methodology

Sphingolipid analysis was conducted with an Agilent 1200 series nanoflow HPLC equipped with a 10pt/2ps µ-valve(G1316-68709), nanoflow ESI operating in positive ion mode (G1992A), and a 6530 Q-TOF mass spectrometer. Chromatographic separations were performed utilizing a Zorbax SB-300 C-8, 0.075 x 50 mm, 3.5 µm column (Agilent Technologies, Cat# 5065-9923). Four mobile phase compositions with two low-flow pumps were used in this analysis. The first pump (pump 1) operated at 0.7 µL/min and was used to load samples directly and wash the analytical column. The loading mobile phase (MPL) composition was 20 mM ammonium acetate in 56% methanol, 14% isopropyl alcohol, 0.1% glacial acetic acid, and water (v/v). The washing mobile phase (MPW) composition was 50% methanol and 50% isopropyl alcohol (v/v). The second pump (pump 2) operated at 0.4 µL/min and was used to carry out the analytical gradient. Mobile phase A (MPA) had a composition of 20 mM ammonium acetate in 0.1% glacial acetic acid and water (v/v). Mobile phase B (MPB) had a composition of 20 mM ammonium acetate in %0.1% glacial acetic acid, 20% isopropyl alcohol, and 80% methanol (v/v). Samples were cooled with a 4°C sample tray, and 1µL was injected and loaded directly onto the analytical column for 4 minutes with 100% MPL. At 4 minutes, the µ-valve switched positions, moving the analytical column into pump 2's flow path, and the gradient began. 70% MPB was held from 4 to 6 minutes; at 35 minutes, MPB reached 93%, and at 36 minutes, MPB reached 100%. The 100% MPB was held until 39 minutes and decreased back to 70% at 40 minutes; equilibration of the

starting composition was held until 47 minutes. Source parameters used nitrogen as the drying gas with a temperature of 300°C flowing at 5L/min and a capillary voltage of 1000V. Auto MS/MS acquisition mode allowed five precursors per cycle with a threshold of 600 counts and quadrupole filtering with a narrow isolation width for the 600-2000 m/z range. Collision-induced disassociation with N2 gas used a precursor-dependent formula y=1.2*(m/z)/100+12 to determine individual collision energies with a 100-2000 m/z range. Continual mass correction with a reference calibration standard of 1221.990637 m/z was used (Agilent Technologies, HP-1221). Sphingolipid compound verification used MassHunter Qual B08.00 software with the 'Find by Molecular Feature' algorithm and an in-house database containing sphingolipid monoisotopic masses and descriptive information.

Statistical analysis

Single glycans with missing values for more than 80% of samples were excluded from further analysis (Supplementary Figure 2.1). The fractions of glycan subtypes (Figure 2.1), sialylated, and fucosylated N-glycans were calculated as the sum of the relative abundances of individual glycans. Differential abundance analysis was performed as linear regression models using the lmerTest package in R as shown here:[24] glycan abundance ~treatment. ANOVA tests and contrasts between treatments and control were evaluated. The AβO and LPS groups were compared to the control group using Dunnett's test. The differences of the three treatment groups on the PCA plot were evaluated using the MANOVA test followed by post-hoc linear discriminant analysis (LDA).

RESULTS

Both AβO and LPS induce significant changes in the N-glycan profiles of hiMG

We analyzed the N-glycan profiles of control (mock treatment), AβO-activated, and LPS-activated hiMG using LC-MS/MS technology, with six replicates per group. We treated hiMG for 24 hr with 3 μM AβO and 100 ng/ml LPS, optimal concentrations to induce pro-inflammatory cytokines IL-1β, TNF-α, and IL-6.[17] Figure 2.1 illustrates the N-linked glycosylation types. The complex-type N-glycans were the most abundant in all groups, making up ~35-40% of total N-glycans (Figure 2.2A). This is in keeping with the general composition of brain glycans.[24] Hybrid glycans were the least abundant in hiMG, making up less than 10% of total N-glycans (Figure 2.2A). Complex-type N-glycans can be further classified as bi-, tri, and tetra-antennary, as well as bisecting GlcNAc, which contains an additional GlcNAc bound to the core (Figure 2.1).
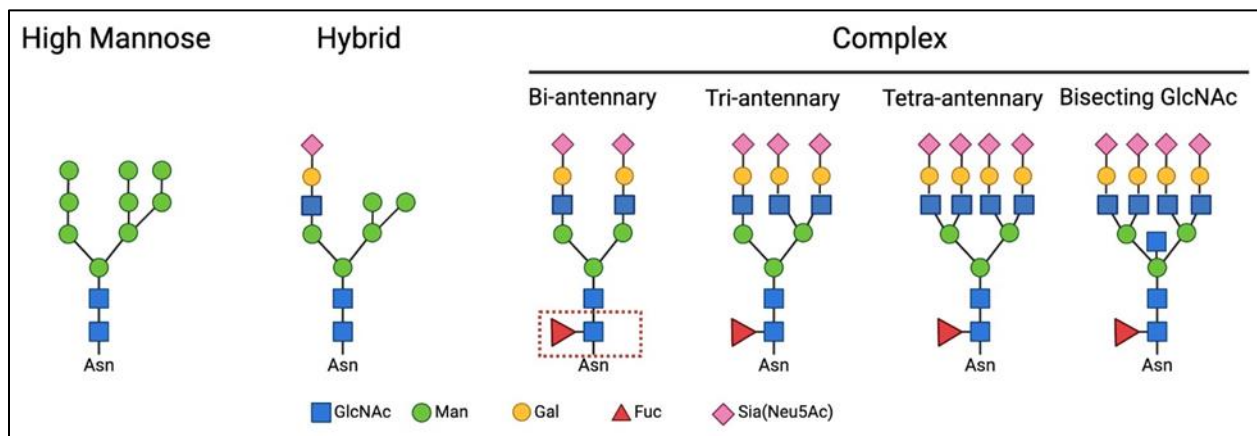
Figure 2.1 Outline of N-glycan classes. Examples from left to right represent high mannose, hybrid, and complex N-glycans. Complex N-glycans can be classified as bi-, tri-, tetra-antennary, and bisecting GlcNAc based on the number of starting GlcNAc residues on the mannose residues. The core fucosylatin is marked with a red dash square. Recommended symbol nomenclature was used. GlcNAc: N-acetylglucosamine; Man: mannose; Gal: galactose; Fuc: fucose; Sia: sialic acid.

In hiMG, the tetra-antennary structure constituted the predominant subtype of complex-type N-glycans, followed by bi-antennary, bisecting GlcNAc, and tri-antennary structures (Figure 2.2B). N-Glycans can be decorated by adding fucose, sialic acid, or both to the terminal end of glycans. Fucose can also be added to the core structure. These modifications are essential for protein functions such as protein stability, cell adhesion, signal transduction, immunological responses, and cell-to-cell interactions.[22,25] We quantified such modifications and found that in hiMG, sialofucosylated N-glycans were the most abundant, making up ~50% of glycans. About 30% of N-glycans were not decorated by fucose or sialic acid residues. The rest of the N-glycans were only decorated by either fucose or sialic acid residues (Figure 2.2C). Considering both subtypes and decorations, sialofucosylated complex N-glycans and undecorated high-mannose N-glycans are the most abundant hiMG structures (C-FS and HM in Figure 2.2D). AβO and LPS treatments had a significant impact on the N-glycan profile of hiMG, as shown by the increased dispersion of the AβO-activated hiMG compared to the control cluster and the separation of the LPS-activated hiMG clusters from the control cluster on the PCA plot (MANOVA p-value = 0.0014). The distance between the LPS cluster and the control cluster was greater than the distance between the AβO cluster and the control cluster, indicating that LPS might induce a higher degree of glycosylation changes than AβO (Figure 2.2E, Supplementary Figure 2.2A).
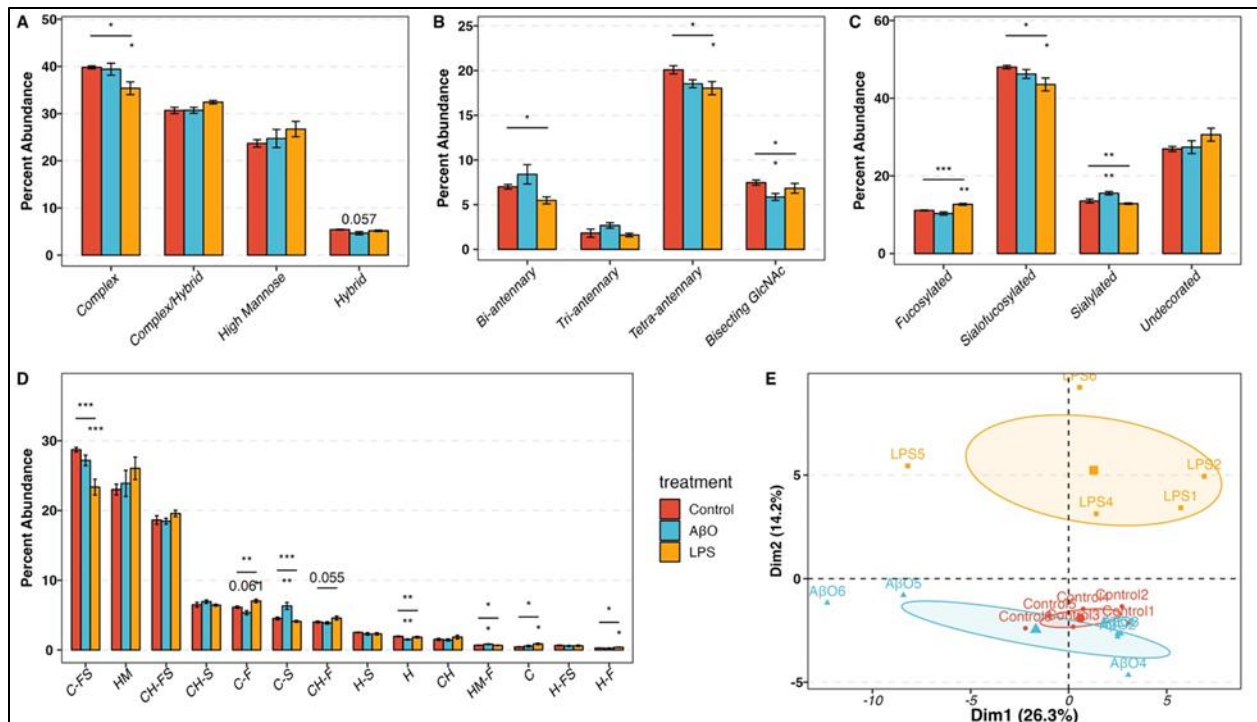
Figure 2.2 N-glycomic profile in control and AβO-, LPS-activated hiMG. A) the percent abundance of complex, complex/hybrid, high mannose and hybrid N-glycan. B) The percent abundance of bi-, tri-, tetra-, and bisecting complex N-glycan. C) The percent abundance of each decoration, including fucosylated, sialofucosylated, sialylated, and undecorated N-glycan. D) The percent abundance of each decoration on each N-glycan type. Glycans are named as "glycan type-decoration". C, CH, H, HM represent Complex, Complex/Hybrid, Hybrid, and High Mannose, respectively. S, F, SF represent sialylated, fucosylated, and sialofucosylated, respectively. E) Principal Component Analysis (PCA) plot showing the clustering of control, AβO- and LPS-activated samples. MANOVA p-value =0.0014. Red, blue, and yellow correspond to control, AβO, and LPS groups. The asterisk (*) marks above the segments indicate the p-values obtained from the one-way ANOVA test. The asterisk marks below the segments indicated the p-values from the Dunnett test for the corresponding treatment group. p values *<0.05, **<0.01, and ***<0.001.

Increased sialylation and decreased bisecting GlcNAc N-glycans in AβO-activated hiMG

According to the N-glycome, AβO, but not LPS, treatment reduced the percent abundance of bisecting GlcNAc N-glycans in hiMG (Figure 2.2B). Consistent with this glycomic change, differential expression (DE) analysis of RNA-seq data revealed that following AβO treatment, beta-1,4-mannosyl-glycoprotein 4-beta-N-acetylglucosaminyltransferase 3 (MGAT3)

was the most downregulated gene across all genes involved in the core N-glycan formation

process (Figure 2.3A). MGAT3 encodes N-acetylglucosaminyltransferase-III (GnT-III), which is

uniquely responsible for transferring a GlcNAc residue to the mannose of the trimannosyl core

of N-glycans to produce a bisecting GlcNAc N-glycan[26] (Figure 2.3D). Thus, the downregulation

of the MGAT3 gene could be the transcriptional basis of the reduction of bisecting GlcNAc N-

glycans observed in AβO treated hiMG cells.
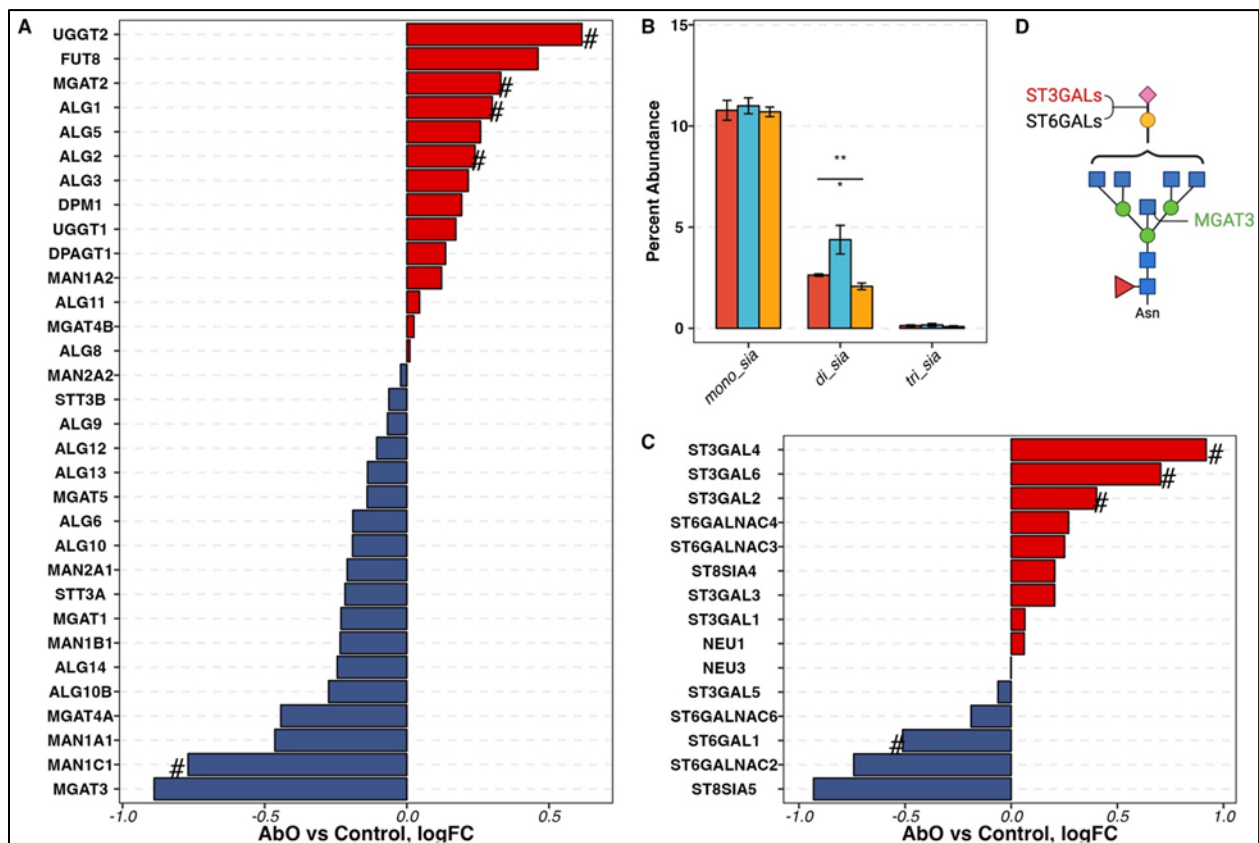
Figure 2.3 Sialylation changes in AβO-activated hiMG. A) The differential expression of genes involved in the biosynthesis of N-glycan core structure. B) The percent abundance of mono-, di-, and tri- sialic acid residues among sialylated only N-glycans. C) The differential expression of genes involved in sialylation. D) The schematics of the N-glycan structure and the corresponding enzymes. Red, blue, and yellow denote control, AβO, and LPS groups. For A) and C), the pound (#) denotes genes with unadjusted p-value < 0.05 but FDP >0.05. For B), red, blue, and yellow correspond to control, AβO, and LPS groups. The asterisk (*) marks above the segments indicate the p-values obtained from the one-way ANOVA test. The asterisk marks below the segments

AβO treatment also increased the percent abundance of sialylated N-glycans (Figure 2.2C), particularly sialylated complex N-glycans (C-S in Figure 2.2D). We, therefore, further explored the changes in the number of sialic acid residues on N-glycans and found that the increased sialylation was largely attributed to an increased percent abundance of di-sialylated N-glycans (Figure 2.3B). DE analysis of RNA-seq data showed that among the genes encoding sialyltransferases and sialidases, ST3GAL2, ST3GAL4, and ST3GAL6 were significantly upregulated by AβO treatment (Figure 2.3C). Given that ST3GALs encode for enzymes responsible for transferring sialic acid to the galactose residues with α-2-3 linkage (Figure 2.3D), the results suggest that α-2,3-linked sialic acids possibly contributed to the increased di-sialylation observed in the AβO-activated hiMG.

DE analysis also revealed increased levels of FUT8 transcript encoding α1-6 fucosyltransferase (fucosyltransferase 8), which is uniquely responsible for core fucosylation in AβO-treated hiMG (Figure 2.3A). This result corroborates our published data reporting that AβO enhances FUT8-catalyzed core fucosylation, a signaling pathway required for AβO-induced microglial activation.[17]

Decreased complex N-glycans and increased fucosylation in LPS-activated hiMG

In contrast to AβO-activated hiMG, LPS-activated hiMG exhibited a reduced percent abundance of complex-type N-glycans, specifically the tetra-antennary complex N-glycans (Figure 2.2A, B). Complex N-glycans are derived from high-mannose N-glycans. In the endoplasmic reticulum (ER) and cis-Golgi, α-mannosidase I (MAN1B1), α1-2 mannosidases IA,

IB, and IC (encoded by MAN1A1, MAN1A2, and MAN1C1, respectively) trim mannose residues

from high mannose N-glycans to yield Man5GlcNAc2, a key intermediate in the pathway to

generate hybrid and complex N-glycans (Figure 2.4E). In the DE analysis of hiMG transcriptomic

data, MAN1A1, MAN1C1, and MAN2A2 were significantly downregulated in LPS-treated hiMG

(Figure 2.4A). The transcript levels of other key mannosidases, including MAN1B1, MAN1A2,

and MAN2A1, were also decreased, though not statistically significant (Figure 2.4A). The

downregulation of these mannosidases may contribute to the reduced abundance of complex
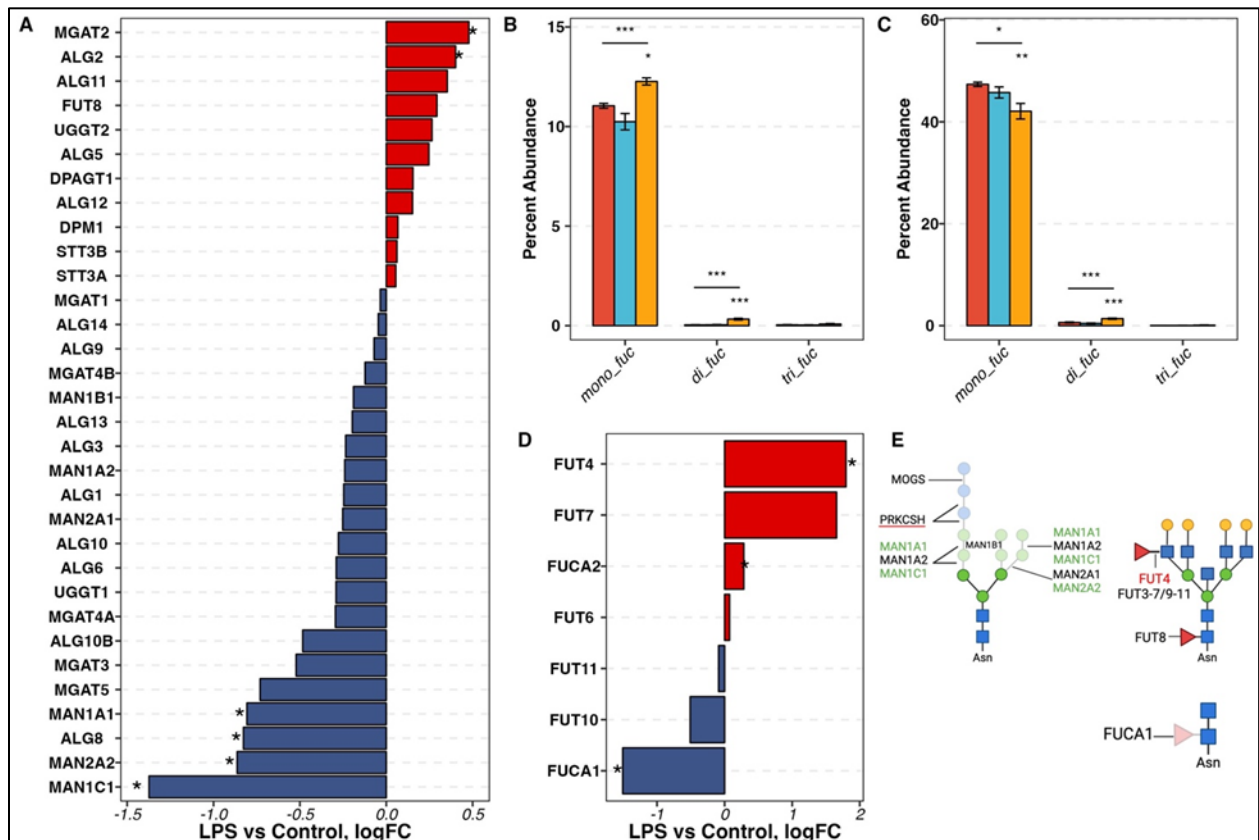
N-glycans.

Figure 2.4 Fucosylation changes in LPS-activated hiMG. A) The differential expression of genes involved in the biosynthesis of N-glycan core structure. B) The percent abundance of mono-, di-, and tri-fucose residues among fucosylated only N-glycans. C) The percent abundance of mono-, di-, and tri-fucose residues among sialofucosylated N-glycans. E) The schematics of complex N-

The changes in LPS-activated hiMG also differed from AβO-activated hiMG. The extent of fucosylation (i.e., fucosylated-only N-glycans), especially complex- and hybrid-type N-glycans, was increased in LPS-activated hiMG but remained unchanged in AβO-activated hiMG (Figure 2.2C-D). This overall change was the sum of changes in individual glycan structures. In contrast, sialofucosylated N-glycans, the most abundant types, were significantly reduced overall in LPS-activated hiMG, especially sialofucosylated complex N-glycans (Figure 2.2C-D). Interestingly, among the sialofucosylated N-glycans, those containing one fucose residue decreased while those containing two fucose residues increased (Figure 2.4C). Thus, the decrease in mono-fucosylated and concomitant increase in di-fucosylated complex-type N-glycans, also containing sialic acid, was the primary effect of LPS treatment.

Fucosyltransferases (FUTs), except FUT8, transfer fucose to antenna GlcNAc residues (Figure 2.4D). According to the DE analysis, FUT4 was significantly upregulated in LPS-treated hiMG, possibly contributing to increased fucosylation, especially increased di-fucosylated N-glycans. Fucose residues on N-glycans can be hydrolyzed by fucosidases (FUCAs). Alpha-L-Fucosidase 1 (FUCA1) specifically hydrolyzes the fucose residue at the core structure (Figure 2.4E). The transcript level of FUCA1 was significantly downregulated (Figure 2.4D), suggesting less hydrolysis of core fucosylated N-glycans. This and enhanced FUT4 action could lead to increased percent abundance of fucosylated N-glycans.

The glycosphingolipid (GSL) profile of hiMG

GSLs are a subclass of lipids composed of a ceramide part and a mono- or oligosaccharide part. In the adult mammalian brain, the major GSLs are the gangliosides of GM1, GD1a, GD1b, and GT1b, which have one to three sialic acid residues, respectively.[27,28] Because sialic acid residues on a glycoprotein or glycolipid may modulate cell signaling mediated by lectins such as selectins and sialic acid-binding immunoglobulin-type lectins (Siglecs) and because we found significant changes in sialic acid levels following AβO and LPS treatment, we profiled the GSL composition as well. The most abundant GSL was ganglioside GM3, the precursor of other complex gangliosides (Figure 2.5A). The second most abundant species was sphingomyelin (SM), a ceramide with a phosphocholine headgroup, followed by neutral GSL GA2. The remaining GSLs were less abundant, with each accounting for less than 5%. Regarding sialylation, GSLs detected in hiMG were predominantly sialylated GSLs (Figure 2.5B). Interestingly, the GSL profile did not change significantly in response to either AβO or LPS activation. The PCA plot showed that the clusters of control, AβO, and LPS groups did not separate from each other (MANOVA p-value = 0.56, Figure 2.5C, Supplementary Figure 2.2B). The genes involved in GSL biosynthesis also did not show significant changes in response to AβO activation (Supplementary Figure 2.3A). In LPS-activated hiMG, even though the genes involved in GSL biosynthesis, i.e., UGCG, B4GALT5, and B4GALNT1, were significantly upregulated, no significant changes were observed when individual GSLs in either treatment were examined (Figure 2.5A, Supplementary Figure 2.3B).
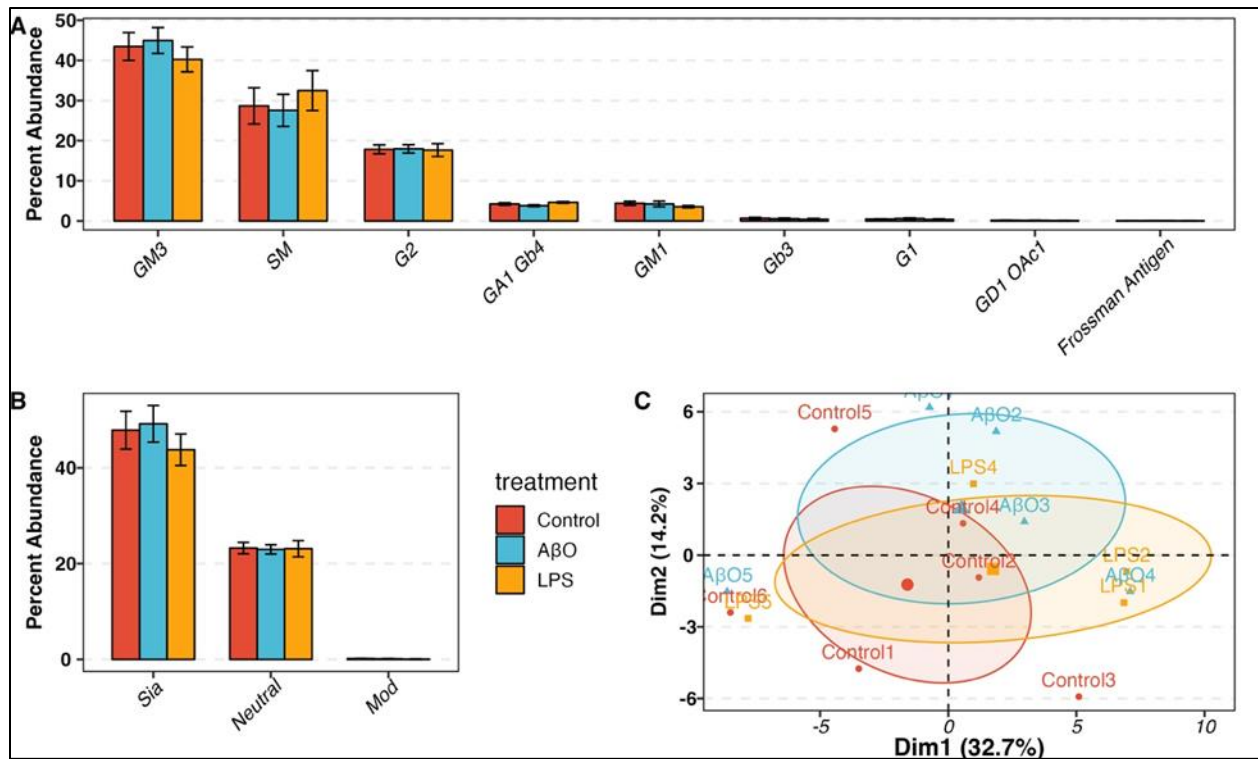
Figure 2.5 Glycosphingolipid (GSL) profile in control and AβO-, LPS-activated hiMG. A) The percent abundance of GSL subtypes. B) The percent abundance of decorated GSLs. C) Principal Component Analysis (PCA) plot showing the clustering of control, AβO- and LPS-activated samples. MANOVA p-value =0.56. Red, blue, and yellow correspond to control, AβO, and LPS groups.

DISCUSSION

The composition and balance between various types of glycans play an essential role in regulating cell functions.[29] Cellular N-glycans can be subclassified as complex-, high mannose-, and hybrid-type N-glycans. High-mannose N-glycans are the precursor of hybrid and complex-type N-glycans. Mannosidases hydrolyze mannose from the high-mannose structure, preparing it for complex- and hybrid-type N-glycan biosynthesis. High mannose glycans have been reported as the major N-glycan type in the undifferentiated human monocytic leukemia cell line THP-1, primary blood-derived CD14+ monocytes, and Caco-2 cells.[30-33] After differentiation, the levels of high mannose glycans in these cells decreased, accompanied by an increase in complex-type structures. The latter became the predominant N-glycan type in differentiated cells. In line with the differentiated state of microglia, hiMG expresses predominantly complex-type N-glycans regardless of activation. On the other hand, our hiMG data (summarized below), when compared to published data from other cell types, show differences mainly in levels of glycan decorations such as mono- or di-sialylation, fucosylation, or sialofucosylation, suggesting their significance in regulating cell-specific functions.

The differential glycosylation changes stimulated by AβO and LPS are summarized in Figure 2.6. Congruent evidence from both glycomic and transcriptomic analyses reveals the transcriptional basis of these changes and enhances the validity of our findings. We found that AβO induces increased sialylation catalyzed by ST3GALs and decreased bisecting GlcNAc N-glycans catalyzed by GnT-III. A third major glycosylation change, previously reported by us,[17] is increased core fucosylation catalyzed by FUT8, corroborated in the current study by increased expression of FUT8 transcript. These three glycosylation changes are known to affect immune

regulation,[29,34,35] suggesting their significance in microglial function. They have also been implicated in AD, as published data using brain or cerebrospinal fluid samples from participants with AD or mild cognitive impairment (MCI) highlighted altered levels of bisecting GlcNAc, sialylation, and core fucose in N-glycans.[3,36-39] Altered glycoforms of individual AD-relevant proteins were also reported; for example, the familial AD mutant of the Aβ-amyloid precursor protein (APP) was shown to have a higher content of bisecting GlcNAc and core fucose residues compared to wild-type APP.[40] However, exact glycosylation-regulated molecular mechanisms, especially those pertaining to neuroinflammation in AD, are largely unknown. Furthermore, a widely recognized feature of glycobiology is that different cell types express distinct glycosyltransferase isozymes. Thus, proteins may have different glycosylation patterns depending on their cell of origin and in response to functional needs.[41] Therefore, analyses of multicellular brain tissues or other cell types do not precisely reflect glycosylation alterations in microglia. In this context, the microglia- and stimulant-specific glycosylation changes we report here would provide the first significant insights into how glycosylation alterations may regulate microglial function.

	Glycan type/Decoration	Example		Associated genes
AβO	Complex/Bisecting GlcNAc ↓	C-F_7710		MGAT3 ↓
	Complex/Di-sialylated ↑	C-S_5402		ST3GAL2 ↑ ST3GAL4 ↑ ST3GAL6 ↑
	Complex/Core fucosylated ↑ *	C-FS_6513		FUT8 ↑
LPS	Complex (tetra-antennary) ↓	C-FS_7611		MAN1A1 ↓ MAN1C1 ↓ MAN2A2 ↓
	Complex or hybrid/Fucosylated ↑ - Mono-fucosylated ↑	C-F_7610		
	- Di-fucosylated ↑	C-F_7620		FUT4 ↑ FUCA1 ↓
	Complex/Sialofucosylated ↓ - Mono-fucosylated ↓	C-FS_7611		
	- Di-fucosylated ↑	C-FS_7621		

*Figure 2.6 Summary of glycosylation and associated gene expression changes in hiMG stimulated by AβO and LPS. Representative examples of indicated glycan structures measured by mass spectrometry (MS) are listed in the middle column, and the genes linked to the indicated glycosylation changes identified by RNA-seq are listed in the right column. Note that current glycomic methods cannot precisely distinguish between core fucose and terminal fucose, and that the fucose residues in the structures such as C-FS_6513 can be either at the core or the terminal position. *The increased core fucosylation following AβO treatment is based on Jin et al., 2023.*

Among the three specific glycosylation changes, sialylation is the most studied in AD due to the high level of interest in Siglec, in part based on the association of the gene of CD33, a Siglec receptor, to AD risk.[42] Neuronal membranes contain a high density of sialic acid residues on glycoproteins, which protect neurons from aberrant microglial phagocytosis[43] via interacting with Siglec receptors such as CD22 and CD33 on microglia.[44-46] However, how sialylation changes in microglia *per se* affect neuron-microglia interaction or microglial function is poorly understood. Previous studies using the mouse BV2 microglia cell line found that BV2

cells activated by LPS, fibrillar Aβ, and tau had increased sialidase activity that desialylated the BV2 cell surface, promoting phagocytosis of neurons mediated by CR3.[46,47] Although we found that oligomeric Aβ-activated hiMG showed an increase in total sialylation, the RNA-seq analysis suggests that the changes in sialylation may be specific to glycosidic linkages, with a decrease in α2-6 and α2-8 linked sialic acids and an increase in α2-3 linked sialic acids. Regarding CD33 ligand binding preference, evidence points to overlapping specificities for α2-3 and α2-6 linked sialic acids,[48] where the binding affinity was increased with sulfation[49] and decreased with branched α1-3 fucosylation.[50] Of note, AβO treatment of hiMG was accompanied by reduced phagocytosis of pHrodo Green BioParticles and of Aβ itself as demonstrated previously,[17] revealing the complexity and need for further investigation. The differences may be explained by different cell models (BV2 vs. hiMG), interspecies differences (mouse vs. human), different modes of microglia activation (fibrillary Aβ or LPS vs. AβO), and different methods of analysis. We used human iPSC-derived microglia as the model due to its strong human relevance, while the BV2 model is a rapidly growing tumor cell line with well-recognized limitations.[51] AβO is considered a primary pathological agent in the early stages of AD preceding Aβ fibril formation,[52] and the respective influences on microglia state by AβO and Aβ fibril may represent different neuroinflammation phases in AD.

Regarding increased core fucosylation, our recent study using the same hiMG model provides the first indication of its significance in microglia activation.[17] We further found that FUT8 expression was increased in both human AD brains and microglia isolated from 5xFAD mice, a model of AD-like cerebral amyloidosis. Moreover, FUT8 is a component of the p53 signaling cascade regulating microglial behavior; FUT8-catalyzed core fucosylation is required

for AβO-activated microglial alterations, including induction of pro-inflammatory cytokines, activation of p38MAPK, and phagocytic deficits.[17]

Bisecting GlcNAc, a β1,4-linked GlcNAc attached to the core β-mannose residue, is a structure specific to complex N-glycans. It is a prominent feature of the human brain complex N-glycans, occurring at a frequency of 40%.[53] The presence of a bisecting GlcNAc on glycoproteins has many implications in biological functions, such as in immune tolerance,[54] tumor metastasis, and brain development.[55,56] The relevance of bisecting GlcNAc to AD is suggested by its altered levels in AD brain samples, together with altered expression of GnT-III mRNA. However, whether it is up- or down-regulated in AD remains inconclusive as conflicting results were reported.[36,37,39] Interestingly, APP and β-site APP cleaving enzyme-1- (BACE1), two key proteins required for Aβ production, contain glycosylation modifications with bisecting GlcNac. Aβ (aggregation state not characterized) treatment was reported to enhance GnT-III mRNA expression in Neuro2a mouse neuroblastoma cells. This was considered neuroprotective as GnT-III-transfected cells showed increased α-secretase activity and decreased production of Aβ40 and Aβ42.[36] Contradicting this notion, Kizuka et al. reported that modifications with bisecting GlcNac stabilized BACE1 to increase Aβ production and that GnT-III deficiency reduced Aβ-plaque formation in the brain by accelerating lysosomal degradation of BACE1.[57] Again, the significance of altered bisecting GlcNac modifications in microglia is poorly understood. Our observation of decreased GnT-III mRNA expression and decreased bisecting GlcNac abundance in AβO-activated hiMG provides the first indication that bisecting GlcNac modifications play a role in regulating microglial function.

Compared to AβO, LPS clearly induced a distinct glycosylation-related transcriptomic and glycomic pattern with a decreased abundance of complex N-glycans and increased fucosylation, consistent with their different signaling pathways. The increased FUT4 and decreased FUCA1 expression may underlie the increased fucosylation we found in LPS-activated hiMG. However, in contrast to AβO effects, we did not find increased core fucosylation following LPS treatment,[17] suggesting that LPS mainly enhances terminal fucosylation. In addition, the fucosylation changes were differential among glycan structure subgroups, with the overall increase in fucosylation consisting predominantly of increased fucosylated-only N-glycans and decreased mono-fucosylated complex N-glycans also containing sialic acid. The functional implications of these novel structural changes warrant further investigation. Our results also prompt a novel hypothesis that LPS downregulates mannosidases, which trim mannose residues from high mannose N-glycans to yield Man5GlcNAc2, a key intermediate in the pathway to generate hybrid and complex N-glycans, resulting in reduced levels of complex N-glycans. This hypothesis would need further investigation.

Little is known about GSL in microglia, despite reported changes in ganglioside profiles in neurodegenerative disorders[58] and the anti-inflammatory effects of GM1 and other gangliosides on microglia.[59] It was observed by dot blot analysis that microglia were characterized by abundant GM1 in mixed murine glia culture. Treatment of mouse primary microglia with LPS resulted in decreased GM1 and GT1b levels.[59,60] However, these previously reported changes were not apparent in our GSL profiling of hiMG. We identified no GSL alterations in hiMG following AβO or LPS stimulation. The most abundant GSL was ganglioside GM3, the precursor of other complex gangliosides (Figure 2.4A). The second most abundant

sphingolipid was SM, followed by ganglioside G2. The remaining GSLs were less abundant, with each accounting for less than 5%. When considering the number of sialic acids, GSLs detected in hiMG were predominantly sialylated GSLs (Figure 2.4B).

In summary, using a human microglia culture model, we identified differential AβO- and LPS-induced glycosylation changes that may impact the functional or cellular interaction outcomes of these two types of pro-inflammatory activation, and we did not identify significant GSL changes. Our data add to currently scant information about microglia- and stimulant-specific "glycosylation codes." They also help generate hypotheses that may lead to a better glycoproteomic and glycolipidomic understanding of microglial function, which is exponentially more complex than the glycomic landscape we report here.

REFERENCES

(1) Nimmerjahn A, Kirchhoff F, Helmchen F. 2005. Resting microglial cells are highly dynamic surveillants of brain parenchyma in vivo. Science (80-) [Internet] 308:1314–1318. Available from: https://pubmed.ncbi.nlm.nih.gov/15831717/

(2) Streit WJ, Kreutzberg GW. 1987. Lectin binding by resting and reactive microglia. J Neurocytol 16:249–260.

(3) Rebelo AL, Chevalier MT, Russo L, Pandit A. 2022. Role and therapeutic implications of protein glycosylation in neuroinflammation. Trends Mol Med 28:270–289.

(4) Marschallinger J, Iram T, Zardeneta M, Lee SE, Lehallier B, Haney MS, Pluvinage J V., Mathur V, Hahn O, Morgens DW, Kim J, Tevini J, Felder TK, Wolinski H, Bertozzi CR, Bassik MC, Aigner L, Wyss-Coray T. 2020. Lipid-droplet-accumulating microglia represent a dysfunctional and proinflammatory state in the aging brain. Nat Neurosci 23:194–208.

(5) Heneka MT, Carson MJ, Khoury J El, Landreth GE, Brosseron F, Feinstein DL, Jacobs AH, Wyss-Coray T, Vitorica J, Ransohoff RM, Herrup K, Frautschy SA, Finsen B, Brown GC, Verkhratsky A, Yamanaka K, Koistinaho J, Latz E, Halle A, Petzold GC, Town T, Morgan D, Shinohara ML, Perry VH, Holmes C, Bazan NG, Brooks DJ, Hunot S, Joseph B, Deigendesch N, Garaschuk O, Boddeke E, Dinarello CA, Breitner JC, Cole GM, Golenbock DT, Kummer MP. 2015. Neuroinflammation in Alzheimer's disease. Lancet Neurol 14:388–405.

(6) Jansen IE, Savage JE, Watanabe K, Bryois J, Williams DM, Steinberg S, Sealock J, Karlsson IK, Hägg S, Athanasiu L, Voyle N, Proitsi P, Witoelar A, Stringer S, Aarsland D, Almdahl IS, Andersen F, Bergh S, Bettella F, Bjornsson S, Brækhus A, Bråthen G, de Leeuw C, Desikan RS, Djurovic S, Dumitrescu L, Fladby T, Hohman TJ, Jonsson P V., Kiddle SJ, Rongve A, Saltvedt I, Sando SB, Selbæk G, Shoai M, Skene NG, Snaedal J, Stordal E, Ulstein ID, Wang Y, White LR, Hardy J, Hjerling-Leffler J, Sullivan PF, van der Flier WM, Dobson R, Davis LK, Stefansson H, Stefansson K, Pedersen NL, Ripke S, Andreassen OA, Posthuma D. 2019. Genome-wide meta-analysis identifies new loci and functional pathways influencing Alzheimer's disease risk. Nat Genet 51:404–413.

(7) Johnson ECB, Dammer EB, Duong DM, Ping L, Zhou M, Yin L, Higginbotham LA, Guajardo A, White B, Troncoso JC, Thambisetty M, Montine TJ, Lee EB, Trojanowski JQ, Beach TG, Reiman EM, Haroutunian V, Wang M, Schadt E, Zhang B, Dickson DW, Ertekin-Taner N, Golde TE, Petyuk VA, De Jager PL, Bennett DA, Wingo TS, Rangaraju S, Hajjar I, Shulman JM, Lah JJ, Levey AI, Seyfried NT. 2020. Large-scale proteomic analysis of Alzheimer's disease brain and cerebrospinal fluid reveals early changes in energy metabolism associated with microglia and astrocyte activation. Nat Med 26:769–780.

(8) Bellenguez C, Küçükali F, Jansen IE, Kleineidam L, Moreno-Grau S, Amin N, Naj AC, Campos-Martin R, Grenier-Boley B, Andrade V, Holmans PA, Boland A, Damotte V, van der Lee SJ, Costa MR, Kuulasmaa T, Yang Q, de Rojas I, Bis JC, Yaqub A, Prokic I, Chapuis J, Ahmad S, Giedraitis V, Aarsland D, Garcia-Gonzalez P, Abdelnour C, Alarcón-Martín E, Alcolea D, Alegret M, Alvarez I, Álvarez V, Armstrong NJ, Tsolaki A, Antúnez C, Appollonio I, Arcaro M, Archetti S, Pastor AA, Arosio B, Athanasiu L, Bailly H, Banaj N, Baquero M, Barral S, Beiser A, Pastor AB, Below JE, Benchek P, Benussi L, Berr C, Besse C, Bessi V, Binetti G, Bizarro A, Blesa R, Boada M, Boerwinkle E, Borroni B, Boschi S, Bossù P, Bråthen G, Bressler J, Bresner C, Brodaty H, Brookes KJ, Brusco LI, Buiza-Rueda D, Bûrger K, Burholt V, Bush WS, Calero M, Cantwell LB, Chene G, Chung J, Cuccaro ML, Carracedo Á, Cecchetti R, Cervera-Carles L, Charbonnier C, Chen HH, Chillotti C, Ciccone S, Claassen JAHR, Clark C, Conti E, Corma-Gómez A, Costantini E, Custodero C, Daian D, Dalmasso MC, Daniele A, Dardiotis E, Dartigues JF, de Deyn PP, de Paiva Lopes K, de Witte LD, Debette S, et al. 2022. New insights into the genetic etiology of Alzheimer's disease and related dementias. Nat Genet 54:412–436.

(9) Maezawa I, Zimin PI, Wulff H, Jin LW. 2011. Amyloid-β protein oligomer at low nanomolar concentrations activates microglia and induces microglial neurotoxicity. J Biol Chem 286:3693–3706.

(10) Maezawa I, Nguyen HM, Di Lucente J, Jenkins DP, Singh V, Hilt S, Kim K, Rangaraju S, Levey AI, Wulff H, Jin LW. 2018. K v 1.3 inhibition as a potential microglia-Targeted therapy for Alzheimer's disease: Preclinical proof of concept. Brain 141:596–612.

(11) Leng F, Edison P. 2021. Neuroinflammation and microglial activation in Alzheimer disease: where do we go from here? Nat Rev Neurol 17:157–172.

(12) Penney J, Ralvenius WT, Tsai LH. 2020. Modeling Alzheimer's disease with iPSC-derived brain cells. Mol Psychiatry 25:148–167.

(13) Smith AM, Dragunow M. 2014. The human side of microglia. Trends Neurosci 37:125–135.

(14) Saito H, Kashida S, Inoue T, Shiba K. 2007. The role of peptide motifs in the evolution of a protein network. Nucleic Acids Res 35:6357–6366.

(15) Gagneux P, Panin V, Hennet T, Aebi M, Varki A. 2022. Evolution of Glycan Diversity. Available from: http://www.ncbi.nlm.nih.gov/pubmed/14109742%0Ahttp://www.pubmedcentral.nih.gov/articlerender.fcgi?artid=PMC3591600

(16) Haenseler W, Sansom SN, Buchrieser J, Newey SE, Moore CS, Nicholls FJ, Chintawar S, Schnell C, Antel JP, Allen ND, Cader MZ, Wade-Martins R, James WS, Cowley SA. 2017. A Highly Efficient Human Pluripotent Stem Cell Microglia Model Displays a Neuronal-Co-culture-Specific Expression Profile and Inflammatory Response. Stem Cell Reports 8:1727–1742.

(17) Jin L-W, Di Lucente J, Ruiz Mendiola U, Tang X, Zivkovic AM, Lebrilla CB, Maezawa I. 2023. The role of FUT8-catalyzed core fucosylation in Alzheimer's amyloid-β oligomer-induced activation of human microglia. Glia 71:1346–1359.

(18) Lambert MP, Barlow AK, Chromy BA, Edwards C, Freed R, Liosatos M, Morgan TE, Rozovsky I, Trommer B, Viola KL, Wals P, Zhang C, Finch CE, Krafft GA, Klein WL. 1998. Diffusible, nonfibrillar ligands derived from Aβ1-42 are potent central nervous system neurotoxins. Proc Natl Acad Sci U S A 95:6448–6453.

(19) Kim D, Paggi JM, Park C, Bennett C, Salzberg SL. 2019. Graph-based genome alignment and genotyping with HISAT2 and HISAT-genotype. Nat Biotechnol [Internet] 37:907–915. Available from: https://www.nature.com/articles/s41587-019-0201-4

(20) Liao Y, Smyth GK, Shi W. 2014. FeatureCounts: An efficient general purpose program for assigning sequence reads to genomic features. Bioinformatics 30:923–930.

(21) McCarthy DJ, Chen Y, Smyth GK. 2012. Differential expression analysis of multifactor RNA-Seq experiments with respect to biological variation. Nucleic Acids Res 40:4288–4297.

(22) Li Q, Xie Y, Wong M, Barboza M, Lebrilla CB. 2020. Comprehensive structural glycomic characterization of the glycocalyxes of cells and tissues. Nat Protoc [Internet] 15:2668–2704. Available from: https://www.nature.com/articles/s41596-020-0350-4

(23) Kuznetsova A, Brockhoff PB, Christensen RHB. 2017. lmerTest Package: Tests in Linear Mixed Effects Models. J Stat Softw 82:1–26.

(24) Gaunitz S, Tjernberg LO, Schedin-Weiss S. 2021. The N-glycan profile in cortex and hippocampus is altered in Alzheimer disease. J Neurochem 159:292–304.

(25) Lünemann JD, von Gunten S, Neumann H. 2021. Targeting sialylation to treat central nervous system diseases. Trends Pharmacol Sci [Internet] 42:998–1008. Available from: https://doi.org/10.1016/j.tips.2021.09.002

(26) Miwa HE, Song Y, Alvarez R, Cummings RD, Stanley P. 2012. The bisecting GlcNAc in cell growth control and tumor progression. Glycoconj J 29:609–618.

(27) Sandhoff R, Sandhoff K. 2018. Emerging concepts of ganglioside metabolism. FEBS Lett 592:3835–3864.

(28) Belarbi K, Cuvelier E, Bonte M-A, Desplanque M, Gressier B, Devos D, Chartier-Harlin M-C. 2020. Glycosphingolipids and neuroinflammation in Parkinson's disease. Mol Neurodegener 15:59.

(29) Chen Q, Tan Z, Guan F, Ren Y. 2020. The Essential Functions and Detection of Bisecting GlcNAc in Cell Biology. Front Chem 8.

(30) Fujitani N, Furukawa J ichi, Araki K, Fujioka T, Takegawa Y, Piao J, Nishioka T, Tamura T, Nikaido T, Ito M, Nakamura Y, Shinohara Y. 2013. Total cellular glycomics allows characterizing cells and streamlining the discovery process for cellular biomarkers. Proc Natl Acad Sci U S A [Internet] 110:2105–2110. Available from: https://www.pnas.org/doi/abs/10.1073/pnas.1214233110

(31) Park D, Brune KA, Mitra A, Marusina AI, Maverakis E, Lebrilla CB. 2015. Characteristic changes in cell surface glycosylation accompany intestinal epithelial cell (IEC) differentiation: High mannose structures dominate the cell surface glycome of undifferentiated enterocytes. Mol Cell Proteomics 14:2910–2921.

(32) Delannoy CP, Rombouts Y, Groux-Degroote S, Holst S, Coddeville B, Harduin-Lepers A, Wuhrer M, Elass-Rochard E, Guérardel Y. 2017. Glycosylation Changes Triggered by the Differentiation of Monocytic THP-1 Cell Line into Macrophages. J Proteome Res [Internet] 16:156–169. Available from: https://pubs.acs.org/doi/full/10.1021/acs.jproteome.6b00161

(33) Hinneburg H, Pedersen JL, Bokil NJ, Pralow A, Schirmeister F, Kawahara R, Rapp E, Saunders BM, Thaysen-Andersen M. 2020. High-resolution longitudinal N- And O-glycoprofiling of human monocyte-to-macrophage transition. Glycobiology [Internet] 30:679–694. Available from: https://dx.doi.org/10.1093/glycob/cwaa020

(34) Li J, Hsu HC, Mountz JD, Allen JG. 2018. Unmasking Fucosylation: from Cell Adhesion to Immune System Regulation and Diseases. Cell Chem Biol [Internet] 25:499–512. Available from: https://doi.org/10.1016/j.chembiol.2018.02.005

(35) Pace A, Scirocchi F, Napoletano C, Zizzari IG, D'angelo L, Santoro A, Nuti M, Rahimi H, Rughetti A. 2022. Glycan-Lectin Interactions as Novel Immunosuppression Drivers in Glioblastoma. Int J Mol Sci 23.

(36) Akasaka-Manya K, Manya H, Sakurai Y, Wojczyk BS, Kozutsumi Y, Saito Y, Taniguchi N, Murayama S, Spitalnik SL, Endo T. 2010. Protective effect of N-glycan bisecting GlcNAc residues on β-amyloid production in Alzheimer's disease. Glycobiology [Internet] 20:99–106. Available from: https://dx.doi.org/10.1093/glycob/cwp152

(37) Gizaw ST, Ohashi T, Tanaka M, Hinou H, Nishimura SI. 2016. Glycoblotting method allows for rapid and efficient glycome profiling of human Alzheimer's disease brain, serum and cerebrospinal fluid towards potential biomarker discovery. Biochim Biophys Acta - Gen Subj 1860:1716–1727.

(38) Palmigiano A, Barone R, Sturiale L, Sanfilippo C, Bua RO, Romeo DA, Messina A, Capuana ML, Maci T, Le Pira F, Zappia M, Garozzo D. 2016. CSF N-glycoproteomics for early diagnosis in Alzheimer's disease. J Proteomics 131:29–37.

(39) Haukedal H, Freude KK. 2021. Implications of Glycosylation in Alzheimer's Disease. Front Neurosci 14.

(40) Akasaka-Manya K, Manya H, Sakurai Y, Wojczyk BS, Kozutsumi Y, Saito Y, Taniguchi N, Murayama S, Spitalnik SL, Endo T. 2010. Protective effect of N-glycan bisecting GlcNAc residues on β-amyloid production in Alzheimer's disease. Glycobiology [Internet] 20:99–106. Available from: https://dx.doi.org/10.1093/glycob/cwp152

(41) Schjoldager KT, Narimatsu Y, Joshi HJ, Clausen H. 2020. Global view of human protein glycosylation pathways and functions. Nat Rev Mol Cell Biol 21:729–749.

(42) Estus S, Shaw BC, Devanney N, Katsumata Y, Press EE, Fardo DW. 2019. Evaluation of CD33 as a genetic risk factor for Alzheimer's disease. Acta Neuropathol 138:187–199.

(43) Klaus C, Hansen JN, Ginolhac A, Gérard D, Gnanapragassam VS, Horstkorte R, Rossdam C, Buettner FFR, Sauter T, Sinkkonen L, Neumann H, Linnartz-Gerlach B. 2020. Reduced sialylation triggers homeostatic synapse and neuronal loss in middle-aged mice. Neurobiol Aging 88:91–107.

(44) Bhattacherjee A, Rodrigues E, Jung J, Luzentales-Simpson M, Enterina JR, Galleguillos D, St. Laurent CD, Nakhaei-Nejad M, Fuchsberger FF, Streith L, Wang Q, Kawasaki N, Duan S, Bains A, Paulson JC, Rademacher C, Giuliani F, Sipione S, Macauley MS. 2019. Repression of phagocytosis by human CD33 is not conserved with mouse CD33. Commun Biol [Internet] 2. Available from: https://doi.org/10.1038/s42003-019-0698-6

(45) Pluvinage J V., Haney MS, Smith BAH, Sun J, Iram T, Bonanno L, Li L, Lee DP, Morgens DW, Yang AC, Shuken SR, Gate D, Scott M, Khatri P, Luo J, Bertozzi CR, Bassik MC, Wyss-Coray T. 2019. CD22 blockade restores homeostatic microglial phagocytosis in ageing brains. Nature [Internet] 568:187–192. Available from: https://www.nature.com/articles/s41586-019-1088-4

(46) Allendorf DH, Puigdellívol M, Brown GC. 2020b. Activated microglia desialylate their surface, stimulating complement receptor 3-mediated phagocytosis of neurons. Glia 68:989–998.

(47) Allendorf DH, Franssen EH, Brown GC. 2020a. Lipopolysaccharide activates microglia via neuraminidase 1 desialylation of Toll-like Receptor 4. J Neurochem [Internet] 155:403–416. Available from: https://onlinelibrary.wiley.com/doi/full/10.1111/jnc.15024

(48) Gonzalez-Gil A, Porell RN, Fernandes SM, Maenpaa E, Li TA, Li T, Wong PC, Aoki K, Tiemeyer M, Yu ZJ, Orsburn BC, Bumpus NN, Matthews RT, Schnaar RL. 2022. Human brain sialoglycan ligand for CD33, a microglial inhibitory Siglec implicated in Alzheimer's disease. J Biol Chem [Internet] 298. Available from: https://doi.org/10.1016/j.jbc.2022.101960

(49) Büll C, Nason R, Sun L, Van Coillie J, Sørensen DM, Moons SJ, Yang Z, Arbitman S, Fernandes SM, Furukawa S, McBride R, Nycholat CM, Adema GJ, Paulson JC, Schnaar RL, Boltje TJ, Clausen H, Narimatsu Y. 2021. Probing the binding specificities of human Siglecs by cell-based glycan arrays. Proc Natl Acad Sci U S A [Internet] 118:e2026102118. Available from: https://www.pnas.org/doi/abs/10.1073/pnas.2026102118

(50) Brinkman-Van Der Linden ECM, Varki A. 2000. New aspects of siglec binding specificities, including the significance of fucosylation and of the sialyl-Tn epitope. J Biol Chem [Internet] 275:8625–8632. Available from: http://www.jbc.org/article/S0021925818301686/fulltext

(51) Stansley B, Post J, Hensley K. 2012. A comparative review of cell culture systems for the study of microglial biology in Alzheimer's disease. J Neuroinflammation 9.

(52) Selkoe DJ, Hardy J. 2016. The amyloid hypothesis of Alzheimer's disease at 25 years. EMBO Mol Med 8:595–608.

(53) Suttapitugsakul S, Stavenhagen K, Donskaya S, Bennett DA, Mealer RG, Seyfried NT, Cummings RD. 2022. Glycoproteomics Landscape of Asymptomatic and Symptomatic Human Alzheimer's Disease Brain. Mol Cell Proteomics 21:100433.

(54) Yoshimura M, Ihara Y, Ohnishi A, Ijuhin N, Nishiura T, Kanakura Y, Matsuzawa Y, Taniguchi N. 1996. Bisecting N-acetylglucosamine on K562 cells suppresses natural killer cytotoxicity and promotes spleen colonization. Cancer Res 56:412–418.

(55) de-Freitas-Junior JCM, Carvalho S, Dias AM, Oliveira P, Cabral J, Seruca R, Oliveira C, Morgado-D\'\iaz JA, Reis CA, Pinho SS. 2013. Insulin/IGF-I signaling pathways enhances tumor cell invasion through bisecting GlcNAc N-glycans modulation. an interplay with E-cadherin. PLoS One 8:e81579.

(56) Tan Z, Wang C, Li X, Guan F. 2018. Bisecting N-acetylglucosamine structures inhibit hypoxia-induced epithelial-mesenchymal transition in breast cancer cells. Front Physiol 9:210.

(57) Kizuka Y, Kitazume S, Fujinawa R, Saito T, Iwata N, Saido TC, Nakano M, Yamaguchi Y, Hashimoto Y, Staufenbiel M, Hatsuta H, Murayama S, Manya H, Endo T, Taniguchi N. 2015. An aberrant sugar modification of BACE1 blocks its lysosomal targeting in Alzheimer's disease. EMBO Mol Med 7:175–189.

(58) Sipione S, Monyror J, Galleguillos D, Steinberg N, Kadam V. 2020. Gangliosides in the Brain: Physiology, Pathophysiology and Therapeutic Applications. Front Neurosci 14.

(59) Galleguillos D, Wang Q, Steinberg N, Zaidi A, Shrivastava G, Dhami K, Daskhan GC, Schmidt EN, Dworsky-Fried Z, Giuliani F, Churchward M, Power C, Todd K, Taylor A, Macauley MS, Sipione S. 2022. Anti-inflammatory role of GM1 and other gangliosides on microglia. J Neuroinflammation 19.

(60) Simon BM, Malisan F, Testi R, Nicotera P, Leist M. 2002. Disialoganglioside GD3 is released by microglia and induces oligodendrocyte apoptosis. Cell Death Differ 9:758–767.
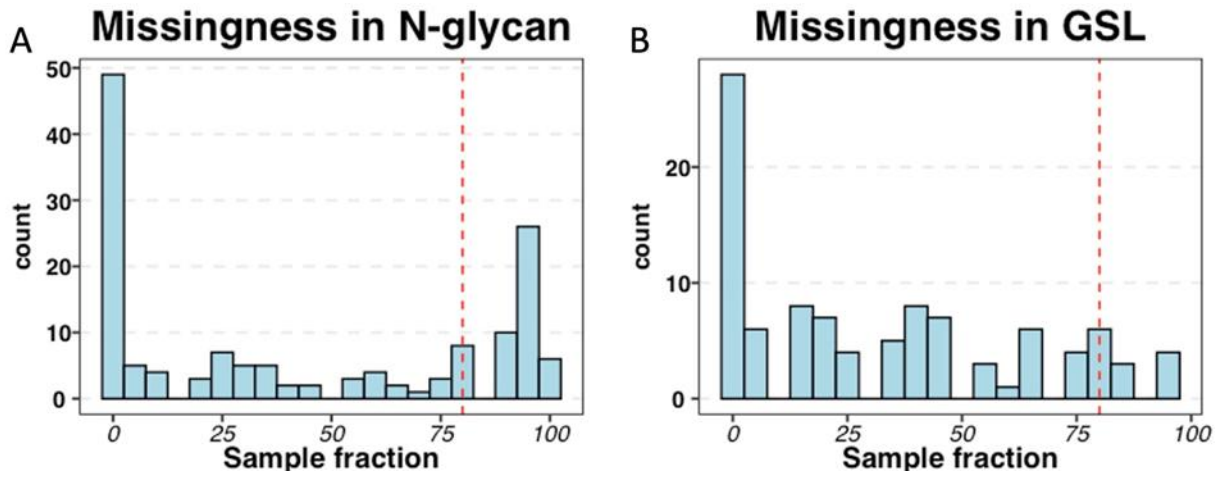
Figure S2.1 The missingness of N-glycans and GSL as the percentage of the number of samples. A) The missingness in N-glycan. B) The missingness in GSL. Red dash lines denote missingness of 80% across all samples.
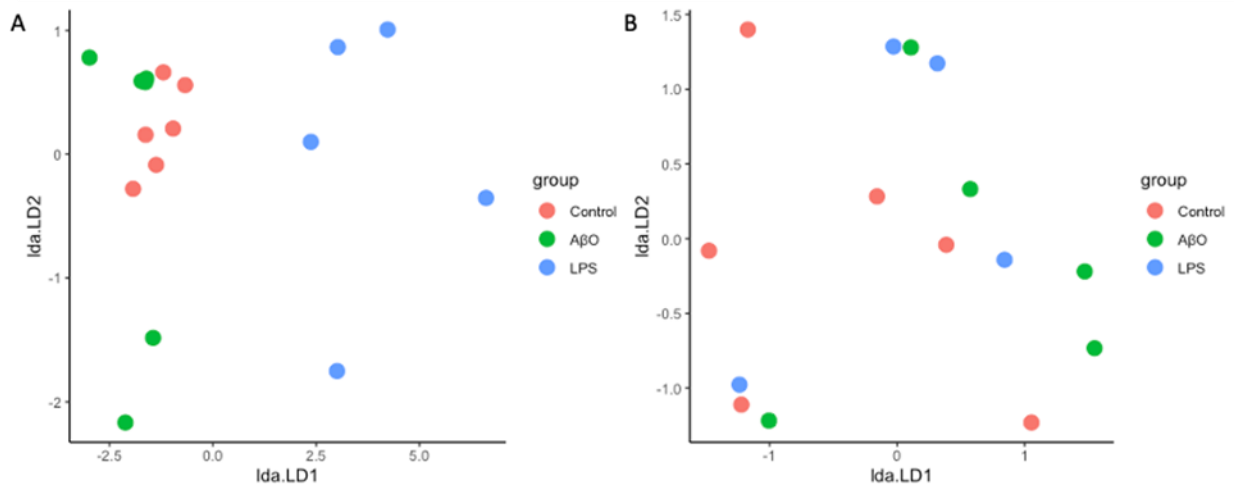
Figure S2.2 The scatter plot of the post-hoc linear discriminant analysis (LDA) of MANOVA for the PCA plots. A) The LDA scatter plot for N-glycan. According to the LDA scatter plot, LPS had the most significant impact on the group mean differences. B) The LDA scatter plot for GSL.
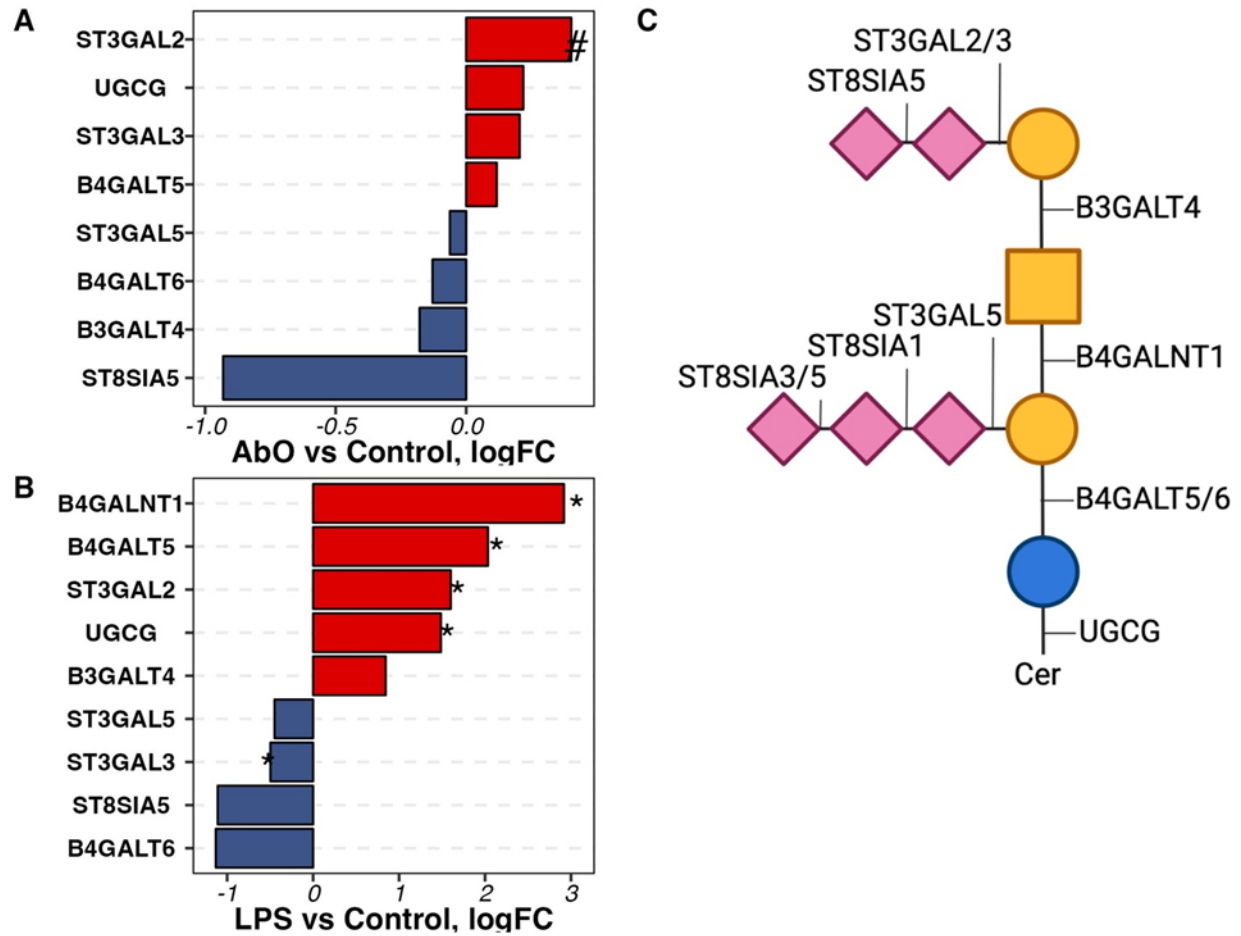
Figure S2.3 The differential expression of genes involved in GSL biosynthesis in in AβO- and LPS-activated hiMG. A) The differential expression of genes involved in GSL biosynthesis in AβO-activated hiMG. B) The differential expression of genes involved in GSL biosynthesis in LPS-activated hiMG. C) The schematics of GSL structure and the corresponding enzymes. The pound (#) denotes genes with unadjusted p-value < 0.05 but FDP >0.05. The asterisk (*) denotes genes with FDP < 0.05.

CHAPTER III

Profiling Intact Glycosphingolipids with automated structural annotation and quantitation

from human samples with Nanoflow Liquid Chromatography Mass Spectrometry

Author Information

Ryan L. Schindler[1], Armin Oloumi[1], Jennyfer Tena[1], Michael Russelle S. Alvarez[1], Yiyun Liu[1],

Sheryl Grijaldo[1], Mariana Barboza[2], Lee-way Jin[3], Angela M. Zivkovic[4], Carlito B. Lebrilla[1]*

[1]Department of Chemistry, University of California, Davis, California, 95616, USA.

[2]Innovation Institute for Food and Health, University of California, Davis, California, 95616, USA.

[3]Department of Pathology and Laboratory Medicine, University of California Davis Medical

Center, Sacramento, California, 95817, USA.

[4]Department of Nutrition, University of California, Davis, California, 95616, USA.

ABSTRACT

Sphingolipids are an essential subset of bioactive lipids found in most eukaryotic cells that contribute to membrane biophysical properties and are involved in cellular differentiation, recognition, and mediating interactions. The described nanoHPLC-ESI-Q/ToF methodology utilizes known biosynthetic pathways, accurate mass detection, optimized collision-induced disassociation, and a robust nanoflow chromatographic separation for the analysis of intact sphingolipids found in human tissue, cells, and serum. The methodology was developed and validated with an emphasis on addressing the common issues experienced in the profiling of these amphipathic lipids which are part of both the glycocalyx and lipidome. The high sensitivity obtained using nano-range flowrates with robust chromatographic reproducibility over a wide range of concentrations and injection volumes results in confident identifications for profiling these low-abundant biomolecules.

INTRODUCTION

Sphingolipids are a class of amphipathic lipids found primarily in the outer membranes of eukaryotic cells.[1] Since their discovery in 1884[2], researchers have explored the intricate degree of structural and functional diversity associated with this class of biomolecules. Their characterizing structural feature is the comprisal of a sphingoid base commonly referred to as a long-chain base (LCB). The addition of an N-linked acyl group forms a two-tailed lipid backbone referred to as a ceramide. Further derivatization is observed with the incorporation of a variety of different polar headgroups such as phosphatidylcholine, monosaccharides, as well as complex oligosaccharides. An example glycosphingolipid, GM1a, is depicted in Figure 3.1, including other possible headgroups and lipid compositions. These molecules contribute to membrane biophysical properties[3], mediate cellular interactions,[4–8] and are involved in signaling,[9] each attributed to the structural features of both the lipid ceramide and polar moiety.[10] Sphingolipids have also been identified for their role in pathology where aberrant

structures or abundances are observed.[11–13]
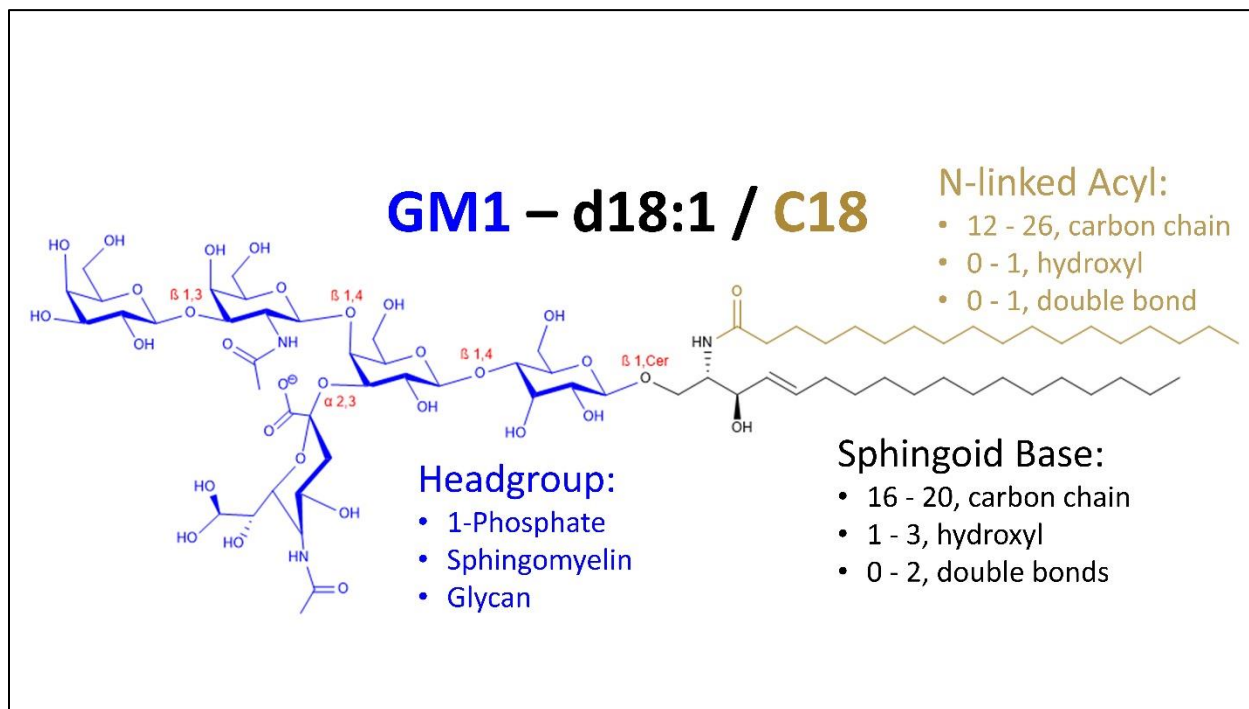
Figure 3.1 Molecular structure of GM1a and summary of the structural diversity of human sphingolipids. The head groups are drawn in blue, and the sphingoid base is in black.

The consistent structural features found in the human sphingolipidome are attributed to the specificity of the enzymes involved in the biosynthetic pathways. De novo synthesis occurs in the endoplasmic reticulum producing the two-tailed ceramides with sphingosine (d18:1) being the most common sphingoid base but minor species such as Dihydroceramide (d18:0), 4-Hydroxydihydrosphinganine (t18:0), 6-Hydroxysphingosine (t18:1), and 4t,14c-Sphingediene (d18:2) are also present.[14–19] Although the number of theoretically possible lipid structures is calculated to be over 4,000 different species, roughly 500 unique ceramide structures have been discovered in humans.[9] After ceramide synthesis, these lipids are translocated to the Golgi where headgroups are incorporated to the C1 position to form species such as ceramide-1-phosphate (1P-), sphingomyelin (SM-), Cerebrosides (Hex-), Sulfatides (SHex-, SLac-), and

complex glycosphingolipids. The enzymatic pathways have been well established for 1P-, SM-, cerebrosides, and sulfatides, as a limited number of enzymes are involved. However, in the case of complex glycosphingolipids, the pathway to the finalized structure is more obscured. The complexity stems from their untemplated construction involving numerous glycosyltransferases with overlapping specificities. The activity of these enzymes is dependent on both localization in the ER and substrate availability. Complex oligosaccharides have been categorized by seven possible core structures; gala-, ganglio-, globo-, isoglobo-, lacto-, neolacto-, and muco-series[1] where the tendency to express a specific core is dependent on the cell type. To date, roughly 450 unique glycan head groups have been discovered, a number which increases when considering likely intermediates and possible modifications such as lactone rings and acetylation.[1] When considering the structural diversity of these molecules intact, the theoretical compound list includes over 200,000 unique species.

The structural diversity and relatively low abundance of these compounds within the overall lipid profile of a cell have made comprehensive analysis challenging. Previous works have used several techniques to elucidate the structural features of both the lipid[20–24] and oligosaccharide headgroups[25] through a combination of analytical and biochemical methods. Significant collaborative efforts have been made to assist in further research of these molecules. LIPID MAPS (https://www.lipidmaps.org/) includes a database of all previously discovered ceramide species as well as SphinGOMAP (https://sphingolab.biology.gatech.edu/), which has documented the complementary complex oligosaccharide headgroups.

Historically, analytical methodologies to profile sphingolipids used fluorophore-labeled monoclonal antibodies that bind to specific glycan structures[13] or endoglycosylceramidase,

which hydrolyzes the bond between the oligosaccharide and the ceramide.[26] Both workflows provided the initial understanding of sphingolipid molecular structures but lacked information for the intact molecules. Modern techniques for sphingolipid profiling and quantitation employ high-performance liquid chromatography (HPLC) for the separation of these intact compounds coupled with accurate mass spectrometry (MS) detection.[27]

In this study, we developed a robust and reproducible method for quantitatively profiling intact GSLs with automated compound identification. In this work, the nomenclature follows the same convention commonly used based on IUPAC-IBU recommendations.[28] The method employed nanoflow reverse-phase high-performance liquid chromatography and quadrupole time-of-flight mass spectrometry (nRP-HPLC-Q/ToF) to separate and detect GSLs from biological samples effectively. Compound identification is key and facilitated by using a combination of biological knowledge, accurate mass detection, collision-induced disassociation, and retention times to assign molecular structures instantaneously. This process is semi-automated with the utilization of Agilent's Personal Compound Database and Library software (PCDL), which drastically reduces false-positive identifications by as much as 50%. Profiling can be accomplished in a fraction of the time with a high degree of confidence and minimal background knowledge of sphingolipids. The most common issues observed in sphingolipid analysis that led to unreliable data are carryover, in-source fragmentation, and false-positive identifications from isobaric lipid species. Improved chromatography and removal of carryover was accomplished by developing an online sample enrichment using a series of timed valve switches with a C-8 trap followed by separation on a C-18 column. Source conditions were

optimized to maximize ion generation with minimal to zero in-source fragmentation with the

specification of the more susceptible compounds.

METHODS

Materials and Chemicals. Sphingomyelin-d18:1/C18 (SM-d18:1/C18, Cat# 860586), Sphingomyelin-d18:1/C24:1 (SM-d18:1/C24:1, Cat# 860593), Glucose-d18:1/C24:1 (Glc-d18:1/C24:1, Cat# 860549), Sulfo-galactose-d18:1/C24:1 (SHex-d18:1/C24:1, Cat# 860571), GM1a-d18:1/C20 (Cat# 860588), GM3-d18:1/C18 (Cat# 860074), GD1a-d18:1/C18 (Cat# 860091), and GT1b-d18:1/C18 (Cat# 860089) standards were purchased from Avanti Polar Lipids (Alabaster, AL). Lymphoblast CESS cells (Cat# TIB-190) were obtained from the American Type Cell Culture (Manassas, VA). α2-3,6,8 Neuraminidase (Cat# P0720) was purchased from New England Biolabs (Ipswich, MA). Human serum (Cat# S7023), sucrose (Cat# S7903), potassium hydroxide (KOH, Cat# P5958), potassium chloride (KCl, Cat# P3911), ammonium acetate (NH4CH3CO2, Cat# 73594), sodium carbonate (Na2CO3, Cat# S5761), trichloromethane (CHCl3, Cat# CS10501), and protease inhibitor cocktail (Cat# 539137) were purchased from Sigma (St. Louis, MO). Fetal bovine serum (Cat# 16000-069), penicillin-streptomycin (Cat# 15140-122), 1M HEPES (Cat# 15630080), methanol (MeOH, Optima LC/MS, Cat# A456-4), and isopropanol (IPA, Optima LC/MS, Cat# A461-4) were purchased from Thermo Fisher Scientific (Waltham, MA). C-8 SPE plate (100mg, Cat# FNSC08.800) was purchased from Glygen. Glacial acetic acid (GAA, Cat# AC110) was purchased from Spectrum (New Brunswick, NJ). Formic acid (Optima LC/MS, Cat# A117-50) was purchased from Fisher Chemical (Hampton, NH).

Brain Tissue. Human brain tissue was obtained through the University of California, Davis – Alzheimer's Disease Center. The specific sample was taken from the lateral cerebellum of a single subject, age of 93, with pathologically confirmed Alzheimer's disease.

Cell Culture. CESS lymphoblast (TIB-190) cells were cultured in RPMI-1640 Medium (ATCC, Cat# 30-2001) containing 10% (v/v) fetal bovine serum and 1% (V/V) penicillin-streptomycin in 75mm2 culture dishes. The cells were maintained in a humidified incubator at 37°C with 5% CO_2 subcultured at 80% confluency for five passages and harvested at 80% confluency in the sixth passage.

Standard Preparation. External standards SM-d18:1/C18, SM-d18:1/C24:1, Glc-d18:1/C24:1, SHex-d18:1/C24:1, and $GM1_a$-d18:1/C18 were received as ammonium salts and diluted to 50µM stock solutions in MeOH/IPA/water (2/8/1, v/v/v%). Further dilution used MeOH/water (1/1, v/v%). GM3-d18:1/C18 (100µg/mL), $GD1_a$-d18:1/C18 (100µg/mL), and $GT1_b$-d18:1/C18 (124µg/mL) were received as MeOH solutions, and diluted in MeOH/water (1/1, v/v%).

Sample Preparation; Tissue, Serum, and Cells. ~10^6 cells, 1-100mg of neural tissue, and 100µL of serum were used to generate sample profiles. The tissue was weighed into 15mL falcon tubes and diluted with a buffer consisting of 0.25 M sucrose, 20mM HEPES adjusted to pH 7.4 with KOH, and a 1:100 protease inhibitor cocktail (1.2mL for cells & 1.5mL for tissue). Tissue samples were homogenized manually before lysis with µ-needle sonication (60 J for cells and 80 J for tissue samples).

The nuclear fraction was precipitated by centrifugation at 2000 RCF for 10 minutes. The supernatant was transferred and ultracentrifuged at 200k RCF for 30 minutes at 4°C to form a membrane pellet. After removing the supernatant, samples were diluted with 0.2 M Na_2CO_3 (0.5 mL for cells & 1.0 mL for tissue) and ultracentrifuged to remove membrane-associated

proteins. The supernatant was removed, and samples were ultracentrifuged again with the same volume of water. After discarding the water, membrane lipids were dissolved using a modified Folch extraction of freshly prepared water/MeOH/CHCl^3 (3/8/4, v/v/v%, 500μL for cells & 800μL for tissue/serum) and sonicated for 30min. Samples were then centrifuged at 9,000RCF for 10min to precipitate the membrane proteins, and the supernatant was collected. 100 μL of 0.1 M KCl was added to induce a liquid-liquid separation, the top layer (aqueous) was transferred and dried by vacuum centrifugation.

Sphingolipids were enriched with a 100mg, C-8, 96-well SPE plate. Wells were first conditioned with 200μL of MeOH/IPA (1/1, v/v%) and primed with 400μL of water/MeOH (1/1, v/v%). Samples were reconstituted with 600 μL of water/MeOH and gravity-loaded. The flow-through was reloaded to ensure maximum recovery. 600μL of water/MeOH was used to wash. Sphingolipids were eluted with 200μL of the MeOH/IPA and then dried. Condition, prime, wash, and elution steps used centrifugation (100 RCF, 1 minute).

Dried samples can be sealed and stored at -20°C for several months until ready for analysis. Before analysis, samples were reconstituted in water/MeOH (1/1, v/v%) (20μL for serum/cells & 0.25mg/μL for tissue), transferred to autosampler vials, and stored in the 4°C cooler for up to 7 days before injection.

Neuraminidase Treatment. α2-3,6,8-Neuraminidase was used following the vendor's recommendation and found to hydrolyze terminal sialic acid residues preferentially. Enzyme-treated samples required an additional sample injection using a unique instrumental method with an increased on-line enrichment step, increasing all gradient and valve switch time points

by 9 minutes. Comparison of the reduction in initial signal and increase in resulting products from non-treated to treated samples allow determination of a- and b-series gangliosides. The crystal structure of C. perfringens sialidase nanH was modeled using AlphaFold[29] using the sequence information from UniProt.[30] Glycolipid models were drawn using CHARMM-GUI.[31] After modeling, the 3D structures of the sialidase enzyme and glycolipid substrates were minimized and prepared for in-silico docking experiments using Chimera.[32] In silico docking, calculations were performed in PyRx[33] using AutoDock VINA[34] by defining a 24 Å x 25 Å x 56 Å search space enclosing the reported active site residues of the enzyme. After performing calculations, the models were visualized, and binding interactions were identified using Discovery Studio (Dassault Systems, 2020).

Nanoflow HPLC-Q/TOF Methodology. Automated sample injection and data collection used an Agilent 1200 series nanoflow HPLC. On-line sample enrichment used a Zorbax 300SB-C8 trap column, 0.3 ID x 5mm, 5μm particle size, 300Å pore size (Agilent Technologies Inc., Cat# 5065-9914). The analytical separation was carried out on a Zorbax 300SB-C18 column, 0.075 ID x 150mm, 3.5μm particle size, 300Å pore size (Agilent Technologies Inc., Cat# 5065-9911). The loading/washing pump was operated at 2.5μL/min. Sample loading used 0.1% GAA and 20mM $NH_4CH_3CO_2$ in water/MeOH/IPA (40/50/10, v/v/v%). Sample washing (MP-W) used MeOH/IPA (1/1, v/v%). The gradient used was as follows: 0% MP-W from 0 to 20min, increased to 99% at 25min, held until 35min, decreased back to 0% at 40 min, and held until 70 min. The gradient pump used a flow rate of 0.3μL/min. Mobile phase A (MP-A) used 0.1% GAA in 20 mM $NH_4CH_3CO_2$ in MeOH/water (25/75, v/v), and mobile phase B (MP-B) with a composition of 0.1% GAA in 20 mM $NH_4CH_3CO_2$ in MeOH/IPA (75/25, v/v). The timed composition changes are as

follows: 76% MP-B from 0 to 20min, a linear increase to 96% at 60min, held until 62min, decreased to 76% by 64min and held until 70min. The C-8 trap column (left) was operated at 70°C and the C-18 analytical column (right) was operated at 60°C. Both the trap and analytical columns have a working range up to 90°C for between 2 to 5 pH. A 10pt/2ps μ-switching valve was configured for efficient enrichment, elution, and washing at low flow rates. Samples are enriched from 0 to 6min (μ-valve 1→10). From 6 to 20min, analytes are backflushed from the C-8 trap to C-18 analytical column under stepped isocratic conditions (μ-valve 1→2). From 20 to 70min the gradient, wash, and equilibration are carried out (μ-valve 1→10).

The analytical column was coupled to an orthogonal nanoESI source (Agilent Technologies, G1992A) and operated in positive ion mode with a 15μm ID SilicaTip (New Objective). Precursor ion mass filtering, fragmentation, and detection were carried out on a quadrupole time-of-flight mass spectrometer (Agilent Technologies, G6520A). Source conditions were optimized by direct infusion and used N_2 drying gas at 325°C with a flow rate of 3.0 L/min. The capillary voltage was 1300V and adjusted during initial system conditioning for a corresponding current of 0.070 μA and stable spray throughout the gradient. The fragmentor, skimmer, and octopoleRF voltages were set to 150V, 90V, and 750V respectively. The quadrupole used automatic precursor ion selection with a mass range of 550 – 2000 m/z and an absolute threshold of 1000 counts corresponding to roughly double the baseline noise. The preferred charge state was set to 2 > 1. Precursor ions were fragmented in an N_2-filled chamber with collision-induced disassociation using an m/z dependent collision energy determined by linear interpolation with the equation $E = 1.2 \times \left(\frac{m/z}{100}\right) + 12$. Active exclusion was enabled after collection of one MS_2 spectrum and released after one-minute corresponding to

approximately one half the average peak width. The time-of-flight detector was operated such that abundance and accurate mass were in the range of 100 – 2000 m/z. An internal reference mass of 1221.9 m/z (Agilent Technologies Inc., Cat# G1982-85001) was used for continuous mass correction (≤ 10ppm). The HPLC modules, valve configuration, and connecting capillaries, and source positioning that were used are included in the supplemental information.

Data Analysis. Post-acquisition compound identification and peak integration were completed using Agilent's MassHunter Qualitative Analysis software version (B08.00) with the Find by Molecular Feature (FMF) algorithm using a CSV database of compounds including the molecular formula, retention time (optional), mass, name, and description. Verification assistance of the identified compounds used Agilent's Personal Compound Database and Library (PCDL) software version (B08.00), where the identified compounds are compared and scored from a spectral library. Library search settings enabled screening and score adjustment with a precursor and fragment mass tolerance of 25 ppm and 50 ppm, respectively. Each sample's compound list was exported to individual CSV files and an in-house Python script was used to organize the data for analysis in Excel.

RESULTS & DISCUSSION

Nanoflow High-Pressure Liquid Chromatography – Mass Spectrometry Profile of Sphingolipids from Brain Tissue. A reverse-phase nanoflow HPLC-Q/ToF method was developed and employed to extensively profile the intact sphingolipids found in human neural tissue, serum, and a lymphoblast cell line. A representative chromatogram is depicted based on the reported method, where the major peaks are labeled with their representative structures (Figure 3.2). This tissue profile, from the lateral cerebellum, yielded 118 unique compounds varying in both headgroup and lipid structure. A summary of the structures present in the chromatogram with the respective relative abundances of ≥0.01% are summarized with a heatmap (Figure 3.3) using IUPAC-IUB nomenclature.[28] The structural assignment is comprehensive and was determined using the methods described in greater detail below. The major sphingolipids observed were gangliosides GD1$_a$, GD1$_b$, and GM1$_a$. These oligosaccharide headgroups are typically observed in the grey matter regions of the brain, which are primarily composed of neuronal cell bodies and their dendrites. We also observed gangliosides with up to four sialic acid residues (GQ1) as well as some fucosylation and galactose extension, which are rarely observed. The most abundant ganglioside-associated lipid was sphingosine (d18:1) with an N-linked acyl group of 18 and 20 carbons. The less abundant lipid species observed varied in their sphingoid long-chain base (LCB) structure with 4-hydroxydihydrosphganine and 4t,14c-sphingediene. Other minor glycosphingolipids included sulfatides and cerebrosides with mostly sphingosine and N-linked acyl groups varying in hydroxylation and unsaturation to a 24-carbon chain (C24:1, C24 OH, C24:1 OH). These species are commonly found in white matter

and are key structural components that provide stability in the multi-layered myelin sheath which functions to protect and insulate the neural axons.
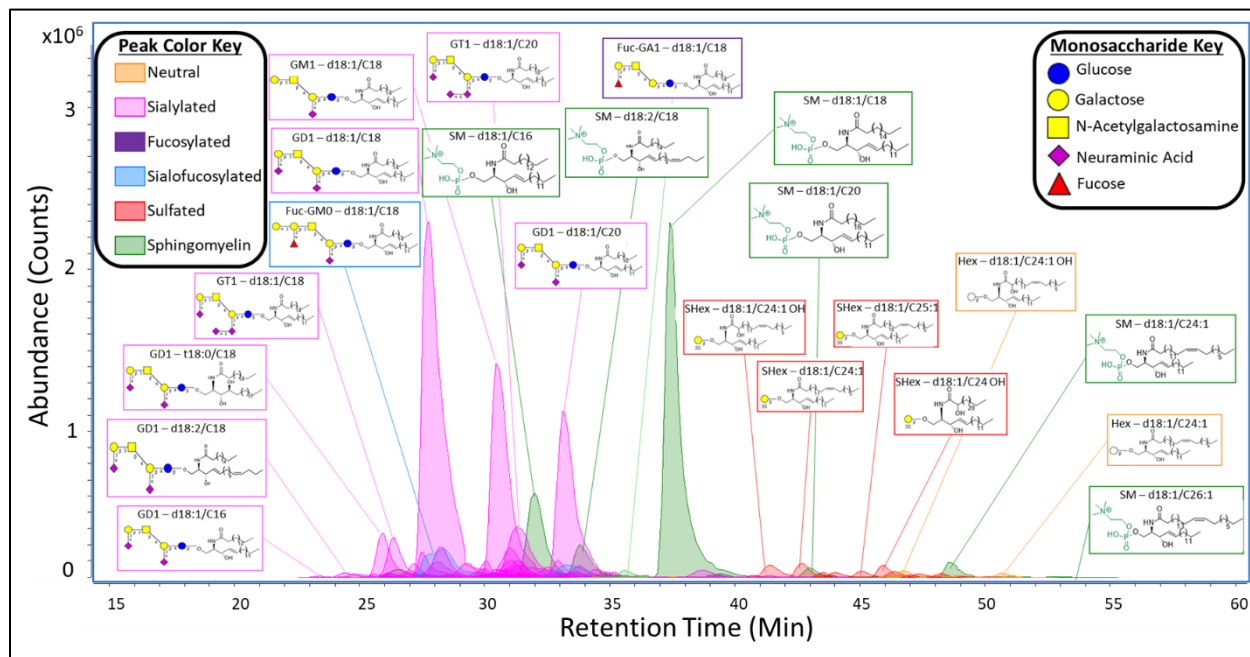
Figure 3.2 Example chromatogram of human brain tissue sphingolipid profile annotating 22 of 118 compounds found. Inset structures were assigned based on the methods described.

We found that using previous methodologies to profile multiple samples in succession resulted in varying degrees of carryover, which affected quantitation, caused retention shifts, and degraded the general analysis.[35] For example, a 1µL injection of a 1mg/µL tissue sample showed carryover in ten subsequent blanks which is depicted in the supplementary information (Figure S3.1A). To eliminate the carryover, we used a series of valve switches with a C-8 trap column to fractionate the sphingolipids, preventing hydrophilic and hydrophobic contaminants from being introduced to the analytical column (Figure S3.1B). This enrichment strategy was validated using a pool of sphingolipid standards over a range of injection volumes which showed consistent elution times and linearly correlated responses (Figure S3.2). Instrumental

duplicate injections for the brain tissue sample produced an average %RSD of 11.5% for all

compounds above 0.1% relative abundance. Biological triplicates of the TIB-190 cell line

generated an average percent relative standard deviation (%RSD) of 18.4% for all compounds

>0.1% relative abundance.

Lateral Cerebellum	GT1	GD1	GD2	GD3	Fuc-GM0	GM1	GM2	GM3	Hex	HexS	SM	Ceramide Totals:
d18:1 / C14	0.0%	0.0%	0.0%	0.0%	0.0%	0.0%	0.0%	0.0%	0.0%	0.0%	0.5%	0.5%
d18:1 / C16	0.0%	0.1%	0.0%	0.0%	0.0%	0.1%	0.0%	0.0%	0.0%	0.1%	4.2%	4.5%
d18:1 / C18	1.9%	23.6%	1.0%	0.2%	2.5%	11.6%	1.0%	1.2%	0.0%	0.2%	15.9%	59.2%
d18:1 / C20	4.0%	10.3%	0.3%	0.4%	0.9%	0.0%	0.1%	0.0%	0.0%	0.0%	0.4%	16.3%
d18:1 / C22	0.1%	0.4%	0.0%	0.0%	0.0%	0.1%	0.0%	0.0%	0.0%	0.1%	0.0%	0.8%
d18:1 / C24:1	0.0%	0.1%	0.0%	0.0%	0.0%	0.0%	0.0%	0.0%	0.0%	0.6%	0.0%	0.7%
d18:1 / C24 OH	0.0%	0.0%	0.0%	0.0%	0.0%	0.0%	0.0%	0.0%	0.2%	0.5%	0.0%	0.7%
d18:1 / C24:1 OH	0.0%	0.0%	0.0%	0.0%	0.0%	0.0%	0.0%	0.0%	0.3%	0.6%	0.0%	0.9%
d18:0 / C18	0.1%	0.0%	0.1%	0.0%	0.0%	0.5%	0.0%	0.0%	0.0%	0.0%	0.2%	0.9%
d18:2 / C18	0.0%	0.2%	0.0%	0.0%	0.0%	0.5%	0.1%	0.0%	0.0%	0.1%	1.6%	2.5%
d18:2 / C20	0.0%	0.3%	0.0%	0.0%	0.0%	0.1%	0.0%	0.0%	0.0%	0.0%	0.0%	0.5%
d18:2 / C24	0.0%	0.0%	0.0%	0.0%	0.0%	0.0%	0.0%	0.1%	0.1%	0.0%	0.6%	0.8%
t18:0 / C18	0.2%	2.0%	0.1%	0.2%	0.0%	1.4%	0.2%	0.0%	0.0%	0.0%	0.0%	4.1%
t18:0 / C20	0.8%	1.8%	0.1%	0.0%	0.0%	0.3%	0.0%	0.0%	0.0%	0.0%	0.0%	2.9%
Headgroup Totals:	7.2%	38.8%	1.5%	0.9%	3.5%	14.6%	1.3%	1.3%	0.6%	2.0%	23.5%	

Figure 3.3 Heatmap summarizing the relative intensities of sphingolipids (≥0.01% relative abundance) in human brain tissue. The major products correspond to GM1, GD1, and SM.

Mass Spectrometric Analysis of Sphingolipids. The identification of individual

sphingolipids (glycosphingolipids and sphingomyelin) employed a combination of tools for

putative molecular structure assignment including (1) the known biosynthetic pathways, which

reduces the number of possible structures, (2) collision-induced dissociation (CID)

fragmentation spectra with accurate mass detection, (3) unique retention times, (4) and

neuraminidase treatment for sialic acid linkages. A biologically informed structure list was used

to initially match the intact molecular weight of compounds to detected precursor ions. This list included species with lipid structures consisting of 32 to 44 carbons, two to three hydroxyl groups, and up to three double bonds for all headgroups. It was observed that the charge states and associated adducts were dependent on the headgroup. For example, sphingomyelin, cerebrosides, sulfatides, and lactosylceramide primarily produced singly protonated quasimolecular ions. However, larger more complex glycosphingolipids contained multiply charged species with combinations of protons and ammonium adducts ([M+H]+, [M+NH4]+, [M+2H]2+, [M+H+NH4]2+, [M+2NH4]2+) which are summed to determine the compound total abundances.

The combination of various adducted species complicated the analysis by increasing the number of overlapping isobars, making CID crucial for identification. CID produced fragments corresponding to dissociation of both the headgroup and the N-linked acyl as well as losses of H_2O were observed. For example, the fragmentation of a cerebrosides (Hex-d18:1/C18) with a molecular weight of 727.6u was detected as a protonated species and produced fragments corresponding to H_2O loss of the intact molecule (710.6 m/z), the ceramide (566.6, 548.5, 530.5 m/z) and the LCB (282.3, 264.3 m/z) (Figure 3.4A). 4t,14c-sphingediene (d18:2; 280.3, 262.3 m/z), 4-hydroxydihydrosphganine (t18:0; 300.3, 282.3 m/z), dihydroceramide (d18:0; 302.3, 284.3 m/z), and 6-hydroxysphingosine (t18:1, 298.3, 280.3 m/z) LCBs were also discernable and imperative to distinguish hydroxyl group and double-bond positioning between the two lipid tails. Although the N-linked acyl and LCB moieties of the ceramide vary in structure, the cleavage sites shown are the most common. Additional ceramide and LCB structures and their corresponding product ions used for identification are included in the supplemental

information (Table S3.1 & S3.2). Sulfatides (SHex-), which contain a sulfate at the C3 position of the hexose, produced a similar CID profile to cerebrosides differing in the major fragment that corresponded to the loss of both H_2O and SO_3 groups (Figure 3.4B). The presence of N-acetylhexosamine (HexNAc) or neuraminic acid (Neu5Ac) in large glycosphingolipids (GSLs) resulted in MS_2 peaks with up to four linked monosaccharides. A comprehensive list of ions that were commonly observed from the fragmentation of the oligosaccharide headgroups were tabulated (Table 1). Neu5Ac modifications, such as acetyl or methyl groups as well as lactone rings, were also readily observed product ions (Figure 3.4C). Glycan fragments containing fucose were also observed, for example 1Hex1HexNAc1Fuc (512.2 m/z). However, fucose-containing compounds were not major fragments due to the labile nature of fucose under CID. Typically, fucosylated structures such as the fucosylated-GM0-d18:1/C18 were instead confirmed by neutral losses of terminal monosaccharides (Figure 3.4D).
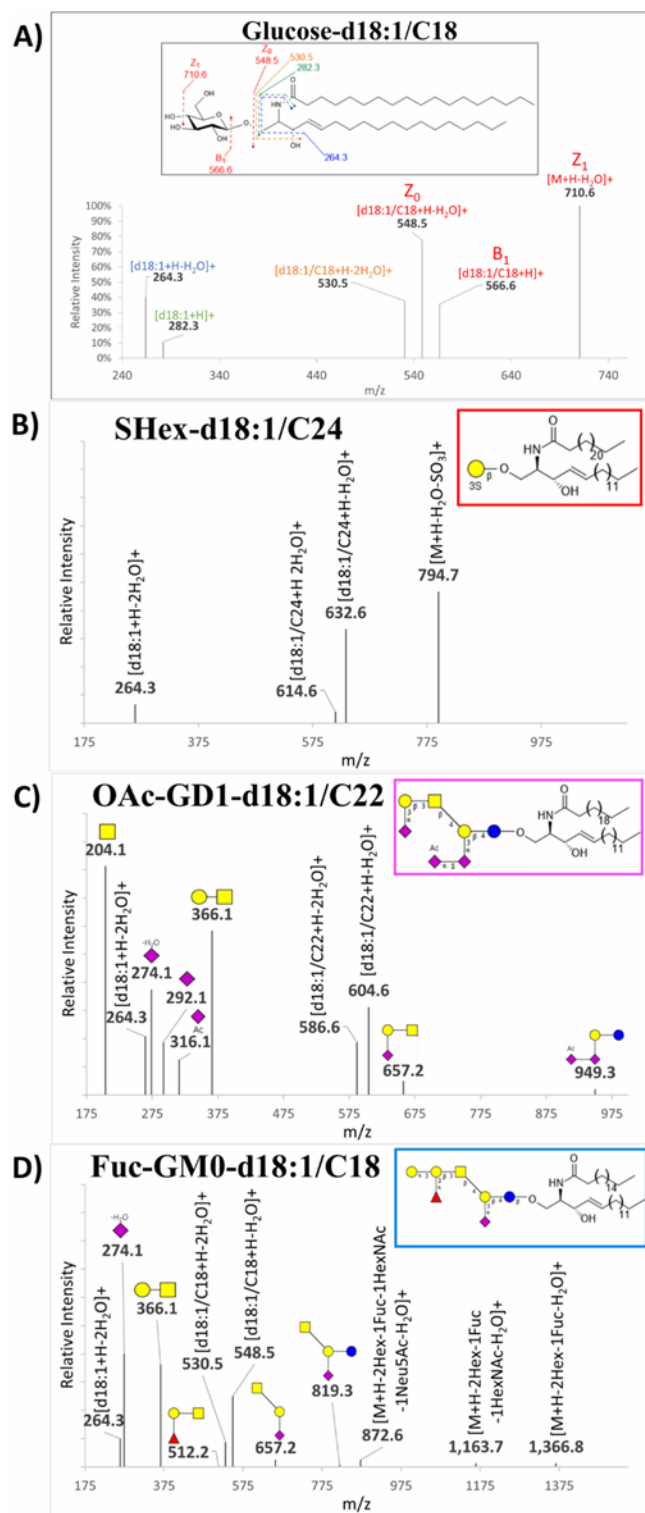
Figure 3.4 Typical fragmentations generated by CID MS/MS for compounds with various headgroups including A) Glucose-, B) SHex-, C) Ac-O-OGD1-, and D) Fuc-GM0-d18:1/C18. Dominant dissociation products correspond to cleavages of glycan linkages.

Sphingomyelins (SM), a sphingolipid but not a glycolipid, with a phosphocholine headgroup was monitored to complete the sphingolipid profile. SM species were distinct from the glycolipids in that the protonated species yielded an odd-numbered nominal mass. A common fragment corresponded to the dissociation of the phosphocholine headgroup to yield a prominent 184.1 m/z ion due to the high gas-phase basicity of the tertiary amine in the headgroup. Ceramide-1-phosphate (1P-Cer), another sphingolipid was also present but in lower abundances.

Of note, phosphatidylcholine (PC) and phosphatidylethanolamine (PE) phospholipids are isobaric compounds observed within the elution gradient that can cause false positive identifications. Both were singly protonated generating even nominal precursors with distinctive MS_2 profiles. PC commonly generated a 184.1 phosphocholine fragment and PE was identified by the neutral loss of 141 amu. An additional source of false-positive identifications can occur from in-source fragmentation of the labile glycan headgroups. Source conditions were optimized to minimize this effect to 1% or less relative abundance. Sulfatides showed the highest degree of in-source fragmentation with loss of sulfate and producing an identical ion mass as HexCer. To a lesser extent, in-source fragmentation of sialic acid residues was observed where, GD3- was initially identified as GM3-. All false positive identifications were easily distinguished and correctly identified.

Chromatographic behavior of Sphingolipids. Chromatographic retention times were primarily dictated by the head group and the ceramides' overall chain lengths. Sphingomyelins showed a broad lipid profile that encompassed the entire chromatogram and were used to assign relative retention time (RRT) values for species containing the same lipid structure but

differing in their headgroup. Although RRT values varied depending on the specific lipid, average RRTs for all observed matching ceramides were assigned to give general headgroup dependent elution trends. With SM (RRT 1.000) being the latest eluting, neutral GSLs showed slightly earlier elution times and differences became more prominent with larger glycans: Hex- (0.987 RRT), Lac- (0.961), Gb3 (0.940), GA1 (0.928), Fuc-GA1 (0.925), and GA0 (0.904). Sulfated and mono-sialylated GSLs with their single anionic moieties eluted earlier: SHex- (0.868 RRT), SLac- (0.822), GM3 (0.861), GM2 (0.833), GM1 (0.839). The most pronounced shifts in retention were observed from polysialylated GSLs; GD3- (0.771 RRT), GD2- (0.764), GD1- (0.755), Fuc-GD1- (0.753), GT1- (0.724), and GQ1- (0.700). Differences in LCB structures were also observed chromatographically for structures with a fixed head group and N-linked acyl. Increasing hydroxide groups and unsaturated bonds resulted in earlier elution times (Figure 3.5A), which was confirmed by CID fragmentation (Figure 3.5B, C, D). Isomeric lipids differing in double bond position were resolved where ceramides containing sphingosine and an unsaturated fatty acid (d18:1/FA:1) eluted earlier than 4t,14c-sphingediene with a saturated acyl group (d18:2/FA) (Figure S3.3).
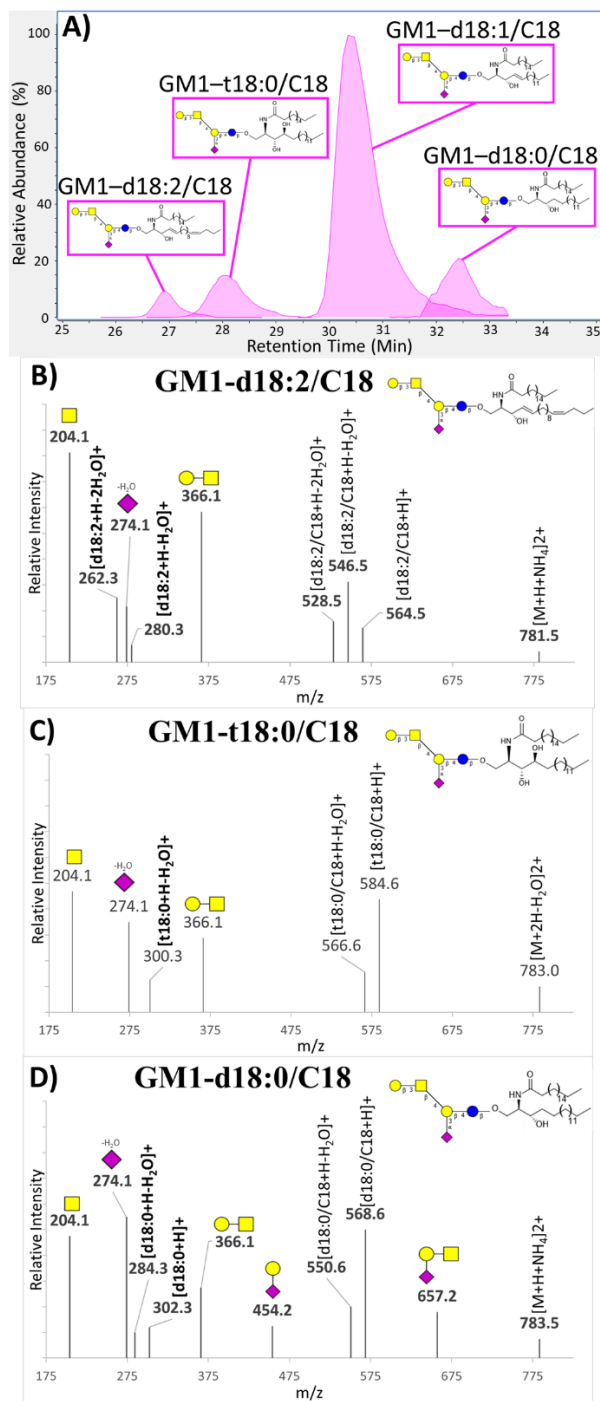
Figure 3.5 Elution pattern for different LCBs and MS2 spectra for GM1-LCB/C18 with B) d18:2, C) t18:0, and D) d18:0.

The identity of some structures that yielded only partially informative CID profiles were

further confirmed by the linear correlation of chromatographic retention times to acyl chain

length (Figure S3.4). The more abundant species of a group (same headgroup and LCB) that contained complete CID spectra, were used to identify the less abundant sphingolipids by matching the observed retention times to the expected values.

Neuraminidase treatments for Structural analysis of Gangliosides. Reverse-phase chromatography was unable to separate glycan isomers with multiple neuraminic acid linkages and positions. For this reason, we employed α2-3,6,8-neuraminidases to determine the sialic acid linkages in $GT1_b$, $GD1_a$, and $GM1_a$. Surprisingly, upon α2-3,6,8 neuraminidase treatment, the completely desialylated ganglioside core GA1 was not observed. Experimental data showed cleavage of sialic acid residues attached to the terminal galactose, but α2-3 and α2-8 sialic acids linked to the first core galactose remained intact. Molecular dynamic simulations were performed and corroborated the experimental data showing a steric hindrance of the neuraminidase active site by the terminal galactose when the tetrasaccharide core was present (Figure S3.5). By accounting for this feature, glycan structures were determined with a single enzyme treatment.

Automated and extrapolated compound ID. We sought to automate structural identification of all sphingolipids (including all glycolipids) using both the accurate mass, MS_2 (CID) and the chromatographic elution patterns. We therefore developed an in-house spectral library containing identified structures including the molecular formula, characteristic charge state, adducts, CID product ions, and retention times using Agilent's Personal Compound Database and Library (PCDL, B08.00) software. This workflow is especially useful when conducting studies with large sample sets as manual verification of MS_2 spectra is tedious and requires a notable degree of user experience. For reference, a generated library score of ≥10

indicated a correct identification, lower scores required further investigation. Although the use of this software greatly expedites the identification of sphingolipids, it is currently limited to compounds that have been manually verified previously. For this reason, initial identification of compounds using the comprehensive CSV database of monoisotopic masses was necessary.

Following the identification and validation of all sphingolipid species observed, the compound list for each sample was exported as an individual CSV file. An in-house Python script was then used that read the exported files, created a running dictionary for each unique structure, and reorganized the abundances from all samples into a single spreadsheet. The processed data was then analyzed in Microsoft excel and heatmaps were generated for visualization of the sphingolipid profiles. The application of this method was used on biological samples described below.

GSL profile of biological samples in Serum and Cells. A sphingolipid profile was generated from a commercial pool of human serum and was used as a quality control to monitor the sample preparation and instrument suitability (Figure S3.6). Of the 78 compounds observed in the serum profile, the most abundant glycosphingolipid was GM3-d18:1/16, a truncated core ganglioside (Figure 3.6). The major source of structural diversity observed in serum can be attributed to the lipid moiety as most of the glycan headgroups contained only one to three monosaccharide residues. GSLs in serum are thought to come from the shedding of membranes from tissues that circulate in micelles and lipoprotein complexes. We have previously found GSLs to be also bound to HDL and other lipoprotein particles.[36] We further examined GSLs in cell lines. We profiled CESS (TIB-190) cells, an immortalized line commonly used to study T-cells. The profile showed comparable results to that of serum in both the major

headgroup and lipid structures, suggesting T-cells and serum shared many common GSLs

(Figure S3.7). The full compound list from brain tissue, serum, and cells has been included

(Appendix I).

Serum	GD3	GM1	GM2	GM3	GA1	Gb3	Lac	SHex	SM	Ceramide Totals:
d18:1 / C14	0.00%	0.00%	0.00%	0.00%	0.41%	0.08%	0.09%	0.00%	3.55%	4.1%
d18:1 / C16	0.61%	1.23%	0.00%	5.63%	2.85%	0.90%	0.68%	0.26%	23.78%	35.9%
d18:1 / C17	0.00%	0.00%	0.00%	0.33%	0.00%	0.00%	0.00%	0.00%	0.45%	0.8%
d18:1 / C18	0.00%	0.19%	0.64%	2.14%	0.10%	0.10%	0.00%	0.00%	3.40%	6.6%
d18:1 / C20	0.11%	0.00%	0.00%	0.83%	0.00%	0.00%	0.00%	0.00%	1.94%	2.9%
d18:1 / C22	0.14%	0.11%	0.00%	2.60%	0.21%	0.00%	0.00%	0.16%	3.63%	6.9%
d18:1 / C23	0.00%	0.00%	0.00%	1.04%	0.00%	0.00%	0.00%	0.00%	1.16%	2.2%
d18:1 / C24	0.00%	0.13%	0.00%	2.26%	0.23%	0.00%	0.00%	0.00%	1.98%	4.6%
d18:1 / C24:1	0.00%	0.00%	0.00%	1.32%	0.00%	0.08%	0.00%	0.00%	1.02%	2.4%
d18:1 / C16 OH	0.00%	0.00%	0.00%	0.00%	0.00%	0.00%	0.00%	0.74%	0.00%	0.7%
d18:1 / C22 OH	0.00%	0.00%	0.00%	0.46%	0.00%	0.00%	0.00%	0.00%	0.00%	0.5%
d18:1 / C24 OH	0.00%	0.00%	0.00%	0.68%	0.00%	0.00%	0.00%	0.00%	0.00%	0.7%
d18:0 / C16	0.00%	0.00%	0.00%	0.00%	0.00%	0.00%	0.00%	0.00%	0.93%	0.9%
d18:2 / C16	0.00%	0.17%	0.00%	0.40%	0.73%	0.15%	0.14%	0.00%	6.50%	8.1%
d18:2 / C18	0.14%	0.09%	0.31%	0.00%	0.00%	0.00%	0.00%	0.00%	2.40%	2.9%
d18:2 / C20	0.00%	0.00%	0.00%	0.33%	0.00%	0.00%	0.00%	0.00%	0.50%	0.8%
d18:2 / C22	0.00%	0.00%	0.00%	1.21%	0.15%	0.00%	0.00%	0.10%	2.13%	3.6%
d18:2 / C24	0.00%	0.34%	0.00%	2.54%	0.78%	0.26%	0.58%	0.00%	5.06%	9.5%
d18:2 / C24:1	0.00%	0.00%	0.00%	0.00%	0.00%	0.00%	0.00%	0.00%	2.66%	2.7%
Headgroup Totals:	1.0%	2.2%	0.9%	21.8%	5.5%	1.6%	1.5%	1.3%	61.1%	

Figure 3.6 Summary heatmap of observed sphingolipids (≥0.01% relative abundance) in human serum.

CONCLUSION

A robust reverse-phase nanoflow HPLC-Q-ToF method was developed for profiling glycosphingolipids (and other sphingolipids) from human brain tissue, serum, and a lymphoblastic cell line. This method was developed to address the typical issues common to sphingolipid analysis such as carry-over and false-positive identifications. By utilizing previously discovered human biosynthetic pathways and correlating structures to fragmentation patterns along with excellent chromatographic reproducibility, exact structures can be assigned with a high degree of confidence. Future work that would greatly benefit the field of sphingolipids would include the development of software that can utilize the identification tools described in this work.

REFERENCES

(1)   Schnaar RL et al. Glycosphingolipids. In: Varki A et al., editors. Essentials of Glycobiology [Internet]. 4th edition. Cold Spring Harbor (NY): Cold Spring Harbor; 2022. Chapter 11. Available from: https://www.ncbi.nlm.nih.gov/books/NBK579905/ doi: 10.1101/glycobiology.4e.11

(2)   Thudichum, J. A Treatise on the Chemical Constitution of the Brain; Based Throughout upon Original Researches. Glasgow Med J. 1884, 22(5), 363–4. PMCID: PMC5907997.

(3)   Mencarelli, C et al. Ceramide Function in the Brain: When a Slight Tilt Is Enough. Cellular and Molecular Life Sciences. 2013, 70(2), 181–203. https://doi.org/10.1007/s00018-012-1038-x.

(4)   Todeschini, A. R et al. Functional role of glycosphingolipids and gangliosides in control of cell adhesion, motility, and growth, through glycosynaptic microdomains. Biochim Biophys Acta. 2008, 1780(3), 421-33. doi: 10.1016/j.bbagen.2007.10.008.

(5)   Young, M. M et al. Sphingolipids: regulators of crosstalk between apoptosis and autophagy. J Lipid Res. 2013, 54(1), 5-19. doi: 10.1194/jlr.R031278.

(6)   Van Kooyk, Y et al. G. A. Protein-Glycan Interactions in the Control of Innate and Adaptive Immune Responses. Nature Immunology. 2008, 9(6), 593–601. doi: 10.1038/ni.f.203.

(7)   D'Angelo, G et al. Glycosphingolipids: Synthesis and Functions. FEBS Journal. 2013, 280(24), 6338–53. doi: 10.1111/febs.12559.

(8)   Sipione, S et al. Gangliosides in the Brain: Physiology, Pathophysiology and Therapeutic Applications. Frontiers in Neuroscience. Frontiers Media S.A. 2020, 14, 572965. doi: 10.3389/fnins.2020.572965.

(9)   Merrill, A. H. Sphingolipid and Glycosphingolipid Metabolic Pathways in the Era of Sphingolipidomics. Chem Rev. 2011, 111(10), 6387–422. doi: 10.1021/cr2002917.

(10)   Quinville, B. M et al. A Comprehensive Review: Sphingolipid Metabolism and Implications of Disruption in Sphingolipid Homeostasis. Int J Mol Sci. 2021, 22(11), 5793. doi: 10.3390/ijms22115793.

(11)   Yamashita, T.; et al. Interruption of ganglioside synthesis produces central nervous system degeneration and altered axon-glial interactions. Proc Natl Acad Sci U S A. 2005, 102(8), 2725-30. doi: 10.1073/pnas.0407785102.

(12)   Schulze, H et al. Lysosomal lipid storage diseases. Cold Spring Harb Perspect Biol. 2011, 3(6), a004804. doi: 10.1101/cshperspect.a004804.

(13)   Kracun, I et al. Human brain gangliosides in development, aging and disease. Int J Dev Biol. 1991, 35(3), 289-95. PMID: 1814411.

(14) Davis, D. L et al. Dynamics of sphingolipids and the serine palmitoyltransferase complex in rat oligodendrocytes during myelination. J Lipid Res. 2020, 61(4), 505-522. doi: 10.1194/jlr.RA120000627.

(15) Ota, A et al. Bifunctional DEGS2 Has Higher Hydroxylase Activity toward Substrates with Very-Long-Chain Fatty Acids in the Production of Phytosphingosine Ceramides. J Bio. Chem. 2023, 299(4), 104603. doi: 10.1016/j.jbc.2023.104603.

(16) Mizutani, Y et al. Identification of the human sphingolipid C4-hydroxylase, hDES2, and its up-regulation during keratinocyte differentiation. FEBS Lett. 2004, 563(1-3), 93-7. doi: 10.1016/S0014-5793(04)00274-1.

(17) Karsai, G et al. T. FADS3 is a Δ14Z sphingoid base desaturase that contributes to gender differences in the human plasma sphingolipidome. J Biol Chem. 2020, 295(7), 1889-97. doi: 10.1074/jbc.AC119.011883.

(18) Robson, K. J et al. 6-Hydroxy-4-sphingenine in human epidermal ceramides. J Lipid Res. 1994, 35(11), 2060-8. PMID: 7868984.

(19) Mizutani, Y et al. Ceramide biosynthesis in keratinocyte and its role in skin function. Biochimie. 2009, 91(6), 784-90. doi: 10.1016/j.biochi.2009.04.001.

(20) Ann, Q et al. Structure Determination of Ceramides and Neutral Glycosphingolipids by Collisional Activation of [M + Li]+ Ions. J Am Soc Mass Spectrom. 1992, 3(3), 260-3. doi: 10.1016/1044-0305(92)87010-V

(21) Barrientos, R. C et al. Fragmentation Behavior and Gas-Phase Structures of Cationized Glycosphingolipids in Ozone-Induced Dissociation Mass Spectrometry. J Am Soc Mass Spectrom. 2019, 30(9), 1609–20. doi: 10.1007/s13361-019-02267-7.

(22) Hsu FF. Electrospray ionization with higher-energy collision dissociation tandem mass spectrometry toward characterization of ceramides as [M + Li]+ ions: Mechanisms of fragmentation and structural identification. Anal Chim Acta. 2021, 1142, 221-34. doi: 10.1016/j.aca.2020.09.056.

(23) Kayal, K et al. On the Formation of A-Hydroxy Fatty Acids. J Biol Chem. 1984, 259(6), 3548-53.

(24) Hartler, J et al. Automated Annotation of Sphingolipids Including Accurate Identification of Hydroxylation Sites Using MS NData. Anal Chem. 2020, 92(20), 14054–62. doi: 10.1021/acs.analchem.0c03016.

(25) Albrecht, S et al. Comprehensive Profiling of Glycosphingolipid Glycans Using a Novel Broad Specificity Endoglycoceramidase in a High-Throughput Workflow. Anal Chem. 2016, 88(9), 4795–802. doi: 10.1021/acs.analchem.6b00259.

(26)   Ishibashi, Y et al. Preparation and Characterization of EGCase I, Applicable to the
         Comprehensive Analysis of GSLs, Using a Rhodococcal Expression System. J Lipid Res.
         2012, 53(10), 2242–51. doi: 10.1194/jlr.D028951.

(27)   Sullards, M. C et al. Analysis of Mammalian Sphingolipids by Liquid Chromatography
         Tandem Mass Spectrometry (LC-MS/MS) and Tissue Imaging Mass Spectrometry (TIMS).
         Biochimica et Biophysica Acta (BBA) - Molecular and Cell Biology of Lipids. 2011,
         1811(11), 838–53. doi: 10.1016/j.bbalip.2011.06.027.

(28)   Chester, M. A. IUPAC-IUB Joint Commission on Biochemical Nomenclature (JCBN).
         Nomenclature of glycolipids--recommendations 1997. Eur J Biochem. 1998, 257(2), 293-
         8. doi: 10.1046/j.1432-1327.1998.2570293.x.

(29)   Jumper, J et al. Highly Accurate Protein Structure Prediction with AlphaFold. Nature.
         2021, 596(7873), 583–9. doi: 10.1038/s41586-021-03819-2.

(30)   Bateman, A et al. UniProt: The Universal Protein Knowledgebase in 2021. Nucleic Acids
         Res. 2021, 49(D1), D480–9. doi: 10.1093/nar/gkaa1100.

(31)   Jo, S et al. CHARMM-GUI 10 Years for Biomolecular Modeling and Simulation. J Comp.
         Chem. John Wiley and Sons Inc. 2017, 38(15), 1114–24. doi: 10.1002/jcc.24660.

(32)   Pettersen, E. F et al. UCSF Chimera - A Visualization System for Exploratory Research and
         Analysis. J Comput Chem. 2004, 25(13), 1605–12. doi: 10.1002/jcc.20084.

(33)   Hempel, J. E et al. Small-molecule library screening by docking with PyRx. Methods Mol
         Biol. 2015, 1263, 243-50. doi: 10.1007/978-1-4939-2269-7_19.

(34)   Trott, O et al. AutoDock Vina: improving the speed and accuracy of docking with a new
         scoring function, efficient optimization, and multithreading. J Comput Chem. 2010, 31(2),
         455-61. doi: 10.1002/jcc.21334.

(35)   Wong, M et al. Intact Glycosphingolipidomic Analysis of the Cell Membrane during
         Differentiation Yields Extensive Glycan and Lipid Changes. Sci Rep. 2018, 8, 10993. doi:
         10.1038/s41598-018-29324-7

(36)   Huang, J et al. Glycomic Analysis of High Density Lipoprotein Shows a Highly Sialylated
         Particle. J Proteome Res. 2014, 13(2), 681–91. doi: 10.1021/pr4012393.

Supplementary Information

Figure S3.1. Total compound chromatograms carryover comparison after the injection of a pooled tissue sample at a concentration of 1mg initial tissue weight / µL of solvent:

A. Neural tissue sample injection and the subsequent 10 blank injections using an Agilent ChipCube system and previously developed methodology from reference 38.
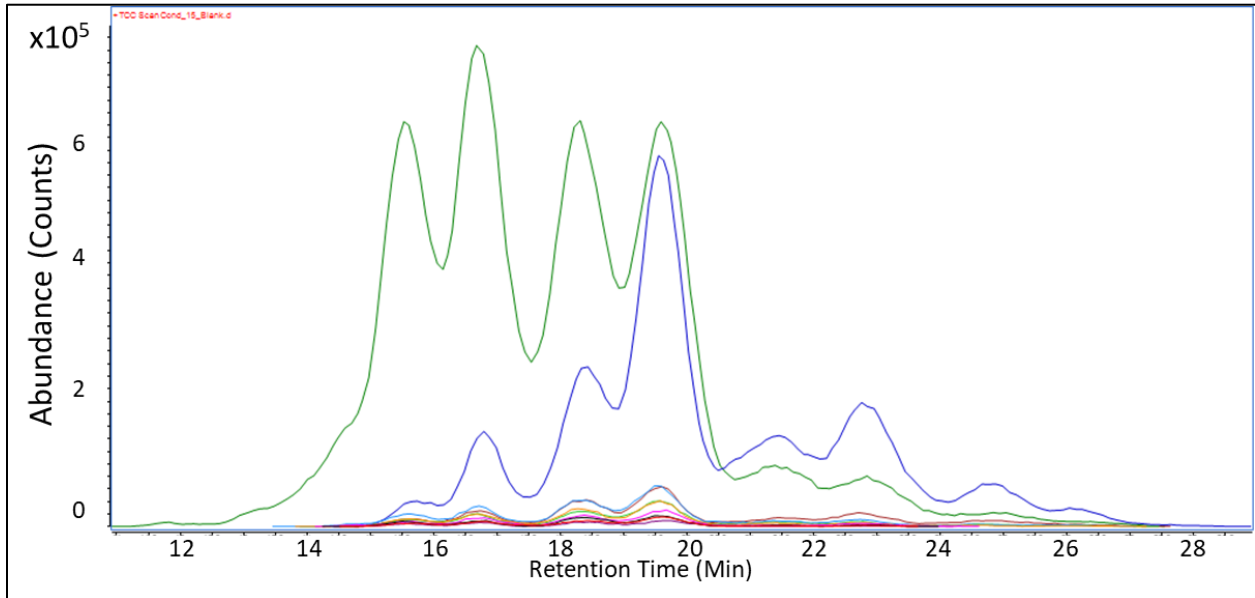
B. Neural tissue sample injection with no detectable compounds in the subsequent blank injection using the developed instrumental configuration and method.
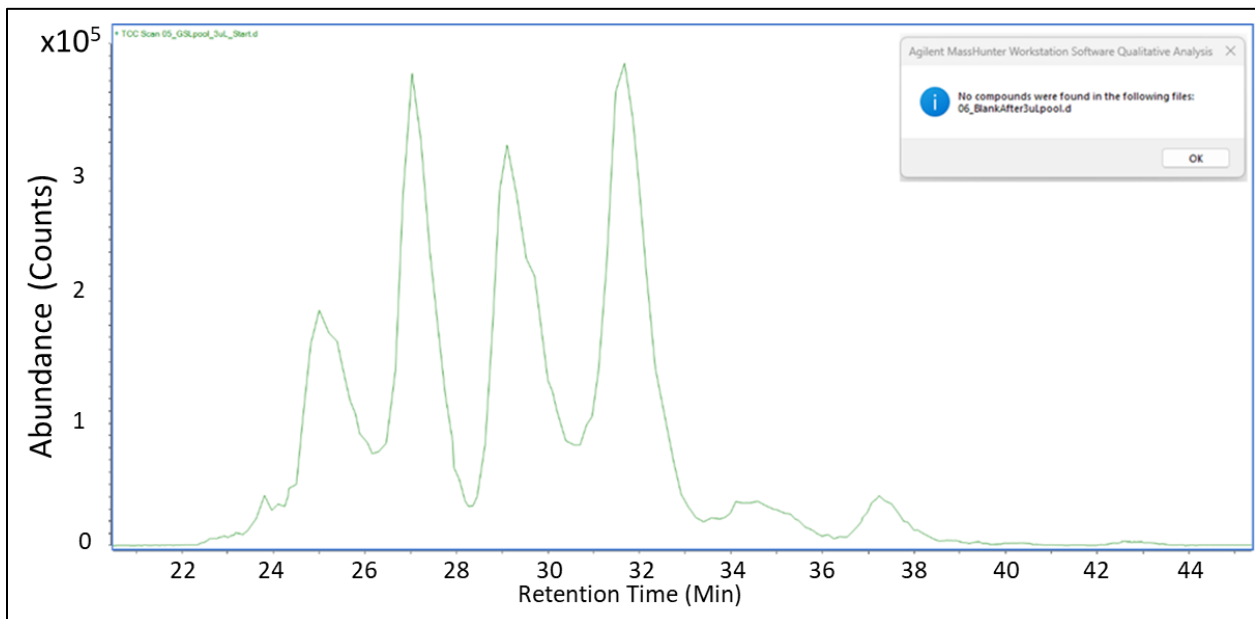
Figure S3.2. Overlaid chromatograms of a standard pool with 0.5µL, 1.0µL, and 1.5µL injections and calibration curve. GM3 and SM4 had similar concentrations and responses, resulting in the calibration curve overlapping.
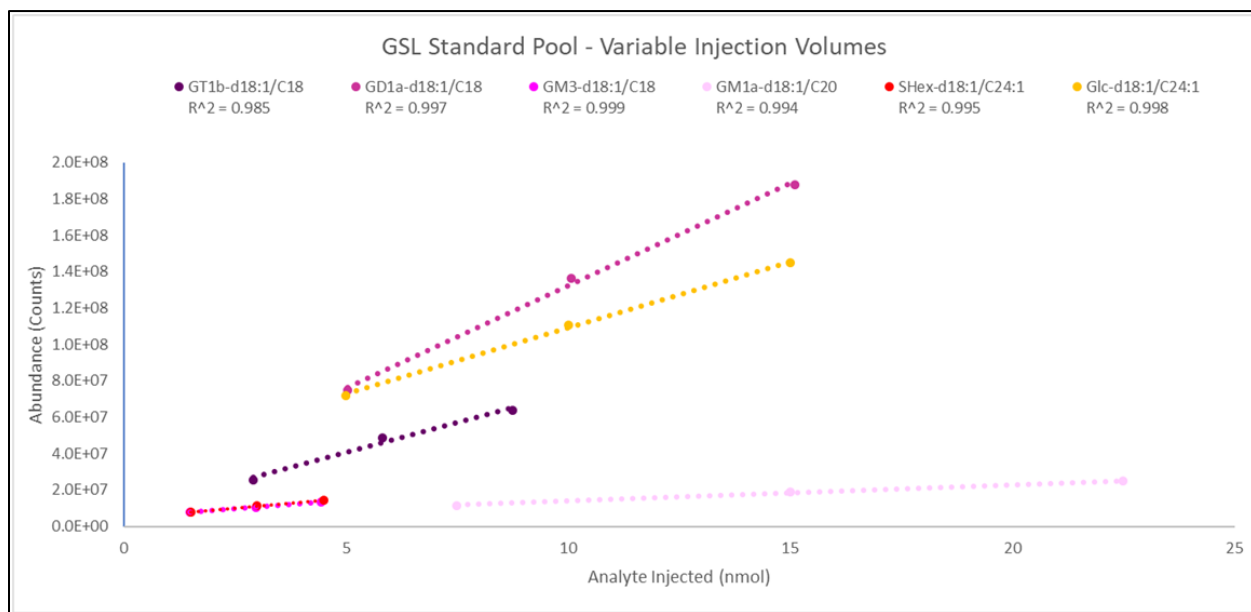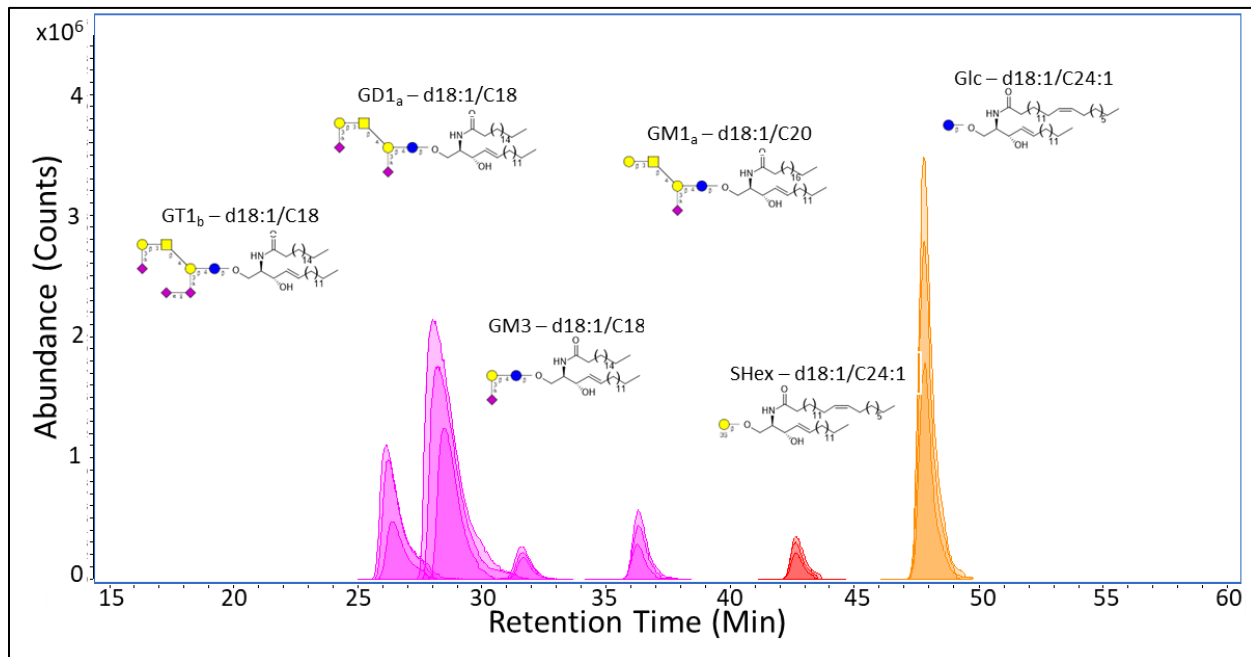
Figure S3.3. Separation of isomeric sphingolipids differing in double bond position.
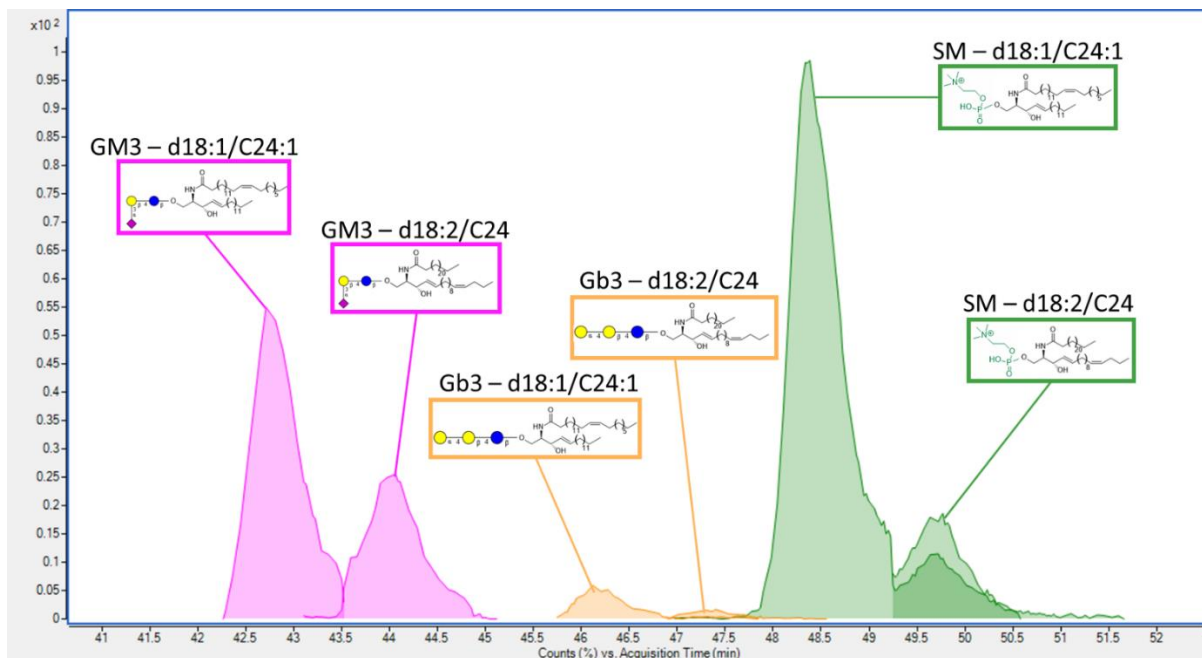
Figure S3.4. Sphingomyelin- and GD1–d18:1/FA species observed in human brain tissue and the correlation between total lipid carbon number and retention time.
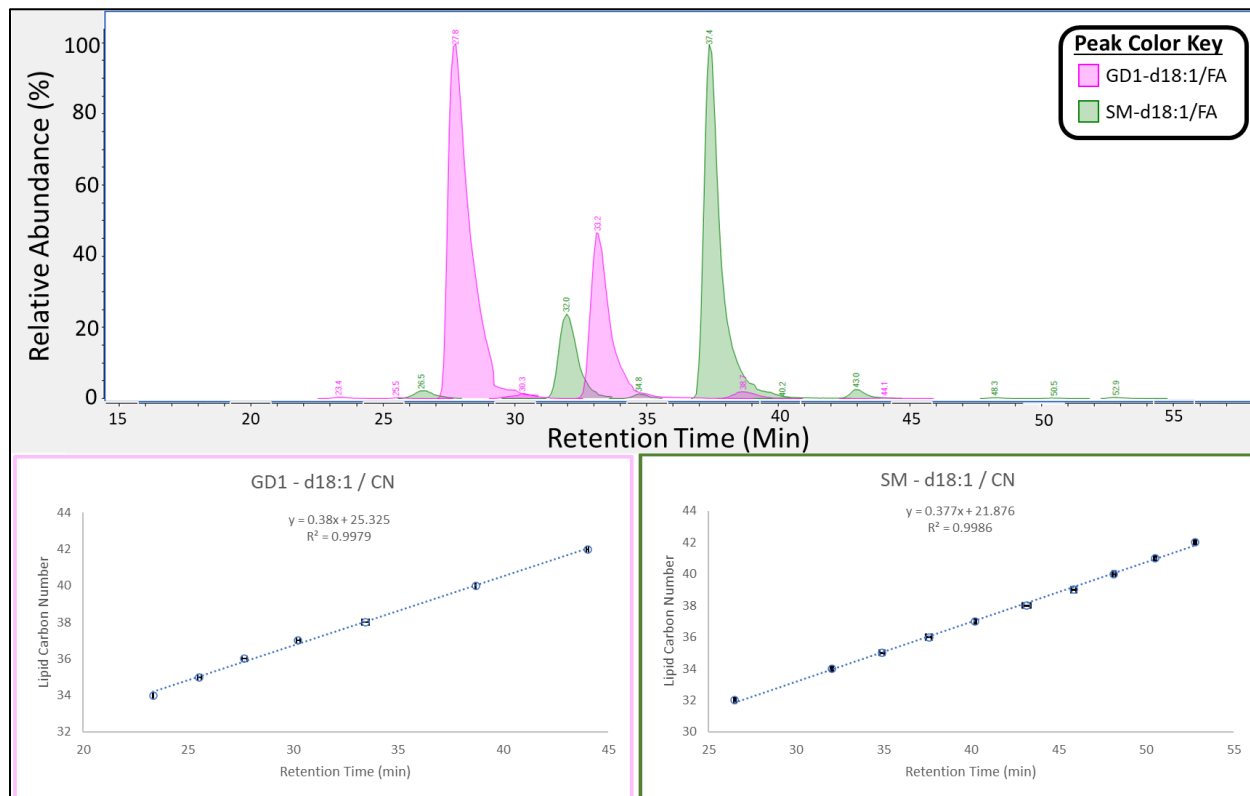
Figure S3.5. Computational depiction of α2-3,6,8 neuraminidase, from Clostridium perfringens, with active site interactions with GM1a. Sialic acid in GM1a is accessible to active site residue Asp62 but is being blocked by terminal galactose from Arg37 and Arg245.
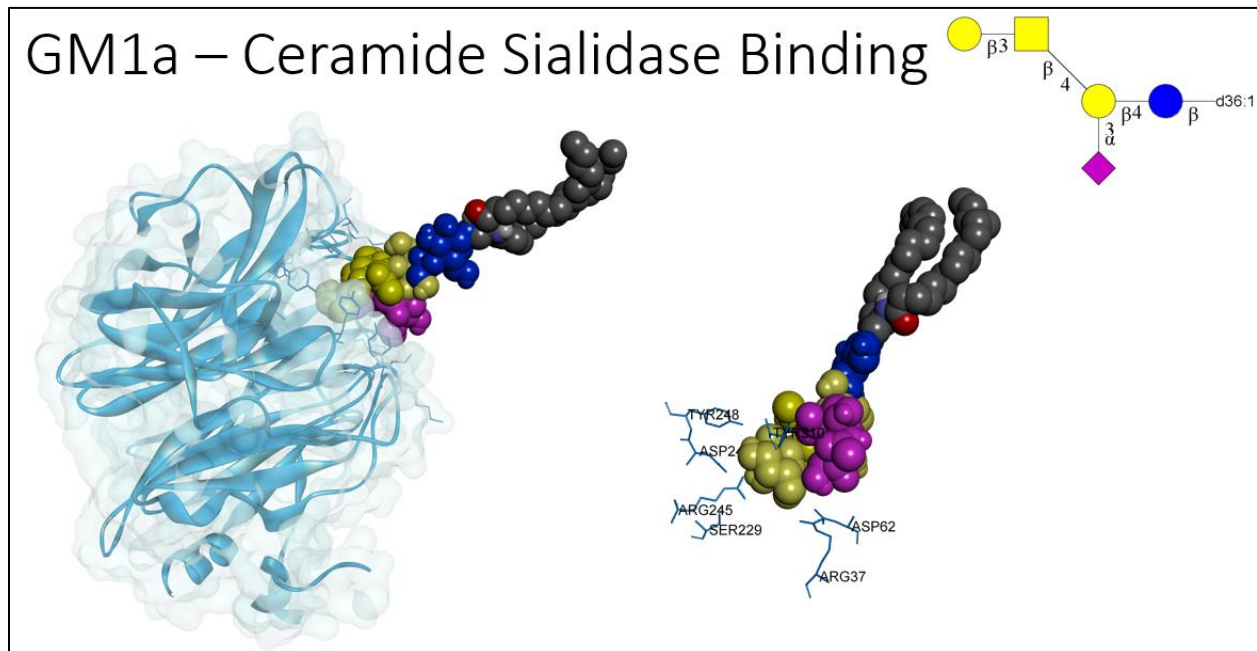
Figure S3.6. Example chromatogram of human serum sphingolipid profile with 25 of 78 compounds depicted.
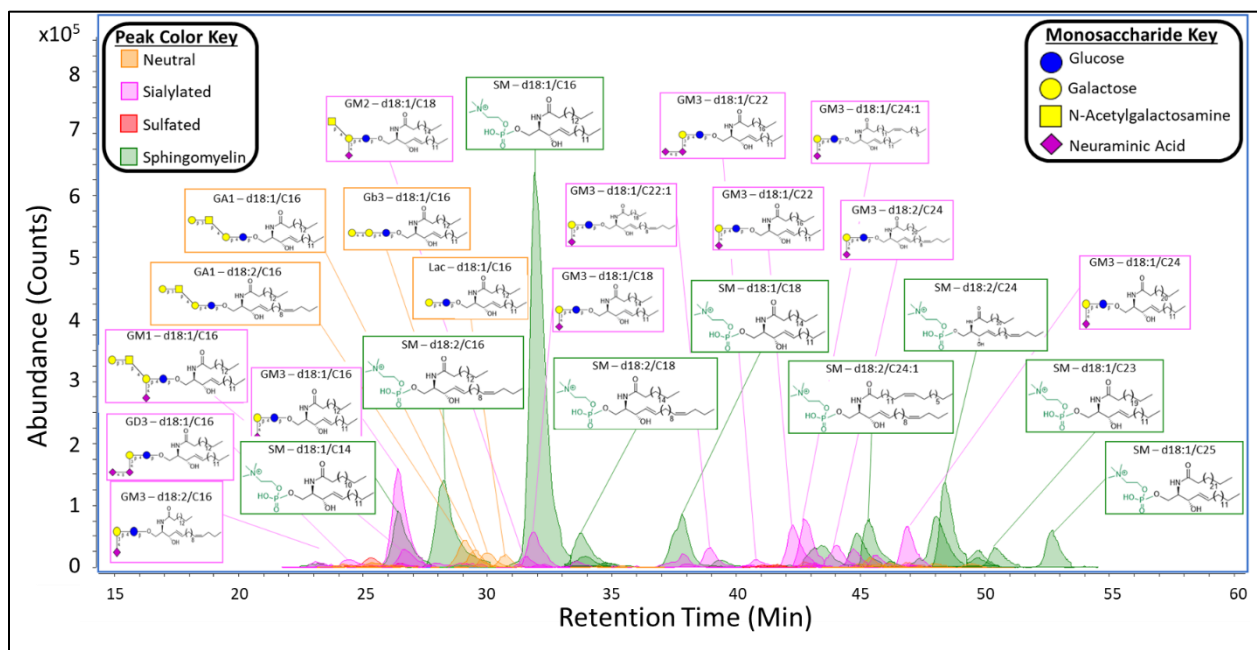
Figure S3.7. Summary heatmap profile of T-cells (TIB-190) for all sphingolipids ≥0.01% relative abundance.

TIB-190 Cells	GD1	GD3	GM2	GM3	GA1	Gb3	SLac	Lac	SM	Ceramide Totals:
d18:1 / C14	0.00%	0.44%	0.00%	1.63%	0.00%	0.10%	0.00%	0.61%	3.07%	**5.9%**
d18:1 / C16	1.36%	5.56%	0.70%	12.31%	1.09%	1.95%	0.94%	3.87%	22.56%	**50.3%**
d18:1 / C18	0.00%	0.43%	0.00%	1.09%	0.00%	0.11%	0.00%	0.33%	0.00%	**2.0%**
d18:1 / C20	0.00%	0.40%	0.00%	2.59%	0.00%	0.00%	0.00%	0.23%	0.00%	**3.2%**
d18:1 / C22	0.00%	0.44%	0.00%	3.22%	0.00%	0.00%	0.06%	0.50%	0.00%	**4.2%**
d18:1 / C24	0.00%	0.69%	0.00%	4.66%	0.00%	0.00%	0.00%	0.35%	0.00%	**5.7%**
d18:1 / C22:1	0.00%	0.00%	0.00%	1.13%	0.00%	0.00%	0.00%	0.00%	0.00%	**1.1%**
d18:1 / C24:1	0.41%	2.01%	0.00%	13.10%	0.00%	0.16%	0.19%	0.73%	1.11%	**17.7%**
d18:1 / C26:1	0.00%	0.00%	0.00%	1.64%	0.00%	0.00%	0.00%	0.00%	0.00%	**1.6%**
d18:0 / C16	0.00%	0.00%	0.00%	4.57%	0.00%	0.00%	0.00%	1.32%	0.00%	**5.9%**
d18:2 / C16	0.00%	0.00%	0.00%	0.22%	0.00%	0.00%	0.00%	0.00%	0.79%	**1.0%**
t18:0 / C24:1	0.00%	0.00%	0.00%	0.37%	0.00%	0.00%	0.00%	0.00%	0.00%	**0.4%**
Headgroup Totals:	**1.8%**	**10.0%**	**0.7%**	**46.5%**	**1.1%**	**2.3%**	**1.2%**	**7.9%**	**27.5%**	

(heatmap scale: 0.00% – 22.56%)

Table S1. Common ceramide fragment ions from headgroup disassociation.

Hydroxyl Groups[1]	Double bonds	Carbon Number	[Cer+H]+	[Cer+H-H2O]+	[Cer+H-2xH2O]+
d	1	32	510.488619	492.478054	474.467489
		33	524.504269	506.493704	488.483139
		34	538.519919	520.509354	502.498789
		35	552.535569	534.525004	516.514439
		36	566.551219	548.540654	530.530089
		37	580.566869	562.556304	544.545739
		38	594.582519	576.571954	558.561389
		39	608.598169	590.587604	572.577039
		40	622.613819	604.603254	586.592689
		41	636.629469	618.618904	600.608339
		42	650.645119	632.634554	614.623989
		43	664.660769	646.650204	628.639639
		44	678.676419	660.665854	642.655289
t	0	32	528.499184	510.488619	492.478054
		34	556.530484	538.519919	520.509354
		36	584.561784	566.551219	548.540654
		38	612.593084	594.582519	576.571954
		40	640.624384	622.613819	604.603254
		41	654.640034	636.629469	618.618904
		42	668.655684	650.645119	632.634554
		43	682.671334	664.660769	646.650204
		44	696.686984	678.676419	660.665854

[1]The number of hydroxyl groups are assigned with letters, d=2, t=3

Table S2. Common Long-chain base fragments from headgroup and N-linked acyl disassociation.

Hydroxyl Groups[1]	Double bonds	Carbon Number	[LCB+H]+	[LCB+H-H2O]+	[LCB+H-2xH2O]+
d	0	18	302.305904	284.295339	266.284774
	1	18	300.290254	282.279689	264.269124
	2	18	298.274604	280.264039	262.253474
	0	20	330.337204	312.326639	294.316074
	1	20	328.321554	310.310989	292.300424
	2	20	326.305904	308.295339	290.284774
t	0	18	318.300819	300.290254	282.279689
	1	18	316.285169	298.274604	280.264039

[1]The number of hydroxyl groups are assigned with letters, d=2, t=3

Figure S8. Active HPLC modules and 10pt/2ps µ-switching valve configuration.
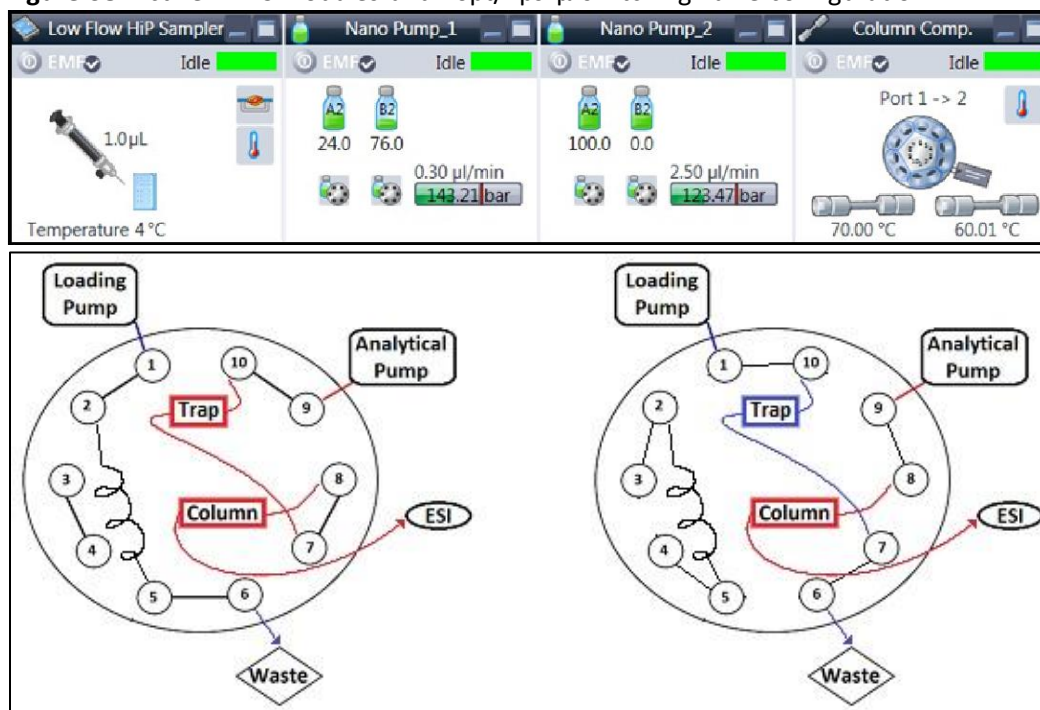
Figure S9. Nanoflow ESI source (Agilent Technologies, G1992A) nebulizer positioning, spray trajectory, and corresponding reference mass response.
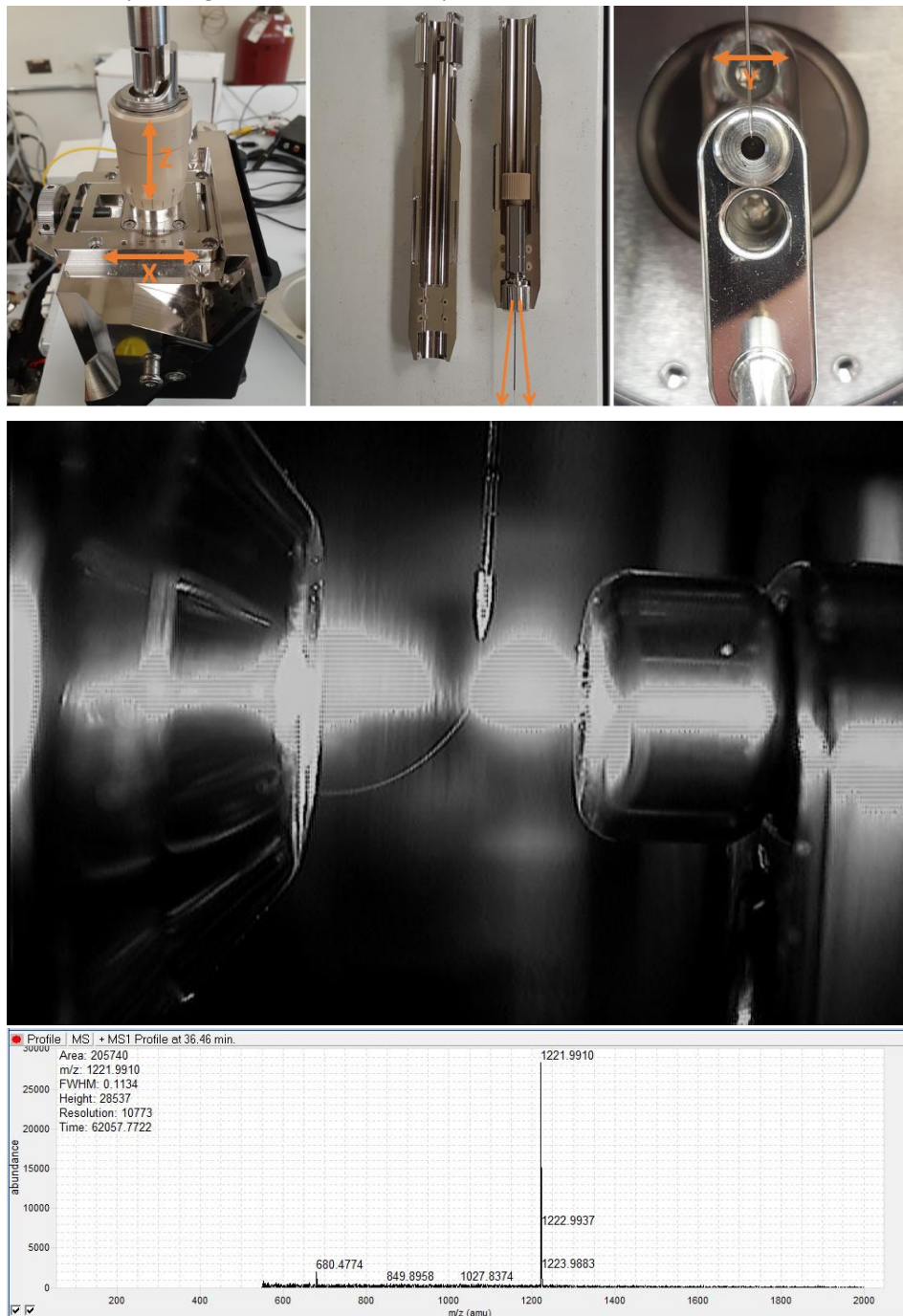
Table S3. HPLC capillary configuration.

Nanoflow 1200 Series HPLC - Connecting Capillaries						
Module	**From (fitting)**	**To (fitting)**	**pn**	**ID (mm)**	**Length (mm)**	**Dwell Volume (µL)**
Nano Pump - Loading (0.1 - 4 µL/min) pn: G2226A	EMPV (WPF)	Flow Sensor (WPF)	G1375-87321	0.025	220	0.108
	Flow Sensor (MP)	µWPS Valve, port 1 (MP)	G1375-87322	0.025	350	0.172
Nano Pump - Analytical (0.1 - 4 µL/min) pn: G2226A	EMPV (WPF)	Flow Sensor (WPF)	G1375-87321	0.025	220	0.108
	Flow Sensor (MP)	µTCC Valve, port 9 (MP)	G1375-87322	0.025	350	0.172
Micro WPS pn: G1377A + Thermostat pn: 1330B	µAS Valve		0101-1050	Internal Channel		0.07
	µWPS, port 1 (MP)	Metering Device (WPF)		-		
	Sample Loop (8µL)		G1375-87315	-		
	µWPS-Needle		G1377-87201	-		
	µWPS-Needle Seat		G1377-87001	-		
	µWPS, port 6 (MP)	µTCC, port 1 (MP)	5067-1582	µ-Inline Filter		0.46
TCC pn: G1316C	10pt/2ps µ-Switching Valve		5067-4144	Internal Channel		0.089
	Port 10 (MP)	Trap Column (WPF)	G1375-87322	0.025	350	0.172
	Trap Column (WPF)	Port 7 (MP)	G1375-87320	0.025	100	0.049
	Port 2 (MP)	Port 5 (MP)	G1375-87320	0.025	100	0.049
	Port 8 (MP)	Analytical Column Inlet (WPF)	G1375-87320	0.025	100	0.049
Nano ESI pn: G1992A	Analytical Column Outlet (WPF)	nESI (Nebulizer)	G4240-87300	0.015	900	0.159
Fittings	**Acronym**	**Part Number**	**Description**			
	MP	5065-4410	PEEK fitting (Metric M4)			
	WPF	5065-4422	Double winged PEEK nut & ferrule			

CHAPTER VI

Region-specific Quantitation of Glycosphingolipids in the Elderly Human Brain with Nanoflow MEAChip Q/ToF Mass Spectrometry

Author Information

Ryan L. Schindler[1], Lee-way Jin[2], Angela M. Zivkovic[3], Carlito B. Lebrilla[1]*

[1]Department of Chemistry, University of California, Davis, California, 95616, USA.

[2]Department of Pathology and Laboratory Medicine and M.I.N.D. Institute, University of California Davis Medical Center, Sacramento, 95817, California, USA.

[3]Innovation Institute for Food and Health, University of California, Davis, California, 95616, USA.

ABSTRACT

Glycosphingolipids are a unique class of bioactive lipids responsible for lateral membrane organization and signaling found in high abundance in the central nervous system. Using nanoflow MEA Chip Q/ToF mass spectrometry, we profiled the intact glycosphingolipids of the elderly human brain in a region-specific manner. By chromatographic separation of glycan and ceramide isomers, we determined gangliosides to be the highest source of heterogeneity between regions with the expression of a- and b-series glycan structures. Investigation of these trends showed that specific glycan structures were, in part, determined by the structure of their lipid backbone. This study provides insight into the dynamic process of membrane remodeling in the brain during aging.

INTRODUCTION

Significant scientific progress has been made to profile the biochemical makeup of the brain to elucidate structure-to-function neurophysiology and pathology. Curated databases are available for the transcriptome[1] and proteome[2] of the human brain on a regional and cellular level. However, there is not a comparable resource for the lipidome. Using a single-cell lipidomic workflow, Bhaduri et al. observed comparable profiles in the most abundant lipids between region-matched human brains but heterogeneity when making regional and age-matched comparisons.[3] This work, with others, emphasized the importance of lipids in the central nervous system (CNS), which may be vital to understanding neurological mechanisms and developing therapeutics for the various forms of neurodegeneration.

Sphingolipids (SL) are a subset of bioactive lipids found in eukaryotic cell membranes and are unique in their amphipathic structure and potential to be glycosylated.[4] The human nervous system contains a significantly higher abundance of glycosphingolipids (GSLs) than the other systems, indicating their physiological importance. A recent study by Blumenreich et al. showed that increased ganglioside expression (Sialic acid containing GSLs) was correlated to subjects with a genetic risk factor for Parkinson's disease in three of the four regions studied.[5] Gangliosides have been indicated to play a role in the pathology of Huntington's disease, amyotrophic lateral sclerosis, Alzheimer's disease, stroke, multiple sclerosis, and epilepsy.[6]

SLs are characterized by their two-tailed lipid backbone - a ceramide consisting of a sphingoid base and an N-linked acyl group. Ceramides tend to have longer, more saturated lipid tails than other major membrane lipids. Along with the ceramide's structural contribution to

membrane biophysical properties, they play a crucial role in cellular homeostasis by regulating apoptosis and autophagy.[7] The bioactive head group of SLs extends from the outer membrane into the extracellular space, mediating interactions such as signaling, adhesion, and differentiation.[8,9] Unlike other membrane lipids, SLs are unique in their ability to contain oligosaccharide (glycan) headgroups. The untemplated biosynthesis of these glycan headgroups is a dynamic process involving families of glycosyltransferases and glycosidases, which fine-tune the glycocalyx and subsequent intra- and inter-cellular interactions.[10] Subtle structural changes such as the position of a sialic acid (Neu5Ac) or the stereochemistry of a glycosidic bond (α or β) can have significant effects on carbohydrate-receptor binding and overall cellular phenotype.[11]

Although constituting a small fraction of the overall lipid profile, SL's contribution to cellular biophysical properties is thought to be spatially amplified due to clustering with proteins and cholesterol into microdomains commonly referred to as lipid rafts.[12] This clustering occurs due to a high degree of hydrogen bonding from the polar moieties and ordered stacking of the lipid backbones. These SL-rich microdomains are categorized by a highly ordered "solid-like" membrane phase with a slow translational diffusion coefficient.[13] These rafts translocate in the bulk liquid-disordered bilayer, self-assembling into functional domains that carry out essential cellular functions such as synaptic transmission in neurons.

General profiling of GSLs in the brain has revealed that white matter is enriched in Gal-Cer and SGal-Cer, where they pair to form carbohydrate-carbohydrate bonds, providing intra-membrane stability to the multi-layered myelin sheath.[14] Grey matter, consisting primarily of neuronal cell bodies and axons, is highly expressed with gangliosides, which play a significant role as ligands for cellular recognition and signaling. In addition, neuronal synaptosomal

microdomains are highly enriched with gangliosides, sialidase, and sialyltransferase for dynamic glycocalyx remodeling.[15] It has been shown that the number and positioning of sialic acid residues in these domains modulate calcium influx, the principal second messenger of synaptic activity.[16,17]

A previous study from our laboratory explored the N-glycoproteomic profile of the elderly human brain across 11 functional brain regions with age-matched Alzheimer-confirmed subjects.[18] In this work, we have continued this path of research by comprehensively analyzing the glycosphingolipids of the frontal cortex, temporal cortex, occipital cortex, parietal cortex, cingulate cortex, posterior hippocampus, caudate nucleus, thalamus, lateral cerebellum, and pons using nanoflow MEAChip Q/ToF mass spectrometry. This methodology quantitatively analyzes these low-abundant lipids to reveal the heterogeneity between regional, age, and disease states. The profiling of these structurally diverse lipids utilized highly sensitive nanoflow chromatography, separation of glycan and ceramide isomers, reproducible chromatographic elution, collision-induced dissociation MS_2, and accurate mass spectrometric detection.

METHODS

Materials and Chemicals. Sphingomyelin-d18:1/C18 (Cat# 860586), Sphingomyelin-d18:1/C24:1 (Cat# 860593), Glucose-d18:1/C24:1 (Cat# 860549), SHex-d18:1/C24:1 (Cat# 860571), GM1a-d18:1/C18 (Cat# 860588), GM3-d18:1/C18 (Cat# 860074), GD1a-d18:1/C18 (Cat# 860091), and GT1b-d18:1/C18 (Cat# 860089) standards were purchased from Avanti Polar Lipids (Alabaster, AL). Lymphoblast CESS cells (Cat# TIB-190) were obtained from the American Type Cell Culture (Manassas, VA). α2-3,6,8 Neuraminidase (Cat# P0720) was purchased from New England Biolabs (Ipswich, MA). Human serum (Cat# S7023), sucrose (Cat# S7903), KOH (Cat# P5958), ammonium acetate ($NH_4CH_3CO_2$, Cat# 73594), sodium carbonate (Cat# S5761), and protease inhibitor cocktail (Cat# 539137) were purchased from Sigma (St. Louis, MO). Fetal bovine serum (Cat# 16000-069), penicillin-streptomycin (Cat# 15140-122), 1M HEPES (Cat# 15630080), methanol (MeOH, Optima LC/MS, Cat# A456-4), and isopropanol (IPA, Optima LC/MS, Cat# A461-4) were purchased from ThermoFisher Scientific (Waltham, MA). C-8 SPE plate (100mg, Cat# FNSC08.800) was purchased from Glygen. Glacial acetic acid (GAA, Cat# AC110) was purchased from Spectrum (New Brunswick, NJ). Formic acid (Optima LC/MS, Cat# A117-50) was purchased from Fisher Chemical (Hampton, NH).

Brain Tissue. Human brain tissue was obtained through the University of California, Davis – Alzheimer's Disease Center from donors' postmortem and stored at -80°C before processing and analysis. Four different brains were profiled; the first showed normal cognitive function and was considered the control sample (**A**, NCF-72). The second had hippocampal sclerosis (**B**, HS-95). The last two subjects were age-matched with autopsy-confirmed Alzheimer's disease (**C**, AD-74 & **D**, AD-93). Up to ten brain regions were collected from each

donor: frontal cortex, temporal cortex, parietal cortex, occipital cortex, cingulate cortex, hippocampus, thalamus, caudate nucleus, lateral cerebellum, and pons.

Standard Preparation. External standards SM-d18:1/C18, SM-d18:1/C24:1, Glc-d18:1/C24:1, SHex-d18:1/C24:1, and GM1a-d18:1/C18 were received as ammonium salts and diluted to 50μM stock solutions in MeOH/IPA/water (2/8/1, v/v/v%). Further dilution used MeOH/water (1/1, v/v%). GM3-d18:1/C18 (100μg/mL), GD1a-d18:1/C18 (100μg/mL), and GT1b-d18:1/C18 (124μg/mL) were received as MeOH solutions, and diluted in MeOH/water (1/1, v/v%).

Sample Preparation. The sample profiles were generated with 10-100mg of human brain tissue. Tissues were individually weighed into 15mL falcon tubes and diluted with 1.5mL of a buffer of 0.25 M sucrose, 20mM HEPES adjusted to pH 7.4 with KOH, and a 1:100 protease inhibitor cocktail. Homogenization was first accomplished manually, then by 1-2 sequences of lysis with μ-needle sonication with a maximum of 80J/sequence until a fine suspension was obtained.

The nuclear fraction was precipitated by centrifugation at 2000 RCF for 10 minutes. The transparent supernatant was transferred and ultracentrifuged at 200k RCF for 30 minutes at 4°C to form a membrane pellet. After removing the supernatant, samples were diluted with 1mL of 0.2 M sodium carbonate and ultracentrifuged to remove membrane-associated proteins. The supernatant was removed, and samples were ultracentrifuged again with the same volume of water. After discarding the water, membrane lipids were dissolved using a modified Folch extraction using 800μL of freshly prepared water/MeOH /CHCL$_3$ (3/8/4, v/v/v%)

and sonicated for at RT for 30min. Samples were then centrifuged at 9,000RCF for 10min to precipitate the membrane proteins and the supernatant was collected. 100 μL of 0.1 M KCl was added to induce a liquid-liquid separation, and the top layer (aqueous) was transferred and dried by vacuum centrifugation.

Sphingolipids were enriched with a 100mg, C-8, 96-well SPE plate. Wells were first washed with 1200μL of MeOH/IPA (1/1, v/v%) and primed with 400μL of water/MeOH (1/1, v/v%). Samples were reconstituted with 600 μL of water/MeOH and gravity loaded; the flow through was reloaded to ensure maximum recovery. Sample wells were washed with a total of 1.2mL of water/MeOH. Sphingolipids were eluted with 600μL of the MeOH/IPA and then dried. Condition, prime, wash, and elution steps used centrifugation (100 RCF, 1 minute).

Dried samples were sealed and stored at -80°C until ready for analysis. Before analysis, samples were reconstituted to 0.25mg of tissue/μL with water/MeOH (1/1, v/v%), transferred to autosampler vials, and stored in the autosampler operating at 4°C prior to injection.

Nanoflow MEAChip Q/TOF Methodology. Automated sample injection and data collection used an Agilent 1200 series nanoflow HPLC. On-line sample enrichment used a Zorbax 300SB-C8 trap column, 0.3 ID x 5mm, 5μm particle size, 300Å pore size (Agilent Technologies Inc., Cat# 5065-9914). The chromatographic separation and analyte ionization were performed using a C-18 MEAChip, 1x 10μm nozzle, 0.07 ID x 150mm, 1.9μm particle size (NewOmics, Cat# C1005). The loading/washing pump was operated at 2.5μL/min. Sample loading used 0.1% GAA and 20 mM $NH_4CH_3CO_2$ in water/MeOH/IPA (40/50/10, v/v/v%). Sample washing (MP-W) used MeOH/IPA (1/1, v/v%). The gradient was as follows: 0% MP-W from 0 to

20min, increased to 95% at 25min, held until 35min, decreased back to 0% at 40min, and held

until 70 min. The analytical gradient used a flow rate of 0.25µL/min. Mobile phase A (MP-A)

used 0.1% GAA in 20 mM $NH_4CH_3CO_2$ in MeOH/water (25/75, v/v), and mobile phase B (MP-B)

with a composition of 0.1% GAA in 20 mM $NH_4CH_3CO_2$ in MeOH/IPA (75/25, v/v). The timed

composition changes are as follows: 85% MPB from 0 to 15min, a linear increase to 100% at

40min, held until 55min, decreased to 85% by 60min, and held until 80min. The C-8 trap column

was operated at 70°C. A 10pt/2ps µ-switching valve was configured for efficient enrichment,

analyte transfer, and washing at low flow rates. Samples are enriched from 0 to 6min (µ-valve

1→10). From 6 to 20min, analytes are backflushed from the C-8 trap to the MEAChip source (µ-

valve 1→2). From 20 to 80min the gradient, wash, and re-equilibration are carried out (µ-valve

1→10).

The MEAChip source was operated in positive ion mode, and the solvent composition

was adjusted through the post-column inlet (PCI) with a flow rate of 0.25µL/min. The PCI

solution was made freshly in 1mL preparations with a composition of formic acid/water/MeOH

(5/2.5/92.5, v/v/v%) and spiked with 1µL of a 200,000x diluted 1221.9 m/z correction mass in

MeOH (Agilent Technologies Inc., Cat# G1982-85001). Precursor ion mass filtering,

fragmentation, and detection were performed on a quadrupole time-of-flight mass

spectrometer (Agilent Technologies, G6520A). Source conditions were optimized by direct

infusion and using N_2 drying gas at 250°C with a flow rate of 2.0 L/min. The capillary voltage was

3200V for a corresponding capillary and chamber current of 0.165µA and 2.20µA, respectively.

The fragmentor, skimmer, and octopoleRF voltages were set to 175V, 90V, and 750V,

respectively. The quadrupole used automatic precursor ion selection with a mass range of 575 −

2000 m/z and an absolute threshold of 10000 counts with a maximum of 5 precursors per cycle and narrow isolation width (~1.3amu). The preferred charge state was set to 2 > 1. Precursor ions were fragmented in an N_2-filled chamber with collision-induced disassociation using an m/z dependent collision energy determined by linear interpolation with the equation $E = 1.2 \times \left(\frac{m/z}{100}\right) + 12$. Active exclusion was enabled after collection of one MS_2 spectrum and released after one-minute corresponding to approximately one half the average peak width. The time-of-flight detector was operated such that abundance and accurate mass were in the range of 100 – 2000 m/z.

Data Analysis. Post-acquisition compound identification and peak integration were completed using Agilent's MassHunter Qualitative Analysis software version (B10.00) with the Find by Molecular Feature (FMF) algorithm using a CSV database of compounds including the molecular formula, mass, name, and description. Each sample's compound list was exported to individual CSV files. An in-house Python script was used to organize the data into a single spreadsheet for analysis in Microsoft Excel and GraphPad Prism.

Absolute Quantitation. 11-point calibration curves were generated with external standards comprising the major headgroups and ceramide structures. However, not all major species had an external standard available, so interpolations were required, which accounted for both the glycan headgroup and ceramide backbone's effect on ionizability. The responses of SM-d18:1/C18 and SM-d18:1/C24:1 were used to calculate the expected response based on the ceramide tail. Next, the response for each headgroup with a standard available was normalized to the SM response of the same ceramide structure to find the change in response based on the

headgroup compared to SM. There was no GD3 standard available, so the response was estimated using the GM3 response with the addition of sialic acid. GM2 and GD2 were estimated by the average response of GM1/GM3 and GD1/GD3. With interpolated slopes for GT1, GD1, GM1, GD2, GD3, GM2, GM3 with ceramides d18:1/C16, C18, C20, and C22 absolute abundances were calculated. After quantitation of each species, the headgroups were summed to calculate the absolute abundance of total gangliosides in nmol per gram of tissue for each sample.

Isomer Identification. Chromatographic separation of a-series and b-series ganglioside isomers was observed in all samples. Identification of each isoform was confirmed with retention times compared to bracketed external standards and fragmentation patterns. GD1b glycans produced an MS2 ion 583.2 m/z corresponding to Neu5Ac-Neu5Ac, while GD1a generated the ion 657.2 m/z corresponding to the terminal Neu5Ac-Gal-GalNac. These MS2 ions are both observed for GT1a and GT1b, so a sample was spiked to confirm the elution order of GT1 gangliosides. A lipid isomer, C20 sphingosine (d20:1), was also observed for the major gangliosides and was identified by MS_2 with a 292.3 m/z fragment.

RESULTS

A total of over 260 intact sphingolipid structures were identified by analyzing the frontal, temporal, parietal, occipital, and cingulate regions of the cerebral cortex as well as the posterior hippocampus, thalamus, caudate nucleus, lateral cerebellum, and pons. Reverse-phase nanoflow Q/ToF accurate mass spectrometry was utilized to quantitatively map the sphingolipid profile of the human brain in the ten different functional regions. The use of biosynthetic pathway knowledge, collision-induced disassociation, and LC retention times used to identify compounds was described in detail in Chapter III. Liquid chromatography and ionization used a nanoLC column as part of an MEA Chip (NewOmics, Berkeley) with 1.9-sized particles and post-column solvent adjustment to acquire chromatograms and generate sphingolipid profiles (Figure 4.1).
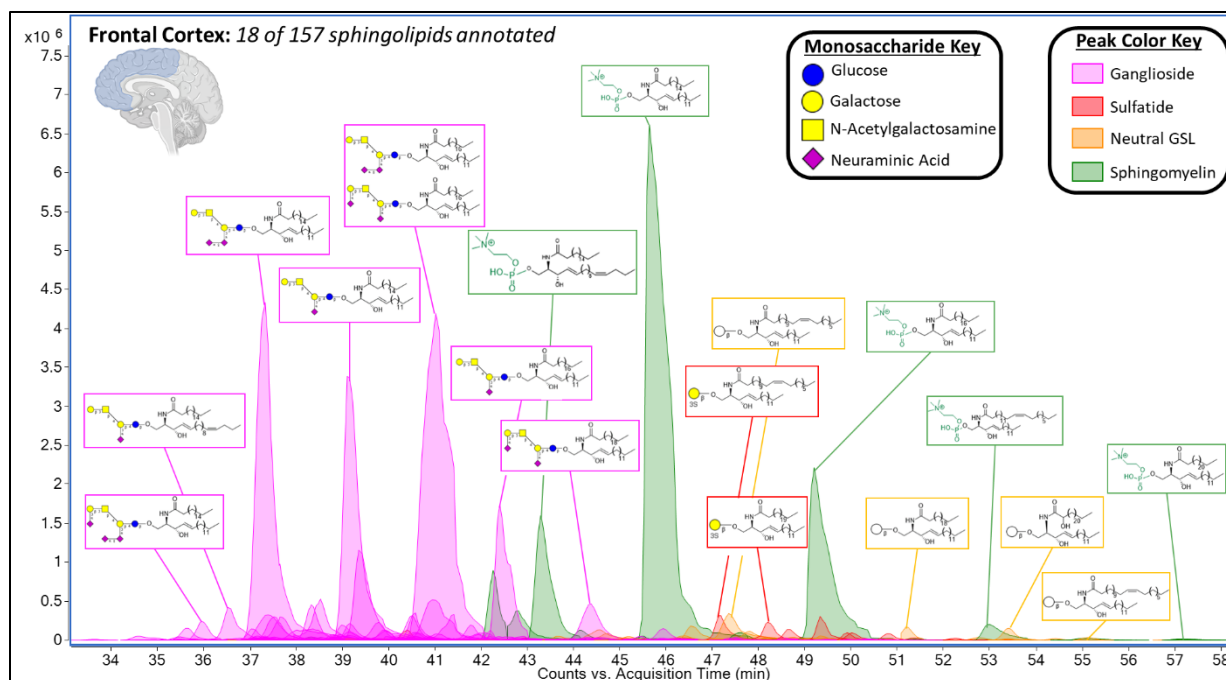
Figure 4.1 Example chromatogram of the frontal cortex used to generate the sphingolipid profile.

Sialic acid containing gangliosides (GM1, GD1$_{a\&b}$, GT1$_b$) and sphingomyelin (SM) were the most prevalent headgroups observed in all brain regions (Figure 4.2). Additional gangliosides that were detected in lower abundances were partial-core structures GD2, GD3, GM2, GM3 as well as extended-core structures with galactose, N-acetylgalactosamine, and fucose residues (GalNAc-Fuc-GM1, Gal-Fuc-GD1, Gal-Fuc-GM1, Fuc-GD1, Fuc-GM1). Acetylation and lactonization of sialic acid residues were also observed, adding to the structural diversity. Neutral (HexCer, LacCer) and sulfated GSLs (SM4, SM3) expressed a diverse ceramide profile with long and unsaturated N-linked acyl groups. The major ceramide structures for all brain regions contained a sphingosine base (d18:1) and N-linked acyl groups with 18 and 20 carbons. Minor sphingoid base species included C20-sphingosine (d20:1), dihydroceramide (d18:0), 4-hydroxydihydrosphinganine (t18:0), and 4t,14c-Sphingediene (d18:2). The N-linked acyl groups

ranged from 14 to 26 carbon lengths with hydroxylation typically observed in C24 and

saturation in C22 to C26 groups. Odd-numbered carbon acyl groups were also detected in lower

abundances. The complete compound list for all brain regions and subjects has been included

(Appendix II).
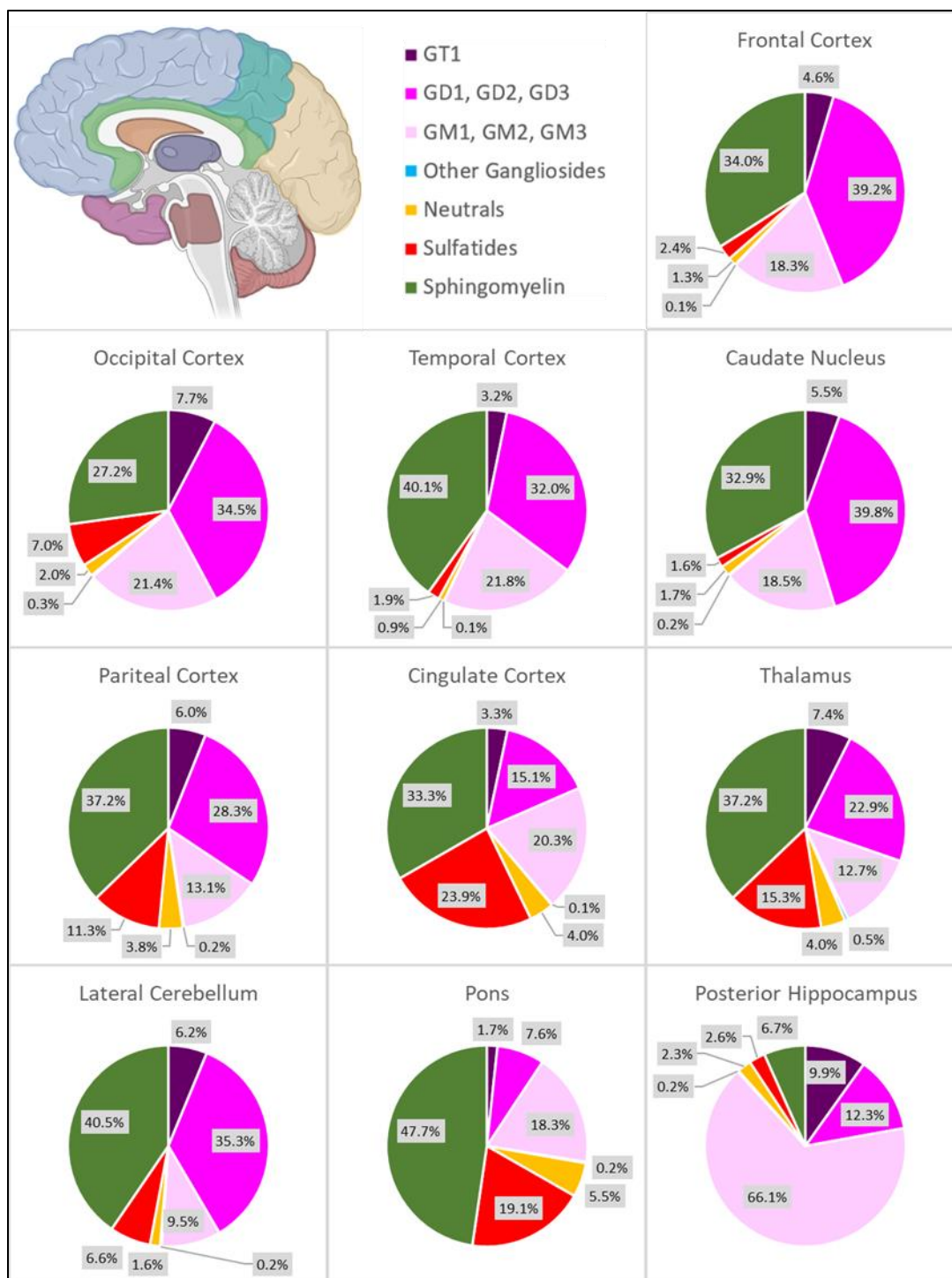
Figure 4.2 Relative abundance of the major headgroups for each of the ten functional brain regions.

Pooled external standards including SM-d18:1/C18, SM-d18:1/C24:1, Glucose-d18:1/C24:1, SGalactose-d18:1/C24:1, GM1a-d18:1/C18, GM3-d18:1/C18, GD1a-d18:1/C18, and GT1b-d18:1/C18 were used at biologically relevant concentrations. The pool was diluted to produce a calibration curve for absolute quantitation of the functional brain regions (Figure S4.1). Using the responses generated from these standards, the gangliosides without available standards were interpolated to quantify each region's major gangliosides (Figure 4.3). All glycan and lipid isomers were assumed to have negligible differences in ionization efficiency and were quantitated with a single regression.
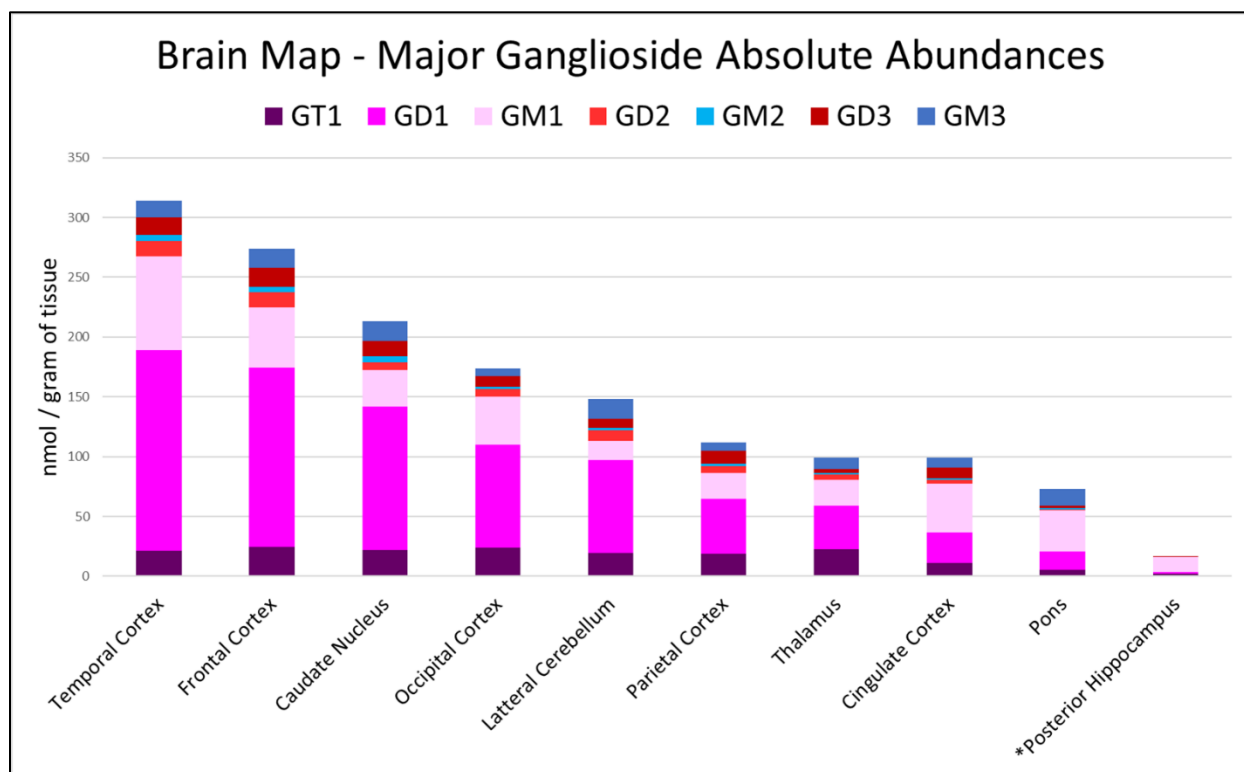
*Figure 4.3 Absolute quantitation of the major ganglioside headgroup structures for the ten functional brain regions. Note: *Posterior Hippocampus weight was estimated for quantitation.*

The temporal cortex had the highest total ganglioside content (314.5 nmol of total gangliosides/g of tissue), followed by the frontal cortex (274.5 nmol/g), caudate nucleus (213.6 nmol/g), occipital cortex (174.7 nmol/g), lateral cerebellum (148.9 nmol/g), parietal cortex (112.3 nmol/g), thalamus (100.4 nmol/g), cingulate cortex (99.6 nmol/g), and pons (73.5 nmol/g). The posterior hippocampus (16.5 nmol/g) was estimated with an initial tissue weight of 2 mg. Exact measurements could not be performed due to limited sample availability, and the estimate was included for completeness. All other regions were normalized by dilution before analysis with 0.25mg of tissue per µL of diluent with their measured weights.

A regional heatmap with the individual intact ganglioside structures (>0.01% relative abundance) was generated to visualize the resulting profiles (Figure 4.4). The relative abundances of all glycosphingolipids were used for a nontargeted principal component analysis (PCA), which resulted in two clusters (Figure S4.2). Group 1 comprised the frontal cortex, temporal cortex, occipital cortex, and caudate nucleus. These regions generated profiles containing primarily gangliosides (GT1, GD1, and GM1). Uniquely, they contained $GD1_a$-d18:/C20 in ratios comparable to the b-series isomer (1_b to 0.45 - 0.8_a). Group 2 showed more variance between regions but included the parietal cortex, cingulate cortex, thalamus, and lateral cerebellum. $GD1_a$-d18:1/C20 was not observed chromatographically for these regions; mass spectral analysis suggests the a-series form is present but in much lower abundances. These profiles also contained an increased abundance of sulfatides (SM4, SM3) and neutral glycosphingolipids (Hex, Lac), generating similar overall ceramide profiles. The pons was not grouped in a cluster as its profile was comprised primarily of GM1, SM4, and HexCer, a profile

typical in white matter brain tissue. The posterior hippocampus contained mostly GM1 (68.5%)

and minor amounts of GD1 and GT1.

Brain Map: Gangliosides (≥0.01% Relative Abundance)

Ganglioside	Temporal Cortex	Frontal Cortex	Caudate Nucleus	Occipital Cortex	Lateral Cerebellum	Parietal Cortex	Thalamus	Cingulate Cortex	Pons	Posterior Hippocampus
GQ1 - d18:1 / C22	0.0%	0.0%	0.0%	0.0%	0.0%	0.0%	0.1%	0.0%	0.1%	0.0%
GQ1b - d18:1 / C20	0.1%	0.2%	0.3%	0.4%	0.4%	0.3%	1.0%	0.2%	0.5%	0.0%
GT1 - d18:1 / C24	0.0%	0.0%	0.0%	0.0%	0.0%	0.0%	0.0%	0.0%	0.0%	0.0%
GT1 - d18:1 / C22	0.1%	0.1%	0.1%	0.2%	0.2%	0.2%	0.3%	0.2%	0.2%	0.0%
GT1-OAc - d18:1 / C22	0.0%	0.0%	0.0%	0.0%	0.0%	0.1%	0.1%	0.1%	0.0%	0.0%
GT1b - d18:1 / C20	3.5%	4.3%	5.1%	6.7%	5.1%	6.7%	8.7%	5.1%	2.9%	1.6%
GT1a - d18:1 / C20	0.4%	0.4%	0.6%	0.4%	0.6%	0.4%	1.0%	0.4%	0.3%	0.2%
GT1-OAc - d18:1 / C20	0.0%	0.4%	0.4%	1.0%	0.3%	1.4%	1.0%	0.5%	0.2%	0.1%
GT1-Lactone - d18:1 / C20	0.1%	0.0%	0.0%	0.0%	0.0%	0.0%	0.0%	0.0%	0.0%	0.0%
GT1b - d20:1 / C18	0.3%	0.7%	0.5%	0.9%	0.6%	1.0%	1.6%	0.9%	0.5%	0.1%
GT1b - d18:1 / C18	0.5%	0.7%	0.6%	1.5%	2.9%	1.4%	2.2%	0.9%	1.1%	6.6%
GT1a - d18:1 / C18	0.0%	0.1%	0.1%	0.1%	0.4%	0.2%	0.2%	0.1%	0.1%	0.4%
GT1-OAc - d18:1 / C18	0.0%	0.1%	0.1%	0.3%	0.2%	0.2%	0.2%	0.0%	0.0%	0.3%
GT1-Lactone - d18:1 / C18	0.0%	0.0%	0.0%	0.0%	0.0%	0.0%	0.0%	0.0%	0.0%	0.2%
GT1b - d20:1 / C16	0.2%	0.1%	0.3%	0.2%	0.2%	0.3%	0.4%	0.1%	0.2%	0.3%
GD1a - d18:1 / C24	0.1%	0.1%	0.2%	0.1%	0.1%	0.1%	0.1%	0.0%	0.1%	0.0%
GD1a - d18:1 / C22	2.1%	2.0%	2.3%	1.3%	1.4%	1.5%	1.5%	1.2%	0.9%	0.1%
GD1b - d18:1 / C20	15.3%	19.3%	17.2%	12.6%	16.4%	24.9%	24.1%	16.9%	9.7%	1.1%
GD1a - d18:1 / C20	8.2%	9.0%	9.1%	10.1%	0.0%	0.0%	0.0%	0.0%	0.0%	0.7%
GD1-OAc - d18:1 / C20	0.7%	1.0%	0.9%	1.1%	0.7%	1.6%	0.6%	0.5%	0.3%	0.0%
GD1-Lactone - d18:1 / C20	0.9%	0.2%	0.4%	0.3%	0.3%	0.2%	0.2%	0.2%	0.1%	0.0%
GD1b - d20:1 / C18	2.8%	2.2%	2.5%	3.3%	1.3%	3.2%	3.8%	2.3%	1.6%	0.2%
GD1b - d18:1 / C18	15.5%	17.7%	17.0%	15.0%	28.5%	16.9%	12.8%	9.5%	9.4%	2.6%
GD1-Lactone - d18:1 / C18	0.5%	0.1%	0.2%	0.1%	0.3%	0.1%	0.1%	0.1%	0.0%	0.1%
GD1b - d20:1 / C16	2.3%	2.4%	2.7%	2.0%	3.8%	1.7%	1.8%	1.2%	1.4%	0.4%
GD2 - d18:1 / C20	1.0%	1.1%	0.7%	1.1%	0.9%	1.2%	0.9%	0.7%	0.0%	0.0%
GD2 - d18:1 / C18	0.9%	1.1%	0.7%	0.8%	2.2%	1.1%	0.9%	0.8%	0.4%	0.1%
GD3 - d18:1 / C20	0.5%	0.6%	0.3%	0.6%	0.9%	0.7%	0.7%	0.4%	0.7%	0.0%
GD3 - d18:1 / C18	1.1%	1.3%	1.8%	1.3%	0.5%	2.3%	0.0%	2.5%	0.0%	0.2%
GD3 - d18:1 / C16	0.0%	0.0%	0.0%	0.0%	0.0%	0.0%	0.1%	0.0%	0.2%	0.0%
GM1 - d18:1 / C22	0.9%	0.5%	0.6%	0.2%	0.2%	0.2%	0.0%	0.2%	0.0%	0.1%
GM1 - d18:1 / C20	7.3%	5.7%	0.3%	5.9%	0.3%	6.6%	3.5%	8.1%	5.1%	14.2%
GM1 - d20:1 / C18	1.4%	1.3%	0.0%	1.0%	0.0%	1.0%	0.0%	1.1%	0.4%	0.1%
GM1 - d18:1 / C18	17.5%	13.1%	14.9%	20.6%	11.3%	11.1%	18.1%	32.8%	46.4%	54.2%
GM1 - d18:1 / C16	0.4%	0.5%	0.7%	0.4%	0.5%	0.8%	0.5%	0.5%	1.1%	0.3%
GM2 - d18:1 / C20	0.0%	0.2%	0.3%	0.1%	0.0%	0.1%	0.0%	0.2%	0.0%	0.0%
GM2 - d18:1 / C18	1.0%	0.8%	1.0%	0.5%	0.9%	0.8%	0.7%	0.7%	0.8%	0.1%
GM2 - d18:1 / C16	0.0%	0.1%	0.1%	0.0%	0.1%	0.1%	0.1%	0.1%	0.1%	0.0%
GM3 - d18:1 / C20	0.0%	0.2%	0.2%	0.1%	0.2%	0.1%	0.0%	0.1%	0.2%	0.0%
GM3 - d18:1 / C18	0.5%	0.4%	0.6%	0.3%	1.0%	0.5%	0.9%	0.7%	1.8%	0.0%
GM3 - d18:1 / C16	0.0%	0.0%	0.0%	0.0%	0.1%	0.1%	0.1%	0.1%	0.4%	0.0%
Fuc-GD1 - d18:1 / C18	0.0%	0.0%	0.0%	0.0%	0.2%	0.0%	0.0%	0.0%	0.0%	0.0%
Gal-Fuc-GM1 - d18:1 / C18	1.7%	1.7%	4.0%	1.4%	0.0%	1.8%	1.2%	1.1%	1.1%	0.0%
Fuc-GM1 - d18:1 / C18	0.0%	0.0%	0.0%	0.0%	0.2%	0.0%	0.0%	0.0%	0.0%	0.0%
A-Series Gangliosides	47%	40%	40%	46%	20%	27%	30%	52%	66%	84%
B-Series Gangliosides	53%	60%	60%	54%	79%	72%	69%	48%	33%	16%

Figure 4.4 Summary relative abundance heatmap of all identified intact gangliosides (≥0.01%) with summation of a- and b-series structures for the ten functional brain regions.

Glycosphingolipids were profiled for the temporal cortex with three additional subjects

for age and age-matched Alzheimer's disease (AD) comparisons (HS-95, AD-74, AD-93). Using

the relative abundance profiles, PCA generated two clusters that resulted in control and AD

groupings (Figure S4.3). Age comparison of the controls showed minimal changes in the relative

glycosphingolipid profile, with a slight increase in GD1, GD2, and fucosylated species and a

decrease in GM1 (Figure 4.5). Summation of both a- and b-series gangliosides showed a slight

shift in the ratio towards b-series gangliosides. Absolute quantitation of age-related changes

provided a more complete picture showing an overall decrease (-9.7%) in total gangliosides

(Figure 4.6). Changes in individual ganglioside abundance due to age were observed by

decreases in GQ1 (-42%), GM1 (-31%), and GD3 (-15%). GD2 (+26%) and GM3 (+42%) were

found to increase. Comparison of the ganglioside relative abundance profiles of AD subjects to

their respective age-matched controls showed the most prominent change to be the absence of

GD1a-d18:1/C20 which was apparent after inspection of each sample's chromatogram (Figure

S4.4) and the primary reason for the shift in a- and b-series gangliosides. Additionally, the

overall ceramide profile showed a trend of decreasing acyl length where C22 and C20

decreased, and an increase in C18 acyls was observed amongst ganglioside structures (Figure

S4.5). Absolute quantitation resulted in an overall reduction in gangliosides for both AD-72 and

AD-95 (-55% & -43%) primarily due to loss of GD1 (-68% & -54%), GT1 (-56% & -50%), and GD3

(-64% & -73%). GM2 (+27% / +23%) and GM3 (+21% / +1%) were found to increase despite the

overall loss of gangliosides.

Temporal Cortex

0.0%	-	26.4%

Ganglioside	NCI-72	HS-95	AD-74	AD-93
GQ1b - d18:1 / C20	0.2%	0.1%	0.2%	0.1%
GT1b - d18:1 / C22	0.1%	0.3%	0.1%	0.1%
GT1b - d18:1 / C20	3.9%	4.0%	3.1%	2.7%
GT1a - d18:1 / C20	0.5%	0.4%	0.2%	0.2%
GT1b - d20:1 / C18	0.4%	0.4%	0.6%	0.4%
GT1b - d18:1 / C18	0.6%	0.8%	1.2%	1.0%
GT1b - d20:1 / C16	0.2%	0.3%	0.1%	0.2%
GD1a - d18:1 / C24	0.1%	0.2%	0.1%	0.1%
GD1a - d18:1 / C22	2.3%	2.8%	1.2%	1.3%
GD1b - d18:1 / C20	17.4%	16.1%	22.2%	21.9%
GD1a - d18:1 / C20	9.4%	10.2%	0.0%	0.0%
GD1-OAc - d18:1 / C20	0.8%	0.3%	0.7%	0.9%
GD1-Lactone - d18:1 / C20	1.0%	1.4%	0.2%	0.1%
GD1b - d20:1 / C18	3.1%	3.2%	3.0%	1.7%
GD1b - d18:1 / C18	17.6%	20.5%	19.8%	26.4%
GD1-Lactone - d18:1 / C18	0.5%	0.9%	0.1%	0.1%
GD1b - d20:1 / C16	2.6%	2.9%	2.5%	3.2%
GD2 - d18:1 / C20	1.1%	1.4%	2.2%	1.3%
GD2 - d18:1 / C18	1.1%	1.5%	2.6%	1.9%
GD3 - d18:1 / C20	0.5%	0.0%	1.0%	0.6%
GD3 - d18:1 / C18	1.2%	1.7%	0.0%	0.0%
GM1 - d18:1 / C22	1.0%	0.9%	0.4%	0.4%
GM1 - d18:1 / C20	8.3%	7.2%	7.8%	6.3%
GM1 - d20:1 / C18	1.6%	1.1%	1.2%	0.0%
GM1 - d18:1 / C18	19.9%	15.8%	22.0%	21.5%
GM1 - d18:1 / C16	0.5%	0.4%	0.6%	0.5%
GM2 - d18:1 / C20	0.0%	0.0%	0.5%	0.3%
GM2 - d18:1 / C18	1.1%	1.3%	2.3%	2.1%
GM3 - d18:1 / C22	0.0%	0.1%	0.2%	0.1%
GM3 - d18:1 / C18	0.6%	0.9%	1.0%	1.0%
Gal-Fuc-GM1 - d18:1 / C18	1.9%	2.2%	2.0%	2.6%
A-Series Gangliosides	47%	44%	40%	37%
B-Series Gangliosides	53%	56%	60%	63%

Figure 4.5 Relative abundance (≥0.01%) comparison of the temporal cortex of NCI-72, HS-95, AD-74, AD-93.
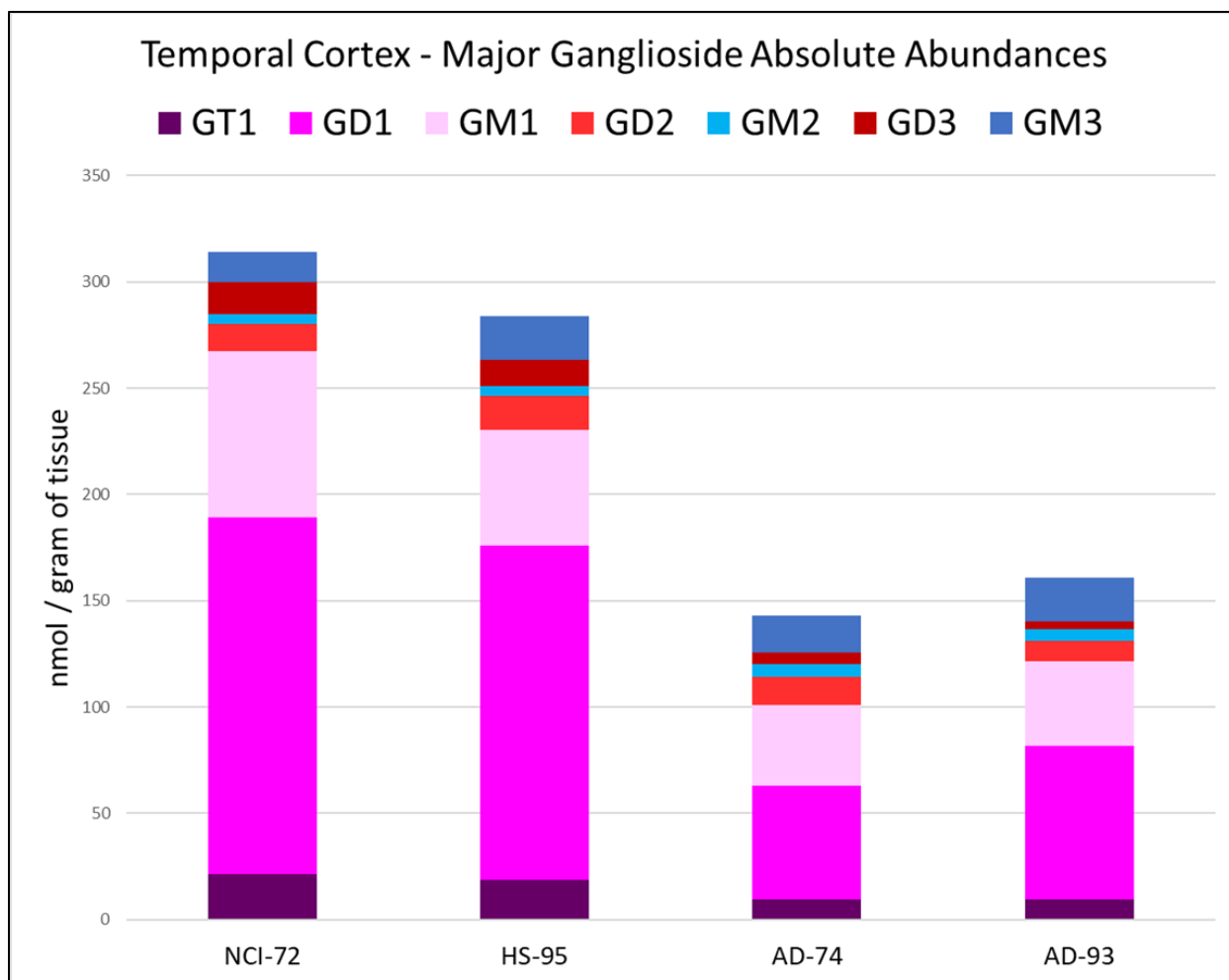
Figure 4.6 Comparison of the temporal cortex of NCI-72, HS-95, AD-74, and AD-93 by absolute quantitation of the major ganglioside glycan structures.

A notable limitation of this work is the limited number of samples for both regions and subjects. This preliminary study profiled ten different human brain regions of a single subject using a single sample per region. Although age-matched regional homogeneity has been observed in human membrane lipids, sampling bias must be considered as <100mg were used to generate the reported sphingolipid profiles. Our goal in this work was to provide data for previously unmapped brain regions and investigate the degree of variability between brain regions, age, and disease state. Our laboratory's initial work in this study analyzed the N-glycans

and N-glycoproteins, which included most regions from the three additional subjects for age (HS-95) and Alzheimer's disease (AD) comparisons (AD-72 & AD-93).[18] Due to sample limitations, this continuation study included the three additional subjects for the temporal cortex only (Table S1).

Additionally, the lack of available standards required interpolating the regression of some of the abundant gangliosides to calculate total absolute abundances. These interpolations considered both the headgroup and ceramide moieties' effect on the analyte response, but there is still an unknown degree of error associated with these estimations.

DISCUSSION

In this study, we used nanoflow high-performance liquid chromatography with a C-18 MEA Chip and accurate mass Q/ToF mass spectrometry to quantitatively map the glycosphingolipids of the elderly human brain in a region-specific manner. The subject was a 72-year-old male who showed no cognitive impairment (NCI-72). The ten functional brain regions analyzed were the frontal cortex, temporal cortex, parietal cortex, occipital cortex, cingulate cortex, hippocampus, thalamus, caudate nucleus, lateral cerebellum, and pons. In agreement with the literature, headgroups GM1, GD1$_a$, GD1$_b$, and GT1$_b$ with d18:1/C18 and C20 ceramides were the most abundant glycosphingolipids among all the regions in this study.[6]

Like previous studies that mapped ganglioside expression in the human brain, we found the most prominent source of regional heterogeneity was due to differences in the ratios of the major ganglioside species.[19] An interesting discovery from this study found that the expression of a- and b-series GD1 isomeric gangliosides was correlated to the ceramide's acyl group. Longer chain acyl groups (C24 & C22) were identified as GD1$_a$, while shorter chain acyls (C16 & C18) were found to be the GD1$_b$ isoform. As mentioned in the results, d18:1/C20 species were predominantly the b-series ganglioside for all regions. Still, they showed a high abundance of GD1$_a$ in the frontal cortex, temporal cortex (NCI-72 & HS-95), occipital cortex, and caudate nucleus regions commonly associated with integrated sensory processing, memory, and motor control.[20] It's unclear if this structural specificity occurs in the Golgi during glycan synthesis, vesicle transportation, after outer membrane incorporation, or in combination. It was reported that V. cholerae sialidase preferentially hydrolyzes the terminal sialic acid of GD1a with shorter lipid chains in vesicles. Further, the sialidase activity was increased by 1.5 to 3-fold in the

presence of Ca2+ ions in vesicular and micellar dispersions.[21] Previous works have also shown

sialic acid enzyme activity in synaptosomal microdomains, which dynamically adjust the local

ganglioside profile.[22,23] The observed correlation between glycan and ceramide structure is

likely due to the positioning of the lipid tail in a cellular membrane, which has a steric effect on

sialidase activity. The mechanism to desiaylate gangliosides favors the hydrolysis of terminal

Neu5Ac residues over those at the membrane interface. This also has significant implications on

lipid raft organization, where full $GT1_b$ and GM3 will behave differently in shaping their

surroundings. The specificity of the interactions with membrane proteins typically depends on

the number and positioning of sialic acid residues.

The standards employed in this study were chosen to determine the response for the

most abundant headgroup and ceramide structures in the human brain. The regression varied

due to both moieties, so interpolations were made to estimate the response for standards that

were not available. There are limited studies that can be directly compared to our results as

comprehensive analysis of intact glycosphingolipids for specific age groups and brain regions is

rare, and the available data shows high variability in the expression of gangliosides for different

regions and developmental stages. Additionally, quantitative results vary based on

normalization techniques to total ion count, lipids, proteins, or tissue mass. Svennerholm et al.

previously reported quantitative information on total gangliosides in the frontal and temporal

cortex for subjects aged 70 and 90.[24] After assigning matching units to our quantitative analysis,

similar conclusions were drawn. Our quantitative results for total gangliosides in the frontal

cortex in the 70-year age range (3.18 µmol bound Neu5Ac/g of tissue), the temporal cortex for

70 (3.45 µmol Neu5Ac/g), and temporal cortex for 90 (3.18 µmol Neu5Ac/g) were within the

biological standard deviation reported in the literature. Similarly, the ratios of individual gangliosides showed consistent trends, with GD1 being the dominant species, followed by GT1, GM1, and the minor gangliosides. The temporal cortex age comparison of control subjects from 70 to 90 years conferred with previous studies showing a minor decrease in total abundance of gangliosides (-8.7%), an increase in GM3, and a shift towards b-series gangliosides. The differences in our results can likely be attributed to the differences in methodologies and our limitations in sampling. Our results from absolute quantitation of total gangliosides produced similar regional trends with a more comprehensive study mapping the bound Neu5Ac content in the human brain.[19] However, quantitative results cannot be directly compared as the results from the literature are normalized to the total protein content.

Alzheimer's disease (AD) is the most common form of neurodegeneration observed in humans, which affects the person's memory, cognition, and behavior. The progressive disorder causes brain shrinkage due to neuronal cell death, and a hallmark symptom is an accumulation of both amyloid-β (Aβ) plaques and Tau tangles. Despite significant resources allocated to understanding this disease, the neuropathological mechanisms are still not fully understood. Gangliosides have been indicated to play a role in AD pathology in numerous instances.[25] Previous work by Kracun et al. showed a significant decrease of GT1b, GD1b, GD1a, and GM1 in the frontal and temporal cortex of AD-affected brains measured in lipid-bound sialic acid.[26] Our results confirm these findings and provide additional information on the ceramide backbone in the changing ganglioside expression. Our observation of GD1a-d18:1/C20 loss in the temporal cortex compared to age-matched controls suggests that neurons expressing this ganglioside are lost in the progression of AD neurodegeneration. A study using GD1a monoclonal antibodies

found this ganglioside was enriched on dystrophic neurites with Aβ plaque, suggesting the ganglioside may play a role in the aggregation of these plaques and the disease pathology.[27]

We also observed that GM1 constituted a larger fraction of the total ganglioside profile in AD subjects. A well-studied interaction involves soluble Aβ to the insoluble β-sheet structure through direct binding with clustered GM1 gangliosides and cholesterol. Insoluble Aβ subsequently acts as a seed for continuous amyloid plaque formation on neuronal synapses.[28] Interestingly, GM1 clustering is enhanced by increased cholesterol in the lipid environment,[29] and over-accumulation of cholesterol has been reported in AD brains.[30] Cholesterol is tightly regulated by apolipoprotein E (APOE), with the APOE ε4 genotype being a genetic marker associated with increased AD risk.

Transcriptomic analysis of AD brains shows an upregulation of ceramide synthase 1 and 2 (CerS1 & CerS2), which are responsible for the addition of C18 only and C18, C20, and C22 acyl groups, respectively.[31] However, Couttas et al. reported that CerS2 shows loss of activity in the temporal cortex as early as Braak stage I despite upregulation.[32] Our results supported this conclusion with decreases in ganglioside-associated C20 and C22 acyls and increases in C18 for both AD-73 (+6.6%) and AD-95 (+9.2%). Whether the changes observed in the ceramide profile are directly correlated to changes in the ganglioside structures is unclear, but differences in lateral organization and interdigitation are likely occurring.

CONCLUSION

A region-specific analysis of the human brain's glycosphingolipid profile was conducted using nanoflow MEA Chip Q/ToF mass spectrometry. In this study found most of the heterogeneity between regions was in ganglioside structures. Further, we found a correlation between ceramide structure and ganglioside structure, where acyl length affected whether an a-series or b-series ganglioside was expressed. Future studies will benefit from a larger sample set with a targeted sampling of neuronal synapses. Additional assays for membrane cholesterol, phosphatidylserine, and proteomics would further elucidate the environment of the bioactive synaptosomal landscape.

REFERENCES

(1)   Keil, J. M.; Qalieh, A.; Kwan, K. Y. Brain Transcriptome Databases: A User's Guide. *Journal of Neuroscience* **2018**, *38* (10), 2399–2412. https://doi.org/10.1523/JNEUROSCI.1930-17.2018.

(2)   Lam, K. H. B.; Faust, K.; Yin, R.; Fiala, C.; Diamandis, P. The Brain Protein Atlas: A Conglomerate of Proteomics Datasets of Human Neural Tissue. *Proteomics*. John Wiley and Sons Inc December 1, 2022. https://doi.org/10.1002/pmic.202200127.

(3)   Bhaduri, A.; Neumann, E. K.; Kriegstein, A. R.; Sweedler, J. V. Identification of Lipid Heterogeneity and Diversity in the Developing Human Brain. *JACS Au* **2021**, *1* (12), 2261–2270. https://doi.org/10.1021/jacsau.1c00393.

(4)   Merrill, A. H. Sphingolipid and Glycosphingolipid Metabolic Pathways in the Era of Sphingolipidomics. *Chemical Reviews*. October 12, 2011, pp 6387–6422. https://doi.org/10.1021/cr2002917.

(5)   Blumenreich, S.; Nehushtan, T.; Barav, O. B.; Saville, J. T.; Dingjan, T.; Hardy, J.; Fuller, M.; Futerman, A. H. Elevation of Gangliosides in Four Brain Regions from Parkinson's Disease Patients with a GBA Mutation. *NPJ Parkinsons Dis* **2022**, *8* (1). https://doi.org/10.1038/s41531-022-00363-2.

(6)   Sipione, S.; Monyror, J.; Galleguillos, D.; Steinberg, N.; Kadam, V. Gangliosides in the Brain: Physiology, Pathophysiology and Therapeutic Applications. *Frontiers in Neuroscience*. Frontiers Media S.A. October 6, 2020. https://doi.org/10.3389/fnins.2020.572965.

(7)   Young, M. M.; Kester, M.; Wang, H. G. Sphingolipids: Regulators of Crosstalk between Apoptosis and Autophagy. *Journal of Lipid Research*. January 2013, pp 5–19. https://doi.org/10.1194/jlr.R031278.

(8)   Fernandis, A. Z.; Wenk, M. R. *Membrane Lipids as Signaling Molecules*; Lippincott Williams & Wilkins, 2007; Vol. 18.

(9)   D'Angelo, G.; Capasso, S.; Sticco, L.; Russo, D. Glycosphingolipids: Synthesis and Functions. *FEBS Journal*. December 2013, pp 6338–6353. https://doi.org/10.1111/febs.12559.

(10)   Schnaar, R. L.; Sandhoff, R.; Tiemeyer, M.; Kinoshita, T. *Essentials of Glycobiology*, 4th ed.; Varki, C., Esko, J., Eds.; Cold Spring Harbor Laboratory Press: La Jolla, 2022.

(11)   van Kooyk, Y.; Rabinovich, G. A. Protein-Glycan Interactions in the Control of Innate and Adaptive Immune Responses. *Nature Immunology*. June 2008, pp 593–601. https://doi.org/10.1038/ni.f.203.

(12) Todeschini, A. R.; Hakomori, S.-I. *Functional Role of Glycosphingolipids and Gangliosides in Control of Cell Adhesion, Motility, and Growth, through Glycosynaptic Microdomains*.

(13) Mencarelli, C.; Martinez-Martinez, P. Ceramide Function in the Brain: When a Slight Tilt Is Enough. *Cellular and Molecular Life Sciences*. January 2013, pp 181–203. https://doi.org/10.1007/s00018-012-1038-x.

(14) Boggs, J. M.; Gao, W.; Hirahara, Y. Myelin Glycosphingolipids, Galactosylceramide and Sulfatide, Participate in Carbohydrate–Carbohydrate Interactions between Apposed Membranes and May Form Glycosynapses between Oligodendrocyte and/or Myelin Membranes. *Biochimica et Biophysica Acta (BBA)* **2008**, *1780* (3), 445–455. https://doi.org/10.1016/j.bbagen.2007.10.015.

(15) Sonnino, S.; Chiricozzi, E.; Grassi, S.; Mauri, L.; Prioni, S.; Prinetti, A. Gangliosides in Membrane Organization. In *Progress in Molecular Biology and Translational Science*; Elsevier B.V., 2018; Vol. 156, pp 83–120. https://doi.org/10.1016/bs.pmbts.2017.12.007.

(16) Ledeen, R. W.; Wu, G. *Ganglioside Function in Calcium Homeostasis and Signaling**; 2002; Vol. 27.

(17) Gleichmann, M.; Mattson, M. P. *Neuronal Calcium Homeostasis and Dysregulation*; Vol. 14. www.liebertpub.com.

(18) Tena, J.; Maezawa, I.; Barboza, M.; Wong, M.; Zhu, C.; Alvarez, M. R.; Jin, L. W.; Zivkovic, A. M.; Lebrilla, C. B. Regio-Specific N-Glycome and N-Glycoproteome Map of the Elderly Human Brain With and Without Alzheimer's Disease. *Molecular and Cellular Proteomics* **2022**, *21* (11). https://doi.org/10.1016/j.mcpro.2022.100427.

(19) Kracun, I.; Rösner, H.; Ćosović, C.; Stavljenić, A. Topographical Atlas of the Gangliosides of the Adult Human Brain. *J Neurochem* **1984**, *43* (4), 979–989. https://doi.org/10.1111/j.1471-4159.1984.tb12833.x.

(20) Micah M. Murray; Mark T. Wallace. *The Neural Bases of Multisensory Processes*; Taylor & Francis, 2012.

(21) Masserini, M.; Tettamanti, G. Interactions of Proteins with Ganglioside-Enriched Microdomains on the Membrane: The Lateral Phase Separation of Molecular Species of GDla Ganglioside, Having Homogeneous Long-Chain Base Composition, Is Recognized by Vibrio Cholerae Sialidase. *American Chemical Society* **1988**.

(22) Preti, A.; Fiorilli, A.; Lombardo, A.; Caimi, L.; Tettamanti, G. Occurrence of Sialyltransferase Activity in the Synaptosomal Membranes Prepared from Calf Brain Cortex. *J Neurochem* **1980**, *35* (2), 281–296. https://doi.org/10.1111/j.1471-4159.1980.tb06263.x.

(23) Tettamanti, G.; Morgan, I. G.; Gombos, G.; Mandel, P. Sub-Synaptosomal Localization of Brain Particulate Neuraminidase. *Brain Res* **1972**, *47* (2), 515–518. https://doi.org/10.1016/0006-8993(72)90661-0.

(24) Svennerholm, L.; Boström, K.; Jungbjer, B.; Olsson, L. Membrane Lipids of Adult Human Brain: Lipid Composition of Frontal and Temporal Lobe in Subjects of Age 20 to 100 Years. *J Neurochem* **1994**, *63* (5), 1802–1811. https://doi.org/10.1046/j.1471-4159.1994.63051802.x.

(25) Ariga, T.; McDonald, M. P.; Yu, R. K. Role of Ganglioside Metabolism in the Pathogenesis of Alzheimer's Disease - A Review. *Journal of Lipid Research*. June 1, 2008, pp 1157–1175. https://doi.org/10.1194/jlr.R800007-JLR200.

(26) Kracun, I.; Kalanj, S.; Talan-Hranilovic, J.; Cosovic, C. Cortical Distribution of Gangliosides in Alzheimer's Disease. *Neurochem Int* **1992**, *20* (3), 433–438. https://doi.org/10.1016/0197-0186(92)90058-Y.

(27) Nishinaka, T.; Iwata, D.; Shimada, S.; Kosaka, K.; Suzuki, Y. Anti-Ganglioside GD1a Monoclonal Antibody Recognizes Senile Plaques in the Brains of Patients with Alzheimer-Type Dementia. *Neurosci Res* **1993**, *17* (2), 171–176. https://doi.org/10.1016/0168-0102(93)90093-6.

(28) Yanagisawa, K. GM1 Ganglioside and Alzheimer's Disease. *Glycoconjugate Journal*. Kluwer Academic Publishers May 26, 2015, pp 87–91. https://doi.org/10.1007/s10719-015-9579-5.

(29) Arumugam, S.; Schmieder, S.; Pezeshkian, W.; Becken, U.; Wunder, C.; Chinnapen, D.; Ipsen, J. H.; Kenworthy, A. K.; Lencer, W.; Mayor, S.; Johannes, L. Ceramide Structure Dictates Glycosphingolipid Nanodomain Assembly and Function. *Nat Commun* **2021**, *12* (1). https://doi.org/10.1038/s41467-021-23961-9.

(30) Feringa, F. M.; van der Kant, R. Cholesterol and Alzheimer's Disease; From Risk Genes to Pathological Effects. *Front Aging Neurosci* **2021**, *13*. https://doi.org/10.3389/fnagi.2021.690372.

(31) Czubowicz, K.; Jęśko, H.; Wencel, P.; Lukiw, W. J.; Strosznajder, R. P. The Role of Ceramide and Sphingosine-1-Phosphate in Alzheimer's Disease and Other Neurodegenerative Disorders. *Mol Neurobiol* **2019**, *56* (8), 5436–5455. https://doi.org/10.1007/s12035-018-1448-3.

(32) Couttas, T. A.; Kain, N.; Suchowerska, A. K.; Quek, L.-E.; Turner, N.; Fath, T.; Garner, B.; Don, A. S. Loss of Ceramide Synthase 2 Activity, Necessary for Myelin Biosynthesis, Precedes Tau Pathology in the Cortical Pathogenesis of Alzheimer's Disease. *Neurobiol Aging* **2016**, *43*, 89–100. https://doi.org/10.1016/j.neurobiolaging.2016.03.027.

Figure S4.1 External standard calibrants used for absolute quantitation.
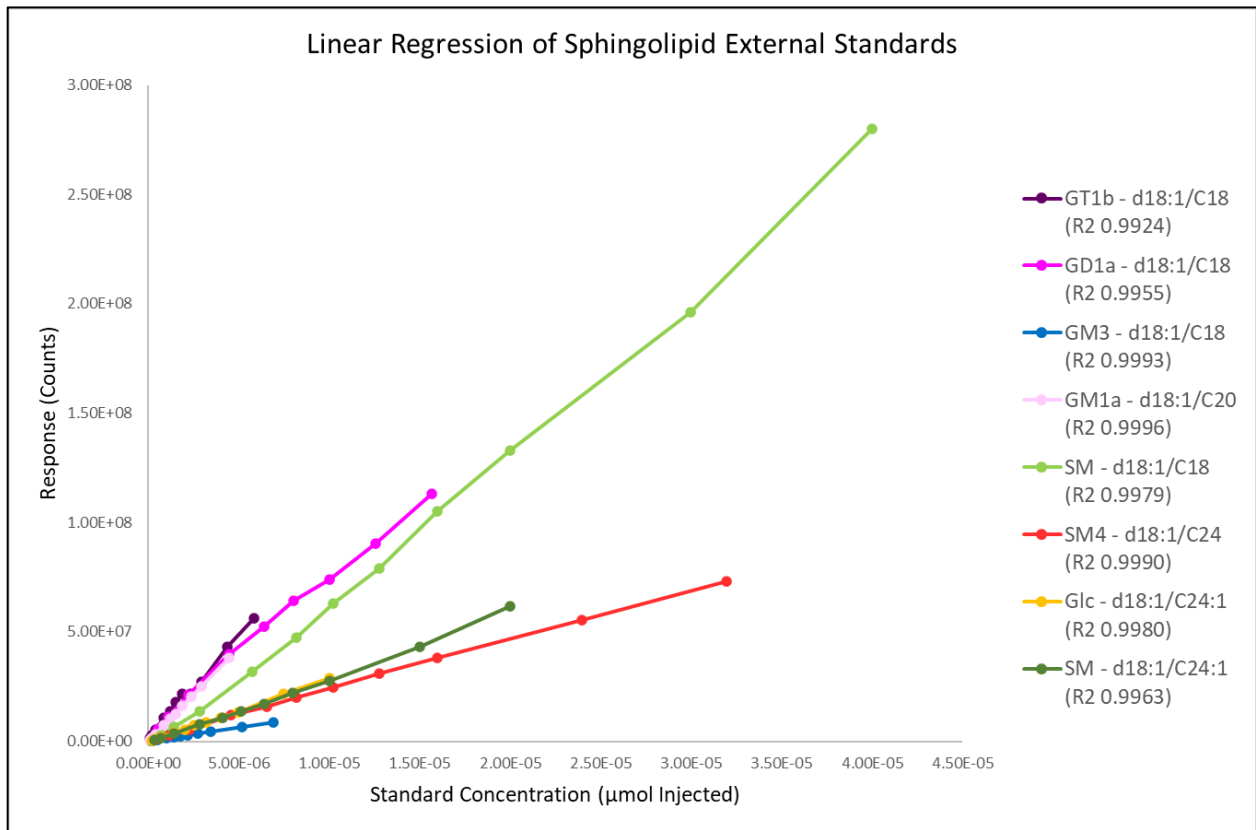
Figure S4.2 Principal component analysis of the glycosphingolipid relative abundances of all ten brain regions resulted in two clusters. Cluster 1 (green) included the frontal cortex, temporal cortex, occipital cortex, and caudate nucleus and cluster 2 (red) included the parietal cortex, cingulate cortex, thalamus, and lateral cerebellum. The posterior hippocampus and pons showed uniqueness in their variance and were not clustered with any other regions.
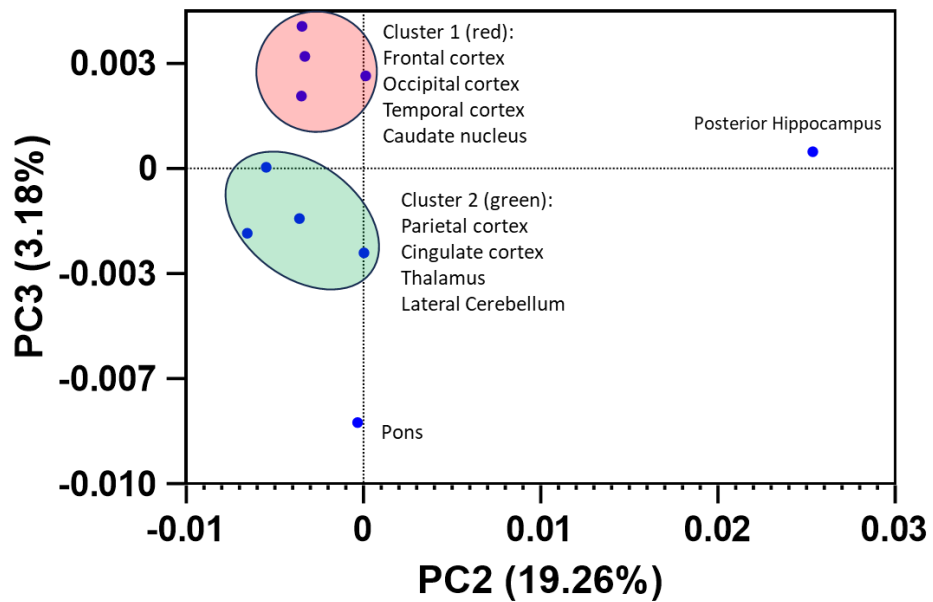
Figure S4.3 Principal component analysis of the glycosphingolipid relative abundances of the temporal cortex for NCI-72, HS-95, AD-74, and AD-93 resulted in two clusters. Cluster 1 (green) included subjects AD-74 and AD-93. Cluster 2 (red) included subjects NCI-72 and HS-95.
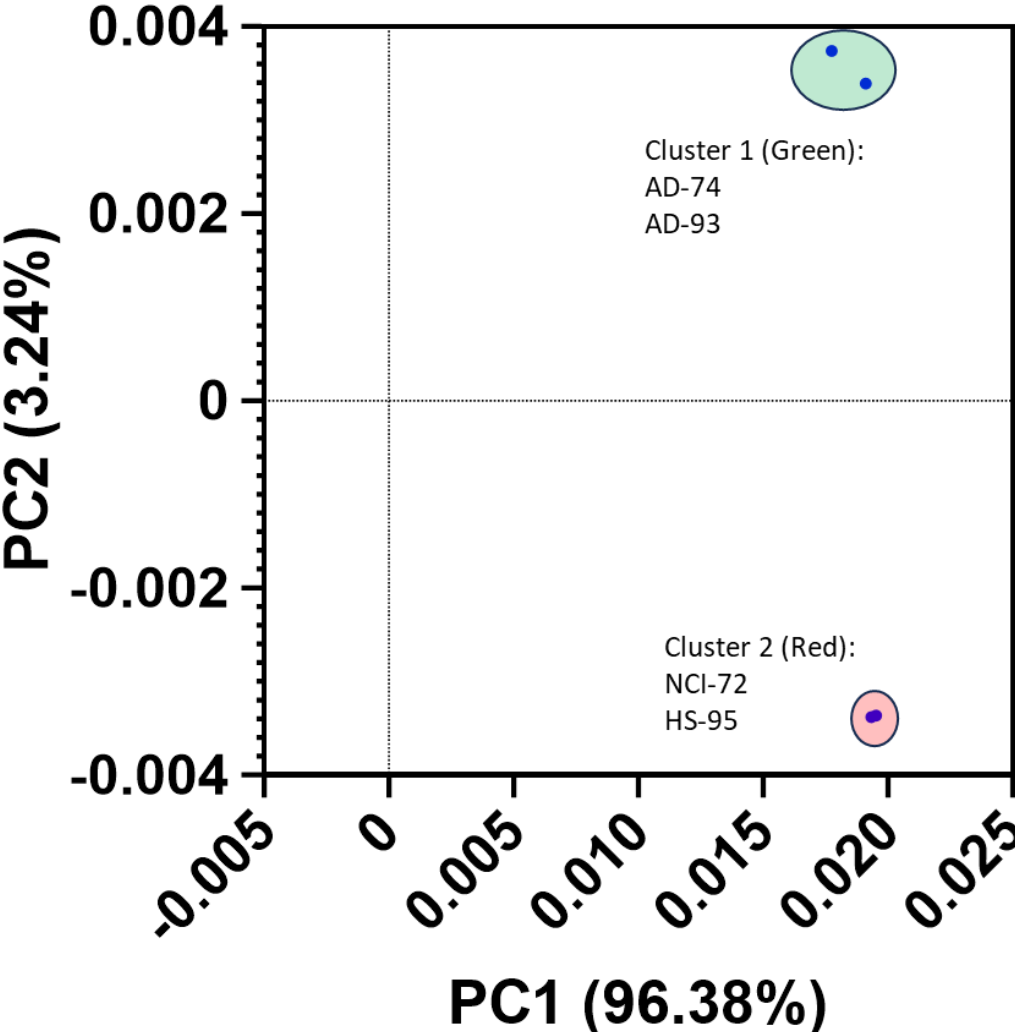
Figure S4.4 Comparison of GD1a and GD1b in the temporal cortex of all 4 subjects. An external standard (GD1a-d18:1/C18) eluted slightly later than GD1b-d18:1/C18 in the samples indicating partial isomeric separation of GD1a and GD1b for the d18:1/C20 ceramide. When looking at GD1-d38:1 in the samples we observed a shouldering peak in NCI-72 & HS-95 which was absent in AD-74 & AD-93, Suggesting loss or significant decrease of GD1a-d18:1/C20 in the temporal cortex of AD effected brains.
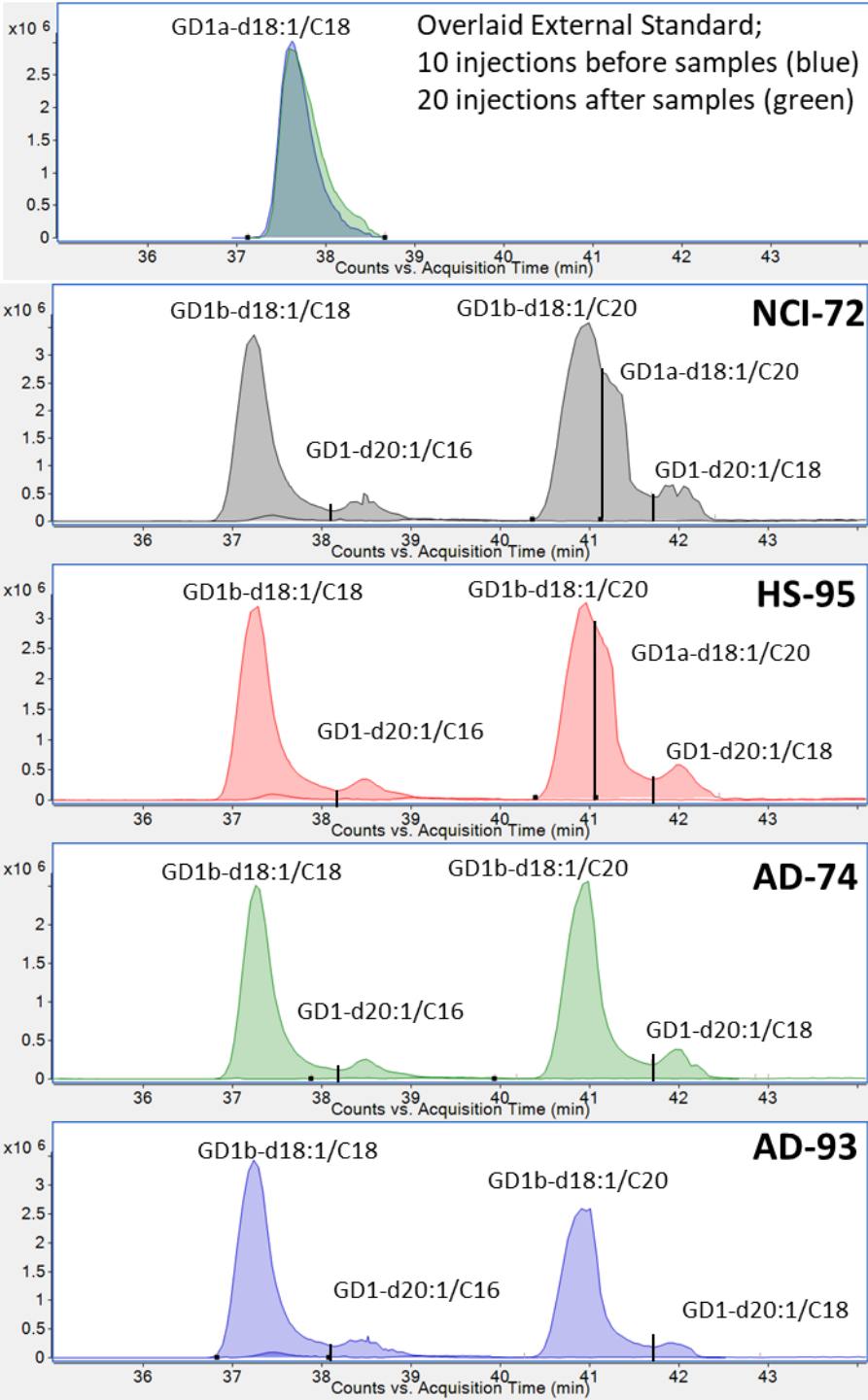
Figure S4.4 Relative abundance profile of ganglioside associated ceramide structures for the temporal cortex of NCI-72, HS-95, AD-74, and AD-93.

Temporal Cortex: Ganglioside Ceramide Profile

	0.00%	-	49.24%

	NCI-72	HS-95	AD-74	AD-93
d18:0 / C18	3.8%	2.9%	3.7%	4.5%
d18:1 / C16	0.7%	0.7%	1.0%	0.6%
d18:1 / C17	0.1%	0.1%	0.1%	0.1%
d18:1 / C18	39.2%	40.0%	45.8%	49.2%
d18:1 / C19	0.6%	0.8%	0.9%	0.4%
d18:1 / C20	38.6%	37.7%	33.9%	31.0%
d18:1 / C21	0.2%	0.2%	0.1%	0.1%
d18:1 / C22	3.1%	4.0%	1.7%	1.7%
d18:1 / C23	0.1%	0.2%	0.1%	0.1%
d18:1 / C24	0.2%	0.3%	0.3%	0.2%
d18:1 / C25	0.1%	0.1%	0.1%	0.1%
d18:1 / C24:1	0.0%	0.5%	0.2%	0.5%
d18:1 / C25:1	0.0%	0.1%	0.1%	0.1%
d18:1 / C26:1	0.2%	0.3%	0.2%	0.1%
d18:2 / C18	2.0%	1.7%	1.9%	2.5%
d18:2 / C20	1.9%	1.8%	1.4%	1.0%
d20:1 / C16	4.2%	3.9%	4.0%	5.3%
d20:1 / C18	4.5%	4.1%	4.2%	1.8%
t18:0 / C18	0.3%	0.3%	0.1%	0.4%
t18:0 / C20	0.4%	0.3%	0.1%	0.2%

APPENDIX I: Relative abundances of all identified sphingolipids from human brain tissue, pooled human serum, and TIB-190 cells from Chapter III.

Sphingolipid[1]	Notes	Sphingoid Base	Acyl Group	Monoisotopic Mass	Tissue Relative Abundances (%)	Serum Relative Abundances (%)	TIB-190 Relative Abundances (%)
*3_1_0_4_0_0_d18:1 / C20	Acidic GQ1	d18:1	20	2447.1928	0.24%	0.00%	0.00%
3_1_0_4_0_0_d18:1 / C18	Acidic GQ1	d18:1	18	2419.1598	0.09%	0.00%	0.00%
3_1_0_3_0_0_d18:1 / C22	Acidic GT1	d18:1	22	2184.1295	0.13%	0.00%	0.00%
3_1_0_3_0_0_t18:0 / C22	Acidic GT1	t18:0	22	2202.1406	0.07%	0.00%	0.00%
3_1_0_3_0_0_d18:1 / C21	Acidic GT1	d18:1	21	2170.1109	0.03%	0.00%	0.00%
*3_1_0_3_0_0_d18:2 / C20	Acidic GT1	d18:2	20	2154.0878	0.03%	0.00%	0.00%
*3_1_0_3_0_0_d18:1 / C20	Acidic GT1	d18:1	20	2156.0974	3.96%	0.00%	0.00%
*3_1_0_3_0_0_t18:0 / C20	Acidic GT1	t18:0	20	2174.1096	0.76%	0.00%	0.00%
*3_1_0_3_0_0_d18:0 / C20	Acidic GT1	d18:0	20	2158.1095	0.28%	0.00%	0.00%
3_1_0_3_0_0_d18:1 / C19	Acidic GT1	d18:1	19	2142.0865	0.06%	0.00%	0.00%
3_1_0_3_0_0_d18:1 / C18	Acidic GT1	d18:1	18	2128.0672	1.94%	0.05%	0.00%
3_1_0_3_0_0_t18:0 / C18	Acidic GT1	t18:0	18	2146.0766	0.21%	0.00%	0.00%
3_1_0_3_0_0_d18:0 / C18	Acidic GT1	d18:0	18	2130.0793	0.14%	0.00%	0.00%
3_1_0_3_0_0_t18:1 / C16	Acidic GT1	t18:1	16	2116.0046	0.04%	0.00%	0.00%
*2_0_0_3_0_0_d18:2 / C20	Acidic GT3	d18:2	20	1788.9133	0.01%	0.00%	0.00%
3_1_0_2_0_0_d18:1 / C26:1	Acidic GD1	d18:1	26:1	1947.09	0.03%	0.00%	0.00%
3_1_0_2_0_0_d18:1 / C24:1	Acidic GD1	d18:1	24:1	1919.053	0.07%	0.00%	0.93%
3_1_0_2_0_0_d18:1 / C24	Acidic GD1	d18:1	24	1921.0727	0.03%	0.00%	0.00%
3_1_0_2_0_0_d18:1 / C22	Acidic GD1	d18:1	22	1893.0363	0.45%	0.00%	0.00%
3_1_0_2_0_0_t18:0 / C22	Acidic GD1	t18:0	22	1911.0468	0.07%	0.00%	0.00%
*3_1_0_2_0_0_d18:2 / C20	Acidic GD1	d18:2	20	1862.9912	0.34%	0.00%	0.00%
*3_1_0_2_0_0_d18:1 / C20	Acidic GD1	d18:1	20	1865.0071	10.31%	0.00%	0.00%
*3_1_0_2_0_0_t18:0 / C20	Acidic GD1	t18:0	20	1883.0156	1.76%	0.24%	0.00%
3_1_0_2_0_0_d18:1 / C19	Acidic GD1	d18:1	19	1850.9945	0.31%	0.00%	0.00%
3_1_0_2_0_0_d18:2 / C18	Acidic GD1	d18:2	18	1834.961	0.20%	0.00%	0.00%
3_1_0_2_0_0_d18:1 / C18	Acidic GD1	d18:1	18	1836.9769	23.63%	0.29%	0.00%
3_1_0_2_0_0_t18:0 / C18	Acidic GD1	t18:0	18	1854.9862	1.99%	0.00%	0.00%
3_1_0_2_0_0_d18:1 / C17	Acidic GD1	d18:1	17	1822.9522	0.04%	0.00%	0.00%
3_1_0_2_0_0_d18:1 / C16	Acidic GD1	d18:1	16	1808.9453	0.07%	0.00%	2.55%
3_1_0_2_0_0_t18:0 / C16	Acidic GD1	t18:0	16	1826.9292	0.03%	0.00%	0.00%
*2_1_0_2_0_0_d18:1 / C20	Acidic GD2	d18:1	20	1702.9626	0.26%	0.00%	0.00%
*2_1_0_2_0_0_d18:0 / C20	Acidic GD2	d18:0	20	1720.9809	0.06%	0.00%	0.00%
2_1_0_2_0_0_d18:1 / C18	Acidic GD2	d18:1	18	1674.9236	0.98%	0.00%	0.00%
2_1_0_2_0_0_t18:0 / C18	Acidic GD2	t18:0	18	1692.9472	0.08%	0.00%	0.00%
2_1_0_2_0_0_d18:0 / C18	Acidic GD2	d18:0	18	1676.945	0.08%	0.00%	0.00%
2_0_0_2_0_0_d18:1 / C24:1	Acidic GD3	d18:1	24:1	1553.9211	0.00%	0.00%	2.95%
2_0_0_2_0_0_d18:1 / C24	Acidic GD3	d18:1	24	1555.9395	0.00%	0.00%	1.05%

2_0_0_2_0_0_d18:1 / C22	Acidic GD3	d18:1	22	1527.913	0.00%	0.15%	0.92%
*2_0_0_2_0_0_d18:1 / C20	Acidic GD3	d18:1	20	1499.8681	0.36%	0.11%	0.68%
2_0_0_2_0_0_d18:1 / C19	Acidic GD3	d18:1	19	1485.8592	0.02%	0.00%	0.00%
2_0_0_2_0_0_d18:2 / C18	Acidic GD3	d18:2	18	1469.8387	0.05%	0.14%	0.00%
2_0_0_2_0_0_d18:1 / C18	Acidic GD3	d18:1	18	1471.8361	0.24%	0.00%	0.68%
2_0_0_2_0_0_t18:0 / C18	Acidic GD3	t18:0	18	1489.8558	0.24%	0.00%	0.00%
2_0_0_2_0_0_d18:1 / C16	Acidic GD3	d18:1	16	1443.8143	0.03%	0.61%	0.00%
2_0_0_2_0_0_d18:1 / C14	Acidic GD3	d18:1	14	1415.7873	0.00%	0.00%	0.76%
4_1_0_1_0_0_d18:0 / C18	Acidic Gal-GM1	d18:0	18	1709.9591	0.02%	0.00%	0.00%
3_1_0_1_0_0_d18:2 / C24	Acidic GM1	d18:2	24	1627.9598	0.00%	0.34%	0.00%
3_1_0_1_0_0_d18:1 / C24	Acidic GM1	d18:1	24	1629.9697	0.00%	0.13%	0.00%
3_1_0_1_0_0_d18:1 / C22	Acidic GM1	d18:1	22	1601.9482	0.09%	0.11%	0.00%
*3_1_0_1_0_0_d18:2 / C20	Acidic GM1	d18:2	20	1571.9044	0.14%	0.00%	0.00%
*3_1_0_1_0_0_t18:0 / C20	Acidic GM1	t18:0	20	1591.9225	0.25%	0.00%	0.00%
3_1_0_1_0_0_d18:2 / C18	Acidic GM1	d18:2	18	1543.8654	0.53%	0.09%	0.00%
3_1_0_1_0_0_d18:1 / C18	Acidic GM1	d18:1	18	1545.8816	11.57%	0.19%	0.00%
3_1_0_1_0_0_t18:0 / C18	Acidic GM1	t18:0	18	1563.8908	1.41%	0.00%	0.00%
3_1_0_1_0_0_d18:0 / C18	Acidic GM1	d18:0	18	1547.8948	0.51%	0.00%	0.00%
3_1_0_1_0_0_d18:1 / C17	Acidic GM1	d18:1	17	1531.8666	0.04%	0.00%	0.00%
3_1_0_1_0_0_d18:2 / C16	Acidic GM1	d18:2	16	1515.8409	0.00%	0.17%	0.00%
3_1_0_1_0_0_d18:1 / C16	Acidic GM1	d18:1	16	1517.8511	0.13%	1.23%	0.00%
2_1_0_1_0_0_d18:1 / C20	Acidic GM2	d18:1	20	1411.8568	0.07%	0.00%	0.00%
*2_1_0_1_0_0_t18:0 / C20	Acidic GM2	t18:0	20	1429.8767	0.03%	0.00%	0.00%
2_1_0_1_0_0_d18:2 / C18	Acidic GM2	d18:2	18	1381.8151	0.07%	0.31%	0.00%
2_1_0_1_0_0_d18:1 / C18	Acidic GM2	d18:1	18	1383.8264	0.98%	0.64%	0.00%
2_1_0_1_0_0_t18:0 / C18	Acidic GM2	t18:0	18	1401.8396	0.17%	0.00%	0.00%
2_1_0_1_0_0_d18:1 / C16	Acidic GM2	d18:1	16	1355.8091	0.00%	0.00%	0.87%
2_0_0_1_0_0_d18:1 / C24:1	Acidic GM3	d18:1	26:1	1290.8586	0.00%	0.00%	1.88%
2_0_0_1_0_0_d18:1 / C24:1	Acidic GM3	d18:1	24:1	1262.8403	0.05%	3.84%	16.36%
2_0_0_1_0_0_t18:0 / C24:1	Acidic GM3	t18:0	24:1	1280.8387	0.00%	0.68%	0.71%
2_0_0_1_0_0_d18:1 / C24	Acidic GM3	d18:1	24	1264.8518	0.00%	2.27%	6.34%
2_0_0_1_0_0_d18:2 / C23	Acidic GM3	d18:2	23	1248.8156	0.00%	0.09%	0.00%
2_0_0_1_0_0_t18:0 / C23:1	Acidic GM3	t18:0	23:1	1266.8166	0.00%	0.17%	0.00%
2_0_0_1_0_0_d18:1 / C23	Acidic GM3	d18:1	23	1250.8287	0.00%	1.04%	0.00%
2_0_0_1_0_0_d18:2 / C22	Acidic GM3	d18:2	22	1234.8062	0.00%	1.21%	0.00%
2_0_0_1_0_0_t18:0 / C22:1	Acidic GM3	t18:0	22:1	1252.8078	0.00%	0.46%	0.00%
2_0_0_1_0_0_d18:1 / C22:1	Acidic GM3	d18:1	22:1	1234.7953	0.00%	0.00%	1.12%
2_0_0_1_0_0_d18:1 / C22	Acidic GM3	d18:1	22	1236.8129	0.00%	2.60%	7.20%
*2_0_0_1_0_0_d18:2 / C20	Acidic GM3	d18:2	20	1206.7714	0.00%	0.33%	0.00%
2_0_0_1_0_0_d18:1 / C20	Acidic GM3	d18:1	20	1208.7952	0.00%	0.83%	5.90%
2_0_0_1_0_0_d18:1 / C18	Acidic GM3	d18:1	18	1180.7471	1.23%	2.14%	1.70%
2_0_0_1_0_0_d18:1 / C17	Acidic GM3	d18:1	17	1166.7296	0.00%	0.33%	0.00%

2_0_0_1_0_0_d18:2 / C16	Acidic GM3	d18:2	16	1150.7055	0.00%	0.40%	0.00%
2_0_0_1_0_0_d18:1 / C16	Acidic GM3	d18:1	16	1152.7209	0.04%	5.63%	12.82%
2_0_0_1_0_0_d18:0 / C16	Acidic GM3	d18:0	16	1154.7261	0.00%	0.00%	1.15%
2_0_0_1_0_0_d18:1 / C14	Acidic GM3	d18:1	14	1124.6821	0.00%	0.00%	1.24%
*3_1_1_2_0_0_d18:1 / C20	Acidic Fuc-GD1	d18:1	20	2011.0637	0.07%	0.00%	0.00%
3_1_1_2_0_0_d18:1 / C18	Acidic Fuc-GD1	d18:1	18	1983.0376	0.14%	0.00%	0.00%
4_1_1_1_0_0_d18:1 / C22	Acidic Gal-Fuc-GM1	d18:1	22	1910.0368	0.02%	0.00%	0.00%
4_1_1_1_0_0_d18:1 / C20	Acidic Gal-Fuc-GM1	d18:1	20	1882.0313	0.93%	0.00%	0.00%
4_1_1_1_0_0_d18:1 / C18	Acidic Gal-Fuc-GM1	d18:1	18	1854.0015	2.50%	0.11%	0.00%
3_1_1_1_0_0_d18:1 / C18	Acidic Fuc-GM1	d18:1	18	1691.9393	0.17%	0.00%	0.00%
3_1_1_1_0_0_t18:0 / C18	Acidic Fuc-GM1	t18:0	18	1709.9591	0.02%	0.00%	0.00%
*4_1_1_0_0_0_d18:2 / C20	Neutral Gal-Fuc-GA1	d18:2	20	1588.9393	0.04%	0.00%	0.00%
4_1_1_0_0_0_d18:1 / C20	Neutral Gal-Fuc-GA1	d18:1	20	1590.9386	0.30%	0.00%	0.00%
*4_1_1_0_0_0_t18:0 / C20	Neutral Gal-Fuc-GA1	t18:0	20	1608.9579	0.10%	0.00%	0.00%
4_1_1_0_0_0_d18:1 / C16	Neutral Gal-Fuc-GA1	d18:1	16	1534.8774	0.00%	0.17%	0.00%
3_1_1_0_0_0_d18:1 / C18	Neutral Fuc-GA1	d18:1	18	1400.8421	0.02%	0.00%	0.00%
3_1_1_0_0_0_d18:1 / C16	Neutral Fuc-GA1	d18:1	16	1372.8151	0.00%	0.14%	0.00%
3_1_0_0_0_0_d18:1 / C24:1	Neutral GA1	d18:1	24:1	1336.8588	0.00%	0.78%	0.00%
3_1_0_0_0_0_d18:1 / C24	Neutral GA1	d18:1	24	1338.8754	0.00%	0.23%	0.00%
3_1_0_0_0_0_d18:2 / C22	Neutral GA1	d18:2	22	1308.8268	0.00%	0.15%	0.00%
3_1_0_0_0_0_d18:1 / C22	Neutral GA1	d18:1	22	1310.8415	0.00%	0.21%	0.00%
3_1_0_0_0_0_d18:0 / C20	Neutral GA1	d18:0	20	1284.8047	0.00%	0.12%	0.00%
3_1_0_0_0_0_d18:1 / C18	Neutral GA1	d18:1	18	1254.7805	0.04%	0.10%	0.00%
3_1_0_0_0_0_d18:2 / C16	Neutral GA1	d18:2	16	1224.7366	0.00%	0.73%	0.00%
3_1_0_0_0_0_d18:1 / C16	Neutral GA1	d18:1	16	1226.7551	0.00%	2.85%	0.78%
3_1_0_0_0_0_d18:1 / C14	Neutral GA1	d18:1	14	1198.7188	0.00%	0.42%	0.00%
3_0_0_0_0_0_d18:2 / C24	Neutral Gb3	d18:2	24	1133.7817	0.00%	0.34%	0.00%
3_0_0_0_0_0_d18:1 / C18	Neutral Gb3	d18:1	18	1051.7056	0.00%	0.10%	0.00%
3_0_0_0_0_0_d18:2 / C16	Neutral Gb3	d18:2	16	1021.6558	0.00%	0.15%	0.00%
3_0_0_0_0_0_d18:1 / C16	Neutral Gb3	d18:1	16	1023.6721	0.00%	0.90%	1.88%
3_0_0_0_0_0_d18:1 / C14	Neutral Gb3	d18:1	14	995.6473	0.00%	0.08%	0.00%
2_0_0_0_0_1_d18:1 / C14	Sulfate SLac	d18:1	16	941.5769	0.00%	0.00%	1.56%
2_0_0_0_0_0_d18:1 / C24:1	Neutral Lac	d18:1	24:1	971.7291	0.02%	0.58%	0.92%
2_0_0_0_0_0_d18:1 / C24	Neutral Lac	d18:1	24	973.7404	0.00%	0.00%	0.42%
2_0_0_0_0_0_d18:1 / C22	Neutral Lac	d18:1	22	945.7196	0.00%	0.00%	0.51%
2_0_0_0_0_0_d18:1 / C20	Neutral Lac	*d18:1	20	917.6686	0.00%	0.00%	0.44%
2_0_0_0_0_0_d18:1 / C18	Neutral Lac	d18:1	18	889.6497	0.07%	0.00%	0.59%
2_0_0_0_0_0_d18:2 / C16	Neutral Lac	d18:2	16	859.6033	0.00%	0.14%	0.00%

2_0_0_0_0_0_d18:1 / C16	Neutral Lac	d18:1	16	861.6189	0.00%	0.68%	5.82%
2_0_0_0_0_0_d18:1 / C14	Neutral Lac	d18:1	14	833.5967	0.00%	0.09%	0.58%
1_0_0_0_0_0_d18:2 / C26 OH	Neutral Hex	d18:2	26 OH	853.7017	0.06%	0.00%	0.00%
1_0_0_0_0_0_d18:2 / C25 OH	Neutral Hex	d18:2	25 OH	839.679	0.07%	0.00%	0.00%
1_0_0_0_0_0_d18:2 / C24 OH	Neutral Hex	d18:2	24 OH	825.6701	0.28%	0.00%	0.00%
1_0_0_0_0_0_d18:1 / C24:1	Neutral Hex	d18:1	24:1	809.6768	0.13%	0.37%	0.00%
1_0_0_0_0_0_t18:0 / C24:1	Neutral Hex	t18:0	24:1	827.6878	0.17%	0.00%	0.00%
1_0_0_0_0_0_t18:0 / C22:1	Neutral Hex	t18:0	22:1	799.6521	0.07%	0.00%	0.00%
1_0_0_0_0_0_d18:1 / C18	Neutral Hex	d18:1	18	727.5984	0.05%	0.00%	0.00%
*1_0_0_0_0_1_d18:1 / C26:1 OH	Sulfate Shex	d18:1	26:1 OH	933.6579	0.25%	0.00%	0.00%
1_0_0_0_0_1_d18:1 / C26:1	Sulfate SM4	d18:1	26:1	917.663	0.15%	0.00%	0.00%
1_0_0_0_0_1_d18:1 / C26 OH	Sulfate SM4	d18:1	26 OH	935.674	0.04%	0.00%	0.00%
1_0_0_0_0_1_d18:1 / C25:1 OH	Sulfate SM4	d18:1	25:1 OH	919.6428	0.23%	0.00%	0.00%
1_0_0_0_0_1_d18:1 / C25:1	Sulfate SM4	d18:1	25:1	903.6463	0.26%	0.00%	0.00%
1_0_0_0_0_1_d18:1 / C25 OH	Sulfate SM4	d18:1	25 OH	921.6599	0.14%	0.00%	0.00%
1_0_0_0_0_1_d18:1 / C25	Sulfate SM4	d18:1	25	905.6598	0.05%	0.00%	0.00%
1_0_0_0_0_1_d18:1 / C24:1 OH	Sulfate SM4	d18:1	24:1 OH	905.6275	0.59%	0.27%	0.00%
1_0_0_0_0_1_d18:1 / C24:1	Sulfate SM4	d18:1	24:1	889.6323	0.59%	0.00%	0.00%
1_0_0_0_0_1_d18:1 / C24 OH	Sulfate SM4	d18:1	24 OH	907.6434	0.47%	0.00%	0.00%
1_0_0_0_0_1_d18:1 / C24	Sulfate SM4	d18:1	24	891.6464	0.09%	0.00%	0.00%
1_0_0_0_0_1_d18:1 / C23:1	Sulfate SM4	d18:1	23:1	875.6035	0.01%	0.00%	0.00%
1_0_0_0_0_1_t18:0 / C24	Sulfate SM4	t18:0	24	909.6566	0.01%	0.00%	0.00%
1_0_0_0_0_1_d18:1 / C23 OH	Sulfate SM4	d18:1	23 OH	893.6275	0.20%	0.00%	0.00%
1_0_0_0_0_1_d18:1 / C23	Sulfate SM4	d18:1	23	877.6321	0.03%	0.00%	0.00%
1_0_0_0_0_1_d18:1 / C22:1	Sulfate SM4	d18:1	22:1	861.5771	0.00%	0.10%	0.00%
1_0_0_0_0_1_d18:1 / C22 OH	Sulfate SM4	d18:1	22 OH	879.6076	0.09%	0.16%	0.00%
1_0_0_0_0_1_d18:2 / C18	Sulfate SM4	d18:2	18	805.541	0.05%	0.00%	0.00%
1_0_0_0_0_1_d18:1 / C18 OH	Sulfate SM4	d18:1	18 OH	823.5509	0.05%	0.00%	0.00%
1_0_0_0_0_1_d18:1 / C18	Sulfate SM4	d18:1	18	807.5502	0.16%	0.00%	0.00%
1_0_0_0_0_1_d18:1 / C16 OH	Sulfate SM4	d18:1	16 OH	795.5245	0.00%	0.74%	0.00%
1_0_0_0_0_1_d18:1 / C16	Sulfate SM4	d18:1	16	779.5219	0.05%	0.26%	0.00%
0_0_0_0_0_0_d18:2 / C26	SM	d18:2	26	840.7087	0.04%	0.00%	0.00%
0_0_0_0_0_0_d18:2 / C25	SM	d18:2	25	826.693	0.05%	0.00%	0.00%
0_0_0_0_0_0_d18:2 / C24:1	SM	d18:2	24:1	810.6593	0.00%	2.67%	0.00%
0_0_0_0_0_0_d18:1 / C25	SM	d18:1	25	828.7147	0.00%	0.06%	0.00%
0_0_0_0_0_0_d18:1 / C24:1	SM	d18:1	24:1	812.6776	0.64%	6.09%	0.59%
0_0_0_0_0_0_t18:0 / C24	SM	t18:0	24	830.6878	0.05%	0.00%	0.00%
0_0_0_0_0_0_d18:1 / C24	SM	d18:1	24	814.6891	0.06%	1.98%	0.00%
0_0_0_0_0_0_d18:2 / C23	SM	d18:2	23	798.6524	0.02%	0.31%	0.00%
0_0_0_0_0_0_d18:1 / C23	SM	d18:1	23	800.6699	0.03%	1.17%	0.00%
0_0_0_0_0_0_d18:2 / C22	SM	d18:2	22	784.643	0.00%	2.13%	0.00%
0_0_0_0_0_0_d18:1 / C22	SM	d18:1	22	786.662	0.04%	3.64%	0.00%

0_0_0_0_0_0_d18:2 / C21	SM	d18:2	21	770.6207	0.00%	0.25%	0.00%
0_0_0_0_0_0_t18:0 / C22	SM	t18:0	22	804.6576	0.04%	0.00%	0.00%
0_0_0_0_0_0_d18:2 / C20	SM	d18:2	20	756.6018	0.00%	0.50%	0.00%
0_0_0_0_0_0_d18:1 / C20	SM	d18:1	20	758.6305	0.43%	1.94%	0.00%
0_0_0_0_0_0_d18:1 / C19	SM	d18:1	19	744.6154	0.04%	0.00%	0.00%
0_0_0_0_0_0_d18:2 / C18	SM	d18:2	18	728.5848	1.57%	2.40%	0.00%
0_0_0_0_0_0_d18:1 / C18	SM	d18:1	18	730.6006	15.89%	3.40%	0.00%
0_0_0_0_0_0_d18:0 / C18	SM	d18:0	18	732.6116	0.18%	0.07%	0.00%
0_0_0_0_0_0_d18:1 / C17	SM	d18:1	17	716.5847	0.19%	0.45%	0.00%
0_0_0_0_0_0_d18:2 / C16	SM	d18:2	16	700.5522	0.12%	6.51%	0.00%
0_0_0_0_0_0_d18:1 / C16	SM	d18:1	16	702.5696	4.22%	23.81%	15.98%
0_0_0_0_0_0_t18:0 / C16	SM	t18:0	16	720.5814	0.03%	0.00%	0.00%
0_0_0_0_0_0_d18:1 / C16	SM	d18:1	16	704.5828	0.06%	0.93%	0.00%
0_0_0_0_0_0_d18:2 / C14	SM	d18:2	14	672.5275	0.00%	0.37%	0.00%
0_0_0_0_0_0_d18:1 / C14	SM	d18:1	14	674.5384	0.46%	3.56%	2.11%
1. Database nomenclature: Hex_HexNAc_Fuc_Neu5Ac_Neu5Gc_Sulf_(OH#)CN:unsat/CN:unsat (OH#)							
*A mixture of Sphingoid bases were observed containing both 18 and 20 carbon length LCBs.							

APPENDIX II: Relative abundances of all identified sphingolipids from regional and subject comparison of the human brain from Chapter IV. NCI-72 regional map of the frontal cortex (A), parietal cortex (B), occipital cortex (C), posterior hippocampus (D), thalamus (E), caudate nucleus (F), Lateral cerebellum (G), pons (H), cingulate cortex (I), temporal cortex (J). HS-95 temporal cortex (K), AD-74 temporal cortex (L), and AD-93 temporal cortex (M).

Sample:	A	B	C	D	E	F	G	H	I	J	K	L	M
Total GSLs:	131	131	130	66	131	136	137	120	130	140	146	133	127
GP1 - d18:1 / C22	0.01%	0.00%	0.00%	0.00%	0.00%	0.00%	0.01%	0.00%	0.00%	0.00%	0.00%	0.00%	0.00%
GQ1 - d18:1 / C22	0.01%	0.02%	0.03%	0.00%	0.07%	0.00%	0.02%	0.04%	0.00%	0.00%	0.00%	0.00%	0.00%
GQ1 - d18:2 / C20	0.00%	0.00%	0.00%	0.00%	0.01%	0.00%	0.00%	0.00%	0.00%	0.00%	0.00%	0.00%	0.00%
GQ1b - d18:1 / C20	0.18%	0.26%	0.32%	0.00%	0.72%	0.26%	0.33%	0.26%	0.12%	0.13%	0.09%	0.13%	0.11%
GQ1 - d18:1 / C18	0.00%	0.00%	0.00%	0.20%	0.06%	0.01%	0.07%	0.04%	0.00%	0.00%	0.01%	0.00%	0.02%
GQ1 - d18:0 / C18	0.00%	0.00%	0.00%	0.00%	0.00%	0.00%	0.01%	0.00%	0.00%	0.00%	0.00%	0.00%	0.00%
GT1 - d18:1 / C26:1	0.00%	0.01%	0.00%	0.00%	0.02%	0.02%	0.00%	0.00%	0.00%	0.01%	0.02%	0.01%	0.01%
GT1 - d18:1 / C26	0.00%	0.00%	0.00%	0.00%	0.00%	0.00%	0.00%	0.00%	0.00%	0.00%	0.00%	0.00%	0.00%
GT1 - d18:1 / C25:1	0.01%	0.00%	0.00%	0.00%	0.01%	0.02%	0.00%	0.01%	0.01%	0.00%	0.02%	0.00%	0.00%
GT1 - d18:1 / C25	0.01%	0.00%	0.00%	0.00%	0.00%	0.02%	0.00%	0.00%	0.00%	0.01%	0.02%	0.00%	0.00%
GT1 - d18:1 / C24:1	0.00%	0.00%	0.00%	0.19%	0.00%	0.02%	0.00%	0.00%	0.02%	0.00%	0.04%	0.00%	0.02%
GT1 - t18:0 / C24:1	0.00%	0.00%	0.00%	0.00%	0.00%	0.00%	0.00%	0.00%	0.00%	0.00%	0.00%	0.00%	0.00%
GT1 - d18:1 / C24	0.02%	0.01%	0.00%	0.00%	0.00%	0.02%	0.01%	0.00%	0.00%	0.02%	0.04%	0.00%	0.01%
GT1 - d18:1 / C23:1	0.00%	0.01%	0.00%	0.00%	0.02%	0.00%	0.01%	0.01%	0.00%	0.00%	0.02%	0.02%	0.02%
GT1 - t18:0 / C24	0.00%	0.00%	0.00%	0.00%	0.00%	0.00%	0.02%	0.00%	0.00%	0.00%	0.00%	0.00%	0.00%
GT1 - d18:1 / C23	0.03%	0.05%	0.02%	0.00%	0.00%	0.05%	0.00%	0.03%	0.00%	0.02%	0.03%	0.02%	0.03%
GT1 - d18:1 / C22	0.12%	0.15%	0.16%	0.00%	0.21%	0.14%	0.15%	0.10%	0.13%	0.13%	0.21%	0.06%	0.05%
GT1-OAc - d18:1 / C22	0.01%	0.04%	0.03%	0.00%	0.04%	0.03%	0.03%	0.00%	0.03%	0.01%	0.02%	0.01%	0.01%
GT1-Lactone - d18:1 / C22	0.00%	0.00%	0.00%	0.00%	0.00%	0.00%	0.00%	0.00%	0.00%	0.01%	0.02%	0.00%	0.00%
GT1 - t18:0 / C22	0.00%	0.00%	0.00%	0.00%	0.00%	0.00%	0.19%	0.00%	0.00%	0.02%	0.02%	0.00%	0.00%
GT1 - d18:1 / C21	0.05%	0.07%	0.05%	0.00%	0.09%	0.06%	0.04%	0.04%	0.04%	0.04%	0.04%	0.03%	0.02%
GT1 - d18:2 / C20	0.00%	0.06%	0.07%	0.47%	0.00%	0.06%	0.08%	0.00%	0.02%	0.05%	0.09%	0.05%	0.06%
GT1b - d18:1 / C20	4.09%	5.11%	5.92%	1.53%	6.12%	4.96%	4.42%	1.55%	2.95%	3.32%	3.31%	2.53%	2.22%
GT1a - d18:1 / C20	0.41%	0.32%	0.40%	0.16%	0.68%	0.54%	0.50%	0.15%	0.22%	0.42%	0.38%	0.20%	0.17%
GT1-OAc - d18:1 / C20	0.40%	1.09%	0.88%	0.06%	0.71%	0.38%	0.29%	0.10%	0.30%	0.00%	0.11%	0.00%	0.15%
GT1-Lactone - d18:1 / C20	0.03%	0.03%	0.04%	0.00%	0.02%	0.04%	0.04%	0.00%	0.00%	0.07%	0.12%	0.02%	0.01%

GT1b - d20:1 / C18	0.68 %	0.79 %	0.79 %	0.07 %	1.12 %	0.51 %	0.52 %	0.26 %	0.50 %	0.31 %	0.36 %	0.46 %	0.33 %
GT1 - t18:0 / C20	0.05 %	0.06 %	0.05 %	0.00 %	0.07 %	0.07 %	0.81 %	0.00 %	0.02 %	0.04 %	0.04 %	0.00 %	0.03 %
GT1 - d18:1 / C19	0.07 %	0.11 %	0.13 %	0.08 %	0.12 %	0.09 %	0.11 %	0.03 %	0.04 %	0.06 %	0.05 %	0.06 %	0.05 %
GT1 - d18:2 / C18	0.00 %	0.00 %	0.00 %	0.64 %	0.00 %	0.00 %	0.00 %	0.00 %	0.00 %	0.00 %	0.00 %	0.00 %	0.00 %
GT1b - d18:1 / C18	0.69 %	1.09 %	1.31 %	6.21 %	1.53 %	0.59 %	2.45 %	0.61 %	0.52 %	0.51 %	0.63 %	1.02 %	0.81 %
GT1a - d18:1 / C18	0.10 %	0.12 %	0.12 %	0.42 %	0.12 %	0.09 %	0.33 %	0.05 %	0.04 %	0.00 %	0.00 %	0.14 %	0.11 %
GT1-OAc - d18:1 / C18	0.05 %	0.15 %	0.28 %	0.26 %	0.16 %	0.08 %	0.13 %	0.00 %	0.00 %	0.04 %	0.02 %	0.10 %	0.06 %
GT1-Lactone - d18:1 / C18	0.00 %	0.00 %	0.00 %	0.18 %	0.00 %	0.00 %	0.03 %	0.00 %	0.00 %	0.00 %	0.00 %	0.00 %	0.00 %
GT1b - d20:1 / C16	0.07 %	0.21 %	0.14 %	0.31 %	0.30 %	0.26 %	0.18 %	0.09 %	0.08 %	0.20 %	0.25 %	0.10 %	0.12 %
GT1 - d18:2 / C17	0.02 %	0.00 %	0.00 %	0.00 %	0.00 %	0.02 %	0.00 %	0.00 %	0.00 %	0.01 %	0.00 %	0.00 %	0.00 %
GT1 - t18:0 / C18	0.00 %	0.00 %	0.00 %	0.00 %	0.00 %	0.00 %	0.10 %	0.00 %	0.00 %	0.00 %	0.00 %	0.00 %	0.00 %
GT1 - d18:0 / C18	0.12 %	0.14 %	0.13 %	0.00 %	0.26 %	0.12 %	0.21 %	0.06 %	0.06 %	0.08 %	0.08 %	0.13 %	0.13 %
GT1 - d18:1 / C17	0.00 %	0.00 %	0.00 %	0.00 %	0.00 %	0.01 %	0.00 %	0.00 %	0.00 %	0.00 %	0.00 %	0.00 %	0.00 %
GT1 - d18:1 / C16	0.01 %	0.01 %	0.00 %	0.00 %	0.00 %	0.00 %	0.00 %	0.00 %	0.01 %	0.01 %	0.01 %	0.00 %	0.00 %
GT1-OAc - d18:1 / C16	0.00 %	0.00 %	0.00 %	0.00 %	0.00 %	0.00 %	0.02 %	0.00 %	0.00 %	0.00 %	0.00 %	0.00 %	0.00 %
GT1-Lactone - d18:1 / C16	0.00 %	0.00 %	0.00 %	0.00 %	0.00 %	0.00 %	0.00 %	0.00 %	0.00 %	0.00 %	0.00 %	0.00 %	0.00 %
GT1 - d18:1 / C14	0.00 %	0.00 %	0.00 %	0.00 %	0.00 %	0.00 %	0.00 %	0.00 %	0.00 %	0.00 %	0.00 %	0.00 %	0.00 %
GT3 - d18:2 / C20	0.00 %	0.00 %	0.00 %	0.00 %	0.00 %	0.01 %	0.00 %	0.00 %	0.00 %	0.00 %	0.01 %	0.00 %	0.00 %
GT3 - d18:1 / C18	0.00 %	0.00 %	0.00 %	0.00 %	0.16 %	0.00 %	0.24 %	0.14 %	0.00 %	0.00 %	0.00 %	0.00 %	0.00 %
GD1 - d18:1 / C26:1	0.10 %	0.06 %	0.06 %	0.00 %	0.06 %	0.17 %	0.00 %	0.00 %	0.00 %	0.09 %	0.16 %	0.10 %	0.05 %
GD1 - t18:0 / C26:1	0.00 %	0.00 %	0.00 %	0.00 %	0.00 %	0.00 %	0.00 %	0.00 %	0.00 %	0.00 %	0.00 %	0.00 %	0.02 %
GD1 - d18:1 / C26	0.01 %	0.00 %	0.00 %	0.00 %	0.00 %	0.02 %	0.00 %	0.00 %	0.00 %	0.00 %	0.02 %	0.00 %	0.00 %
GD1 - d18:1 / C25:1	0.02 %	0.00 %	0.02 %	0.00 %	0.02 %	0.05 %	0.00 %	0.00 %	0.00 %	0.01 %	0.04 %	0.04 %	0.04 %
GD1 - d18:1 / C25	0.04 %	0.00 %	0.02 %	0.00 %	0.01 %	0.08 %	0.00 %	0.00 %	0.01 %	0.04 %	0.06 %	0.04 %	0.03 %
GD1 - d18:1 / C24:1	0.00 %	0.00 %	0.00 %	0.00 %	0.00 %	0.04 %	0.00 %	0.00 %	0.01 %	0.00 %	0.32 %	0.00 %	0.33 %
GD1 - t18:0 / C24:1	0.00 %	0.00 %	0.11 %	0.00 %	0.00 %	0.00 %	0.00 %	0.07 %	0.00 %	0.00 %	0.00 %	0.09 %	0.00 %
GD1a - d18:1 / C24	0.08 %	0.04 %	0.05 %	0.00 %	0.06 %	0.15 %	0.05 %	0.03 %	0.03 %	0.12 %	0.18 %	0.08 %	0.08 %
GD1 - d18:1 / C23:1	0.01 %	0.00 %	0.00 %	0.00 %	0.00 %	0.00 %	0.00 %	0.00 %	0.00 %	0.01 %	0.00 %	0.00 %	0.00 %
GD1 - d18:1 / C23	0.07 %	0.00 %	0.00 %	0.00 %	0.00 %	0.13 %	0.00 %	0.00 %	0.00 %	0.06 %	0.10 %	0.00 %	0.08 %
GD1 - d18:1 / C22:1	0.00 %	0.00 %	0.00 %	0.00 %	0.00 %	0.00 %	0.00 %	0.00 %	0.01 %	0.00 %	0.00 %	0.02 %	0.00 %
GD1a - d18:1 / C22	1.90 %	1.14 %	1.12 %	0.14 %	1.07 %	2.22 %	1.17 %	0.48 %	0.68 %	1.97 %	2.33 %	1.00 %	1.10 %
GD1-OAc - d18:1 / C22	0.00 %	0.06 %	0.06 %	0.00 %	0.02 %	0.06 %	0.00 %	0.00 %	0.03 %	0.00 %	0.00 %	0.05 %	0.00 %

GD1-Lactone - d18:1 / C22	0.00 %	0.00 %	0.00 %	0.00 %	0.00 %	0.00 %	0.00 %	0.00 %	0.00 %	0.01 %	0.13 %	0.00 %	0.00 %
GD1 - t18:0 / C22	0.00 %	0.00 %	0.00 %	0.00 %	0.00 %	0.00 %	0.16 %	0.00 %	0.00 %	0.00 %	0.00 %	0.00 %	0.00 %
GD1 - d18:1 / C21	0.06 %	0.09 %	0.13 %	0.00 %	0.14 %	0.06 %	0.00 %	0.00 %	0.10 %	0.01 %	0.00 %	0.00 %	0.00 %
GD1 - d18:2 / C20	1.07 %	0.62 %	0.58 %	0.59 %	0.41 %	0.00 %	0.65 %	0.00 %	0.37 %	0.86 %	0.93 %	0.60 %	0.83 %
GD1b - d18:1 / C20	18.26 %	18.89 %	11.07 %	1.01 %	17.03 %	16.76 %	14.06 %	5.15 %	9.83 %	14.61 %	13.41 %	18.26 %	17.78 %
GD1a - d18:1 / C20	8.50 %	0.00 %	8.90 %	0.70 %	0.00 %	8.86 %	0.00 %	0.00 %	0.00 %	7.87 %	8.52 %	0.00 %	0.00 %
GD1-OAc - d18:1 / C20	0.92 %	1.24 %	0.92 %	0.00 %	0.45 %	0.91 %	0.57 %	0.14 %	0.32 %	0.65 %	0.26 %	0.59 %	0.69 %
GD1-Lactone - d18:1 / C20	0.21 %	0.15 %	0.28 %	0.00 %	0.12 %	0.37 %	0.23 %	0.06 %	0.10 %	0.88 %	1.13 %	0.15 %	0.09 %
GD1b - d20:1 / C18	2.12 %	2.41 %	2.92 %	0.15 %	2.68 %	2.38 %	1.15 %	0.83 %	1.36 %	2.63 %	2.68 %	2.43 %	1.36 %
GD1 - t18:0 / C20	0.00 %	0.15 %	0.14 %	0.00 %	0.10 %	0.26 %	2.08 %	0.05 %	0.05 %	0.20 %	0.21 %	0.13 %	0.12 %
GD1 - d18:1 / C19	0.64 %	0.00 %	0.64 %	0.00 %	0.00 %	0.70 %	0.00 %	0.00 %	0.00 %	0.00 %	0.38 %	0.36 %	0.00 %
GD1 - d18:2 / C18	0.22 %	0.19 %	0.24 %	6.04 %	0.18 %	0.22 %	0.29 %	0.13 %	0.16 %	0.21 %	0.25 %	0.21 %	0.27 %
GD1b - d18:1 / C18	16.73 %	12.87 %	13.17 %	2.50 %	9.04 %	16.50 %	24.46 %	5.01 %	5.57 %	14.84 %	17.09 %	16.28 %	21.46 %
GD1-Lactone - d18:1 / C18	0.11 %	0.09 %	0.13 %	0.10 %	0.04 %	0.18 %	0.28 %	0.00 %	0.04 %	0.45 %	0.79 %	0.09 %	0.11 %
GD1b - d20:1 / C16	2.23 %	1.28 %	1.73 %	0.36 %	1.29 %	2.66 %	3.28 %	0.75 %	0.70 %	2.20 %	2.39 %	2.05 %	2.59 %
GD1 - t18:0 / C18	0.14 %	0.00 %	0.00 %	0.00 %	0.06 %	0.22 %	2.42 %	0.00 %	0.04 %	0.16 %	0.17 %	0.00 %	0.18 %
GD1 - d18:0 / C18	2.03 %	1.33 %	1.02 %	0.32 %	1.04 %	1.96 %	1.51 %	0.52 %	0.56 %	1.81 %	1.58 %	1.55 %	1.95 %
GD1 - d18:1 / C17	0.00 %	0.00 %	0.06 %	0.00 %	0.03 %	0.04 %	0.07 %	0.03 %	0.00 %	0.03 %	0.04 %	0.04 %	0.04 %
GD1 - d18:1 / C16	0.00 %	0.03 %	0.04 %	0.65 %	0.00 %	0.00 %	0.08 %	0.00 %	0.00 %	0.00 %	0.00 %	0.00 %	0.00 %
GD1-OAc - d18:1 / C16	0.02 %	0.00 %	0.11 %	0.15 %	0.11 %	0.31 %	0.00 %	0.00 %	0.07 %	0.20 %	0.20 %	0.00 %	0.00 %
GD1 - d18:0 / C14	0.00 %	0.00 %	0.00 %	0.00 %	0.00 %	0.00 %	0.00 %	0.00 %	0.00 %	0.02 %	0.03 %	0.00 %	0.00 %
GD2 - d18:1 / C24:1	0.02 %	0.00 %	0.00 %	0.00 %	0.00 %	0.00 %	0.00 %	0.02 %	0.00 %	0.00 %	0.00 %	0.00 %	0.00 %
GD2 - d18:1 / C22	0.00 %	0.00 %	0.00 %	0.00 %	0.00 %	0.00 %	0.00 %	0.00 %	0.00 %	0.00 %	0.16 %	0.00 %	0.00 %
GD2 - d18:1 / C20	1.05 %	0.93 %	0.93 %	0.00 %	0.66 %	0.66 %	0.75 %	0.00 %	0.38 %	0.92 %	1.20 %	1.81 %	1.03 %
GD2 - d18:1 / C19	0.03 %	0.02 %	0.02 %	0.00 %	0.01 %	0.02 %	0.02 %	0.00 %	0.01 %	0.03 %	0.03 %	0.04 %	0.02 %
GD2 - d18:1 / C18	1.08 %	0.85 %	0.72 %	0.10 %	0.65 %	0.70 %	1.86 %	0.22 %	0.45 %	0.89 %	1.22 %	2.16 %	1.53 %
GD2 - d18:0 / C18	0.12 %	0.07 %	0.05 %	0.00 %	0.06 %	0.06 %	0.12 %	0.00 %	0.02 %	0.09 %	0.10 %	0.21 %	0.12 %
GD3 - d18:1 / C24:1	0.00 %	0.00 %	0.00 %	0.00 %	0.03 %	0.00 %	0.10 %	0.16 %	0.00 %	0.00 %	0.00 %	0.00 %	0.00 %
GD3 - d18:1 / C22	0.00 %	0.00 %	0.00 %	0.00 %	0.00 %	0.00 %	0.00 %	0.00 %	0.00 %	0.00 %	0.11 %	0.00 %	0.00 %
GD3 - d18:2 / C20	0.00 %	0.00 %	0.00 %	0.00 %	0.00 %	0.00 %	0.00 %	0.04 %	0.00 %	0.00 %	0.00 %	0.00 %	0.00 %
GD3 - d18:1 / C20	0.54 %	0.53 %	0.54 %	0.00 %	0.50 %	0.30 %	0.78 %	0.37 %	0.23 %	0.44 %	0.00 %	0.86 %	0.48 %
GD3 - d18:1 / C19	0.02 %	0.02 %	0.02 %	0.00 %	0.04 %	0.02 %	0.04 %	0.05 %	0.02 %	0.03 %	0.02 %	0.03 %	0.02 %

GD3 - d18:2 / C18	0.00 %	0.00 %	0.00 %	0.17 %	0.13 %	0.06 %	0.12 %	0.00 %	0.00 %	0.00 %	0.00 %	0.11 %	0.08 %
GD3 - d18:1 / C18	1.27 %	1.78 %	1.15 %	0.17 %	0.00 %	1.79 %	0.45 %	0.00 %	1.45 %	1.04 %	1.40 %	0.00 %	0.00 %
GD3 - t18:0 / C18	0.00 %	0.00 %	0.00 %	0.00 %	0.00 %	0.01 %	0.20 %	0.00 %	0.00 %	0.00 %	0.00 %	0.02 %	0.00 %
GD3 - d18:0 / C18	0.02 %	0.00 %	0.09 %	0.00 %	0.10 %	0.06 %	0.09 %	0.23 %	0.00 %	0.00 %	0.00 %	0.14 %	0.05 %
GD3 - d18:1 / C17	0.02 %	0.03 %	0.01 %	0.00 %	0.04 %	0.01 %	0.03 %	0.06 %	0.00 %	0.00 %	0.00 %	0.00 %	0.00 %
GD3 - d18:1 / C16	0.01 %	0.02 %	0.00 %	0.00 %	0.04 %	0.02 %	0.04 %	0.08 %	0.02 %	0.00 %	0.01 %	0.03 %	0.01 %
GD3 - d18:0 / C16	0.00 %	0.00 %	0.00 %	0.00 %	0.00 %	0.00 %	0.00 %	0.02 %	0.00 %	0.00 %	0.00 %	0.00 %	0.00 %
GM1 - d18:1 / C26:1	0.05 %	0.02 %	0.03 %	0.00 %	0.00 %	0.09 %	0.00 %	0.00 %	0.02 %	0.06 %	0.07 %	0.05 %	0.06 %
GM1 - d18:1 / C26	0.00 %	0.00 %	0.00 %	0.00 %	0.00 %	0.01 %	0.00 %	0.00 %	0.00 %	0.01 %	0.00 %	0.00 %	0.00 %
GM1 - d18:1 / C25:1	0.00 %	0.00 %	0.00 %	0.00 %	0.00 %	0.06 %	0.00 %	0.00 %	0.00 %	0.00 %	0.05 %	0.03 %	0.03 %
GM1 - d18:1 / C25	0.00 %	0.00 %	0.00 %	0.00 %	0.00 %	0.05 %	0.00 %	0.00 %	0.00 %	0.03 %	0.03 %	0.03 %	0.02 %
GM1 - d18:1 / C24 OH	0.00 %	0.00 %	0.00 %	0.00 %	0.00 %	0.06 %	0.00 %	0.00 %	0.00 %	0.04 %	0.06 %	0.00 %	0.00 %
GM1 - d18:1 / C23	0.00 %	0.00 %	0.00 %	0.00 %	0.00 %	0.12 %	0.00 %	0.00 %	0.00 %	0.00 %	0.06 %	0.00 %	0.00 %
GM1 - d18:1 / C22	0.47 %	0.16 %	0.22 %	0.12 %	0.00 %	0.61 %	0.14 %	0.00 %	0.12 %	0.81 %	0.76 %	0.35 %	0.36 %
GM1 - d18:1 / C21	0.09 %	0.00 %	0.07 %	0.00 %	0.04 %	0.15 %	0.00 %	0.00 %	0.00 %	0.15 %	0.12 %	0.06 %	0.06 %
GM1 - d18:2 / C20	0.00 %	0.37 %	0.00 %	0.23 %	0.23 %	0.00 %	0.25 %	0.10 %	0.00 %	0.87 %	0.65 %	0.64 %	0.00 %
GM1 - d18:1 / C20	5.34 %	5.05 %	5.19 %	13.47 %	2.49 %	0.27 %	0.26 %	2.72 %	4.73 %	6.95 %	6.05 %	6.45 %	5.10 %
GM1 - d20:1 / C18	1.26 %	0.73 %	0.87 %	0.13 %	0.00 %	0.00 %	0.00 %	0.19 %	0.67 %	1.38 %	0.89 %	1.00 %	0.00 %
GM1 - t18:0 / C20	0.03 %	0.00 %	0.00 %	0.00 %	0.04 %	0.13 %	0.52 %	0.00 %	0.03 %	0.09 %	0.00 %	0.00 %	0.00 %
GM1 - d18:1 / C19	0.29 %	0.24 %	0.19 %	0.00 %	0.24 %	0.39 %	0.15 %	0.22 %	0.17 %	0.35 %	0.26 %	0.27 %	0.24 %
GM1 - d18:2 / C18	1.36 %	1.02 %	0.68 %	2.52 %	0.46 %	1.51 %	0.67 %	0.47 %	0.55 %	1.60 %	1.26 %	1.33 %	1.87 %
GM1 - d18:1 / C18	12.37 %	8.47 %	18.13 %	51.35 %	12.75 %	14.46 %	9.66 %	24.74 %	19.14 %	16.71 %	13.23 %	18.13 %	17.46 %
GM1 - d20:1 / C16	0.72 %	0.59 %	0.67 %	0.27 %	0.53 %	0.79 %	0.60 %	1.21 %	0.66 %	1.58 %	1.11 %	1.54 %	2.24 %
GM1 - t18:0 / C18	0.11 %	0.05 %	0.00 %	0.00 %	0.00 %	0.22 %	0.88 %	0.10 %	0.00 %	0.13 %	0.06 %	0.07 %	0.16 %
GM1 - d18:0 / C18	1.05 %	0.63 %	0.37 %	0.12 %	0.48 %	1.09 %	0.54 %	1.25 %	0.51 %	1.49 %	0.91 %	1.24 %	1.53 %
GM1 - d18:1 / C17	0.09 %	0.11 %	0.06 %	0.00 %	0.07 %	0.16 %	0.05 %	0.14 %	0.05 %	0.07 %	0.07 %	0.07 %	0.10 %
GM1 - d18:1 / C16	0.46 %	0.59 %	0.39 %	0.30 %	0.33 %	0.73 %	0.42 %	0.56 %	0.29 %	0.43 %	0.37 %	0.46 %	0.42 %
GM1 - d18:0 / C16	0.00 %	0.00 %	0.00 %	0.00 %	0.01 %	0.03 %	0.01 %	0.03 %	0.00 %	0.02 %	0.01 %	0.00 %	0.03 %
GM1 - d18:0 / C14	0.00 %	0.00 %	0.00 %	0.00 %	0.00 %	0.02 %	0.00 %	0.05 %	0.00 %	0.00 %	0.00 %	0.00 %	0.02 %
GM2 - d18:1 / C21	0.00 %	0.00 %	0.00 %	0.00 %	0.00 %	0.00 %	0.00 %	0.00 %	0.00 %	0.01 %	0.00 %	0.00 %	0.00 %
GM2 - d18:2 / C20	0.03 %	0.00 %	0.00 %	0.00 %	0.00 %	0.00 %	0.00 %	0.00 %	0.00 %	0.00 %	0.00 %	0.02 %	0.02 %
GM2 - d18:1 / C20	0.19 %	0.11 %	0.12 %	0.04 %	0.00 %	0.30 %	0.00 %	0.00 %	0.11 %	0.00 %	0.00 %	0.42 %	0.26 %

GM2 - t18:0 / C20	0.01 %	0.00 %	0.00 %	0.00 %	0.00 %	0.01 %	0.04 %	0.00 %	0.00 %	0.01 %	0.00 %	0.00 %	0.00 %
GM2 - d18:1 / C19	0.02 %	0.01 %	0.01 %	0.00 %	0.01 %	0.02 %	0.01 %	0.00 %	0.00 %	0.02 %	0.02 %	0.03 %	0.02 %
GM2 - d18:2 / C18	0.06 %	0.03 %	0.03 %	0.05 %	0.04 %	0.09 %	0.00 %	0.03 %	0.04 %	0.05 %	0.07 %	0.08 %	0.09 %
GM2 - d18:1 / C18	0.77 %	0.58 %	0.44 %	0.09 %	0.50 %	0.95 %	0.75 %	0.44 %	0.40 %	0.95 %	1.08 %	1.90 %	1.67 %
GM2 - t18:0 / C18	0.01 %	0.00 %	0.00 %	0.00 %	0.00 %	0.04 %	0.07 %	0.00 %	0.00 %	0.02 %	0.02 %	0.02 %	0.00 %
GM2 - d18:0 / C18	0.00 %	0.02 %	0.01 %	0.00 %	0.03 %	0.00 %	0.03 %	0.04 %	0.02 %	0.05 %	0.04 %	0.13 %	0.09 %
GM2 - d18:1 / C17	0.01 %	0.00 %	0.00 %	0.00 %	0.00 %	0.02 %	0.00 %	0.00 %	0.00 %	0.00 %	0.00 %	0.00 %	0.00 %
GM2 - d18:1 / C16	0.05 %	0.06 %	0.04 %	0.00 %	0.04 %	0.10 %	0.05 %	0.07 %	0.05 %	0.03 %	0.04 %	0.05 %	0.00 %
GM2 - d18:0 / C14	0.00 %	0.00 %	0.00 %	0.00 %	0.00 %	0.00 %	0.00 %	0.00 %	0.00 %	0.00 %	0.00 %	0.00 %	0.00 %
GM3 - d18:1 / C26:1	0.00 %	0.00 %	0.01 %	0.00 %	0.00 %	0.00 %	0.00 %	0.00 %	0.00 %	0.00 %	0.00 %	0.00 %	0.00 %
GM3 - d18:1 / C26	0.00 %	0.00 %	0.00 %	0.00 %	0.00 %	0.00 %	0.00 %	0.00 %	0.00 %	0.00 %	0.00 %	0.02 %	0.00 %
GM3 - d18:1 / C25:1	0.00 %	0.01 %	0.04 %	0.00 %	0.02 %	0.00 %	0.00 %	0.01 %	0.03 %	0.00 %	0.00 %	0.00 %	0.00 %
GM3 - d18:1 / C24:1	0.00 %	0.00 %	0.11 %	0.00 %	0.09 %	0.02 %	0.06 %	0.11 %	0.17 %	0.00 %	0.06 %	0.16 %	0.08 %
GM3 - d18:1 / C24 OH	0.00 %	0.00 %	0.00 %	0.00 %	0.00 %	0.00 %	0.00 %	0.00 %	0.00 %	0.00 %	0.01 %	0.03 %	0.02 %
GM3 - d18:1 / C24	0.02 %	0.00 %	0.02 %	0.00 %	0.00 %	0.01 %	0.00 %	0.00 %	0.02 %	0.01 %	0.06 %	0.18 %	0.11 %
GM3 - d18:1 / C23	0.00 %	0.00 %	0.00 %	0.00 %	0.00 %	0.00 %	0.01 %	0.00 %	0.00 %	0.00 %	0.01 %	0.03 %	0.02 %
GM3 - d18:1 / C22:1	0.00 %	0.00 %	0.00 %	0.00 %	0.00 %	0.00 %	0.00 %	0.00 %	0.00 %	0.00 %	0.00 %	0.02 %	0.02 %
GM3 - d18:1 / C22	0.00 %	0.00 %	0.00 %	0.00 %	0.00 %	0.02 %	0.01 %	0.00 %	0.01 %	0.02 %	0.06 %	0.15 %	0.10 %
GM3 - d18:2 / C20	0.00 %	0.00 %	0.00 %	0.00 %	0.01 %	0.00 %	0.00 %	0.01 %	0.00 %	0.00 %	0.03 %	0.02 %	0.00 %
GM3 - d18:1 / C20	0.22 %	0.09 %	0.10 %	0.00 %	0.03 %	0.22 %	0.18 %	0.09 %	0.08 %	0.01 %	0.03 %	0.06 %	0.22 %
GM3 - d18:1 / C19	0.01 %	0.00 %	0.00 %	0.00 %	0.01 %	0.00 %	0.01 %	0.02 %	0.00 %	0.01 %	0.00 %	0.01 %	0.01 %
GM3 - d18:2 / C18	0.00 %	0.02 %	0.00 %	0.00 %	0.06 %	0.00 %	0.03 %	0.09 %	0.04 %	0.01 %	0.01 %	0.00 %	0.02 %
GM3 - d18:1 / C18	0.40 %	0.38 %	0.28 %	0.00 %	0.66 %	0.57 %	0.87 %	0.94 %	0.39 %	0.48 %	0.73 %	0.83 %	0.83 %
GM3 - d18:0 / C18	0.00 %	0.00 %	0.00 %	0.00 %	0.00 %	0.00 %	0.00 %	0.06 %	0.01 %	0.00 %	0.00 %	0.05 %	0.04 %
GM3 - d18:1 / C16	0.02 %	0.05 %	0.02 %	0.00 %	0.07 %	0.04 %	0.09 %	0.21 %	0.08 %	0.02 %	0.04 %	0.15 %	0.08 %
Gal-Fuc-GD1 - d18:1 / C22:1	0.00 %	0.00 %	0.00 %	0.00 %	0.00 %	0.00 %	0.00 %	0.00 %	0.00 %	0.00 %	0.01 %	0.00 %	0.00 %
Gal-Fuc-GD1 - d18:1 / C22	0.00 %	0.00 %	0.00 %	0.00 %	0.00 %	0.01 %	0.00 %	0.00 %	0.00 %	0.00 %	0.00 %	0.00 %	0.00 %
Gal-Fuc-GD1 - d18:1 / C20	0.14 %	0.15 %	0.21 %	0.00 %	0.19 %	0.15 %	0.14 %	0.04 %	0.08 %	0.11 %	0.00 %	0.06 %	0.07 %
Gal-Fuc-GD1 - d18:1 / C19	0.00 %	0.00 %	0.00 %	0.00 %	0.00 %	0.00 %	0.00 %	0.00 %	0.00 %	0.00 %	0.01 %	0.00 %	0.00 %
Gal-Fuc-GD1 - d18:1 / C18	0.00 %	0.04 %	0.06 %	0.00 %	0.05 %	0.00 %	0.00 %	0.00 %	0.00 %	0.00 %	0.00 %	0.04 %	0.00 %
Gal-Fuc-GD1 - d18:0 / C18	0.00 %	0.00 %	0.01 %	0.00 %	0.00 %	0.00 %	0.00 %	0.00 %	0.00 %	0.00 %	0.00 %	0.00 %	0.00 %
Fuc-GD1 - d18:1 / C20	0.03 %	0.03 %	0.03 %	0.00 %	0.00 %	0.03 %	0.13 %	0.00 %	0.01 %	0.03 %	0.04 %	0.00 %	0.00 %

Fuc-GD1 - d18:1 / C18	0.02 %	0.02 %	0.02 %	0.00 %	0.00 %	0.00 %	0.18 %	0.00 %	0.00 %	0.01 %	0.04 %	0.03 %	0.06 %
Gal-Fuc-GM1 - d18:2 / C20	0.00 %	0.00 %	0.00 %	0.58 %	0.00 %	0.09 %	0.00 %	0.00 %	0.00 %	0.00 %	0.00 %	0.00 %	0.00 %
Gal-Fuc-GM1 - d18:1 / C20	0.00 %	0.00 %	0.00 %	1.10 %	0.00 %	0.00 %	0.00 %	0.44 %	1.26 %	0.00 %	0.00 %	0.00 %	0.00 %
Gal-Fuc-GM1 - d18:1 / C19	0.00 %	0.05 %	0.00 %	0.00 %	0.04 %	0.07 %	0.04 %	0.00 %	0.06 %	0.04 %	0.04 %	0.04 %	0.03 %
Gal-Fuc-GM1 - d18:2 / C18	0.04 %	0.00 %	0.00 %	0.00 %	0.00 %	0.02 %	0.03 %	0.00 %	0.00 %	0.02 %	0.03 %	0.00 %	0.00 %
Gal-Fuc-GM1 - d18:1 / C18	1.59 %	1.35 %	1.26 %	0.00 %	0.85 %	3.85 %	0.00 %	0.56 %	0.65 %	1.59 %	1.83 %	1.67 %	2.13 %
Gal-Fuc-GM1 - d18:0 / C18	0.09 %	0.00 %	0.05 %	0.00 %	0.05 %	0.11 %	0.07 %	0.00 %	0.04 %	0.08 %	0.08 %	0.00 %	0.33 %
Gal-Fuc-GM1 - d18:1 / C16	0.00 %	0.00 %	0.00 %	0.49 %	0.00 %	0.00 %	0.00 %	0.00 %	0.00 %	0.00 %	0.00 %	0.00 %	0.00 %
GalNAc-Fuc-GM1 - d18:1 / C18	0.00 %	0.05 %	0.00 %	0.00 %	0.00 %	0.00 %	0.00 %	0.00 %	0.00 %	0.00 %	0.00 %	0.03 %	0.00 %
GalNAc-Fuc-GM1 - t18:0 / C18	0.00 %	0.04 %	0.00 %	0.00 %	0.00 %	0.00 %	0.00 %	0.00 %	0.00 %	0.00 %	0.00 %	0.00 %	0.05 %
Fuc-GM1 - d18:1 / C18	0.03 %	0.02 %	0.00 %	0.00 %	0.00 %	0.00 %	0.15 %	0.01 %	0.01 %	0.04 %	0.07 %	0.05 %	0.11 %
Gal-Fuc-GA1 - d18:2 / C20	0.00 %	0.00 %	0.00 %	0.00 %	0.00 %	0.00 %	0.00 %	0.00 %	0.06 %	0.00 %	0.00 %	0.00 %	0.00 %
Gal-Fuc-GA1 - d18:1 / C20	0.00 %	0.00 %	0.00 %	0.00 %	1.30 %	1.76 %	0.00 %	0.00 %	0.00 %	0.00 %	1.25 %	0.00 %	0.72 %
Fuc-GA1 - d18:1 / C18	0.00 %	0.00 %	0.01 %	0.00 %	0.04 %	0.01 %	0.07 %	0.15 %	0.02 %	0.00 %	0.06 %	0.06 %	0.05 %
Fuc-GA1 - d18:1 / C16	0.00 %	0.00 %	0.00 %	0.00 %	0.00 %	0.00 %	0.01 %	0.04 %	0.00 %	0.00 %	0.00 %	0.01 %	0.00 %
GA1 - d18:1 / C24:1	0.00 %	0.00 %	0.00 %	0.00 %	0.00 %	0.00 %	0.00 %	0.00 %	0.00 %	0.00 %	0.03 %	0.06 %	0.00 %
GA1 - d18:1 / C24	0.00 %	0.00 %	0.00 %	0.00 %	0.00 %	0.00 %	0.00 %	0.00 %	0.00 %	0.00 %	0.00 %	0.03 %	0.00 %
GA1 - d18:1 / C20	0.14 %	0.00 %	0.12 %	0.00 %	0.00 %	0.20 %	0.03 %	0.00 %	0.00 %	0.27 %	0.24 %	0.10 %	0.09 %
GA1 - d18:1 / C18	0.00 %	0.00 %	0.03 %	0.00 %	0.00 %	0.07 %	0.11 %	0.12 %	0.00 %	0.01 %	0.24 %	0.15 %	0.00 %
GA1 - d18:1 / C16	0.00 %	0.00 %	0.00 %	0.00 %	0.00 %	0.04 %	0.02 %	0.00 %	0.00 %	0.00 %	0.00 %	0.21 %	0.09 %
Lac - d18:1 / C26:1	0.01 %	0.01 %	0.01 %	0.00 %	0.00 %	0.00 %	0.00 %	0.01 %	0.01 %	0.01 %	0.01 %	0.00 %	0.00 %
Lac - d18:1 / C25:1	0.00 %	0.02 %	0.01 %	0.00 %	0.01 %	0.00 %	0.00 %	0.00 %	0.02 %	0.01 %	0.01 %	0.00 %	0.00 %
Lac - d18:1 / C24:1	0.04 %	0.07 %	0.04 %	0.04 %	0.06 %	0.01 %	0.04 %	0.06 %	0.09 %	0.03 %	0.06 %	0.06 %	0.03 %
Lac - d18:1 / C24	0.00 %	0.01 %	0.00 %	0.00 %	0.00 %	0.00 %	0.00 %	0.01 %	0.01 %	0.00 %	0.00 %	0.01 %	0.00 %
Lac - d18:1 / C22	0.00 %	0.00 %	0.00 %	0.00 %	0.00 %	0.00 %	0.00 %	0.00 %	0.00 %	0.00 %	0.02 %	0.02 %	0.00 %
Lac - d18:2 / C20	0.00 %	0.00 %	0.01 %	0.00 %	0.00 %	0.00 %	0.00 %	0.00 %	0.00 %	0.01 %	0.01 %	0.00 %	0.00 %
Lac - d18:1 / C20	0.03 %	0.00 %	0.00 %	0.00 %	0.00 %	0.00 %	0.00 %	0.00 %	0.00 %	0.06 %	0.10 %	0.05 %	0.04 %
Lac - d18:2 / C18	0.01 %	0.02 %	0.01 %	0.00 %	0.00 %	0.01 %	0.02 %	0.03 %	0.00 %	0.02 %	0.02 %	0.02 %	0.03 %
Lac - d18:1 / C18	0.13 %	0.16 %	0.10 %	0.06 %	0.19 %	0.12 %	0.23 %	0.39 %	0.17 %	0.22 %	0.31 %	0.21 %	0.24 %
Lac - d18:1 / C16	0.03 %	0.05 %	0.02 %	0.00 %	0.06 %	0.03 %	0.06 %	0.17 %	0.05 %	0.03 %	0.04 %	0.38 %	0.12 %
Hex - d18:1 / C26:1	0.06 %	0.12 %	0.00 %	0.09 %	0.07 %	0.00 %	0.05 %	0.15 %	0.13 %	0.00 %	0.00 %	0.03 %	0.02 %
Hex - d18:1 / C26 OH	0.03 %	0.04 %	0.02 %	0.03 %	0.02 %	0.00 %	0.02 %	0.03 %	0.02 %	0.02 %	0.01 %	0.00 %	0.00 %

Hex - d18:1 / C25:1	0.10 %	0.29 %	0.16 %	0.14 %	0.15 %	0.02 %	0.09 %	0.23 %	0.25 %	0.05 %	0.04 %	0.04 %	0.03 %
Hex - d18:1 / C25 OH	0.10 %	0.27 %	0.14 %	0.17 %	0.13 %	0.03 %	0.11 %	0.17 %	0.19 %	0.09 %	0.05 %	0.05 %	0.02 %
Hex - d18:1 / C25	0.01 %	0.04 %	0.01 %	0.00 %	0.01 %	0.00 %	0.01 %	0.06 %	0.03 %	0.01 %	0.00 %	0.00 %	0.00 %
Hex - d18:1 / C24:1	0.44 %	1.56 %	0.67 %	0.56 %	0.95 %	0.00 %	0.54 %	1.88 %	1.29 %	0.20 %	0.16 %	0.20 %	0.12 %
Hex - d18:1 / C24 OH	0.44 %	1.38 %	0.78 %	0.98 %	0.81 %	0.12 %	0.57 %	1.32 %	1.07 %	0.35 %	0.21 %	0.22 %	0.12 %
Hex - d18:1 / C24	0.02 %	0.10 %	0.03 %	0.07 %	0.05 %	0.00 %	0.03 %	0.13 %	0.11 %	0.00 %	0.00 %	0.00 %	0.00 %
Hex - t18:0 / C24	0.02 %	0.05 %	0.00 %	0.03 %	0.02 %	0.00 %	0.00 %	0.05 %	0.04 %	0.01 %	0.00 %	0.00 %	0.00 %
Hex - d18:1 / C23	0.04 %	0.11 %	0.06 %	0.06 %	0.05 %	0.00 %	0.04 %	0.11 %	0.09 %	0.02 %	0.02 %	0.01 %	0.00 %
Hex - d18:1 / C22	0.00 %	0.08 %	0.00 %	0.00 %	0.05 %	0.00 %	0.00 %	0.16 %	0.09 %	0.00 %	0.00 %	0.00 %	0.00 %
Hex - d18:1 / C20	0.00 %	0.00 %	0.00 %	0.00 %	0.07 %	0.00 %	0.00 %	0.18 %	0.09 %	0.00 %	0.00 %	0.00 %	0.00 %
Hex - d18:1 / C18	0.36 %	1.67 %	0.55 %	0.20 %	2.17 %	0.04 %	0.78 %	4.89 %	2.05 %	0.09 %	0.23 %	0.12 %	0.07 %
Hex - d18:1 / C17	0.00 %	0.01 %	0.00 %	0.00 %	0.02 %	0.00 %	0.00 %	0.07 %	0.02 %	0.00 %	0.00 %	0.00 %	0.00 %
Hex - d18:1 / C16	0.01 %	0.04 %	0.02 %	0.00 %	0.06 %	0.00 %	0.01 %	0.13 %	0.05 %	0.01 %	0.00 %	0.01 %	0.00 %
SM3 - d18:1 / C26:1	0.00 %	0.02 %	0.01 %	0.00 %	0.01 %	0.00 %	0.01 %	0.00 %	0.00 %	0.00 %	0.00 %	0.00 %	0.00 %
SM3 - d18:1 / C25:1	0.00 %	0.02 %	0.01 %	0.00 %	0.02 %	0.00 %	0.01 %	0.01 %	0.02 %	0.00 %	0.00 %	0.00 %	0.00 %
SM3 - d18:1 / C25	0.00 %	0.00 %	0.00 %	0.00 %	0.00 %	0.00 %	0.00 %	0.00 %	0.00 %	0.00 %	0.00 %	0.00 %	0.00 %
SM3 - d18:1 / C24:1	0.00 %	0.04 %	0.04 %	0.00 %	0.08 %	0.00 %	0.01 %	0.06 %	0.07 %	0.00 %	0.00 %	0.00 %	0.00 %
SM3 - d18:1 / C24	0.00 %	0.01 %	0.00 %	0.00 %	0.03 %	0.00 %	0.00 %	0.00 %	0.02 %	0.00 %	0.00 %	0.00 %	0.00 %
SM3 - d18:1 / C23	0.00 %	0.00 %	0.00 %	0.00 %	0.01 %	0.00 %	0.00 %	0.01 %	0.00 %	0.00 %	0.00 %	0.00 %	0.00 %
SM3 - d18:1 / C22	0.00 %	0.00 %	0.00 %	0.00 %	0.00 %	0.00 %	0.00 %	0.00 %	0.00 %	0.00 %	0.00 %	0.00 %	0.00 %
SM3 - d18:1 / C20	0.02 %	0.01 %	0.02 %	0.00 %	0.00 %	0.02 %	0.00 %	0.00 %	0.01 %	0.00 %	0.00 %	0.01 %	0.00 %
SM3 - d18:1 / C18	0.04 %	0.06 %	0.04 %	0.00 %	0.09 %	0.06 %	0.07 %	0.10 %	0.07 %	0.05 %	0.04 %	0.03 %	0.03 %
SM4 - d18:1 / C26:1	0.27 %	1.19 %	0.62 %	0.22 %	2.49 %	0.22 %	0.80 %	2.72 %	2.37 %	0.21 %	0.21 %	0.46 %	0.51 %
SM4 - d18:1 / C26 OH	0.06 %	0.15 %	0.10 %	0.05 %	0.24 %	0.07 %	0.12 %	0.22 %	0.21 %	0.06 %	0.04 %	0.06 %	0.07 %
SM4 - d18:1 / C26	0.02 %	0.07 %	0.02 %	0.00 %	0.17 %	0.02 %	0.07 %	0.27 %	0.17 %	0.02 %	0.01 %	0.02 %	0.02 %
SM4 - d18:1 / C25:1	0.43 %	1.68 %	1.23 %	0.00 %	3.21 %	0.39 %	1.25 %	3.02 %	3.33 %	0.30 %	0.34 %	0.68 %	0.63 %
SM4 - d18:1 / C25 OH	0.22 %	0.70 %	0.52 %	0.21 %	1.37 %	0.25 %	0.54 %	0.96 %	1.15 %	0.24 %	0.16 %	0.27 %	0.25 %
SM4 - d18:1 / C25	0.09 %	0.42 %	0.15 %	0.10 %	0.89 %	0.07 %	0.25 %	1.28 %	1.33 %	0.10 %	0.06 %	0.13 %	0.13 %
SM4 - d18:1 / C24:1	0.94 %	6.34 %	3.28 %	0.79 %	0.00 %	0.00 %	3.65 %	0.00 %	12.37 %	0.69 %	0.74 %	1.59 %	1.47 %
SM4 - t18:0 / C25	0.00 %	0.02 %	0.00 %	0.00 %	0.05 %	0.00 %	0.01 %	0.04 %	0.05 %	0.01 %	0.00 %	0.00 %	0.01 %
SM4 - d18:1 / C24 OH	0.74 %	2.52 %	1.72 %	0.89 %	5.16 %	0.78 %	2.21 %	5.74 %	5.05 %	0.84 %	0.62 %	1.00 %	0.88 %
SM4 - d18:1 / C24	0.25 %	1.26 %	0.55 %	0.29 %	2.56 %	0.20 %	0.62 %	4.44 %	3.42 %	0.24 %	0.15 %	0.30 %	0.35 %

SM4 - d18:1 / C23:1	0.03 %	0.16 %	0.10 %	0.00 %	0.00 %	0.00 %	0.09 %	0.10 %	0.06 %	0.02 %	0.02 %	0.05 %	0.04 %
SM4 - t18:0 / C24	0.03 %	0.14 %	0.10 %	0.00 %	0.27 %	0.04 %	0.06 %	0.38 %	0.31 %	0.04 %	0.04 %	0.05 %	0.04 %
SM4 - d18:1 / C23	0.06 %	0.41 %	0.21 %	0.11 %	0.56 %	0.05 %	0.19 %	1.15 %	0.80 %	0.08 %	0.05 %	0.08 %	0.10 %
SM4 - d18:1 / C22:1	0.00 %	0.16 %	0.00 %	0.00 %	0.39 %	0.00 %	0.00 %	0.52 %	0.33 %	0.00 %	0.00 %	0.00 %	0.00 %
SM4 - d18:1 / C22	0.00 %	0.19 %	0.11 %	0.00 %	0.36 %	0.00 %	0.18 %	0.90 %	0.52 %	0.04 %	0.00 %	0.00 %	0.00 %
SM4 - d18:1 / C21	0.00 %	0.05 %	0.02 %	0.00 %	0.00 %	0.00 %	0.00 %	0.10 %	0.06 %	0.00 %	0.00 %	0.00 %	0.00 %
SM4 - d18:1 / C19	0.00 %	0.04 %	0.00 %	0.00 %	0.08 %	0.00 %	0.00 %	0.16 %	0.07 %	0.00 %	0.00 %	0.00 %	0.00 %
SM4 - d18:2 / C18	0.07 %	0.28 %	0.08 %	0.04 %	0.64 %	0.08 %	0.17 %	1.15 %	0.31 %	0.04 %	0.04 %	0.13 %	0.10 %
SM4 - d18:1 / C18 OH	0.06 %	0.19 %	0.09 %	0.00 %	0.60 %	0.08 %	0.17 %	0.89 %	0.28 %	0.05 %	0.07 %	0.05 %	0.04 %
SM4 - d18:1 / C18	0.31 %	1.73 %	0.50 %	0.08 %	4.93 %	0.00 %	0.97 %	11.89 %	3.29 %	0.16 %	0.14 %	0.36 %	0.27 %
SM4 - d18:1 / C17	0.00 %	0.02 %	0.01 %	0.00 %	0.05 %	0.00 %	0.00 %	0.00 %	0.03 %	0.00 %	0.00 %	0.00 %	0.00 %
SM4 - d18:1 / C16	0.00 %	0.04 %	0.02 %	0.00 %	0.16 %	0.02 %	0.07 %	0.31 %	0.12 %	0.02 %	0.00 %	0.03 %	0.00 %
SM4 - d18:0 / C16	0.00 %	0.00 %	0.00 %	0.00 %	0.00 %	0.00 %	0.00 %	0.01 %	0.00 %	0.00 %	0.00 %	0.00 %	0.00 %